

Analytical and Numerical Modelling of Contact Forces in Rotordynamics with Experimental Verification

Master Thesis

$$(EI\nu'')'' = q - \rho A \ddot{\nu} + \Theta^{\sqrt{17}} \int_a^b \mathcal{E} \Omega \int_0^{\infty} \chi^2 \Sigma$$

Svend Erik Andersen
Anders Blichfeldt Markvorsen
September 2019

DANMARKS TEKNISKE UNIVERSITET

**Analytical and Numerical Modelling of Contact Forces in
Rotordynamics with Experimental Verification**

Master Thesis

Authors: Svend Erik Andersen (s133037)
Anders Blichfeldt Markvorsen (s134130)

Supervisor: Professor, Dr.-Ing. Dr.techn. livre-docente Ilmar F. Santos

Technical University of Denmark
Department of Mechanical Engineering
Nils Koppels Allé, building 404,
2800 Kongens Lyngby, Denmark
Phone: (+45) 4525 1960
Fax: (+45) 4525 1961
info.fam@mek.dtu.dk
www.mek.dtu.dk

Abstract

This master's thesis investigates the dynamical behavior of rotor to stator contact. In the industry, rotor to stator contact is found in many types of rotor-dynamical machinery, from bearings and seals to virtually any other stationary component mounted in the vicinity of a rotor. Thus, insights into the dynamical behavior of rotor-stator contact, and impact, may be of great value. In the current work, a mathematical model is formulated for a particular rotor-stator system constituted by a test-rig located at the Department of Mechanical Engineering at DTU. Contact dynamics in the context of rotordynamics is best modeled by combining different mathematical formulations from the respective fields of vibro-impact dynamics and rotordynamics. The same goes for the multi-body mathematical model, presented in this work, as it is pieced together using methods native to both fields. For describing the contact dynamics, the models proposed by Lankarani and Nikravesh, for the normal force, and Ambrósio, for the friction force, are used. For describing the dynamics of the rotor, two formulations are investigated, that is one assuming the rotor to be rigid, and one which includes its flexibility. The rigid formulation results from Euler's second law, while the flexible formulation is obtained using the finite element method. The dynamics of the stator is modeled using Newton's second law. The resulting mathematical model is used to build two simulation codes, i.e. employing the respective rigid- and flexible formulation, in MATLAB. To be able to compare and access the adequacy of the mathematical model and its implementations, the model is fitted to the experimental rotor-stator impact setup. This is done using various experimental data including experimental modal analysis, as well as a finite element model of the impact house. With the system parameters identified, two particular impact cases are studied, that is for the cases of rotational speed of $\Omega = 0$ Hz and $\Omega = 17$ Hz. Here the simulation results from the rigid- and flexible code are compared with each other and the experimentally obtained data from the test rig. From the analysis of the results it is concluded that for the particular rotor-stator system, constituted by the test-rig, the flexibility of the rotor and the houses is significant. Another key result is that the estimation of the first mode of the impact house, in the horizontal direction, is found to completely agree with the experimental results, a result that is a prerequisite for modeling the response correctly, at least in the horizontal direction. Furthermore the general dynamic responses are found to agree somewhat well, albeit with some rather large uncertainties caused by a lack of available information from data obtained experimentally. That is, it is found that the results are encumbered by a lack of sensor information in certain DOFs as well as by the test-rig's

own intrinsic dynamical characteristics, which is found to disturb the dynamics related to rotor-stator contact/impact. The sources of this unwanted dynamics are thought to mostly be attributed to two components in the test-rig. The first being the spherical bearing, which fails to lock the shaft in place the axial direction, while it also introduces anisotropic damping to the rotor. The other component is the PMB which is thought to introduce dynamic cross-coupling stiffness terms, while the mathematical model only includes a static cross-coupling. Nevertheless, this thesis in its entirety should be seen a solid foundation for further work to be done.

Preface

The present thesis serves as being the conclusion of the authors' Master of Science program in the field of Mechanical Engineering at the Technical University of Denmark (DTU). The project was conducted under the supervision of Professor, Dr.-Ing. Dr.techn. livre-docente Ilmar Ferreira Santos, and is a continuation of the work done by Svend in his bachelor thesis as well as in a subsequent special course, also under Professor Santos. The current report is the result of the collective efforts of the authors and the work that have been conducted in the project period from February to September, 2019. The project was originally planned to be finished the 22nd of July, however, due to personal matters in Svend's family that demanded him to be with his father during his last days, the deadline was extended.

The sincerest gratitude must be expressed to our supervisor Ilmar. You have been a great source of inspiration ever since our paths crossed in the introductory course to mechanical vibrations. It is rare to see a professor with such passion, even after so many years of lecturing. Your guidance have been irreplaceable throughout the project, and we thank you for always taking the time out of your busy schedule, and always keeping your door open.

A special thanks shall also sound to: Anders' father Professor Steen Markvorsen, for the casual discussions regarding various mathematical topics, engineering Assistant Per Nielsen, whose commitment to this project, and the test-rig in general, have been indispensable, laboratory engineer Benny Edelsten, for his technical support regarding the electronics and measurement system, engineer assistant Claus Grølsted, for his helpful guidance, and Professor Peder Klit, for lending us his time to discuss the mechanical challenges faced during the construction work.

Lastly we would like to say thank you to our families, and especially our girlfriends. Thank you for your support and comfort when the project demanded the most of us.

September 2019
Kgs. Lyngby, Copenhagen.

Svend Erik Andersen

Anders Blichfeldt Markvorsen

Contents

1	Introduction	1
1.1	Background	1
1.2	Project Scope	2
1.3	The Experimental Setup	2
1.3.1	The Data Acquisition System	5
1.3.2	Control and Acquisition Program	7
2	Test-Rig Preparation and Calibration	9
2.1	Test-Rig Updates	9
2.1.1	PMB Tower Redesign	9
2.1.2	Update of the Inner Houses	11
2.1.3	External Excitation Device	12
2.1.4	Spherical Bearing	14
2.1.5	Miscellaneous	16
2.2	Calibration of Proximity Sensors	17
2.3	Calibration of Force Transducers	18
2.3.1	Impact House Force Transducers	18
2.3.2	Electromagnet Force Transducer	20
2.4	Force Transducer Stiffness	20
2.5	Test-Rig Properties	21
3	Modeling	24
3.1	Contact Dynamics	24
3.1.1	Normal Force Model	25
3.1.2	Friction Force Model	26
3.2	Impact House Dynamics	28
3.2.1	Analytical Model of the Impact House	29
3.2.2	Stiffness and Damping Estimates	31
3.2.3	Modal Properties of the Impact House	33
3.2.4	House Flexibility Effect	34
3.3	Rigid Rotor	36
3.3.1	Assumptions	36
3.3.2	Coordinate Systems	36

3.3.3	Kinematics	37
3.3.4	Kinetics	38
3.3.5	Moments and Products of Inertia	40
3.4	Flexible Rotor	41
3.4.1	Mathematical Representation and the Eigenvalue-Problem	42
3.4.2	The Flexible Shaft	42
3.4.3	Rigid Discs	45
3.4.4	The Unsupported Rotor System	46
3.4.5	Rayleigh Damping	49
3.4.6	The Supported Rotor System	49
3.4.7	Modal Reduction	52
3.4.8	Computational Time Analysis	53
3.4.9	Unbalance of the Rotor System	54
3.4.10	Critical Speeds	55
3.4.11	The Rotor Stator System	57
3.5	Simulation Codes	57
4	Experimental Model Fitting	60
4.1	Experimental Modal Analysis of Rotor System	60
4.1.1	Experimental Setup	60
4.1.2	Experimental Results	62
4.1.3	Modal Damping Parameters	65
4.1.4	Comparison of Experimental Versus Theoretical Results	66
4.2	Experimental Test of Coupling	68
4.2.1	Experimental Setup	68
4.2.2	Experimental Results	70
4.3	Experimental Modal Analysis of the Impact House	70
4.3.1	Experimental Setup	70
4.3.2	Results	72
4.3.3	Comparison of Experimental versus Theoretical Results	75
4.4	Transient response of rigid rotor	75
4.4.1	Experimental Setup	75
4.4.2	Experimental Results	77
4.4.3	Comparison of Experimental Versus Theoretical Results	78
4.5	Experimental unbalance response	80
4.5.1	Experimental Setup	80
4.5.2	Experimental Results	83
5	Results	86
5.1	Non-Rotating Impact Test Results	86
5.1.1	Experimental Setup	86
5.1.2	Experimental Results	87
5.1.3	Comparison of Experimental Versus Theoretical Results	90
5.1.4	Conclusion of Results	92

5.2	Rotating Impact Test Results	92
5.2.1	Experimental Setup	93
5.2.2	Experimental Results	93
5.2.3	Comparison of Experimental Versus Theoretical Results	95
5.2.4	Conclusion of Results	96
6	Conclusion	97
	Bibliography	101
A	Miscellaneous	103
A.1	PMB Adjustment Tool	103
A.2	Excitation Circuit	104
A.3	Rotor Properties from SolidWorks	105
B	Datasheets	106
B.1	Damping Plates	107
B.2	Holding Magnet	108
B.3	Magnet Force Transducer	111
C	Machine Drawings	112
C.1	PMB Tower	113
C.2	Steel Target	116
C.3	Steel House Modifications	119
C.4	Excitation Magnet Tower	121
D	Code	126
D.1	G-code (LabVIEW)	127
D.2	Rigid Equations of Motion	128
D.3	MATLAB Code	133
D.3.1	Rigid Program	133
D.3.2	Flexible Program	154

List of Abbreviations

CAD	Computer-aided design (software)
CCW	Counterclockwise
CW	Clockwise
DOF	Degrees of freedom
EMA	Experimental modal analysis
FEM	Finite Element Method
FRF	Frequency response function
I/O	Input/output
ME	Machine elements
MOSFET	MOS transistor
ODE	Ordinary differential equation
PMB	Permanent magnetic bearing
SDOF	Single degree-of-freedom
SMPS	Switch-mode power supply
SP	Spherical bearing

Nomenclature

V	Matrix (upper case, bold)
----------	---------------------------

v	Vector (lower case, bold)
v, V	Scalar (regular font)
$\mathbf{v}^T, \mathbf{V}^T$	Vector and matrix transpose
m	Mass
d	Damping
k	Stiffness
M	Mass matrix
D	Damping matrix
K	Stiffness matrix
ρ	Density
ν	Poisson's ratio
E	Young's Modulus
ω_n	Undamped natural frequency
ω_d	Damped natural frequency
ζ	Damping ratio
I	Identity matrix
I_T	Transverse mass moment of inertia
I_P	Polar mass moment of inertia
Ω	Rotational velocity of the rotor
δ	Indentation
$\dot{\delta}$	Indentation velocity
$\dot{\delta}^-$	Indentation velocity at impact
F_N	Indentation/Normal force

v_T	Relative tangential velocity
F_T	Tangential friction force
α / β	Damping parameters
ε	Unbalance mass eccentricity
$\varepsilon_x / \varepsilon_y$	Unbalance mass eccentricity components
m_0	Unbalance mass
ft	Force transducer

Chapter 1

Introduction

1.1 Background

The dynamical behavior found when a rotating shaft makes contact with a stationary component, for instance a seal or a bearing, has historically been a popular research topic in the field of rotordynamics. A great part of this interest is probably attributed to the fact that rotor to stator contact is found often in real rotor-dynamical machinery. Here the contact can be intended or unintended. Unintended rotor-stator contact may occur for several reasons, for instance power loss in active magnetic bearings, failure of machine elements, external disturbance et cetera. Conversely, intended rotor-stator contact could occur, for instance when it is needed to catch and carry a shaft supported by hydrodynamic fluid film bearings as the shaft approaches standstill. In either case, it is highly valuable, and sometimes a prerequisite, to be able to predict the details pertaining to the contact dynamics.

Insights into the characteristics of the rotor to stator contact may be gained either from experiments or from mathematical models. Each approach has its pros and cons, but on a general level experiments provide detailed insight into one specific system while coming at a financial cost, whereas mathematical models provide general predictions while only being as good as its assumptions allow it to be. With basis in this underlying construct, the main objective of this thesis is to be able to model the contact dynamics between a rotor and a stator in a rotor-dynamical system mathematically. To this end, for any mathematical model to be adequate, the model has to be able to describe the following: the kinetics of the rotor, the kinetics of the stator, and the contact forces originating once the rotor surpasses the clearance and comes into contact with the stator. In the search of such a model, a plethora mathematical formulations and tools can be employed, that is there are multiple ways to model the contact force, multiple ways to model the rotor and so on.

In this master project two mathematical models are used, where the key difference between the two is that one describes a rigid rotor and have been derived from equilibrium of moments, whereas the other incorporates rotor flexibility by employing the finite element method. Confer the argument concerning the validity of the employed assumption, the validity of the two models is accessed by comparing the theoretically-obtained

results with experimental results obtained from a specific rotor-dynamical system constituted by an experimental setup located at the Department of Mechanical Engineering at DTU.

1.2 Project Scope

The main objective of this project is to investigate the dynamics occurring during rotor to stator impacts, specifically for the newly rebuilt test-rig. In order to do so, a thorough mathematical model of the test-rig dynamics is required.

The original intention with this project was formulated with a special interest in the contact force modeling during impact. However, various shortcomings in regards to the test-rig components and the modeling of the sub-systems constituting the full system, manifested the necessity of a more rigorous analysis than what was first assumed.

A mathematical model of the rotor stator system is to be established, being able to describe the dynamics within a frequency range of 0–1000 Hz. The necessary troubleshooting of any unwanted dynamics caused by the test-rig components will be undergone, modifying these accordingly, as well as implementing new essential components and features, with the objective of constructing a test-rig aiming to better investigate the rotor-stator dynamics.

A mathematical model of a rigid and flexible rotor is conducted, in order to examine the significance of the rotor flexibility, with a special interest at rotor-stator impact. A more thorough mathematical model of the stator impact house, compared to the previously conducted work in regards to this, is to be established on the grounds that previous data suggests the dynamics of the stator to be of greater significance than previously assumed. The mathematical modeling of the contact forces originating at impact is then to be covered and discussed.

A series of experimental tests are performed, with the aim of fitting and validating the various mathematical models pertaining the test-rig dynamics. Finally, a rotating and non-rotating rotor impact experiment is conducted, comparing the adequacy of the mathematical model established, as well as examining the experimental dynamic findings during impact.

1.3 The Experimental Setup

In order to redeem the efforts of trying to model and simulate rotor-stator contact forces, it is paramount to be able to study the actual contact dynamics originating in a physical system. Only by having the reference that an experimental setup can provide, is it possible to validate any mathematical model as well as the numerical implementation. The experimental setup used in this master project is seen in Figure 1.1. The test-rig was originally constructed in 2011 as part of the master’s thesis [12]. In 2018 it received a fundamental redesign during the special course [17]. Finally, some moderate changes were implemented during the course of this project, which is described in detail in the next chapter.

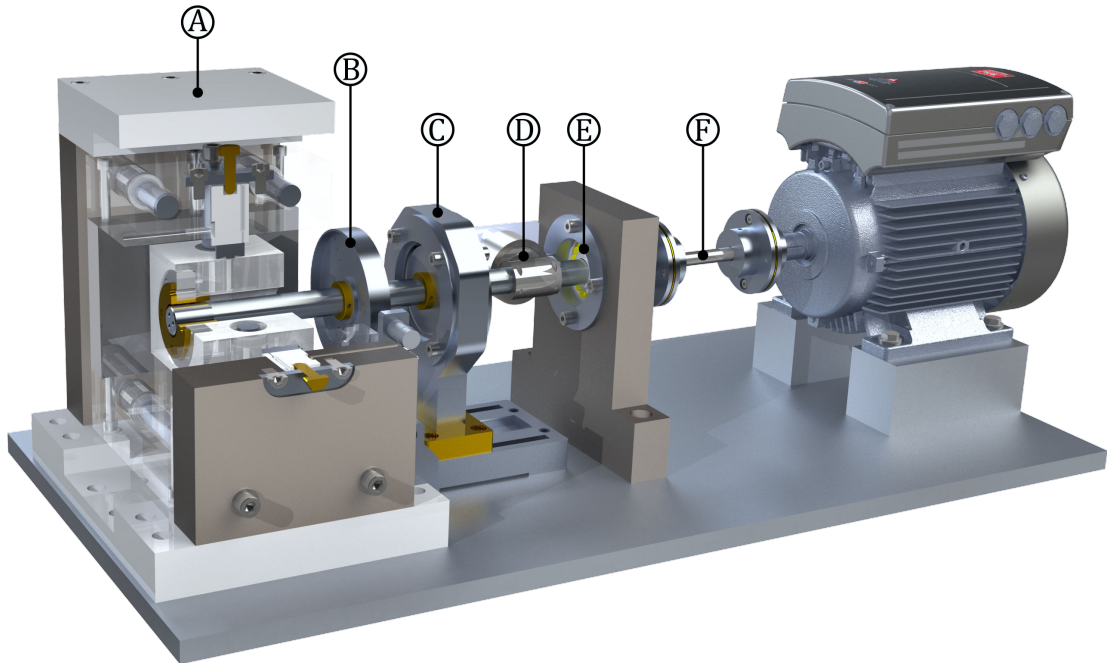


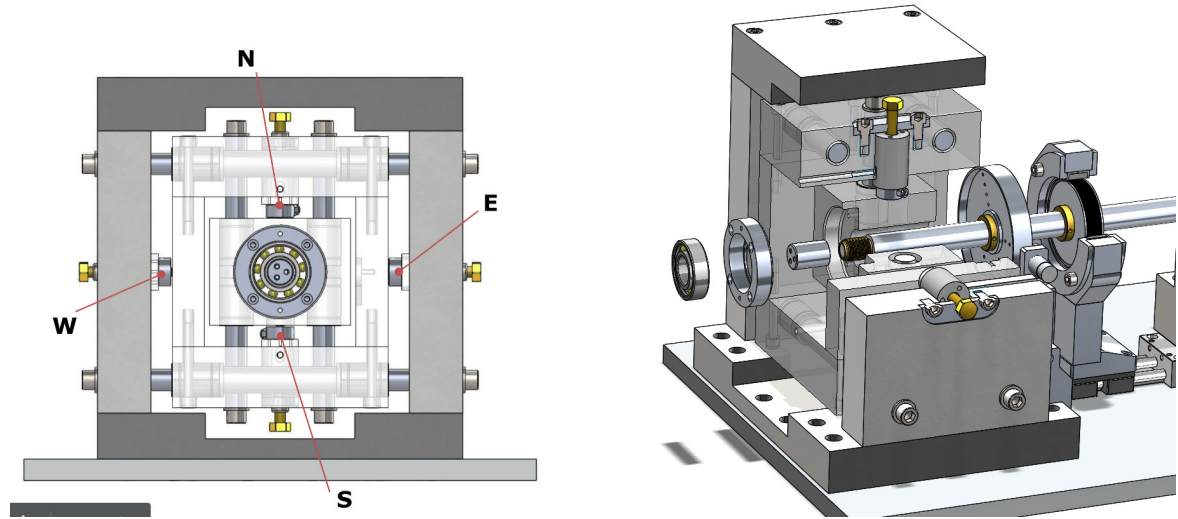
Figure 1.1: CAD model of the rotor-stator contact test-rig, with the main components: (A) the impact house, (B) the unbalance disc, (C) the PMB, (D) the external excitation device, (E) the spherical bearing, and (F) the coupling.

In brief, the test-rig consists of: a rotor, i.e. a shaft with additional components, an *impact-house* containing a replaceable stator component, an excitation device to disturb the rotor, and an electric motor connected to the rotor via a coupling. These components are accompanied by an array of sensors, that is: two displacement sensors, four force transducers, two accelerometers, a rotary encoder, and an additional force transducer installed onto the external excitation device. The shaft is made of aluminum and is located by a spherical roller bearing at one point and levitated by a passive magnetic bearing (PMB) at another point. This way, the rotor is only free to move by pivoting around the spherical bearing, while the PMB provides a restoring force upon displacement. The PMB design utilizes two axially-magnetized ring magnets, where one is mounted onto the rotor and the other is placed around the rotor. The magnets are mounted with parallel polarization to create a permanent magnetic repulsive force that permits the levitation of the rotor. The details pertaining to the magnetic material is given in Table 2.5, in Section 2.5.

In total, the shaft carries four components (machine elements), that is: the *unbalance disc*, the rotor-part of the PMB, the *steel target*, and the coupling. The unbalance disc is the reference where two lateral proximity sensors track the rotor orbit. Furthermore, the disc can also be used to apply discrete unbalance masses to the system via three equidistant rows of threads on the disc. However, contrary to what the name implies, the

disc does not carry any unbalance by default, other than the intrinsic residual unbalance left from manufacturing. The steel target is a sleeve of ordinary ferrous steel that is mounted around the shaft. The target is necessary in order to be able to excite the aluminum shaft laterally by the external excitation device, which consists of a solenoid, i.e. an electromagnet, that is mounted close to the shaft.

The shaft is driven by a four-pole 3 kW electrical motor that is able to provide 19.1 Nm of torque. Thus the motor is assumed to be sufficiently surplus that it will be able to maintain a constant angular velocity throughout the experiments. The motor is connected to the shaft via a flexible coupling, which serves to reduce bending moments while transferring the motor power via its high torsional stiffness. The rotary encoder installed on the main shaft of the motor keeps track of the angular position of the shaft.



(a) The front view of the impact house, showing the two inner houses and placement of the force transducers.

(b) Exploded view of the modular stator system and the replaceable rotor sleeve.

Figure 1.2

The impact house device is an assembly of three components: an outer steel structure and two houses made of polycarbonate referred to as the middle- and inner house. The primary purpose of the impact house is to estimate the contact forces originating in the interface between the rotor and the stator upon rotor-stator impacts or rubs. The design of the impact house, seen in Figure 1.2a, allows for the contact force estimate to be decoupled into a horizontal- and vertical component. This is achieved by a system of guide rods, made of steel, and twelve sliding bearings installed in the two polycarbonate houses. As a result, the innermost house can only move in the vertical direction, while the middle house can only move in the horizontal direction. Between the outer steel walls and the middle house, two force transducers measure the horizontal force component, while two additional transducers between the middle- and the innermost house measure

the vertical force component. By this design the contact forces are measured indirectly, i.e. the acquired force signals are partly attributed to the contact force and partly due to the inertia of the moving inner houses. Therefore, in order to obtain the estimate of the actual force between the contacting bodies, the inertia force of the moving houses must be subtracted from the force signal. The inertia force is measured using two accelerometers, mounted onto the inner houses, where one is aligned vertically with the innermost house while the other is aligned horizontally with the middle house.

Since the primary objective of the test-rig is to study the rotor-stator dynamics in the contact interface, the test-rig has been designed such that it is possible to control the main parameters pertaining to the rotor-stator interface. These parameters include: the material of the rotor, the nominal radial clearance, and the overall stator component. The rotor material property is controlled by a replaceable contact sleeve found at the tip of the shaft, as seen in Figure 1.2b. The contact sleeve is screwed onto a threaded bushing, that is pressed on the shaft. Thus a sleeve of any feasible material can be tested, and by controlling the diameter of the sleeve one also has control over the size of the gap between the rotor and the stator. In this project an aluminum tip is used with a diameter of 25 mm. The stator part of the rotor-stator interface is installed in the inner-most polycarbonate house in the impact house assembly via an adapter piece. Various types of stators can be tested on the test-rig, e.g. bushings, ball bearings or more exotic designs. Thus the test-rig is well-suited for investigating properties of different *back-up bearings*. In this project a brass bushing is used with an internal diameter of 29 mm.

1.3.1 The Data Acquisition System

In the previous section, the sensors central to the test-rig were mentioned. The following section provides an overview of all sensors as well as the details pertaining to the data acquisition system.

The details pertaining each of the sensors used in the experimental setup is listed below:

Force transducers: The four strain gauge force transducers used to estimate the contact forces in the impact house are the 9CB model from HBM. The specific model used in the test-rig is rated to 5 kN. They can only be used to measure compression, thus they are preloaded in the inner houses via the preloading system seen in Figure 1.2a. The strain gauge force transducer mounted at the electromagnet is a bidirectional U9B (2 kN) from HBM.

Accelerometers: The two accelerometers used to estimate the inertia of the inner houses are made by *Metra Mess- und Frequenztechnik* and are of the respective models: KS77C10 for the inner-most house measuring in the vertical direction, and KS77C100 for the middle house measuring in the horizontal direction.

Displacement sensors: The two displacement sensors, mounted around the unbalance disc, keeps track of the rotor orbit at the disc node. The sensors used are KJ8-M18MN50-

<i>Square</i>	<i>Description</i>
Blue	12 V and 24 V power supplies for the circuit board.
Green	MMF M33 signal conditioners for the accelerometers, with IEPE and a permanent analog low-pass filter of 5 kHz.
Red	HBM AE101 signal conditioners for each of the four force transducers, set to a low-pass cutoff of 6 kHz.
Purple	The National Instruments USB-6363 BNC multifunction I/O device, used for control and data acquisition.

Table 1.1: Overview of the highlighted components in the figure to the right.

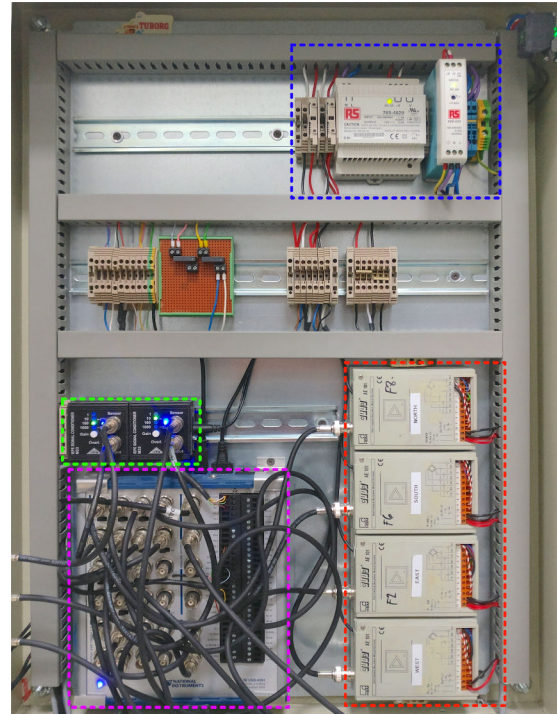


Figure 1.3: Overview of the electronics cabinet.

ANU inductive displacement sensors from Pulsotronic, which work by measuring eddy-currents in the target material and converting the measure into a voltage. Since the sensors in the test-rig are used to track a target that is not flat and made of aluminum (the unbalance disc), the sensor output is only linear in a very limited range. Therefore it is necessary to define a calibration curve for the output voltage in proportion to the displacement of the target.

Rotary Encoder: The rotatory encoder connected to the motor's main shaft, is a three-signaled (A, B, 0) encoder, providing the angle measurement as well as a revolution counter, with a fixed zero-point. The resolution of the sensor is approximately 1° , as it has 360 switches built in.

Before the onset of this project, all the electronics for sensors and control of the test-rig were installed in an unstructured manner, which resulted in loose connection from time to time. Furthermore the electronics cabinet was placed on the steel foundation beside the test-rig, which meant that the cabinet would vibrate during tests due to the dynamics of the test-rig. Therefore it was decided to use a new cabinet and install the components in an orderly fashion, as seen in the result in Figure 1.3. Table 1.1, left of the figure, describes the highlighted electrical components.

1.3.2 Control and Acquisition Program

A program has been implemented in *LabVIEW* to control the test-rig. Its main purposes are: to acquire the data from the sensors, control the external excitation magnet, and provide immediate visual feedback of the dynamics in the system during testing. The front-panel of the program, i.e. the graphical user interface (GUI), is seen in Figure 1.4 and the G-code diagram is included in Appendix D.1. The graphs on the front-panel displays the sensor data in close to real-time. As seen in the figure, starting from the uppermost graph to the left and going counter-clockwise, the following is displayed: the orbit of the rotor centre, the pulling force of the external excitation solenoid, an array of the four force transducer signals, and lastly the two acceleration signals of the impact house.

The programmatic task of acquiring data consists of setting up the USB-6363 I/O device by defining the analogue input channels to be sampled and defining the sampling rate. For most of the experiments a sample rate of 8 kHz has been used. If only the Nyquist–Shannon sampling theorem¹ was to be fulfilled, a sample rate of 2 kHz would be sufficient since the mathematical models are said to be valid up to 1 kHz. However, it is important to take the *aliasing effect* into account, that is anti-aliasing filters must be applied to the analogue signals before sampling. These filters are found in the signal conditioners as analogue low-pass filters. As stated in Table 1.1, the signal conditioners for the accelerometer have a permanent cutoff frequency of 5 kHz, while the conditioners for the force transducers can be set to either 10 Hz or 6 kHz, where the latter of course must be used in order to capture the impact dynamics. Consequently, the 6 kHz cutoff is determinant for the lowest possible sampling frequency if aliasing is to be avoided. To be sure that the power of frequencies spectrum above 6 kHz is in fact zero, it has been chosen to oversample by 2 kHz to 8 kHz, which comes with the additional benefit of yielding a period with the rational value of 0.125 ms.

The other main purpose of the LabVIEW-program is to control the external excitation provided by the solenoid. Here the program is in charge of sending a digital signal to activate the solenoid via a MOSFET relay. The signal is active for the specified duration entered in the **Impact duration** field in the **Impact Control** box, found on the front panel. A typical test is performed as follows: when the rotor orbit appears to have reached steady state, the **Hit** button is pressed in the LabVIEW front panel, here after the program tracks the current rotational angle of the shaft until it surpasses the specified threshold, at which it sends the signal to the MOSFET relay, and thus initiates the impact. More elaborate details regarding the overall implementation of the external excitation is given in Section 2.1.3 in the following chapter.

¹Also known as the cardinal theorem of interpolation. It provides a criterion for choosing lowest sample rate that will permit a perfect reconstructing of the original analogue signal from the samples.

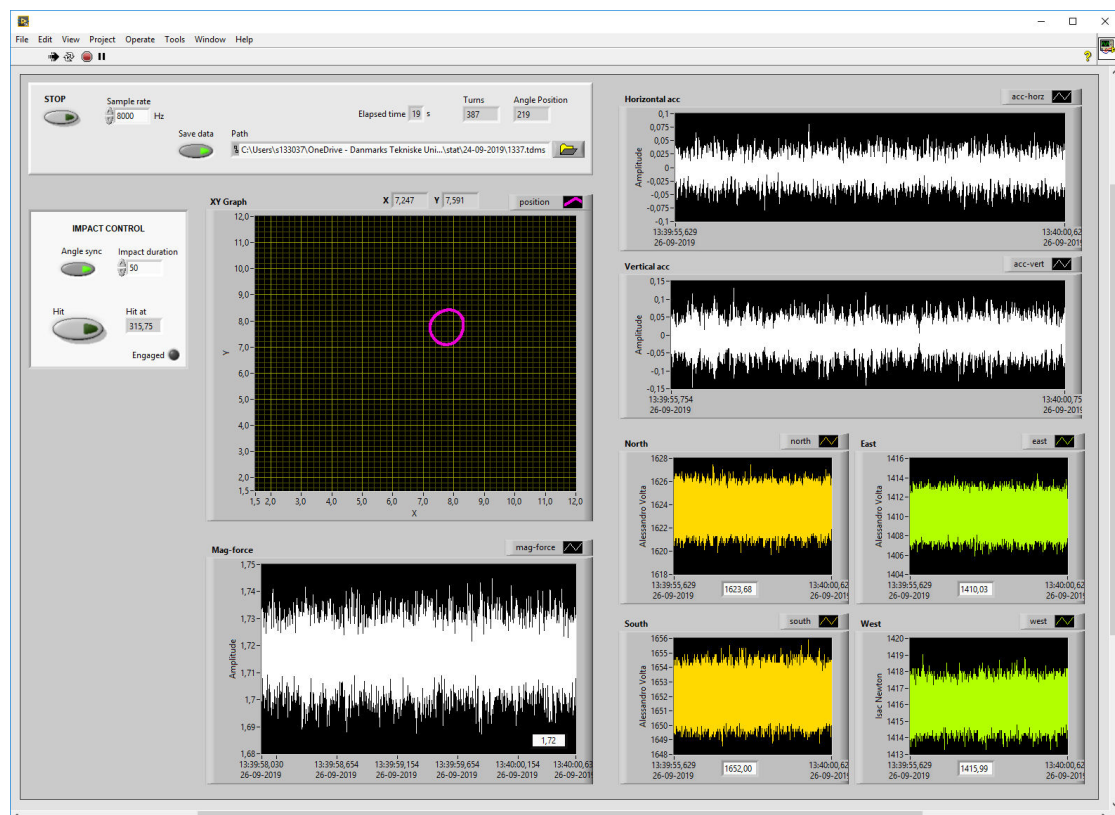


Figure 1.4: The front-panel of the LabVIEW program.

Chapter 2

Test-Rig Preparation and Calibration

The experimental test-rig, presented in the previous section, underwent a substantial number of updates and fundamental design changes just prior to this master's project. Hence the new design and its performance was not thoroughly verified upon the onset of the project. As a result of this, some shortcomings of the test-rig were identified along the course of the project. Some of these shortcomings were deemed to be of such significance that they had to be rectified. In the following chapter the accommodation of these shortcomings as well as calibration of the sensors in the setup is presented.

2.1 Test-Rig Updates

In this section the significant design updates, that have been implemented during the project, are presented.

2.1.1 PMB Tower Redesign

The passive magnetic bearing is a crucial component in the test-rig, since it provides the main source of restoring force to the rotor, whereby it determines a large part of the dynamics of the rotor. Upon commencing on the experimental part of this project, it was found that rotor did not display a unique static equilibrium at zero angular velocity. That is, upon applying small perturbations to the shaft in any direction, the shaft would find rest at noticeably different locations. Since this behavior would be infeasible to model mathematically, the discovery was deemed to be a defect that had to be accommodated before proceeding with any experimental work. The cause of this behavior was found to originate in the newly-designed positioning system.

Due to the configuration of the rotor- and stator part of the PMB, to obtain a radial load-carrying capacity, the two magnets will additionally exert a mutual axial repulsive force. Thus the two parts need to be placed and held in a position so that the centers of each magnet reside in planes close to each other for the bearing to work. As presented in [17], it was chosen to implement an off-the-shelf lead-screw positioning system, seen in Figure 2.1, for this task. In part the system helped to mount the shaft,

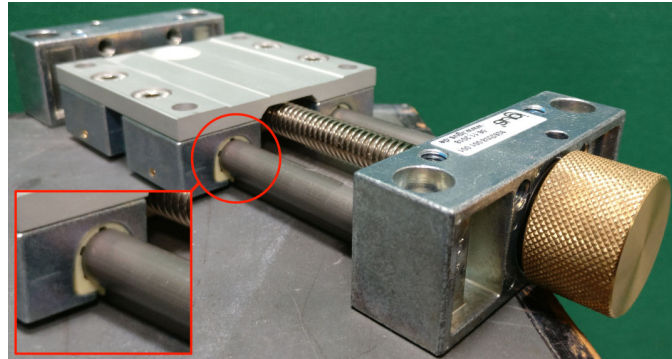
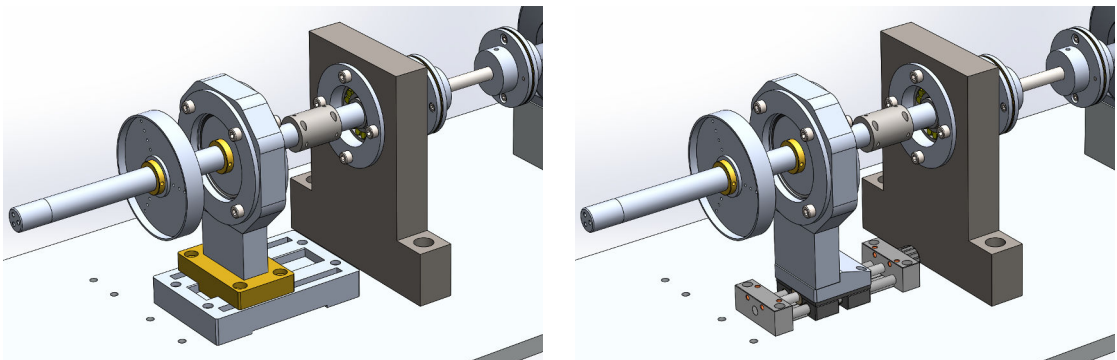


Figure 2.1: The positioning system from *igus GmbH*, with one of the sliding bearings highlighted.

where the powerful magnetic forces hamper the assembly process, and partly the system also allowed to adjust the magnetic forces, as displacing the centers planes attenuates the load-carrying capacity.

The positioning system had a pre-loading feature as well as a locking mechanism, so initially the component seemed very suitable for its proposed task. However, it was found that the inbuilt sliding bearings, highlighted in Figure 2.1, were too compliant. To obtain a maximum load-carrying capacity, the two PMB parts should be aligned perfectly, however, at this point the PMB is unstable in the axial direction, due to the force gradient changing very rapidly, i.e. mathematically this location is a saddle point. Because of this fact, the large axial forces would induce a moment that was found to compress the sliding bearings, making the whole bearing tower tilt a considerably amount. As an effect, the shaft would adopt different equilibria, as described, when perturbed.



(a) The new design, using a simple T-slot positioning system.

(b) The old design, using the lead-screw system.

Figure 2.2: Comparison of the *new* and *old* PMB design. Note the impact house has been removed in these figures.

Amongst different proposed solutions to accommodate the issue, it was chosen to design a new and more robust bearing tower for the PMB. The new design simply consists of an aluminum base with a slot, where a T-shaped brass foot fixes the rotation of the bearing tower, containing the stator magnet. To position the tower, a special tool has been manufactured which consists of an ordinary 10 mm bolt and a hexagonal extruded profile containing a thread, as seen in Figure A.1 in the appendix. Screwing the tool completely together, and positioning the bearing tower behind the rotor magnet (towards to motor), the bolt can be untightened which steadily forces the tower forward. While doing so, a vise is loosened accordingly to stop the bearing tower once it reached the unstable point as the magnets align perfectly. Once in position, four bolts, sliding in two T-slots, are tightened to finally lock the bearing tower in the axial direction. The new- and the old PMB design are compared in Figure 2.2.

2.1.2 Update of the Inner Houses

As mentioned when presenting the various sensors in the test-rig, the force transducers need to be preloaded since they only work in compression, thus when preloaded, tension is perceived by the transducers as *less* compression. The inner polycarbonate houses are key components as they contain this preloading feature, as illustrated in Figure 2.3. During the initial setup of the preload, it was noticed that the adjustable transducer base was sticking in its seating, where it normally should be sliding smoothly. Furthermore the inner houses also displayed quite a lot of friction when moving the houses along the guide rods with the forces transducers removed. When dissembling the impact house during troubleshooting, it was noticed that spacers had been placed between the sides and the top of the middle house. Further investigation unveiled that these spacers had been put there to compensate for an unmet tolerance of the middle house sides.

In addition to the sticking transducer bases, the spacers also weaken the bolted connection between the sides and the top in the middle house. This weakens the adequacy of the assumption that middle house is a rigid body, an assumption used in the mathematical models. Consequently it was chosen rectify the gap created by the drift in the tolerances. Originally the plan was to have two new sides made in polycarbonate according to the original tolerances, however, it was not possible to acquire the material in the right dimensions within a reasonable time, relative to this project's deadline. Instead it was decided to mill around 5 mm off the sides and insert an aluminum spacer in each side, so that the two parts together fulfilled the specified tolerances. In addition, since the impact house already was disassembled, most of the sliding bearings were replaced, as an additional effort for reducing the friction between the inner houses and the guide rods.

With these modification implemented, the transducer bases were found to slide more easily, however, some sticking was still present. According to measurements, this is likely to be caused by the base seating being oval to a small extend instead of perfectly round. As a step to decrease the remaining sticking, a thin lubricant was applied to the transducer bases before assembly. On the other hand, the friction, when moving the inner houses along the guide rods, was found to have been reduced significantly.

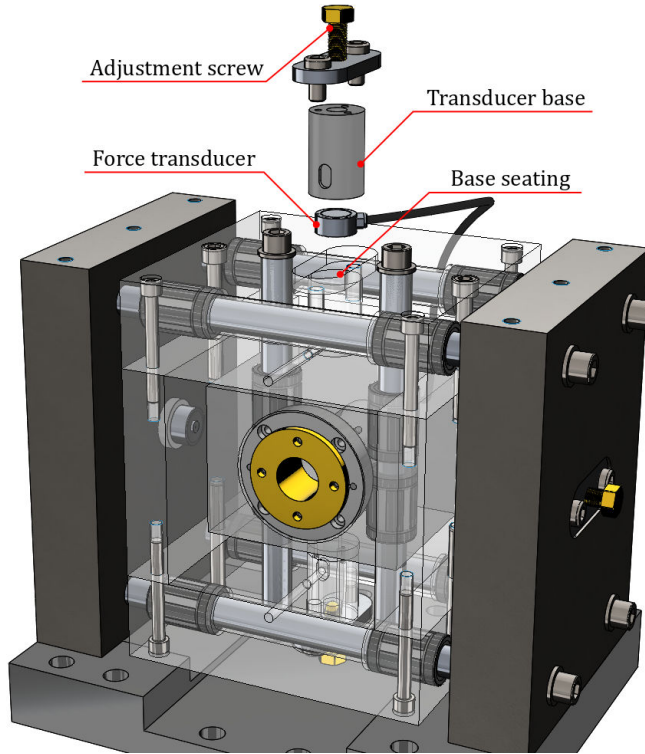


Figure 2.3: Exploded view of the housing, with the top of the steel construction removed, showing the preloading mechanism.

2.1.3 External Excitation Device

In the special course [17], a new device for exciting the shaft laterally was devised. Instead of previously, where the shaft has been excited by physical contact, either by a manual pendulum or an automatic solenoid, it was decided to pull the shaft into the contact state using an electromagnet. The advantage with this method is that it is thought to be less invasive since it does not induce a friction force upon engagement. Conversely, this method adds some complexity pertaining to the hysteresis of the solenoid and the associated control task.

Preceding this project the electromagnet (solenoid) was already available, so the remaining practical tasks that have been addressed in this project were: **1.** To make it possible to pull the aluminum shaft via the solenoid. **2.** To mount the electromagnet. **3.** To drive the solenoid and synchronize its actuation. The chosen solution for the first and second task can be seen in Figure 2.4. The electromagnet is fastened to a stiff bracket tower through a bidirectional U9B (2 kN) force transducer from HBM. The magnet may be adjusted in its position relative to the shaft by a slot in the bracket. The details of the bracket tower design is given in Appendix C.4.

Since aluminum is paramagnetic, it is only attracted very little by the magnetic field induced by the solenoid. Thus, in order to pull the shaft, it was necessary to

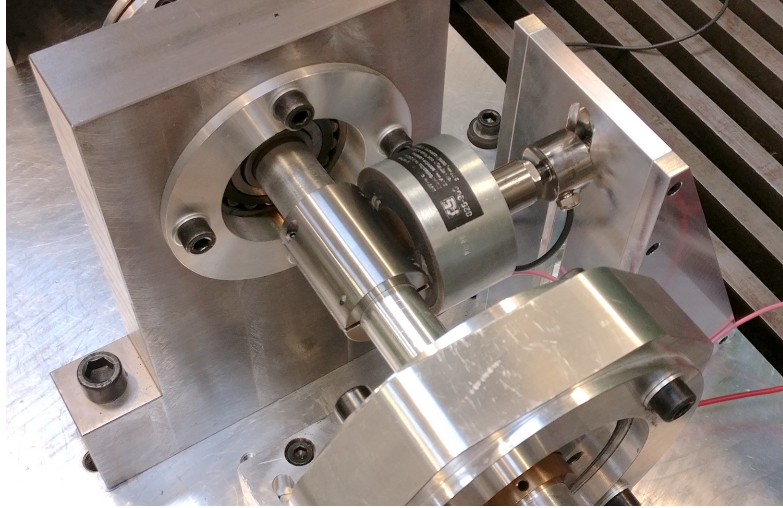


Figure 2.4: The system used to excite the rotor, consisting of an electromagnet, connected to a force transducer, and a steel target.

install a ferromagnetic material around the shaft to function as a *target* for the magnet. The target, as seen in the figure, consists of two pieces of steel, which are screwed together, which effectively clamps it to the shaft. Originally the target was to be cut into three pieces, as seen in the machine drawing in Appendix C.2, to make it rotationally symmetric. However, due to difficulties in manufacturing at the time, the design was simplified into one using two pieces, but considering its location close to the spherical bearings, the negative effect of its slight asymmetry is assumed to be rather small.

To obtain a satisfactory level of repeatability during tests, it is necessary to take the timing of the actuation relative to the rotor unbalance into account. Thus a central improvement in this project, compared with previous work, is that the external excitation

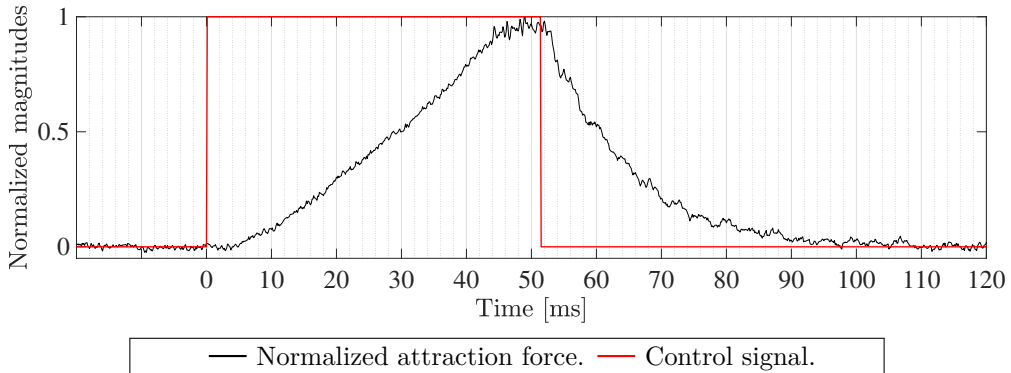


Figure 2.5: The course of the pulling force together with the digital gate signal to the MOSFET for a nominal duration of 50 ms.

is synchronized with the unbalance force of the rotor. In [16] and [15] synchronization was attempted, however this was only in a limited form, where the external excitation would be triggered by a revolution switch in the encoder. In this work an arbitrary angle can be chosen for investigation, so at a given angle, the contribution of the unbalance force should be consistent. The implemented synchronization is achieved by using the signal from the rotary encoder. Based on this signal, the power to the solenoid is switched on from a computer running LabVIEW, which sends a small DC signal to a MOSFET relay, which opens for the supply voltage to the solenoid. The wiring diagram of the implemented circuit is included in Appendix A.2. According to the data sheet, included in Appendix B.2, the solenoid is rated to a supply voltage of 24 V given a 100% duty cycle, however, at this voltage the particular solenoid does not deliver enough attraction force on the steel target to induce contact between the rotor and the stator. Therefore it has proved necessary to increase the voltage to a range in between 35 – 45 V. It must be noted that at this voltage the solenoid is likely to be damaged if the voltage is applied longer than short impulses. As a provisional setup for this project, the solenoid is powered by two laboratory switch-mode power supplies (SMPS). The employed SMPS can each supply up to 31 V with a maximum current of 3 A on their own, so to reach the sufficient voltage, the two SMPS have been connected in series.

A graph of the course of an engagement of the solenoid is shown in Figure 2.5. The duration at which the control signal to the relay is active is controlled by the operator through the LabVIEW-program, as described in the previous chapter. However, as seen in Figure 2.5, the duration of the excitation period is not an exact entity. From the figure, it is seen that the actual attraction force takes time to build up after the digital control signal is given from the I/O device. Similarly, the force remains present after the control signal is removed, after which it decreases over the course of roughly 40 ms. This behavior can be attributed to electrodynamic effects, stemming from magnetic hysteresis of the steel target, and the fact that the magnetized steel target is moving (ascribable to Faraday's law and Lenz's law). The tail of the attractive force graph could be eliminated by implementing an H-bridge, such that after, or just prior to, the 50 ms mark, the current could be flipped which would drive the residual magnetism to zero. Another contribution to the uncertainty regarding timing is the software timing. Observing the digital square signal in the figure, it is found that even though the excitation duration was set at 50 ms in LabVIEW, the signal exceeds the 50 ms mark by a couple of milliseconds. This is likely caused by the fact that the duration of force application is implemented as a sleep-timer in the control software, while the actual switching of the digital output is dependent on a non-deterministic while loop. Thus this implementation can be improved, however, it is not trivial to amend the present solution on the current hardware.

2.1.4 Spherical Bearing

The spherical bearing plays a crucial role in the test-rig since it defines the origin of the mathematical model, at which the rotor is assumed to only be able to move by rotation. The bearing's own dynamics is not accounted for in the mathematical model as it is



Figure 2.6: The two spherical bearings tested. Left: the roller bearing. Right: the ball bearing.

assumed to be of little significance. However, for this to be an adequate assumption, the bearing must behave transparently compared with the dynamics of the actual components that are studied. While dismounting and remounting the rotor, for unrelated reasons, it was discovered that the original 21306-CCK spherical bearings, made by *SKF*, was not operating properly. The bearing was found to exhibit a significant amount of friction as well as a large amount of axial play, where the friction in particular had a high dampening effect on the shaft. Nearly all standard rolling element bearings used in practical machinery has an intended clearance in one principal direction to account for thermal expansion. It was found that the level of friction found in the original bearings was deemed to be too significant to be used in the main experiments.

Having decided to replace the bearing in the first place, the original bearing type was reevaluated. The 21306-CCK bearing contains a lot of rollers and uses a steel cage. Inherently, this means that there are many contacting surfaces with large contact areas. Consequently, this can cause a considerable amount of friction with stick-and-slip during reciprocal motion (vibrations) when used in the test-rig. Therefore instead of just replacing the bearing, it was chosen to try an alternative bearing with better preconditions on paper. Thus a new bearing of the original type and a new alternative was ordered.

The chosen alternative bearing was the 1306 EKTN9/C3 double-row ball bearing from *SKF*. Comparing the two in Figure 2.6, it is seen that the ball bearing, to the right, has fewer rolling elements with its 2×14 balls as opposed to 2×17 rollers in the roller bearing, to the left. Furthermore the balls should provide the smallest contact area per rolling element. The axial clearance in the new bearing of the original roller type was found to be similar to the play noticed in the original bearing, while the axial clearance in the ball bearing seemed smaller. Thus by default the ball bearing seemed to be the superior of the two. However, after mounting the ball bearing it exhibited a very

pronounced stick-slip mode, which caused an audible rubbing sound. After dismounting the bearing it was found to have a production error, which was causing it to not operate correctly. So in the end, due to time considerations, the new *21306-CCK* bearing was used for the remainder of the project.

2.1.5 Miscellaneous

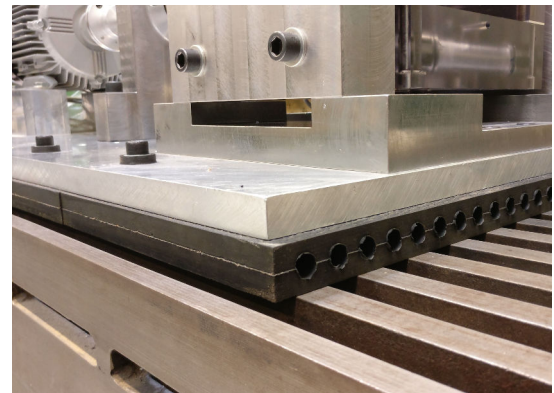
In addition to what has been presented above, some less extensive modifications have been implemented. The list of these are:

1. A hole was made in the top of the steel structure to give access to the force transducer adjustment screw. Furthermore threads were made in the top and both sides of the structure to connect a shaker for modal tests (Appendix C.3).
2. New coupling discs were manufactured as the old exhibited signs of permanent deformations which would induce a buckling behavior in the coupling.
3. During the modal analysis of the impact house, presented in Section 4.3, the dynamics of the foundation under the test-rig was found to be highly coupled to the test-rig. Therefore it was decided to isolate the base of the test-rig from the foundation using dampening plates (Appendix B.1) and rubber washers, as seen in Figure 2.7b.

The modifications described under point 1 and 3 above are shown in Figure 2.7.



(a) Adjustment hole on the top of the outer steel structure.



(b) Damping mat and rubber washers installed between the test-rig and the foundation.

Figure 2.7: Two of the lesser extensive modifications made to the test-rig.

2.2 Calibration of Proximity Sensors

The proximity sensors, positioned laterally around the unbalance disc in the test-rig, i.e. in the vertical and horizontal direction, have been calibration following the same procedure as presented in [17]. The calibration setup is shown in Figure 2.9, where one of the sensors and the unbalance disc dummy is mounted and displaced a particular distance using a micrometer gauge.

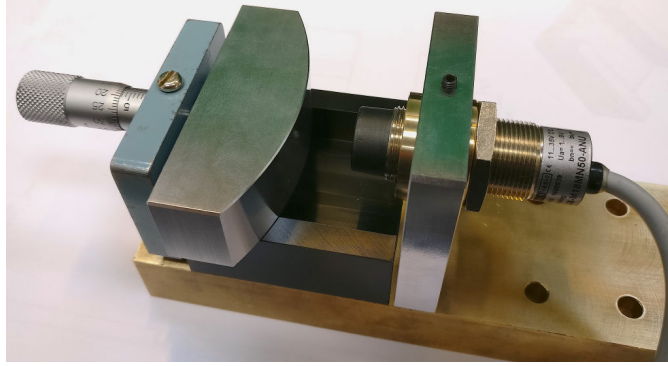


Figure 2.8: Calibration setup for the proximity sensors.

Reading the voltage outputs from the sensors at specific displacements, a set of calibration point is obtained from each of the sensors. The particular calibration data used in the preceding is displayed in Figure 2.9. From the obtained data points, a 6th order polynomial fit has been performed for both of the sensors. As seen from the figure, the two sensors exhibit highly similar curves. The calibration curve can thus be used when evaluating the experimental data.

Having the sensors installed in the test-rig, minor discrepancies in the voltage read-

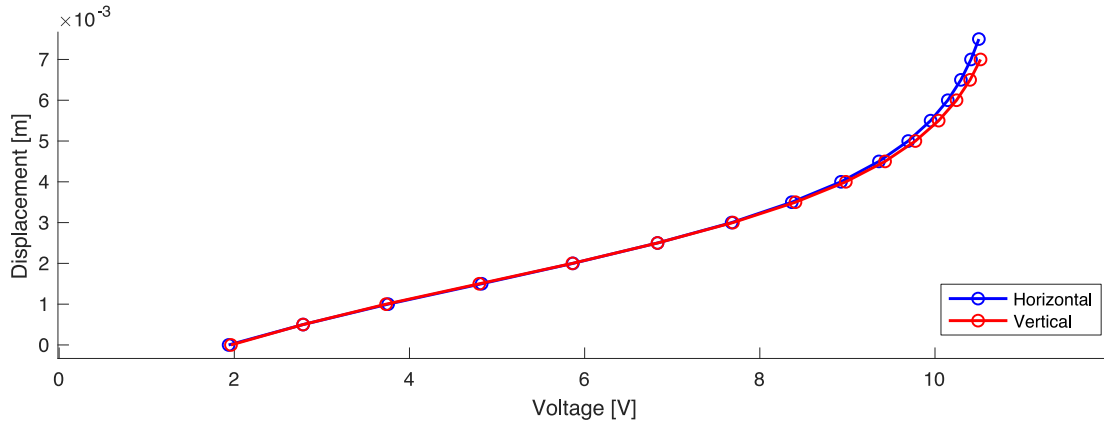


Figure 2.9: The calibration points found for the two displacement sensors superimposed with the fitted calibration curves.

ings were found to appear with the rotor resting in its equilibrium position. This was expected since it is nearly impossible to install the two proximity sensors at exactly the same distance away from the rotor. Thus the voltage readings are each used to shift their corresponding displacement/voltage curve, acquiring a displacement zero-point at the given voltage reading. Since we are only interested in reading the displacement in a range of ± 2.5 mm around equilibrium, the data points within this range are the only ones used for fitting. In doing so, a conversion function is obtained, which can be used to convert the obtained voltage signals into the corresponding displacements.

2.3 Calibration of Force Transducers

In this section the calibration of the force transducers installed in the impact house, and the force transducer installed with the electromagnet is presented.

2.3.1 Impact House Force Transducers

The force transducers installed in the impact house are essential for reading the actual dynamics of the system when impact occurs. Thus, before installing the force transducers a calibration was performed. The north- and west force transducers were each calibrated by incrementally adding weights using a test fixture that serves to isolate only the compression of the force transducer. The setup is seen in Figure 2.10.

With the force transducers installed in the calibration setup, masses in the range of 20–50 kg were added, while reading the voltage output proportional to the applied



Figure 2.10: Force transducer calibration setup.

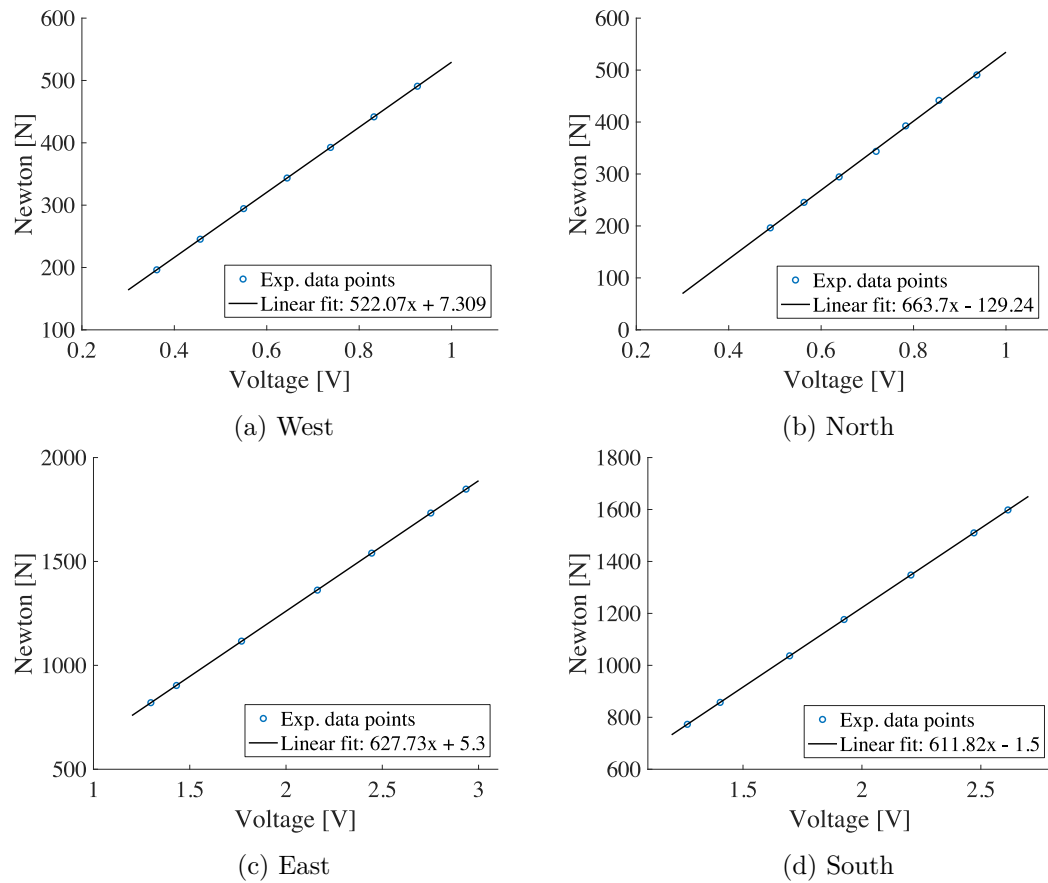


Figure 2.11: Calibration curves of the west, east, north, and south force transducer.

force. As seen in Figure 2.11, the relationships were found to be linear, as stated from the manufacture. Using the data, the linear fit, shown in the figure, was made. Using this given voltage can hence be converted into the corresponding force for the particular transducers.

With the north- and west transducers calibrated, the remaining south- and east transducers were calibrated "in position" using the two former transducers as the reference. This was done by installing the north- and west transducers in the impact houses, and subsequently varying the preload in both directions. In this way both force transducers in the respective direction, e.g. the north- and south transducer, were loaded equally, or at least presumably equal, whereby calibration points could be found. Like for the former two transducers a linear regression fit was made from the calibration points, which are also shown in Figure 2.11.

2.3.2 Electromagnet Force Transducer

As mentioned in Section 2.1, a bidirectional force transducer is installed in between the electromagnet and its mounting bracket. The details pertaining to the transducer can be found in Appendix B.3. In this work the transducer is only subjected to the tension caused by the reaction force induced when the solenoid is engaged and attracts the steel target.

A calibration of the force transducer has been performed by sequentially applying masses in the range of 1–25 kg and subsequently reading the voltage output proportional to the equivalent force. As seen in Figure 2.12, the obtained data points lie well on the linear regression fit, thus the transducer is considered to be linear, and the curve can be used to obtain the attraction force of the electromagnet.

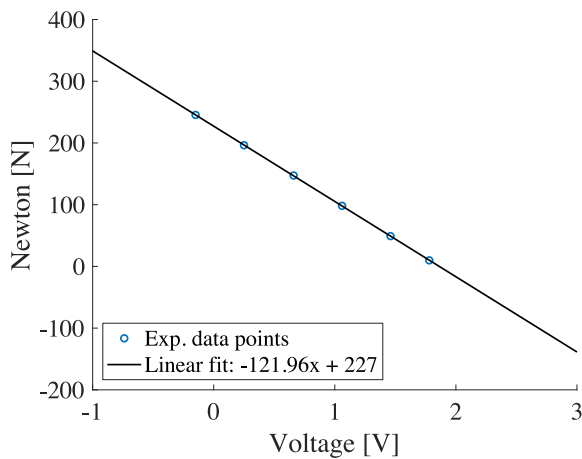


Figure 2.12: Calibration curve of electromagnet force transducer.

2.4 Force Transducer Stiffness

The dynamics of the impact house are of special interest in this project, in order to describe the rotor to stator impact accurately. A rigorous analysis of the impact house is presented later in Section 3.2. Estimating the dynamics of the impact house, the force transducer stiffness is essential in acquiring the modal properties of the system. Thus, an approximate equivalent stiffness of the transducers are obtained experimentally, in order to get a preliminary impression of these dynamics. Doing the experiment, the flexibility of the inner house, the middle house, the screw and the force transducer are all constituting an equivalent stiffness as a series of springs. This stiffness is for simplicity referred to as an equivalent stiffness of the force transducer k_{ft} , while the screw, inner- and middle house are assumed rigid, as depicted in Figure 3.2b in Section 3.2. It must be mentioned that, for testing convenience, the vertical set of force transducers are chosen to be tested in this experiment.

One of the screws, that are used to pre-tension the transducers, is in this experiment

incrementally screwed in by an angle of rotation of 30 degrees in each increment. The angle of rotation then yields an equivalent linear compressive displacement, using the pitch of the screw (0.75 mm), assuming that the axial compression of the screw is negligible. Thus, having two force transducers in series, along with the assumed rigid house, the traveled distance of the screw is the double of each transducer. The linear compressive displacements and the corresponding forces are then noted, from which the stiffness is obtained by a linear fit.

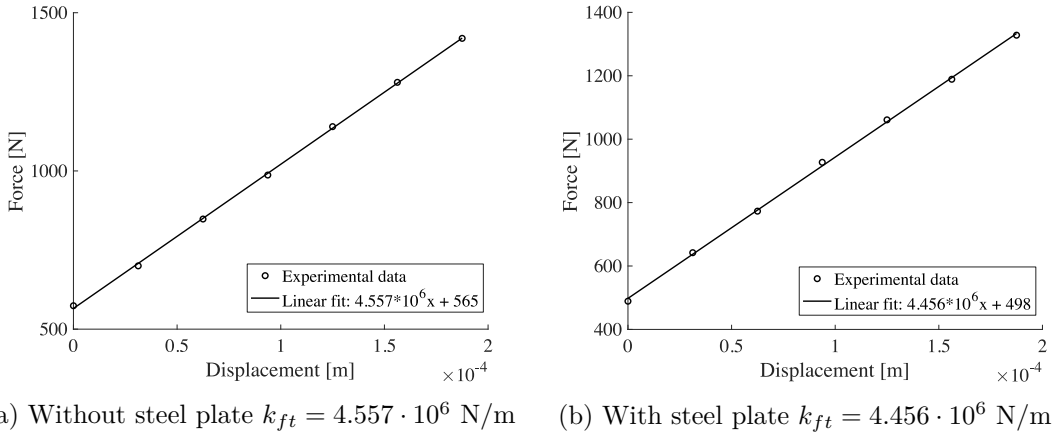


Figure 2.13: Force transducer stiffness test.

In order to investigate the significance of the indentation of the force transducers going into the inner house, a steel plate (considered much more stiff than the polycarbonate house) is inserted in between the two contacting bodies. The experimental results are plotted in Figure 2.13, for which the stiffness is obtained using a linear fit, presented in the figure caption. Considering the discrepancy of the equivalent stiffness, with and without the steel plate, it is concluded that a negligible part of the equivalent flexibility stems from the transducer indenting the inner house. Thus, the obtained equivalent stiffness of the system is estimated to be $k_{ft} = 4.557 \cdot 10^6 \text{ N/m}$.

2.5 Test-Rig Properties

In this section the measured and given properties related to the test-rig, that is used throughout the project, are tabulated. The lengths given in Table 2.1 are all absolute distances between the spherical bearing and the point of interest. All the tabulated lengths are illustrated in Figure 3.7, except l_{shaft} which is the total length of the shaft.

Parameter	Value	Unit
l_{OE}	72.5	mm
l_{OM}	171.7	mm
l_{OU}	259.7	mm
l_{OC}	428.7	mm
l_{shaft}	492	mm

Table 2.1: Length properties of the test-rig.

The masses given in Table 2.2 have all been obtained by weight measurements in the laboratory at DTU. It constitutes the masses of the rotor machine elements, as well as the inner- and middle impact house.

Parameter	Value	Unit
m_{shaft}	0.627	kg
m_{disc}	0.250	kg
m_{PMB}	0.560	kg
$m_{coupling}$	0.429	kg
m_{rotor}	2.122	kg
m_{ih}	1.79	kg
m_{mh}	8.44	kg

Table 2.2: Mass properties of the test-rig.

The material properties used throughout the entire project are tabulated in Table 2.3. It must be noted that the material properties of aluminum have been adjusted as a fitting parameter in order to acquire the best possible natural frequencies in the finite element (flexible) model of the rotor, treated in Section 3.4. The material properties of brass is used for the stator backup bearing, while the polycarbonate properties govern the middle- and inner housings in the impact house.

Parameter	Value	Unit
E_{steel}	$210 \cdot 10^9$	Pa
ρ_{steel}	7800	kg/m ³
E_{alu}	$71 \cdot 10^9$	Pa
ρ_{alu}	2600	kg/m ³
ν_{alu}	0.35	—
$E_{polycarb}$	$2.2 \cdot 10^9$	Pa
$\rho_{polycarb}$	1200	kg/m ³
E_{brass}	$100 \cdot 10^9$	Pa
ν_{brass}	0.35	—

Table 2.3: Material properties of test-rig.

The transverse- and polar mass moment of inertia of the individual rotor machine elements have all been obtained using SolidWorks. These values are listed in Table 2.4.

Parameter	Value	Unit
Disc - I_T	$219584.55 \cdot 10^{-9}$	kg m^2
Disc - I_P	$426774.25 \cdot 10^{-9}$	kg m^2
PMB - I_T	$287431.88 \cdot 10^{-9}$	kg m^2
PMB - I_P	$521378.74 \cdot 10^{-9}$	kg m^2
Coupling - I_T	$240578.44 \cdot 10^{-9}$	kg m^2
Coupling - I_P	$172380.0 \cdot 10^{-9}$	kg m^2
Steel Target - I_T	$79854.29 \cdot 10^{-9}$	kg m^2
Steel Target - I_P	$63014.72 \cdot 10^{-9}$	kg m^2
Rotor - I_T	$7.085371 \cdot 10^{-2}$	kg m^2
Rotor - I_P	$0.130053 \cdot 10^{-2}$	kg m^2

Table 2.4: Mass moment of inertia of the machine elements.

The details pertaining to the magnetic material of the permanent magnetic bearing, described in the introduction, is given below in Table 2.5.

Property	Value
Grade type	N48
Magnetization, M_0	1, 114, 085 A/m
Remanence, B_r	13.7 – 14.0 kG
Coercive force, H_c	812 – 859 kA/m
Intrinsic coercive force, H_{ci}	875 kA/m
Max. energy product, BH_{max}	358 – 382 kJ/m ³
Curie temperature	310 °C
Max. working temp.	80 °C

Table 2.5: Main properties of the magnetic material used in the PMB.

Chapter 3

Modeling

In the following sections the mathematical models necessary to describe the complete rotor-stator system is established.

The analytical model consists of three bodies, that is: the rotor, the inner house, and the middle house. Partitioning the three bodies into two subsystems, i.e. one being the rotor by itself, and the other being the two houses, such that these collectively constitute the stator, a rotor-stator system is defined. The response of such a system is modeled by a system of ordinary differential equations, where some of these equations are mutually coupled. The inner and outer houses are coupled through the stiffness of the linear guides and the force transducers, while the rotor and stator subsystems are coupled only when they are in contact with each other. The resulting system of equations that is obtained can be written generally as

$$\dot{\mathbf{x}} = \mathbf{f}(\mathbf{x}), \quad \mathbf{x} \in \mathbb{R}^n, \quad (3.1)$$

where the dot denotes the time derivative. The mathematical device which is used to link the rotor and the stator dynamically is obtained via the contact force models. Here the so-called *penalty method* is applied, that is the contact forces are introduced once a geometric condition is met, specifically when the clearance between the rotor and the stator is exceeded.

Initially the contact dynamics are described, here being dynamics related to the indentation and friction at contact. Next, the impact house is investigated, for which a mathematical model describing its dynamics is established. The dynamics of the rotor is then considered, both with the assumption of being rigid and subsequently being flexible by employing the finite element method. Finally, the simulation implementation of the mathematical model is treated.

3.1 Contact Dynamics

The contact model consists of two parts. The first part is concerned with the normal force originating during impact indentations, while the other pertains to the tangential force originating during friction induced by the relative velocity between the bodies in

contact. In this section, a description of the contact force models are presented and discussed.

3.1.1 Normal Force Model

As two bodies collide, the primary contact force arises in the normal direction, due to a relative indentation δ . Thus, for describing the contact dynamics, it is necessary to express this normal force (acting with equal magnitude and opposite direction on the two bodies) as a function of this relative indentation.

This can, at its simplest, be described by the linear Hooke contact model

$$F_N = k\delta,$$

where F_N is the normal force, k is the spring stiffness and δ is the indentation. However, the stiffness k can be difficult to quantify as it depends on the geometrical and material properties. Additionally, it assumes that there is a linear relationship between the force and indentation, which is a rough approximation as it depends on shape and mechanical properties.

Slightly more advanced, the contact force can be described by the non-linear Hertz contact model [18]

$$F_N = K\delta^n, \\ K = \frac{4}{3(h_i + h_j)} \left(\frac{R_i R_j}{R_i + R_j} \right)^{1/2}, \quad h_l = \frac{1 - \nu_l^2}{E_l}, \quad (l = i, j),$$

where K is the generalized stiffness parameter for two spheres, R_i and R_j are the radii of the two colliding bodies. The exponent n is given by 3/2 for a parabolic distributed contact stress. It must be mentioned that the radii are negative for concave surfaces and positive for convex surfaces. Although the Hertz model is non-linear and includes the geometrical and material properties, it does not allow for any dissipation of energy.

One of the first contacts models that took the dissipative energy into account, was proposed by Kelvin and Voigt, modeling a linear spring in conjunction with linear viscous damper, both in parallel [18]:

$$F_N = K\delta + D\dot{\delta},$$

where $\dot{\delta}$ is the relative velocity of the two bodies, i.e. the indentation velocity. Besides the simplicity of the model and the inclusion of damping, it might not be very accurate in describing the impact realistically. The issue emerges at zero indentation $\delta = 0$, either at contact or separation, where the damping term is non-zero, effectively yielding a non-zero normal force. Furthermore, at separation the damping term is negative for which a negative force is generated. This means that the two bodies are pulling each other, which does not make physical sense.

To accommodate this problem, Hunt and Crossley [1] developed a model based on the Hertzian theory, augmented with an additional term allowing the dissipation of energy:

$$F_N = K\delta^n + D\dot{\delta}, \quad D = \chi\delta^n, \quad \chi = \frac{3K(1-e)}{2\dot{\delta}}, \quad (3.2)$$

where χ is the hysteresis damping factor, e is the coefficient of restitution, and $\dot{\delta}^-$ denotes the indentation velocity just prior to the onset of the impact. This model ensures a normal force equal to zero when the indentation is zero, which means that the model is continuous at contact and separation.

The model of Hunt and Crossley gave rise to a large number of modified models, one of which is the contact model by Lankarani and Nikravesh [3], build on the form of Equation (3.2), i.e.

$$F_N = K\delta^n \left[1 + \frac{3(1-e^2)}{4} \frac{\dot{\delta}}{\dot{\delta}^-} \right], \quad \chi = \frac{3K(1-e^2)}{4\dot{\delta}^-}. \quad (3.3)$$

The model is based on the conservation of linear momentum, and assumes that the magnitude of the dissipated energy during contact is small compared to the maximum elastically absorbed energy (i.e. a coefficient of restitution close to unity) and that the impact velocities are lower than the propagation velocity of the elastic waves.

This model has been widely used by numerous authors and within different domains, such as impacts in multi-body systems and impacts in clearance joints, as well as being a versatile model with easy implementation and simplicity. Thus, the model of Lankarani and Nikravesh (3.3) is used in this project, describing the normal force of the contact dynamics.

Alternative dissipative contact force models that have been developed over the last decades are presented and discussed in [18]. These models are all based on the form:

$$F_N = K\delta^n + \chi\delta^m\dot{\delta},$$

where the power relation is considered either Hookean ($n = 1$) or Hertzian ($n = 3/2$), as well as presenting either a discontinuity on initial contact ($m = 0$) or having the damping term weighted by the elastic force ($m = n$). The different contact models are here listed in Table 3.1.

3.1.2 Friction Force Model

As the rotor impacts the stator, a tangential force is generated due to the friction between the two contacting bodies. This friction is caused by a non-zero relative velocity and the normal force, at contact, and may lead to different modes such as sliding or sticking.

The most simple and commonly used friction model, is Coulomb's friction law, depicted in Figure 3.1a. The model is expressed as

$$F_T = \text{sgn}(v_T)c_f F_N,$$

where F_T is the tangential force, v_T is the relative velocity between the two contact bodies, c_f is friction coefficient, and F_N is the normal force.

However, considering Coulomb's friction model it becomes evident that no velocity dependency is present. In practice, the friction depends on several parameters such as temperature, material properties and relative velocity. Especially the velocity dependency is considered important in this project for modeling the rotor stator impact.

Models	Constitutive law	Damping factor
Anagnostopoulos	$F_N = K\delta + \chi\delta\dot{\delta}$	$\chi = 2\frac{-\ln(e)}{\sqrt{\pi^2 + (\ln(e))^2}}\sqrt{Km_{eff}}$
Ristow	$F_N = K\delta^{3/2} + \chi\delta\dot{\delta}$	Empirical
Lee and Herrmann	$F_N = K\delta^{3/2} + m_{eff}\chi\delta\dot{\delta}$	Empirical
Hunt and Crossley	$F_N = K\delta^{3/2} + \chi\delta^{3/2}\dot{\delta}$	$\chi = \frac{3(1-e)}{2}\frac{K}{\dot{\delta}^-}$
Herbert and McWhannell	$F_N = K\delta^{3/2} + \chi\delta^{3/2}\dot{\delta}$	$\chi = \frac{6(1-e)}{((2e-1)^2+3)}\frac{K}{\dot{\delta}^-}$
Lee and Wang	$F_N = K\delta^{3/2} + \chi\delta^{3/2}\dot{\delta}$	$\chi = \frac{3(1-e)}{4}\frac{K}{\dot{\delta}^-}$
Lankarani and Nikravesh	$F_N = K\delta^{3/2} + \chi\delta^{3/2}\dot{\delta}$	$\chi = \frac{3(1-e^2)}{4}\frac{K}{\dot{\delta}^-}$
Gonthier et al.	$F_N = K\delta^{3/2} + \chi\delta^{3/2}\dot{\delta}$	$\chi \approx \frac{1-e^2}{e}\frac{K}{\dot{\delta}^-}$
Zhiying and Qishao	$F_N = K\delta^{3/2} + \chi\delta^{3/2}\dot{\delta}$	$\chi = \frac{3(1-e^2)e^{2(1-e)}}{4}\frac{K}{\dot{\delta}^-}$
Flores et al.	$F_N = K\delta^{3/2} + \chi\delta^{3/2}\dot{\delta}$	$\chi = \frac{8(1-e)}{5e}\frac{K}{\dot{\delta}^-}$
Gharib and Hurmuzlu	$F_N = K\delta^{3/2} + \chi\delta^{3/2}\dot{\delta}$	$\chi = \frac{1}{e}\frac{K}{\dot{\delta}^-}$
Kuwabara and Kono	$F_N = K\delta^{3/2} + \chi\delta^{1/2}\dot{\delta}$	$\chi = \frac{K}{3}\frac{(3\eta_2-\eta_1)^2}{3\eta_2+2\eta_1}\frac{(1-\nu)(1-2\nu)}{E\nu^2}$
Tsuji et al.	$F_N = K\delta^{3/2} + \chi\delta^{1/4}\dot{\delta}$	$\chi = \alpha\sqrt{Km_{eff}}$
Bordbar and Hyppänen	$F_N = K\delta^{3/2} + \chi\delta^{0.65}\dot{\delta}$	Empirical
Hu and Guo	$F_N = K\delta^{3/2} + \chi\delta^{3/2}\dot{\delta}$	$\chi = \frac{3(1-e)}{2e}\frac{K}{\dot{\delta}^-}$

Table 3.1: Overview over common and more specialized dissipative contact force models. The collection was originally presented in [18].

Another weakness of the model, is that it does not take a zero velocity into consideration, at which an infinite gradient is generated. This can cause computational difficulties in the integration process, as an instantaneous change in direction of the tangential force F_T appears at zero velocity, thus causing instability [8].

A more advanced model is proposed by Ambrósio [7], depicted in Figure 3.1b. The model is expressed as

$$F_T = \text{sgn}(v_T) c_f c_d F_N, \quad c_d = \begin{cases} 0 & v_T \leq v_0 \\ \frac{v_T - v_0}{v_1 - v_0} & v_0 \leq v_T \leq v_1 \\ 1 & v_T \geq v_1 \end{cases}, \quad (3.4)$$

where c_d is a dynamic correction coefficient, for which v_0 and v_1 are given velocity tolerances. This model allows for a numerical stabilization of the integration algorithm in the case that the relative tangential velocity becomes zero. This is achieved by introducing a velocity range $|v_T| = [0, v_0]$, within which pure rolling is assumed, i.e. the friction force becomes zero. Furthermore, in the range $|v_T| = [v_0, v_1]$ the tangential force is velocity-depended and continuous. All this is seen Figure 3.1 where it is compared to Coulomb's model.

The friction model of Ambrósio is considered adequate for describing the dynamics of the rotor stator impact, and thus it is used as the primary friction model in this project.

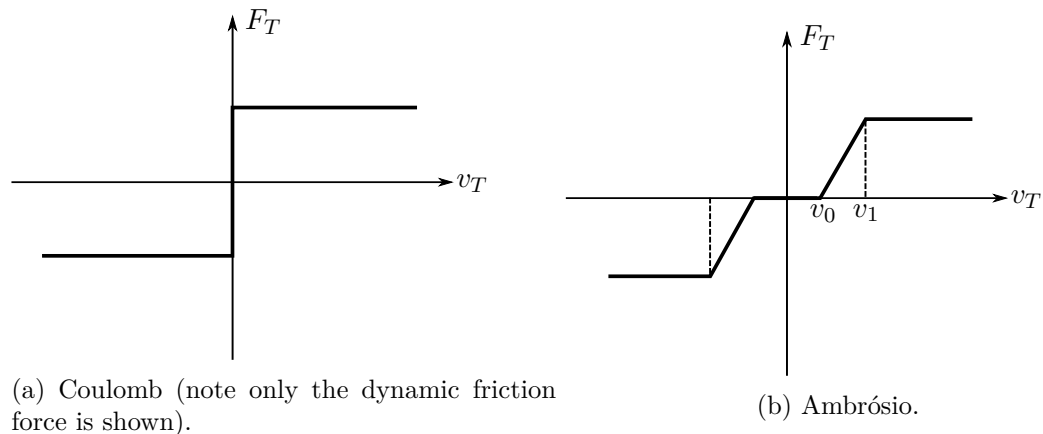


Figure 3.1: Relation between the friction force and relative tangential velocity.

3.2 Impact House Dynamics

Upon impacts in the experimental setup, the shaft is found to remain in contact with the stator for a significant duration in time. Previous studies suggests that a more comprehensive model of the impact house dynamics is necessary in order to fully understand the dynamics. Thus, the dynamics of the stator is investigated in the following section.

First, an analytical expression of the impact house dynamics is established based on a given set of assumptions. Second, estimates of the stiffnesses and damping defined in the

analytical expression are obtained and presented. Third, the equivalent stiffnesses k_{ft1} and k_{ft2} are fitted with the objective of matching the analytical and experimental natural frequencies, through an experimental modal analysis. Finally, a finite element model of the impact house is constructed, for which the rigidity assumption is investigated, as well as the flexibility effect of the impact houses.

3.2.1 Analytical Model of the Impact House

The movement of the impact house is modeled by letting the inner- and middle house act as two rigid bodies, each with a degree of freedom in the horizontal and vertical direction, as can be interpreted looking at Figure 3.2a visualizing the houses sliding on the guide beams. Considering the equivalent mechanical system shown in Figure 3.2b, the stiffness and damping of the vertical and horizontal beams are defined as k_{vb} , k_{hb} , d_{vb} and d_{hb} , while the equivalent stiffness of the force transducers are denoted as k_{ft1} and k_{ft2} for the vertical- and horizontal direction, respectively. It is important to mention that the force transducer stiffnesses are in fact *equivalent* stiffnesses in this model, as they physically describe a series of stiffnesses, that is: the flexibility of the house, screw, and transducer, as described in Section 2.4. The inner- and middle houses interact through the restoring and dissipative forces due to the vertical force transducers and due to the vertical beams, as seen in Figures 3.2a and 3.2b, which is also seen considering the non-diagonal terms of the damping and stiffness matrix in Equation (3.5). Considering the free-body diagrams shown in Figures 3.2c and 3.2d, four equilibria of forces can be made to obtain the equations of motion for the stator. The system dynamics are described around its equilibrium position, thus the gravitational force have been disregarded in the equations of motion.

The equations of motion for the inner- and middle house, subjected to an external force F_c , thus become:

$$\begin{aligned} m_{ih}\ddot{x}_{ih} + d_{vb}(\dot{x}_{ih} - \dot{x}_{mh}) + k_{vb}(x_{ih} - x_{mh}) &= F_{cx}, \\ m_{ih}\ddot{y}_{ih} + 2k_{ft1}(y_{ih} - y_{mh}) &= F_{cy}, \\ m_{mh}\ddot{x}_{mh} + d_{vb}(\dot{x}_{mh} - \dot{x}_{ih}) + 2k_{ft2}x_{mh} + k_{vb}(x_{mh} - x_{ih}) &= 0, \\ m_{mh}\ddot{y}_{mh} + d_{hb}\dot{y}_{mh} + k_{hb}y_{mh} + 2k_{ft1}(y_{mh} - y_{ih}) &= 0, \end{aligned} \quad (3.5)$$

where the subscripts ih and mh denote the inner- and middle house, respectively. From the expression above one notes that the preloads of the force transducers, denoted by F_{hpre} and F_{vpre} in the Figures 3.2c and 3.2d, vanish.

Recasting the above equations of motion in a matrix form, the following system of equations is obtained:

$$\underbrace{\begin{bmatrix} m_{ih} & 0 & 0 & 0 \\ 0 & m_{ih} & 0 & 0 \\ 0 & 0 & m_{mh} & 0 \\ 0 & 0 & 0 & m_{mh} \end{bmatrix}}_{\mathbf{M}} \begin{Bmatrix} \ddot{x}_{ih} \\ \ddot{y}_{ih} \\ \ddot{x}_{mh} \\ \ddot{y}_{mh} \end{Bmatrix} + \underbrace{\begin{bmatrix} d_{vb} & 0 & -d_{vb} & 0 \\ 0 & 0 & 0 & 0 \\ -d_{vb} & 0 & d_{vb} & 0 \\ 0 & 0 & 0 & d_{hb} \end{bmatrix}}_{\mathbf{D}} \begin{Bmatrix} \dot{x}_{ih} \\ \dot{y}_{ih} \\ \dot{x}_{mh} \\ \dot{y}_{mh} \end{Bmatrix} \dots \\
 + \underbrace{\begin{bmatrix} k_{vb} & 0 & -k_{vb} & 0 \\ 0 & 2k_{ft1} & 0 & -2k_{ft1} \\ -k_{vb} & 0 & 2k_{ft2} + k_{vb} & 0 \\ 0 & -2k_{ft1} & 0 & 2k_{ft1} + k_{hb} \end{bmatrix}}_{\mathbf{K}} \begin{Bmatrix} x_{ih} \\ y_{ih} \\ x_{mh} \\ y_{mh} \end{Bmatrix} = \underbrace{\begin{Bmatrix} F_{cx} \\ F_{cy} \\ 0 \\ 0 \end{Bmatrix}}_{\mathbf{F}}$$
(3.6)

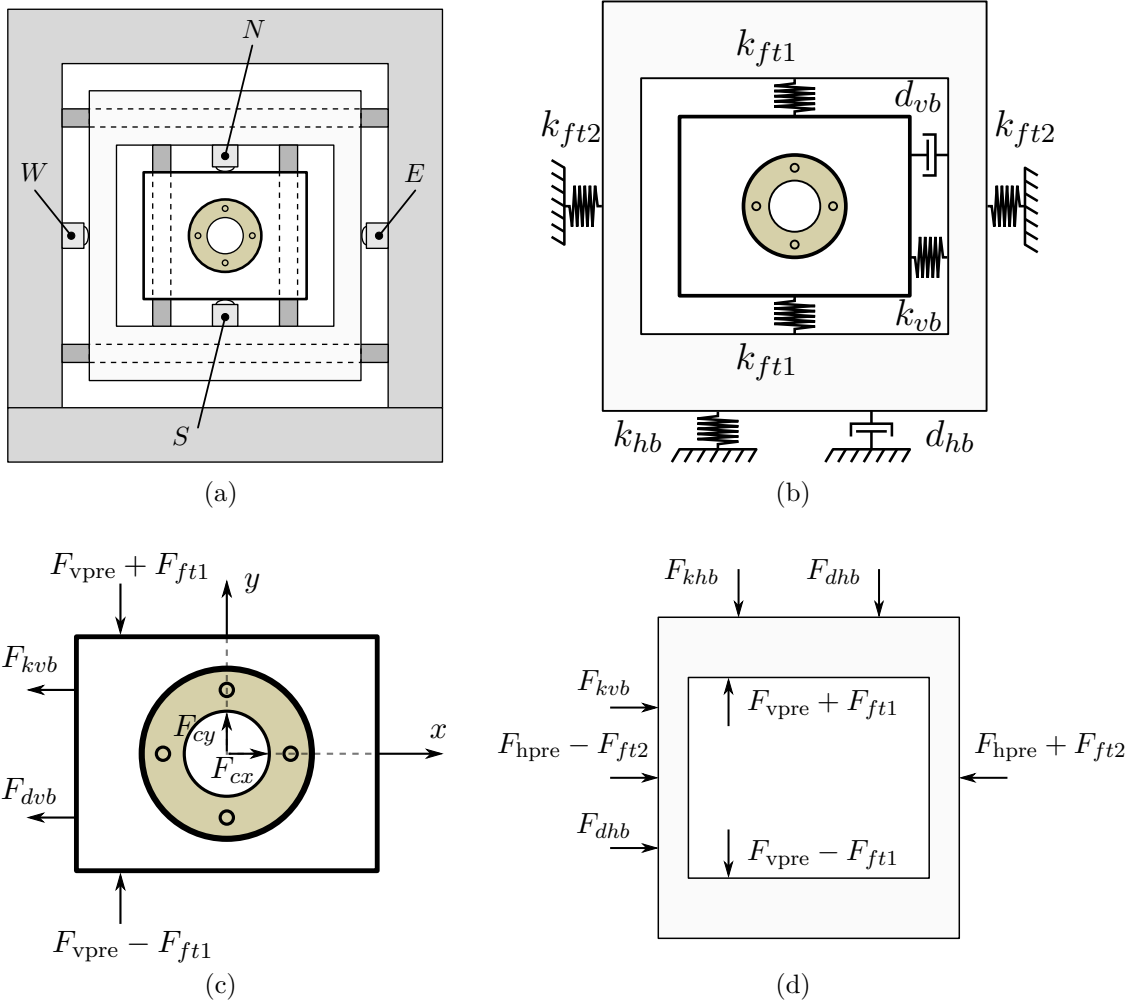


Figure 3.2: (a): The impact-house assembly. (b): Mechanical model. (c) Free-body diagram of the inner house. (d) Free-body diagram of the middle house.

3.2.2 Stiffness and Damping Estimates

The stiffnesses contained in the equations of motion for the impact houses, i.e. k_{vb} , k_{hb} , k_{ft1} and k_{ft2} , are in this section estimated, presented, and discussed, along with an estimate of the guide rods' damping coefficients, d_{vb} and d_{hb} .

An estimate of the equivalent stiffness of the force transducer k_{ft} is experimentally obtained in order to get a preliminary perception of the dynamics, as presented in Section 2.4, to be $k_{ft} = 4.557 \cdot 10^6$ N/m. This is initially assumed to approximate the stiffnesses k_{ft1} and k_{ft2} by the same order of magnitude.

The stiffness of the horizontal and vertical beams are estimated using Bernoulli-Euler beam theory for a clamped-clamped condition. It is assumed that the considered system is plane symmetric and that the forces acting on the beam can be decomposed

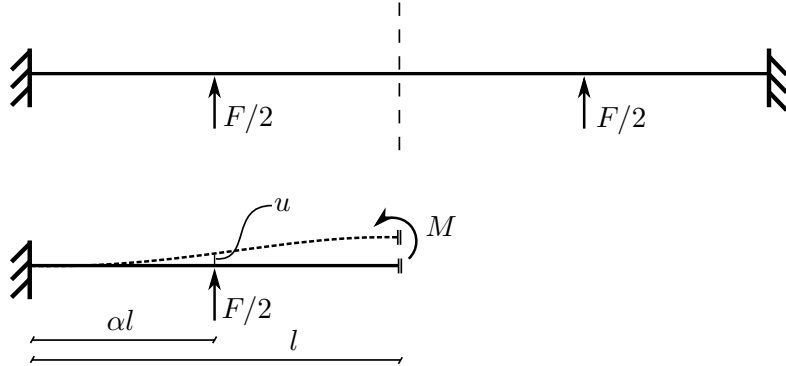


Figure 3.3: Mechanical model of the guiding rods as beams.

into two equal magnitude forces. In doing so, the symmetry condition can be exploited introducing a moment force M , as shown in Figure (3.7), such that the boundary condition $\theta(l) = 0$ is introduced. The half of the force acting on a single beam is then applied as a linear force at the middle of the guiding bearing, at which the deflection is derived, assuming that the translatory movement of the house is moving together with this point.

In Figure 3.3, l is the half beam length and αl is the distance to the linear force and the point of interest. Using simple beam theory, the forces can be evaluated individually and subsequently added together using the principle of superposition, where θ denotes the angle of rotation, u denotes the deflection, and k denotes the stiffness of a single guiding beam. The derivation becomes:

$$\theta(l) = \frac{(F/2)l^2}{2EI}\alpha^2 + \frac{Ml}{EI} = 0 \Rightarrow M = -\frac{1}{4}Fl\alpha^2, \quad (3.7)$$

$$u(\alpha) = \frac{(F/2)l^3}{3EI}\alpha^3 + \frac{(-1/4Fl\alpha^2)l^2}{2EI}\alpha^2 = \frac{Fl^3\alpha^3}{EI} \left(\frac{1}{6} - \frac{1}{8}\alpha \right), \quad (3.8)$$

$$k = \frac{F}{\frac{Fl^3\alpha^3}{EI} \left(\frac{1}{6} - \frac{1}{8}\alpha \right)} = \frac{EI}{l^3\alpha^3 \left(\frac{1}{6} - \frac{1}{8}\alpha \right)}. \quad (3.9)$$

Using Equation (3.7), the stiffness of the vertical- and horizontal beams are presented and found using the parameters given in Table 3.2.

Parameter	Value	Unit
E_{steel}	$210 \cdot 10^9$	Pa
I	$1.57 \cdot 10^{-8}$	m^4
l_{vb}	0.07	m
α_{vb}	0.6	—
k_{vb}	$9.709 \cdot 10^8$	N/m
d_{vb}	2168	Ns/m
l_{hb}	0.121	m
α_{hb}	0.35	—
k_{hb}	$1.41 \cdot 10^9$	N/m
d_{hb}	12983	Ns/m

Table 3.2: Design parameters of impact house beams.

Comparing the estimated equivalent stiffness of the force transducers $k_{ft} = 4.557 \cdot 10^6$ N/m, the stiffness estimate of the vertical beam, $k_{vb} = 9.709 \cdot 10^8$ N/m, and the stiffness estimate of the horizontal beam, $k_{hb} = 1.41 \cdot 10^9$ N/m, we see that the beam stiffness is two orders of magnitude higher than the estimated equivalent force transducer stiffness.

Thus, a part of the system dynamics can be approximated by a 2-DOF system where the guiding beams are assumed rigid, and the force transducer stiffnesses are dominating the natural frequencies for the 2-DOF system.

The damping coefficients, assigned to the guiding beams, are estimated as an equivalent viscous damper. Previous studies done by [13] has found the damping ratios of the impact house experimentally. The values were then estimated to be $\zeta_{vb} = 0.026$ and $\zeta_{hb} = 0.054$. These ratios are assumed to be identical to the slightly modified impact house used in this project. Having this, the damping coefficients are approximated by:

$$d_{vb} = 2\zeta_{vb}\sqrt{k_{vb}m_{ih}} = 2168 \text{ Ns/m},$$

$$d_{hb} = 2\zeta_{hb}\sqrt{k_{hb}(m_{ih} + m_{mh})} = 12983 \text{ Ns/m},$$

where ζ denotes the equivalent damping ratio of the system.

3.2.3 Modal Properties of the Impact House

Considering the experimentally found modal properties of the impact house, presented in Section 4.3, the equivalent stiffness parameters k_{ft1} and k_{ft2} are fitted in the analytical model, while the stiffness of the guiding rod is assumed to be correct. Obtaining the modal properties of the analytical model, the eigenvalue problem of the equations of motion (3.6) can be expressed as

$$(-\omega^2 \mathbf{M} + \mathbf{K})\mathbf{v} = 0, \quad (3.10)$$

for $\mathbf{D} = \mathbf{0}$, as the damped and undamped natural frequencies and mode shapes are assumed to yield insignificant discrepancies. In Equation (3.10), ω is the undamped natural frequency and \mathbf{v} is the corresponding eigenvector.

Experimentally, the natural frequencies were found to be $\omega_1 = 250$ Hz and $\omega_2 = 485$ Hz, for which the stiffnesses k_{ft1} and k_{ft2} have been fitted in the analytical model. In doing so, the following stiffnesses are found:

$$k_{ft1} = 8.42 \cdot 10^6 \text{ N/m}, \quad k_{ft2} = 1.26 \cdot 10^7 \text{ N/m}. \quad (3.11)$$

Applying the stiffnesses, the undamped natural frequencies and mode shapes of the analytical model become:

$$\omega_1 = 249.7 \text{ [Hz]}, \quad \mathbf{v}_1 = \begin{Bmatrix} 1 \\ 0 \\ 0.995 \\ 0 \end{Bmatrix}, \quad \omega_2 = 485.1 \text{ [Hz]}, \quad \mathbf{v}_2 = \begin{Bmatrix} 0 \\ 1 \\ 0 \\ 0.01 \end{Bmatrix}. \quad (3.12)$$

Considering the mode shapes of the analytical model, given in Equation (3.12), the inner- and middle house are found to be in phase with equal magnitude at the first natural frequency, while being in phase with almost no movement of the middle house at the second natural frequency. This is also found experimentally in Section 4.3.

3.2.4 House Flexibility Effect

A finite element model of the impact house has been made, in order to verify the analytical model using the rigidity assumption, as well as to investigate the effect of the impact house flexibility. The FE-program *ANSYS Workbench* has been used to conduct this modal analysis, based on a simplified model of the impact house. The model essentially resembles the flexible guiding beams and the two houses which can either be made rigid or flexible. The model has been assigned the two materials steel and polycarbonate accordingly, having the steel outer house assumed rigid, as seen in Figure 3.4. Additionally, the k_{ft1} and k_{ft2} stiffnesses are implemented using a discrete *spring element* provided by the program. The connection between the simplified guiding bearings and the guiding beams have been assigned as being frictionless and the densities of the polycarbonate houses have been modified in order to obtain the exact same masses as used in the analytical model.

The FE-model has first been solved under the assumption of rigid impact houses, for which the fitted stiffnesses k_{ft1} and k_{ft2} given in Equation (3.11) are used.

The two first mode shapes are shown in Figure 3.5, along with their corresponding natural frequencies noted in their respective caption. Looking at the natural frequencies, a good match between the FE-model and the analytical model is found. Furthermore, the same mode shape characteristics are seen. This verifies the conclusion of the beam stiffnesses being much greater than the equivalent force transducer stiffnesses, as the two first natural frequencies are dominated by the stiffness of the force transducer stiffness.

The FE-model is now to be solved while allowing the impact houses to be flexible. For this purpose the previously fitted equivalent stiffnesses of the force transducers can no longer be used, since they already include the flexibility of the housing. Instead an

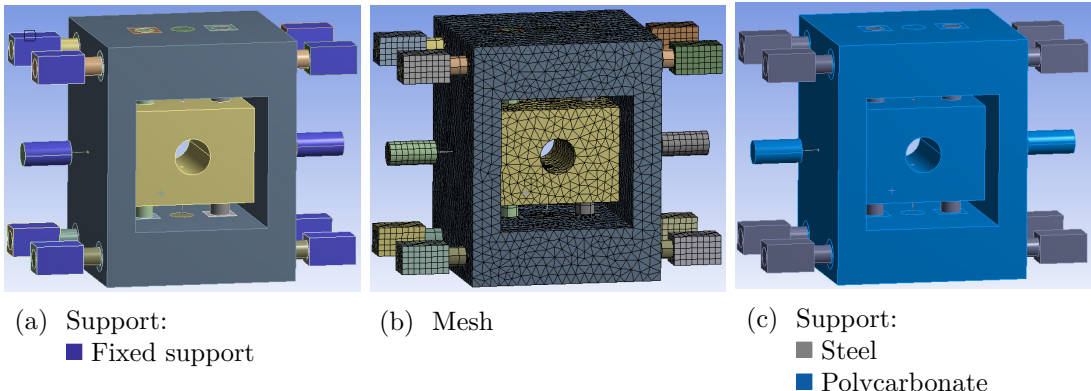


Figure 3.4: The finite element model.

estimate of the single force transducer is found using the stiffness properties of the manufacturer, as done in [13], [12]. and [16]. Here the stiffness is simply estimated by taking the relationship between the nominal force and nominal max displacement which yields $k_{ft} = 8.33 \cdot 10^7$ N/m. In Figure 3.6 the three first mode shapes are shown, along with their corresponding natural frequencies. It is first noted that the first eigenmode appear at almost the same natural frequency as for the rigid case, showing the same mode shape characteristic. The reason for this, is due to the FE-modeled "spring" stiffness has been increased, while the flexibility of the house has been introduced, equating to a similar equivalent stiffness as for the rigid case. Secondly, it is found that a horizontal bending mode shape appears at 329 Hz, due to the flexibility of the impact house material. This bending mode shape is also found experimentally at 445 Hz as an anti-resonance, having the accelerometer mounted on the middle house near a mode shape node. An explanation for the difference in experimental and FE frequency, is said to be caused by the difficulty of modeling and accurately describing the dynamics of the guiding bearings in

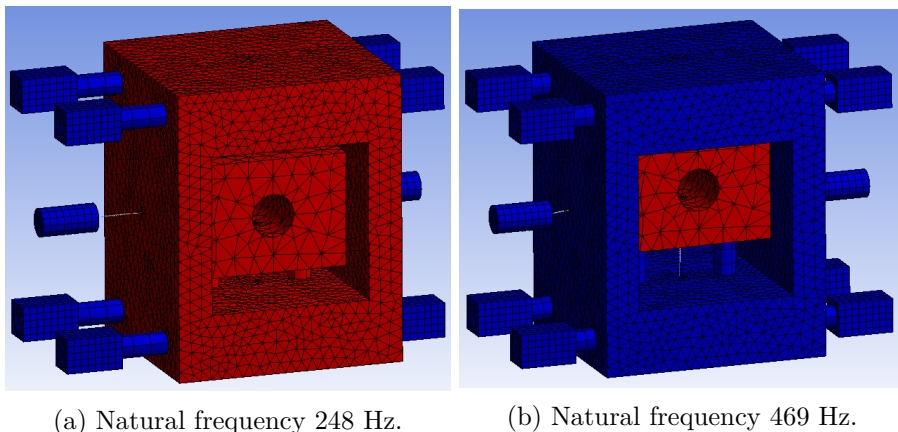
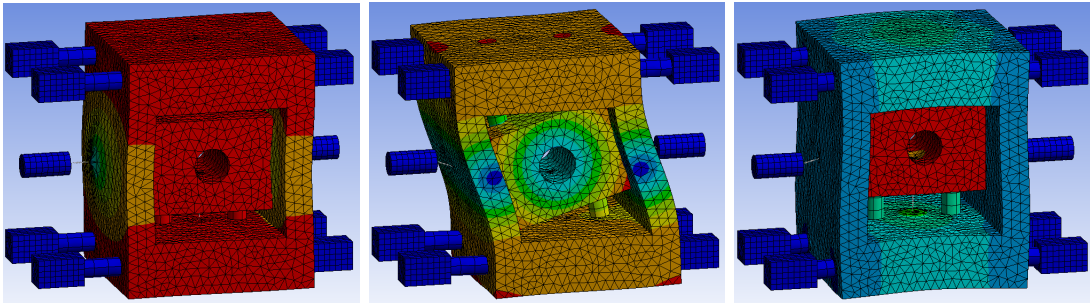


Figure 3.5: Two first mode shapes of rigid impact house.



(a) Natural frequency 254 Hz. (b) Natural frequency 329 Hz. (c) Natural frequency 577 Hz.

Figure 3.6: Three first mode shapes of rigid flexible house.

the FE-model, for which this mode shape is highly dependent. Finally, the third mode shape of the FE-model is found to show a similar mode characteristic as for the rigid case and the experimentally obtained, however at a different natural frequency. Again, the guiding bearing modeling is said to cause this discrepancy.

Considering the overall results of the rigid and flexible FE-model, it is concluded that the flexibility of the impact houses plays a significant role in describing the dynamics. It has also been shown that this flexibility can be incorporated into a rigid model, by the use of an equivalent stiffness describing both the force transducer and house flexibility.

3.3 Rigid Rotor

The rigid rotor is now considered, for which the equations of motion are obtained using the Newton-Euler equations. In this case, Euler's second law is applied evaluating the three angular rotations depicted in Figure 3.7.

3.3.1 Assumptions

The analytical model is constructed around the following assumptions:

1. The rotor is considered rigid.
2. The rolling element bearing is considered rigid.
3. The magnetic bearing exerts a linear restoring- and dissipative force.
4. The rotor is rotational symmetric.

3.3.2 Coordinate Systems

In order to describe the movement of the rotor efficiently, three auxiliary coordinate systems B_1 , B_2 and B_3 are defined in addition to the inertial coordinate system, which itself is denoted by I . The auxiliary coordinate systems are all fixed in terms of translation

on top of I . Here they each rotate around one the axes of I according to the movement of the rotor. Thus B_1 moves around x -axis by the angle Γ , B_2 rotates around the y -axis by β and B_3 rotates around the z -axis by θ . These angles are seen in Figure 3.7. The pre-subscript denotes the reference frame in which the matrix is defined.

To transform between these coordinate system the following transformation matrices are used:

$${}_I \mathbf{T}_\Gamma = \begin{bmatrix} 1 & 0 & 0 \\ 0 & \cos \Gamma & \sin \Gamma \\ 0 & -\sin \Gamma & \cos \Gamma \end{bmatrix}, \quad {}_{B1} \mathbf{T}_\beta = \begin{bmatrix} \cos \beta & 0 & -\sin \beta \\ 0 & 1 & 0 \\ \sin \beta & 0 & \cos \beta \end{bmatrix}, \quad {}_{B2} \mathbf{T}_\theta = \begin{bmatrix} \cos \theta & \sin \theta & 0 \\ -\sin \theta & \cos \theta & 0 \\ 0 & 0 & 1 \end{bmatrix}.$$

These matrices thus define three consecutive coordinate transformations from I to B_3 , which may be used to simplify the analysis when considering forces. The actual coordinate system used when determining forces is dictated by the line of action of the forces as well as the inertia matrix, the details of which is described in the proceeding sections.

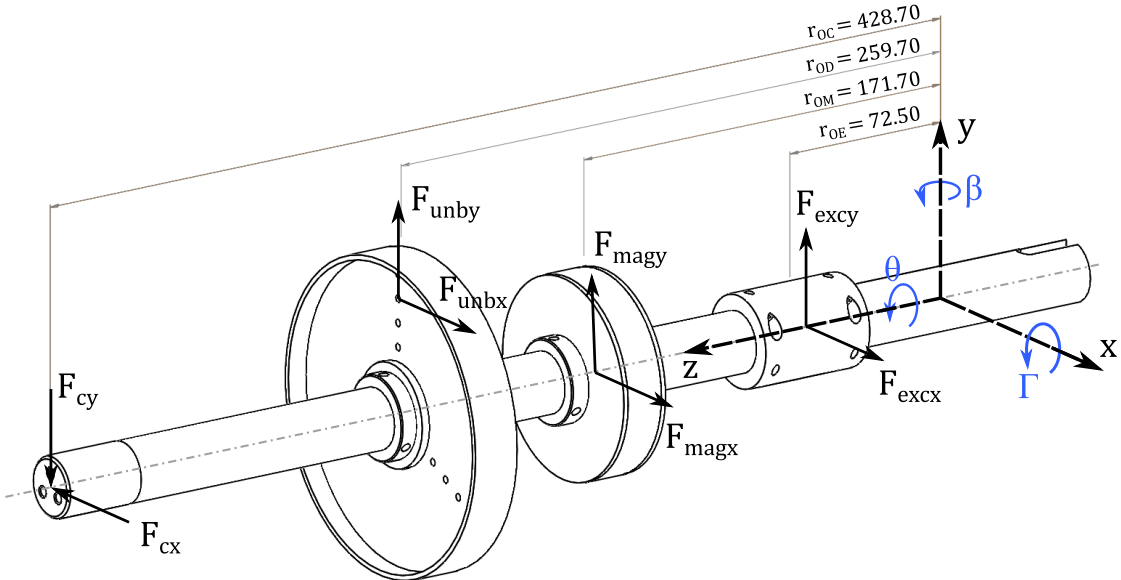


Figure 3.7: Overview of coordinate definitions as well as the forces acting on the rotor.

3.3.3 Kinematics

The angular velocities of the reference frames, described in their respective coordinate systems, is defined and expressed as:

$${}_I \dot{\Gamma} = \begin{Bmatrix} \dot{\Gamma} \\ 0 \\ 0 \end{Bmatrix}, \quad {}_{B1} \dot{\beta} = \begin{Bmatrix} 0 \\ \dot{\beta} \\ 0 \end{Bmatrix}, \quad {}_{B2} \dot{\theta} = \begin{Bmatrix} 0 \\ 0 \\ \dot{\theta} \end{Bmatrix}.$$

Defining the kinematics of the rotor system, it becomes advantageous to describe the relations in the moving reference frame B2 later when the kinetics are introduced and evaluated.

The absolute angular velocity $\boldsymbol{\Omega}$ of the the moving reference frame B2, described in the moving reference frame B2, is then given by:

$${}_{B2}\boldsymbol{\Omega} = {}_{B1}\mathbf{T}_\beta \cdot {}_I\mathbf{T}_\Gamma \cdot {}_I\dot{\boldsymbol{\Gamma}} + {}_{B1}\mathbf{T}_\beta \cdot {}_{B1}\dot{\boldsymbol{\beta}} = \begin{Bmatrix} \dot{\Gamma} \cos \beta \\ \dot{\beta} \\ \dot{\Gamma} \sin \beta \end{Bmatrix}. \quad (3.13)$$

The absolute angular velocity of rotor $\boldsymbol{\omega}$, described in the moving reference frame B2 where the rotation θ appears, is written as:

$${}_{B2}\boldsymbol{\omega} = {}_{B2}\boldsymbol{\Omega} + {}_{B2}\dot{\boldsymbol{\theta}} = \begin{Bmatrix} \dot{\Gamma} \cos \beta \\ \dot{\beta} \\ \dot{\Gamma} \sin \beta + \dot{\theta} \end{Bmatrix}. \quad (3.14)$$

3.3.4 Kinetics

Introducing the kinetics, the mass moments and products of inertia are first considered. The general inertia tensor pertaining to the rotor is given by:

$$\mathbf{I} = \begin{bmatrix} I_{xx} & I_{xy} & I_{xz} \\ I_{yx} & I_{yy} & I_{yz} \\ I_{zx} & I_{zy} & I_{zz} \end{bmatrix}. \quad (3.15)$$

Here the $i = j$ elements and the $i \neq j$ elements denote the moments of inertia and products of inertia of the rotor, respectively.

Looking at the inertia tensor in Figure (3.15) it can now be seen how the additional coordinate systems is advantageous to use. If one were to describe the inertia of the rotor in the inertial coordinate system I , the terms in the inertia tensor would change with time. However, for an inertia tensor defined in the moving reference frame B2 around the pivot point at the spherical bearing, the products of inertia becomes zero under the assumption of a rotational-symmetric system. Furthermore, as the system is rotationally symmetric the two transverse moments of inertia I_{xx} and I_{yy} becomes identical independent of the angular rotation θ . Thus, the inertia tensor in the B2 reference frame is constant and defined as:

$${}_{B2}\mathbf{I}_0 = \begin{bmatrix} I_T & 0 & 0 \\ 0 & I_T & 0 \\ 0 & 0 & I_P \end{bmatrix}, \quad (3.16)$$

where I_T and I_P are the transverse- and the polar mass moment of inertia around the pivot point 0.

The forces acting on the shaft is now considered, for which all are defined in the inertial reference frame, except the unbalance force that is defined in the moving reference

frame B3. The respective position vectors are also defined, all given in the reference frame B2. Furthermore the model is defined around its equilibrium position, thus the gravitational force is disregarded.

- The restoring and dissipative force, defined at the PMB:

$$\mathbf{F}_{mag} = \begin{Bmatrix} F_{mag,x} \\ F_{mag,y} \\ 0 \end{Bmatrix} = \begin{Bmatrix} -d_x\beta l_{OM} - k_x\beta l_{OM} + k_{xy}\Gamma l_{OM} \\ d_y\beta l_{OM} + k_y\Gamma l_{OM} - k_{yx}\beta l_{OM} \\ 0 \end{Bmatrix}, \mathbf{r}_{OM} = \begin{Bmatrix} 0 \\ 0 \\ l_{OM} \end{Bmatrix}. \quad (3.17)$$

- The unbalance force, defined at the unbalance disc:

$$\mathbf{F}_{unb} = \begin{Bmatrix} m_0\varepsilon\Omega^2 \cos \varphi \\ m_0\varepsilon\Omega^2 \sin \varphi \\ 0 \end{Bmatrix} = \begin{Bmatrix} m_0\varepsilon_x\Omega^2 \\ m_0\varepsilon_y\Omega^2 \\ 0 \end{Bmatrix}, \mathbf{r}_{OU} = \begin{Bmatrix} 0 \\ 0 \\ l_{OU} \end{Bmatrix}, \quad (3.18)$$

where m_0 is the unbalance mass, ε is the radial eccentricity of this mass, φ is the phase angle, and the eccentricity components are given by $\varepsilon_x = \varepsilon \cos \varphi$ and $\varepsilon_y = \varepsilon \sin \varphi$.

- The contact force, defined at the impact house:

$$\mathbf{F}_c = \begin{Bmatrix} -F_{cx} & -F_{cy} & 0 \end{Bmatrix}^T, \quad \mathbf{r}_{OC} = \begin{Bmatrix} 0 & 0 & l_{OC} \end{Bmatrix}^T. \quad (3.19)$$

- The magnetic excitation force, defined at the steel target:

$$\mathbf{F}_{exc} = \begin{Bmatrix} F_{exc,x} & F_{exc,y} & 0 \end{Bmatrix}^T, \quad \mathbf{r}_{OE} = \begin{Bmatrix} 0 & 0 & l_{OE} \end{Bmatrix}^T. \quad (3.20)$$

Using the kinematics and the defined kinetics of the rotor system, Euler's equation can be used to derive the equations of motion of the rigid rotor:

$$\sum \mathbf{M}_0 = \mathbf{I}_0 \frac{d}{dt} \mathbf{\omega} + \mathbf{\Omega} \times \mathbf{I}_0 \cdot \mathbf{\omega} + \mathbf{r}_{OG} \times m \cdot \underbrace{\mathbf{a}_0}_{=0}, \quad (3.21)$$

where \mathbf{a}_0 is the absolute linear acceleration of the shaft in the pivot point, \mathbf{M}_0 is a given moment force and \mathbf{I}_0 is the mass moment of inertia matrix, all acting at or around the pivot point (0). It must be mentioned that \mathbf{a}_0 is equal to zero following the assumption of a rigid rolling element bearing i.e. no linear acceleration. Note that Euler's equation is evaluated in the moving reference frame B2, which is advantageous when describing the inertia matrix \mathbf{I}_0 , since it is assumed constant in this reference frame.

Evaluating the non-linear equations of motion derived from Equation (3.21), the following is obtained:

- Γ direction:

$$(d_y l_{OM}^2 \dot{\Gamma} + (\Gamma k - \beta k_{yx}) l_{OM}^2 + F_{exc,y} l_{OE} - F_{c,y} l_{OC}) \cos \Gamma + \dot{\beta} \dot{\Gamma} (I_P - 2I_T) \sin \beta \quad (3.22)$$

$$+ I_P \dot{\beta} \dot{\theta} + I_T \cos \beta \ddot{\Gamma} - l_{OU} m_0 \dot{\theta}^2 (\sin \theta \varepsilon_x - \cos \theta \varepsilon_y) = 0.$$

- β direction:

$$(-\dot{\Gamma}^2 (I_P - I_T) \sin \beta + (-\Gamma k_{xy} + \beta k + \dot{\beta} d_x) l_{OM}^2 - \dot{\Gamma} I_P \dot{\theta} + l_{OC} F_{c,x} - l_{OE} F_{exc,x}) \cos \beta \quad (3.23)$$

$$-((\Gamma k - \beta k_{yx} + d_y \dot{\Gamma}) l_{OM}^2 - F_{c,y} l_{OC} + F_{exc,y} l_{OE}) \sin \Gamma \sin \beta$$

$$+ I_T \ddot{\beta} - l_{OU} m_0 \dot{\theta}^2 (\sin \theta \varepsilon_y + \cos \theta \varepsilon_x) = 0.$$

- θ direction:

$$I_P (\dot{\beta} \cos \beta \dot{\Gamma} + \sin \beta \ddot{\Gamma} + \ddot{\theta}) = 0. \quad (3.24)$$

The solved equations of motion that have been obtained from *Maple* can be found in Appendix D.2.

3.3.5 Moments and Products of Inertia

The inertia tensor is now analytically derived and subsequently verified using the *Solid-Works* CAD program.

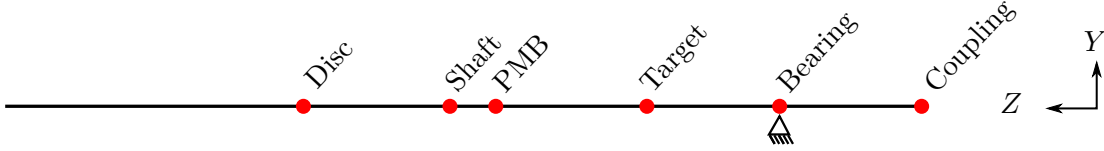


Figure 3.8: Rigid rotor system.

In Figure 3.8 the full system with all the individual machine elements including the shaft is seen. From this, it is possible to obtain the transverse mass moment of inertia I_T around the bearing pivot point. For simplicity, we assume that all the machine element masses can be described as particles, located at their individual center of mass. The mass moment of inertia of the shaft, around the bearing point, is found using the parallel axis theorem. All the masses and their locations can be found in Section 2.5. The total mass moment of inertia around the bearing pivot point is then given by:

$$I_T = I_{xx} = I_{yy} = \frac{1}{12} m_s l_s^2 + m_s r_s^2 + \sum_{i=1}^N m_i r_i^2 = 7.001153554 \cdot 10^{-2} \text{ kg m}^2, \quad (3.25)$$

where N is the number of machine elements considered, m is the mass, r is the distance from the pivot point to the elements center of mass and l_s is the length of the shaft.

Using SolidWorks, the equivalent mass moment of inertia is found yielding $7.08371 \cdot 10^{-2} \text{ kg m}^2$. The acquired program data can be found in Appendix A.3. The discrepancy between the analytically derived inertia and the inertia obtained by SolidWorks comes from the simplifications made in Equation (3.25). All the elements in the analytical expression are assumed lumped masses except for the shaft, where the program yields a more accurate mass moment by including the transverse mass moment of inertia of each element around its own transverse axis. Thus, while the lumped mass model verifies this, the mass moment of inertia generated by SolidWorks is considered to be the better estimator, hence it is used going forward.

3.4 Flexible Rotor

The finite element method has been used to establish a mathematical model of a flexible rotor coupled with the stator system. The motivation for modeling the rotor as a flexible body is partly to compare it with the rigid rotor model, to asses its adequacy in describing the physical system, and partly to study the effect that a flexible rotor has on the contact dynamics.

The FE-model has been formulated gradually by first considering the shaft alone in a free-free condition, and then advancing the model to the point where the entire physical system has been defined in a supported condition. While developing the FE-model, intermediate verifications and validations have been performed to asses the mathematical model and its assumptions. The comparison between the theoretical- and experimental results is given in Chapter 4. An overview of the following sections is given below:

- Mathematical representation and eigenvalue-problem
- Modeling of rotor system
 - Flexible shaft
 - Rigid discs (machine elements)
 - Unsupported rotor system (with and without coupling considered)
 - Rayleigh damping implementation
 - Supported rotor system
 - Modal reduction
 - Computational time analysis
- Modeling of coupled rotor stator system

The entire rotor-stator contact test-rig has been modeled with its associated material properties in the CAD using SolidWorks. Thus it is possible to accurately obtain the specific moments of inertia related to the measured masses for the mathematical model. These properties are tabulated in Section 2.5.

3.4.1 Mathematical Representation and the Eigenvalue-Problem

The general system of equations of motion for the rotor system is on the form:

$$\mathbf{M}\ddot{\mathbf{q}} + (-\Omega \mathbf{G} + \mathbf{D})\dot{\mathbf{q}} + \mathbf{K}\mathbf{q} = \mathbf{Q}, \quad (3.26)$$

where \mathbf{q} is the degrees of freedom DOF, which is a vector of length N , \mathbf{M} is the mass matrix, Ω is the rotational speed, \mathbf{G} is the gyroscopic matrix, \mathbf{K} is the stiffness matrix, and \mathbf{Q} is the external force vector. The system (3.26) may also be put into a *state-space* formulation, that is

$$\underbrace{\begin{bmatrix} \mathbf{0} & \mathbf{M} \\ \mathbf{M} & -\Omega \mathbf{G} + \mathbf{D} \end{bmatrix}}_{\mathbf{M}_{glob}} \underbrace{\begin{Bmatrix} \ddot{\mathbf{q}} \\ \dot{\mathbf{q}} \end{Bmatrix}}_{\dot{\mathbf{z}}} + \underbrace{\begin{bmatrix} -\mathbf{M} & \mathbf{0} \\ \mathbf{0} & \mathbf{K} \end{bmatrix}}_{\mathbf{K}_{glob}} \underbrace{\begin{Bmatrix} \dot{\mathbf{q}} \\ \mathbf{q} \end{Bmatrix}}_{\mathbf{z}} = \underbrace{\begin{Bmatrix} \mathbf{0} \\ \mathbf{Q} \end{Bmatrix}}_{\mathbf{f}} \Rightarrow \mathbf{M}_{glob}\dot{\mathbf{z}} + \mathbf{K}_{glob}\mathbf{z} = \mathbf{f}, \quad (3.27)$$

where \mathbf{M}_{glob} and \mathbf{K}_{glob} are the *state matrices*, \mathbf{z} is the *state vector* of length $2N$, and \mathbf{f} is the *input vector*. The state-space representation is useful because it allows the equation of motion to be solved as a standard eigenvalue problem, which otherwise would be difficult to solve due to the velocity-depended internal forces, i.e. the gyroscopic- and the damping force. Furthermore the state-space form is also convenient for implementing the numerical solution of the mathematical model.

To determine the natural frequencies and associated mode shapes of the system, the generalized eigenvalue problem is setup on the state-space formulation (3.27). The problem becomes

$$(\mathbf{M}_{glob}\lambda_j + \mathbf{K}_{glob})\varphi_j = 0, \quad \lambda_j = a_j + ib_j, \quad \varphi_j = \mathbf{r}_j + i\mathbf{s}_j, \quad (3.28)$$

where λ_j and φ_j denote the j -th eigenvalue and right eigenvector, respectively. The eigenvalues come in complex pairs where the real and imaginary part represents the damping level and damped natural frequency, respectively. The undamped natural frequency is equal to the magnitude of the complex eigenvalues. The eigenvectors do also come in pairs where the first and second half describes the relative velocity and displacement, respectively (as it has been normalized in this model).

3.4.2 The Flexible Shaft

The mathematical model of the flexible rotor-system is formulated by discretizing the shaft into a number of finite elements which are joined at points referred to as *nodes*. The remaining components of the rotor-system, i.e. the individual machine elements (ME), are then mounted as lumped entities at the nodes. Thus the equation of motion of the flexible shaft is to be determined in the following.

The Mathematical Model of the Shaft

The physical model of the shaft, as well as the coordinate system used for reference, is seen in Figure 3.9. The geometric complexities shown in the figure, that is: the keyway, the turned end, and the milled surfaces, are all neglected in the mathematical model.

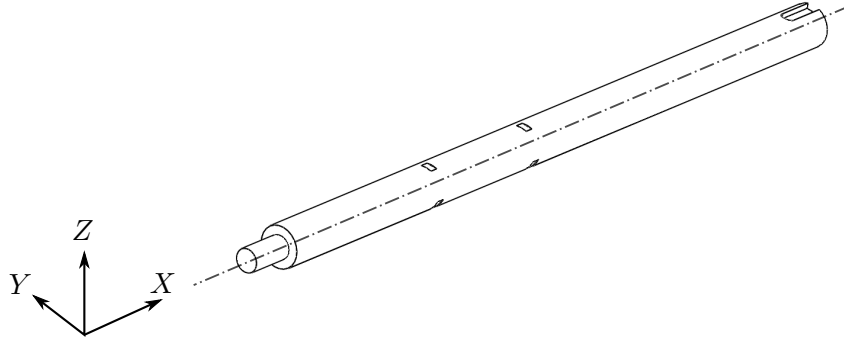


Figure 3.9: The physical model of shaft in the free-free configuration, and the reference coordinate system used in the mathematical model.

For the discretization of the shaft, two-node beam elements are used. Each element has 8 DOFs, consisting of two translational- and two rotational DOFs at each node. The equation-of-motion system pertaining to the flexible shaft is then determined following the same method as derived in [21]. In brief, this entails some fundamental shape functions, describing the movements of any point within the shaft element, introducing boundary conditions at the nodes, and lastly applying Lagrange's energy equation with the expressions for the potential and kinetic energy in the shaft. The equation of motion of a single flexible shaft element, containing the *local*- mass, stiffness, and gyroscopic matrices, then becomes

$$\mathbf{M}^S \ddot{\mathbf{q}} - \boldsymbol{\Omega} \mathbf{G}^S \dot{\mathbf{q}} + \mathbf{K}^S \mathbf{q} = \mathbf{0}, \quad (3.29)$$

where the superscript *S* refers to the shaft.

Having the local matrices, the individual contribution of each shaft element can be collected and assembled into the *global* equation-of-motion system (3.26), in accordance with each element's corresponding global DOF.

Assumptions Concerning the Shaft

The mathematical model (3.29) for the flexible shaft employs the following assumptions:

- Lateral vibrations are dominant, thus torsional vibrations are neglected.
- The shaft is isotropic and symmetrical around its longitudinal axis of rotation.
- Bernoulli-Euler beam theory is adequate, and the shaft is linearly elastic.

- The system is conservative, i.e. no dissipation of energy can occur.
- The shaft is completely unsupported, and no external forces act on the shaft.

Convergence Study and Verification of the Shaft Model

Since the finite element method is an approximate numerical method, great care must be taken in finding a sufficient number of shaft-elements needed to describe the actual dynamics of the physical shaft. Furthermore, the discretization must also fall in accordance with the location of the machine elements in the physical system.

To determine the necessary number of elements, a convergence study has been conducted. The study was performed by inspecting the first three natural frequencies, associated with the bending mode shapes of the shaft in a free-free condition, while varying the number of elements, i.e. the coarseness of the discretization. The decision of using only the first three bending modes is merited by the fact that the sought mathematical model is to be valid in the frequency range 0–1000 Hz. The shaft elements were all kept at an uniform length and for each discretization halved/doubled to remain on the node locations. The maximum error criterion of the natural frequencies was chosen to be 2%.

The result of the study is given in Table 3.3. The *error* is defined relative to the natural frequencies obtained from the analytical solution of a simple flexible beam [14]. Thus it is an assumption that the analytical result is adequate for describing the dynamic behavior of the physical shaft. Considering the discrepancies found between the analytically- and numerically found natural frequencies, the error is found to lie within the criterion for all of the four discretization schemes. Furthermore, the natural frequencies are found to converge at a frequency close to the analytical estimate.

	ω_1 [Hz]	Error [%]	ω_2 [Hz]	Error [%]	ω_3 [Hz]	Error [%]
4 elements	455.1	0.3	1254.8	0.3	2449.5	0.7
8 elements	454.6	0.4	1247.9	0.8	2435	1.3
16 elements	454.6	0.4	1247.2	0.9	2430.3	1.5
16 adj. elements	454.6	0.4	1247.2	0.9	2430.3	1.5
32 elements	454.6	0.4	1247.1	0.9	2429.8	1.5
Analytical	456.4	-	1258.1	-	2466.3	-

Table 3.3: Natural frequencies the unsupported shaft, with material the parameters: $E = 69 \cdot 10^9$ Pa, $\rho = 2800$ kg/m³.

While all the discretization levels were found to have converged relative to the first two bending modes, it was chosen to use 16 elements for the final shaft model. The reasoning behind this surplus number of elements is that it is desirable to have a sufficiently high level of discretization so that the elements ends up having close to uniform lengths, while there is still enough nodes such that subsequently it is still possible to

mount the machine elements at roughly their exact position on the shaft, applying only minor adjustments and in turn only minor disturbances to the otherwise equidistant placements of the shaft nodes. The discretization of the shaft can be seen in Figure 3.10 with the later assigned machine elements.

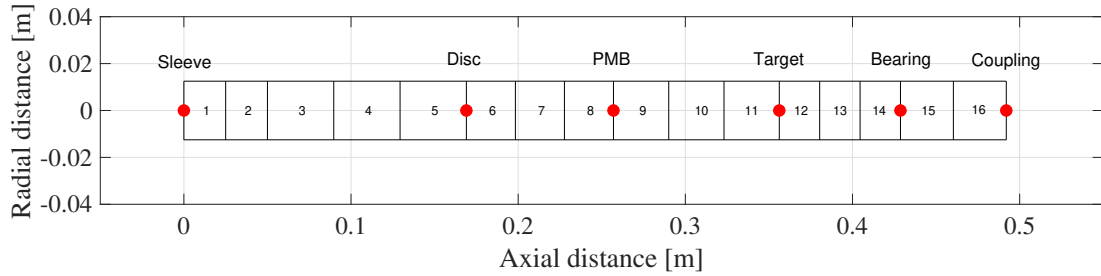


Figure 3.10: Element discretization plot.

3.4.3 Rigid Discs

As described in Chapter 1, four rotor components are mounted on the shaft, i.e. the unbalance disc, the rotor part of the PMB, the steel target, and the coupling. These machine elements all add mass and inertia to the system, while any potential stiffening effect on the shaft, due to their presence, is neglected. The contribution of the disc components are to be added to the global system in the following section.

Mathematical Model of the Discs

The equations of motion for the discs are determined similarly as for the shaft elements by using the Lagrangian energy formulation, according to procedure given in [21]. However, this time, since the discs are rigid, no source of potential energy is present. Considering the remaining kinetic energy expressions, the system of equations of motion become

$$\mathbf{M}^D \ddot{\mathbf{q}} - \boldsymbol{\Omega} \mathbf{G}^D \dot{\mathbf{q}} = \mathbf{0}, \quad (3.30)$$

where the superscript D refers to the discs.

As was the case with the shaft elements, having determined the local mass and gyroscopic matrices, these can also be assembled into the global equation system (3.26), again in accordance with each element's corresponding global DOF.

Assumptions Concerning the Discs

The mathematical model (3.30) for the discs makes the following assumptions:

- The discs are rigid, i.e. unable to store potential energy.
- There is no dissipation of energy nor external forces present.
- The rigid discs are rotationally symmetric.

3.4.4 The Unsupported Rotor System

The four rigid discs mounted onto the flexible shaft constitutes the rotor system, which is shown below without the coupling mounted:

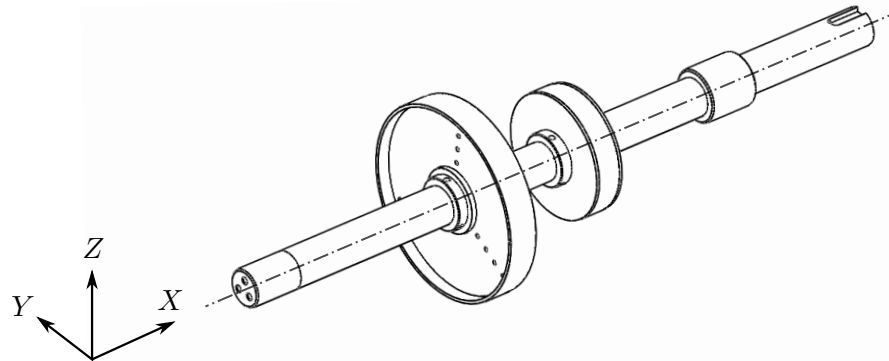


Figure 3.11: Physical model of rotor.

For comparison reasons, the rotor system is first considered without the coupling being installed, in order to verify the dynamics using the EMA carried out in Section 4.1, in which the coupling has not been installed. The natural frequencies and mode shapes of the undamped, unsupported, and non-rotating system is found by solving the eigenvalue problem, presented in (3.28). The eigenvalues come out as pure imaginary as no damping is yet introduced. Solving the EVP of the rotor (as was done for the flexible shaft), the MATLAB function `eig` is used. Stabilizing the algorithm for the free-free system, a small stiffness of 3.468 N/m and 10 N/m is added at the location of the permanent magnetic bearing and the spherical bearing preventing rigid body motions (furthermore it has been checked that the added stiffness does not affect the bending modes). The four first mode shapes in the YX -plane of the free-free rotor and their corresponding natural frequencies are given below (the frequencies and modes are identical in the XZ -plane due to symmetric rotor and support):

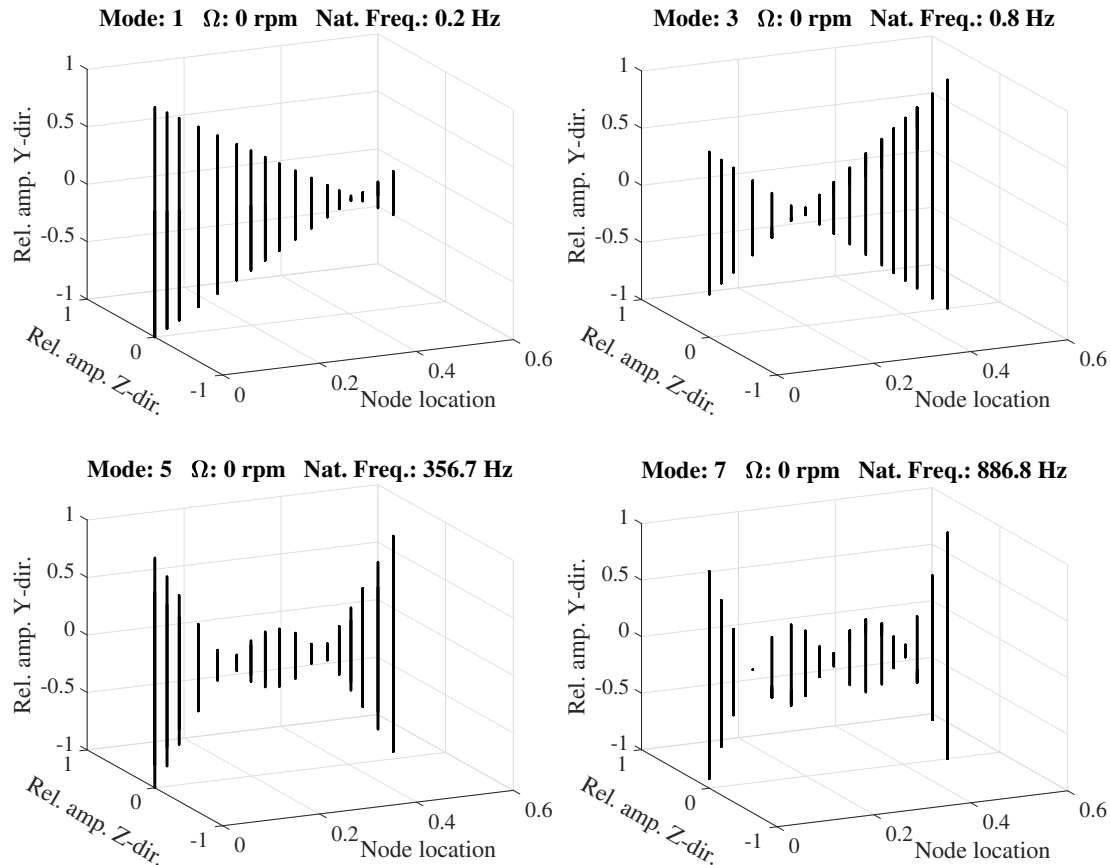


Figure 3.12: Four first free-free mode shapes of rotor - without the coupling.

Considering Figure 3.12 we see that the rigid body modes are not given by the classical translatory and conical mode shape. This is due to support positions and the non-uniform mass distribution along the shaft. The bending modes resemble the generic mode shapes of a uniform symmetric system, however slightly asymmetric due to the added ME masses. The belonging natural frequencies of 356.7 Hz and 886.8 Hz seems to be reasonably in accordance with the two first frequencies of the pure flexible shaft, since the added mass should reduce the natural frequencies.

The equivalent free-free mode shapes of the rotor with the coupling mounted are shown in Figure 3.13.

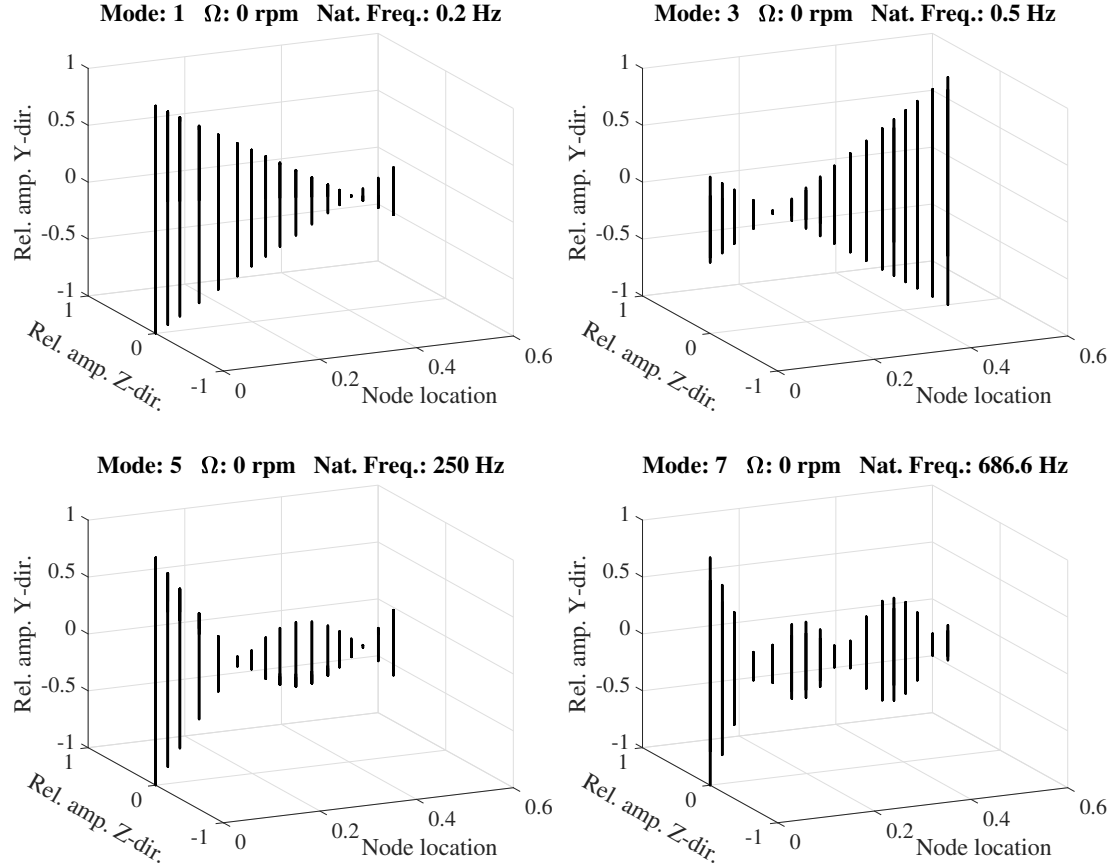


Figure 3.13: Four first free-free mode shapes of rotor - with coupling.

A second convergence study has also been made, considering the unsupported rotor system with the four rigid discs mounted:

	ω_1 [Hz]	ω_2 [Hz]	ω_3 [Hz]	ω_4 [Hz]	Error [%]	ω_5 [Hz]	Error [%]
10 elements	0.2	0.5	250	686.7	0.01	1263.7	< 0.01
16 elements	0.2	0.5	250	686.6	< 0.01	1263.6	< 0.01
32 elements	0.2	0.5	250	686.6	-	1263.6	-

Table 3.4: Natural frequency convergence of unsupported rotor.

Looking at the differences in natural frequencies in Table 3.4 it becomes evident that the system is considered converged for the three different number of elements, with the requirement of describing the system using the rigid-body mode shapes and the two first bending modes.

3.4.5 Rayleigh Damping

Up till now, no damping has been considered. For modeling the dissipation of energy in the rotor, Rayleigh damping (or proportional damping) is introduced. The damping is assumed to be proportional to the mass and stiffness matrices, which physically relates to the external- and internal friction, respectively. The two matrices are weighted by the damping parameters α and β , which yields the expression:

$$\mathbf{D} = \alpha \mathbf{M} + \beta \mathbf{K}. \quad (3.31)$$

The damping parameters have been obtained through an experimental modal analysis, as shown in Section 4.1.3, from which the following parameters were found:

$\zeta_1 [-]$	$\zeta_2 [-]$	$\omega_1 [\text{Hz}]$	$\omega_2 [\text{Hz}]$	α / β	α	β
$2.8 \cdot 10^{-3}$	$1.9 \cdot 10^{-3}$	354.9	883	$10.57 / 3.53 \cdot 10^{-7}$	12.32	$2.48 \cdot 10^{-6}$

Table 3.5: Modal parameters from obtained from the EMA.

Considering the three possible assumptions which can be made regarding the damping parameters, i.e. the damping either depends only on α , only on β , or on both, it is found that using only α the rigid-body modes are damped significantly. This is unwanted since these modes are to be damped using an equivalent discrete viscous damping on the PMB later in the report. Thus only the β coefficient is used to obtain the damping matrix \mathbf{D} by (3.31). Thus this will be used throughout the rest of the project.

Furthermore, the material properties tabulated in Section 2.5, namely the material densities and modulus of elasticity, have been tuned such that the unsupported rotor systems natural frequencies are matching the natural frequencies obtained by the EMA. The comparison of the theoretical and experimental results can be found in Section 4.1.4.

3.4.6 The Supported Rotor System

The bearing stiffness and damping of the PMB and the spherical bearing is now added to the rotor system including the coupling, along with the Rayleigh damping introduced in the previous section.

The equivalent stiffness and damping of the PMB is first found through transient decay experiments, as presented in Section 4.4, yielding the equivalent direct-related stiffness and damping coefficients k_{yy} , k_{zz} , d_{yy} , and d_{zz} . However, in doing the experimental fitting of the unbalance parameters in Section 4.5, different damping characteristics were found when the rotor system was rotating at a speed different from zero, in comparison to what was found for the transient decay response in a non-rotating condition. Thus, two damping matrices for the PMB are established and used accordingly. Additionally, the experimental fitting of the unbalance revealed that a cross coupled stiffness is present yielding $k_{yz} = 3.09 \cdot 10^4 \text{ N/m}$ and $k_{zy} = 292 \text{ N/m}$ (here represented in the FE-model coordinate system). This cross-coupled stiffness is fitted to the experimentally found unbalance response around the first critical speed. Thus, the cross stiffness estimate is

only considered properly fitted and used in the model when the rotational speed is in the vicinity of the first critical speed, while it is disregarded for zero rotational speed.

The following coefficients are thus used in the FE-model:

$$\mathbf{K}_{PMB} = \begin{bmatrix} 3.09 \cdot 10^4 & 2.456 \cdot 10^3 \\ 292 & 3.09 \cdot 10^4 \end{bmatrix} \left[\frac{N}{m} \right], \quad \mathbf{K}_{SP} = \begin{bmatrix} 10^9 & 0 \\ 0 & 10^9 \end{bmatrix} \left[\frac{N}{m} \right], \quad (3.32)$$

$$\mathbf{D}_{SP} = \begin{bmatrix} 100 & 0 \\ 0 & 100 \end{bmatrix} \left[\frac{Ns}{m} \right], \quad (3.33)$$

$$\mathbf{D}_{PMB-ROT} = \begin{bmatrix} 8 & 0 \\ 0 & 7.7 \end{bmatrix} \left[\frac{Ns}{m} \right], \quad \mathbf{D}_{PMB-NOROT} = \begin{bmatrix} 40.9 & 0 \\ 0 & 7.7 \end{bmatrix} \left[\frac{Ns}{m} \right], \quad (3.34)$$

where the *PMB* subscript denotes the permanent magnetic bearing, *SP* denotes the spherical bearing, and *PMB – ROT* and *PMB – NOROT* denotes a rotational speed different from zero and equal to zero, respectively. The damping and stiffness of the spherical bearing are both set at an arbitrary magnitude, both assumed much greater than that for the PMB. The stiffness of a ball bearing is typically greater than 10^8 N/m, above which a change in stiffness does not change the dynamics. Hence, using a roller bearing the stiffness is assumed to be 10^9 N/m. The damping in the spherical roller is introduced to stabilize the simulation, appearing due to numerical precision errors.

Introducing the bearing stiffnesses, it is favorable to analyze the effect on the natural frequencies. The stiffnesses have been varied with a logarithmic interpolation from the above stated full stiffness of each bearing (each normalized to 1 individually), down to a free-free condition with stiffness 3.468 N/m and 10 N/m used at the PMB and the spherical bearing (each normalized to 0), respectively. In Figure 3.14 we see that the two first natural frequencies, related to the rigid body motions, increase gradually as would be expected. The next couple of natural frequencies, related to the bending modes, are initially unaffected by the bearing stiffness, until the stiffness gets sufficiently high, introducing a small increase.

The normalized bearing stiffness of zero, is simulating the free-free condition with the mode shapes previously shown in Figure 3.13. The proportionally-damped mode shapes and their corresponding natural frequencies with full added bearing stiffness, are shown in Figure 3.15. Comparing the mode shapes of the free-free system and the supported system, it becomes evident that one of the rigid body mode shapes of the free-free system is not within the four first natural frequencies of the supported system. The reason for this, is due to the mode shape yielding relatively high amplitudes at the spherical bearing location, thus being highly depended on this support stiffness. Since the support stiffness is of ninth order of magnitude, the natural frequency related to this rigid body mode shape is greatly increased.

Considering again the bearing stiffness resonance sensitivity in Figure 3.14, we see that even though the natural frequencies are increased continuously from the free-free condition to the fully supported condition, the mode shapes are freely capable of changing and swapping characteristics.

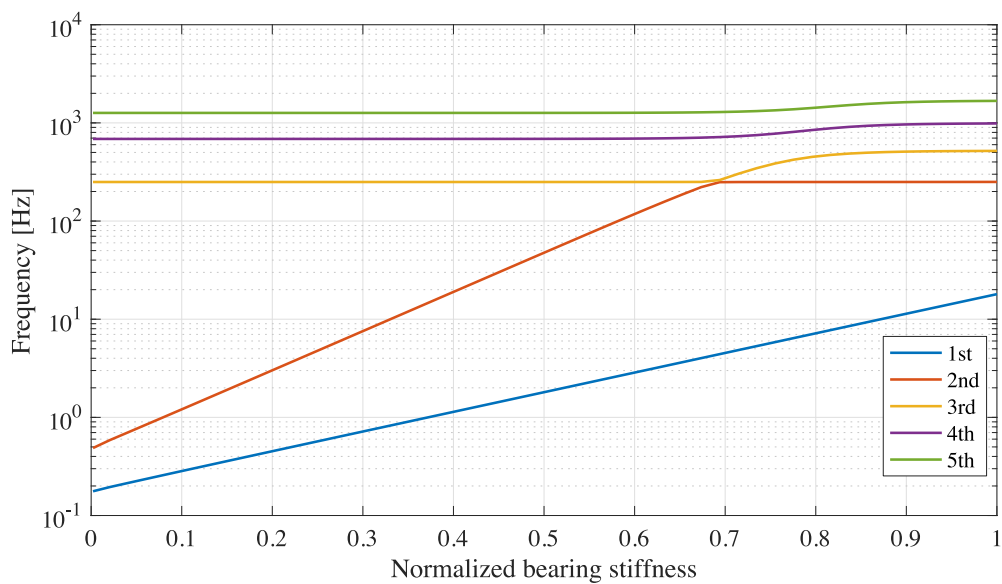


Figure 3.14: Bearing stiffness resonance sensitivity - plotting the first five natural frequencies.

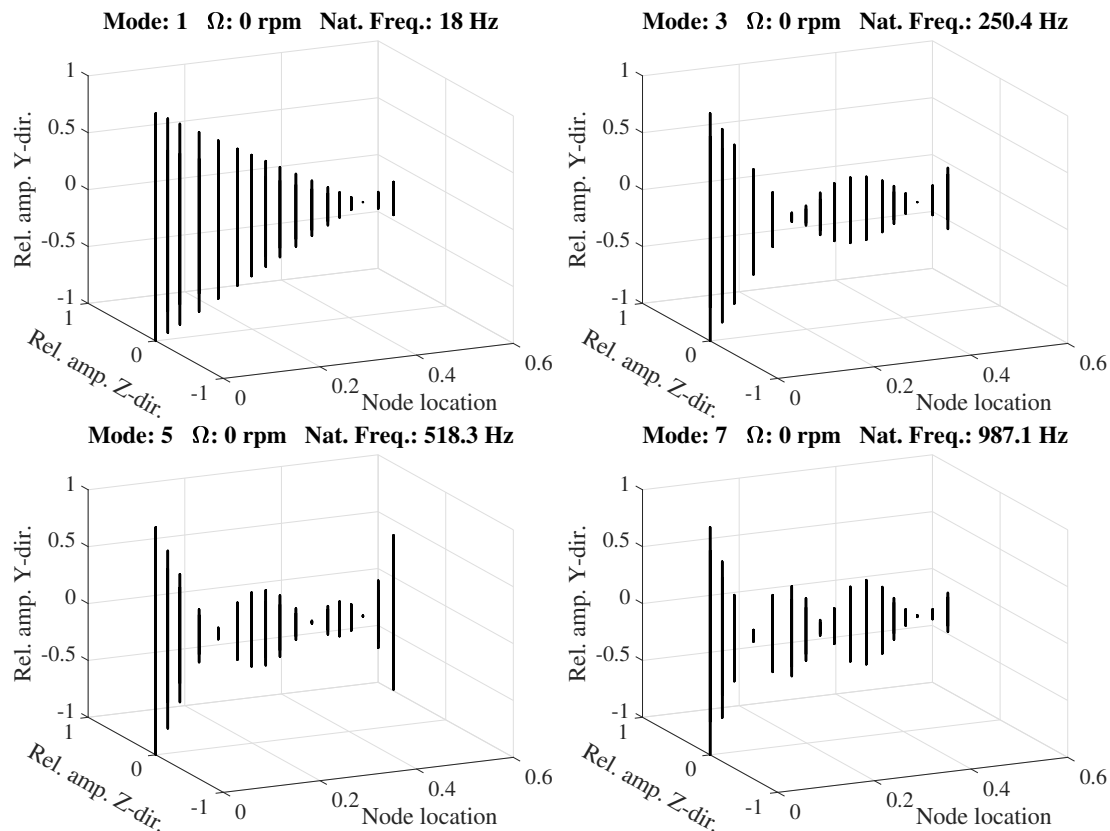


Figure 3.15: Four first damped mode shapes.

3.4.7 Modal Reduction

As it is wanted to perform a time integration of the rotor system, a modal reduction is desirable for an otherwise computationally-heavy model. It is assumed that vibrations of the rotor can be described by a linear combination of its mode shapes, each at their corresponding natural frequency. However, only the mode shapes related to the first couple of frequencies are normally sufficient to accurately describe the dynamics. Thus, a modal reduction has been made.

The modal reduction has been made for the state-space form presented in (3.27), for which both the left- and right eigenvectors of the generalized eigenvalue problem (3.28) are required. The eigenvalues and both set of eigenvectors are found by solving the generalized eigenvalue problem. The left- and right eigenvectors are then defined as columns in the matrices \mathbf{L} and \mathbf{R} , respectively. Subsequently the eigenvectors are orthonormalized such that the following relations are guaranteed:

$$\mathbf{L}^T \mathbf{M}_{\text{glob}} \mathbf{R} = \mathbf{I}, \quad \mathbf{L}^T \mathbf{K}_{\text{glob}} \mathbf{R} = [\lambda].$$

where \mathbf{I} is the identity matrix, and $[\lambda]$ is a matrix containing the eigenvalues in its diagonal elements.

The system of equations of motion on the state space form, presented in (3.27), is given by:

$$\mathbf{M}_{\text{glob}} \dot{\mathbf{z}} = -\mathbf{K}_{\text{glob}} \mathbf{z} + \mathbf{f}.$$

Inserting the solution $\mathbf{z} = \mathbf{R} \boldsymbol{\eta}$, where $\boldsymbol{\eta}$ is the modal vector, and pre-multiplying by the left eigenvector matrix transpose (\mathbf{L}^T), we arrive at:

$$\underbrace{\mathbf{L}^T \mathbf{M}_{\text{glob}} \mathbf{R}}_{\mathbf{I}} \dot{\boldsymbol{\eta}} = -\underbrace{\mathbf{L}^T \mathbf{K}_{\text{glob}} \mathbf{R}}_{[\lambda]} \boldsymbol{\eta} + \mathbf{L}^T \mathbf{f}. \quad (3.35)$$

Hence, the equations of motion in the modal coordinates decouple, and we obtain the possibility of truncating the eigenvector matrices, i.e. describing the dynamics by a subset of mode shapes.

The above stated relations of the identity matrix and eigenvalue diagonal matrix is always "polluted" to a certain degree with some numerical errors, using numeric tools, yielding $\mathbf{LMR}(i \neq j) \neq \mathbf{0}$ and $\mathbf{LKR}(i \neq j) \neq \mathbf{0}$. Even though this pollution is often insignificant for a well-conditioned systems, the matrices are checked in this case:

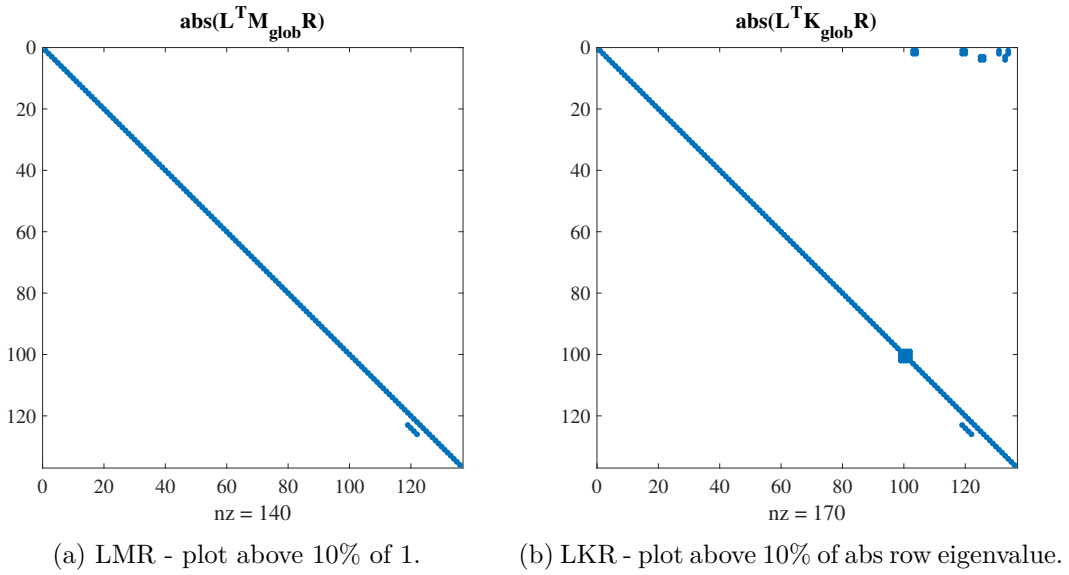


Figure 3.16: Conditioning of the eigenvectors.

The identity matrix "LMR" and eigenvalue diagonal matrix "LKR" given in (3.35) are calculated using the sorted and normalized left- and right eigenvectors of the previously presented eigenvalue-problem. Despite the fact that the LMR yields unity in the diagonal and LKR yields accurate eigenvalues in the diagonal, the above Figure 3.16 shows non-zero terms outside the diagonal greater than 10% of their respective ideal diagonal value. This "contamination" is thought to stem from an ill-conditioned eigenvalue-problem, due to the ill-conditioned \mathbf{M} and \mathbf{K} matrix. This emerges from the difference in order magnitude of the terms in both the matrices (mostly the \mathbf{K} matrix), that appears due to the disproportionate use of SI-units and the magnitude of the element dimensions. However, the top left square of 16x16 yields well conditioned relations, which is important for the later used modal truncation to the 8 first mode shapes (16 first in the state-space form). Also, it must be noted that the contamination becomes more irrelevant for the higher mode shapes, since these are mostly of an insignificant magnitude in the actual response. It must be mentioned that the EVP problem has been solved both on a standard form, as well as a generalized form, whereas the generalized showed better results.

3.4.8 Computational Time Analysis

In order to simulate the dynamics of the rotor system using the modal reduction, the bearing stiffness and damping must be excluded from the state-matrices \mathbf{M}_{glob} and \mathbf{K}_{glob} . However, the stiffness and damping of the support is applied as an external force directly in the solver, being a function of displacement and velocity.

The modal reduction gives the possibility of describing the dynamics of the rotor sufficiently accurate, using only a few mode shapes. Thus, a computational time com-

parison is made for the full system and the reduced system using a different number of mode shapes. A simple set of initial conditions is used, being that in the XY -plane $\mathbf{q}_0(t = 0) = 0.001 \text{ m}$ and in the XZ -plane $\dot{\mathbf{q}}_0(t = 0) = 0.2 \text{ m/s}$ is simulated for 0.1 s. The computational time is captured eight times for each number of mode shapes, whereas the computational time used for the full system, without modal reduction, is averaged.

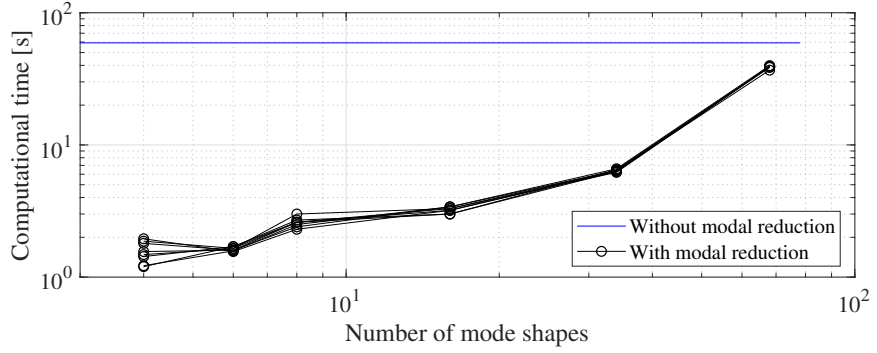


Figure 3.17: Simulation of modal reduction with [4, 6, 8, 16, 34, 68] mode shapes included.

Looking at Figure 3.17 it becomes evident that a great time reduction is acquired by the modal reduction. The full system average computational time is 59.2 s for a simulation of 0.1 s, whereas the average computational time with the modal reduction using 8 mode shapes (corresponding to a rigid rotor) is 1.7 s.

3.4.9 Unbalance of the Rotor System

The unbalance of the rotor system is now introduced in the finite element model, and assumed to be concentrated at the unbalance disc due to the unavoidable residual unbalance in the rotor system. The unbalance is defined as a lumped mass m_0 at a radial distance ε away from the rotor center at the node related to the unbalance.

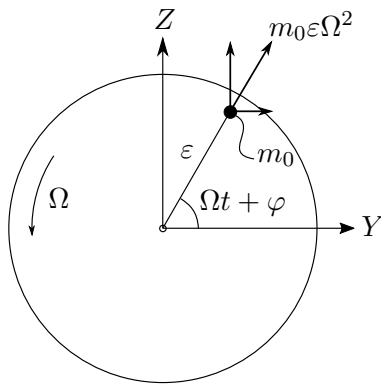


Figure 3.18: Overview of the unbalance force.

Considering Figure 3.18 we find that the unbalance force Q_u is given by:

$$\mathbf{Q}_u = \begin{Bmatrix} F_Y \\ F_Z \end{Bmatrix} = m_0 \varepsilon \Omega^2 \begin{Bmatrix} \cos(\Omega t + \varphi) \\ \sin(\Omega t + \varphi) \end{Bmatrix}, \quad (3.36)$$

where F_Y and F_Z are the lateral forces acting at a given node.

Rewriting the equation into complex form using Euler's formula yields:

$$\mathbf{Q}_u = \begin{Bmatrix} F_Y \\ F_Z \end{Bmatrix} = \frac{m_0 \varepsilon \Omega^2}{2} \begin{Bmatrix} 1 \\ 1/i \end{Bmatrix} e^{i\Omega t} + \frac{m_0 \varepsilon \Omega^2}{2} \begin{Bmatrix} 1 \\ -1/i \end{Bmatrix} e^{-i\Omega t} = \mathbf{f}_+ e^{i\Omega t} + \mathbf{f}_- e^{-i\Omega t}, \quad (3.37)$$

where \mathbf{f}_+ and \mathbf{f}_- describes the forward and backward force, respectively.

Inserting \mathbf{Q}_u into the corresponding DOF of \mathbf{Q} in (3.26), such that only the lateral DOF of the unbalance disc is non-zero, the steady-state solutions to the given equation of motion are assumed to be:

$$\mathbf{q}_+(t) = \bar{\mathbf{q}}_+ e^{i\Omega t} \quad \text{and} \quad \mathbf{q}_-(t) = \bar{\mathbf{q}}_- e^{-i\Omega t}.$$

By insertion, the unbalance response become

$$\bar{\mathbf{q}}_+ = (-\Omega^2 \mathbf{M} + i\Omega(-\Omega \mathbf{G} + \mathbf{D}) + \mathbf{K})^{-1} \mathbf{f}_+, \quad (3.38)$$

$$\bar{\mathbf{q}}_- = (-\Omega^2 \mathbf{M} - i\Omega(-\Omega \mathbf{G} + \mathbf{D}) + \mathbf{K})^{-1} \mathbf{f}_-, \quad (3.39)$$

$$\bar{\mathbf{q}}_u = \bar{\mathbf{q}}_+ + \text{conj}(\bar{\mathbf{q}}_-). \quad (3.40)$$

Using Equation (3.38), the unbalance response can be found, as shown in Figure 3.19, for the angular velocity ranges 0–1000 Hz and 0–30 Hz, noting that the latter is the operational range used in this project. The radial distance is simply approximated as the euclidean distance, although the response at some rotational velocities are highly elliptical.

3.4.10 Critical Speeds

The first critical speed is obtained by the use of Campbell diagram for a 1X unbalance excitation. The Campbell diagram is shown below in Figure 3.20, plotting the damped natural frequency as a function of the rotational velocity of the rotor.

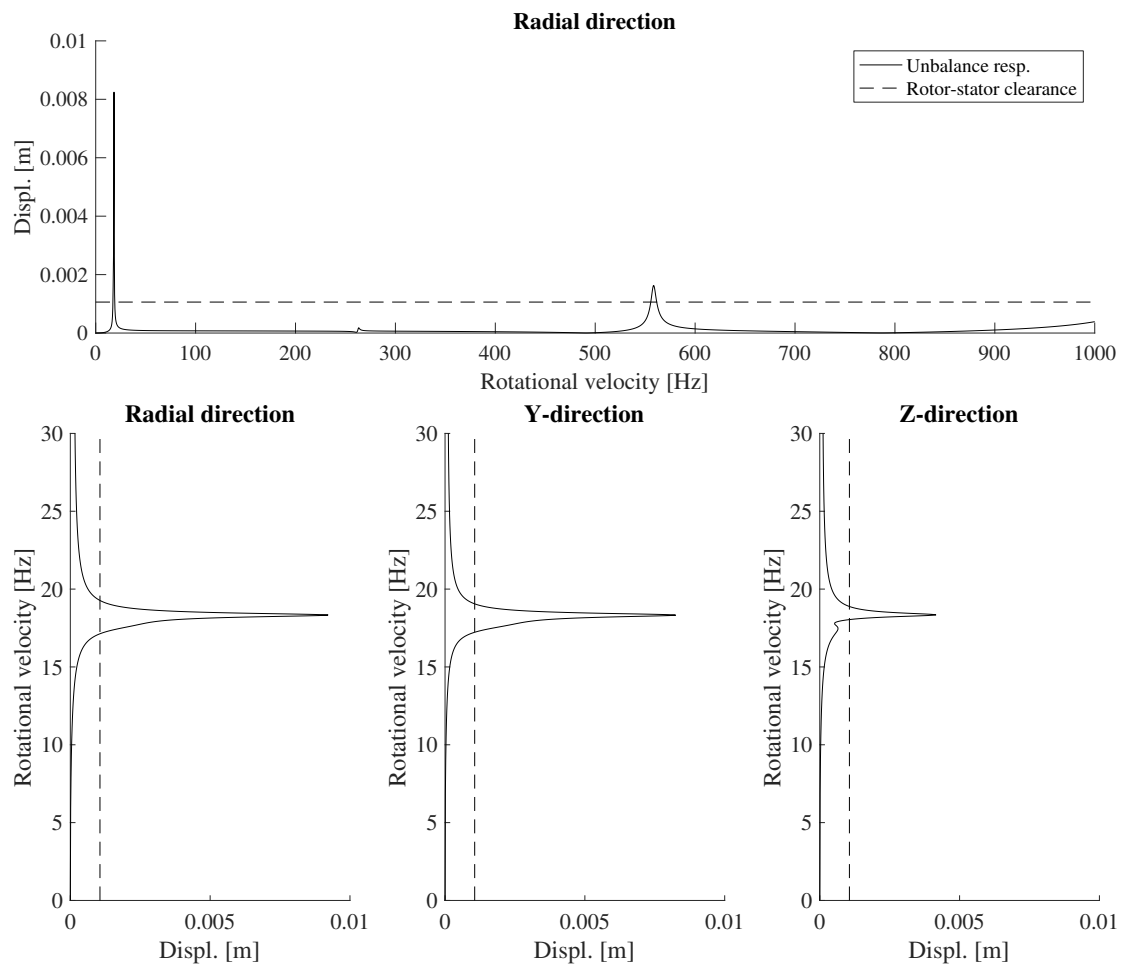


Figure 3.19: Unbalance response.

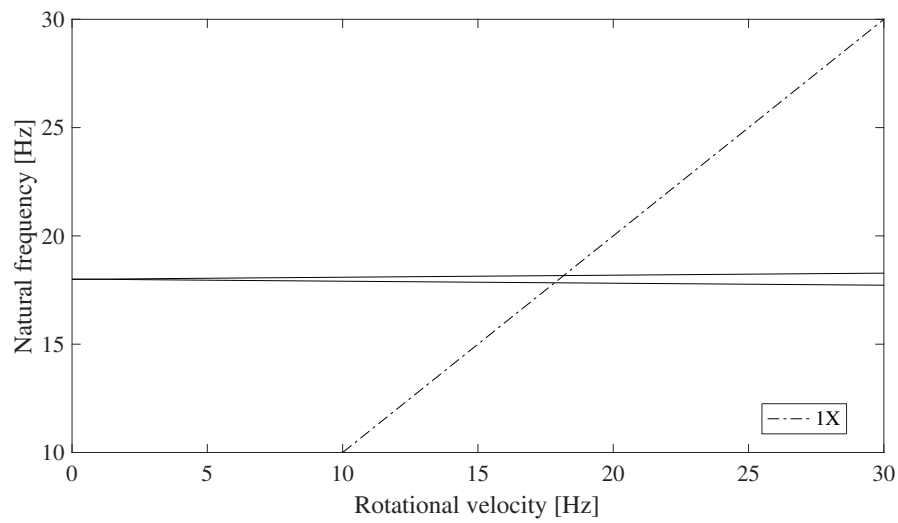


Figure 3.20: Campbell diagram - 1st Critical Speed: 18.17 Hz.

Considering the natural frequencies of the Campbell diagram it becomes evident that the gyroscopic effect has almost no effect when the rotor spins within the range 0–30 Hz. The first critical speed is in this system defined as the intersection of the $1\times$ line and the forward-mode line, considering the symmetric rotating system.

3.4.11 The Rotor Stator System

The stator system, being the impact house, is now implemented in the finite element model simulation with the equations of motion given in Equation (3.6). As done in Equation (3.27), the equations of motion are put into state-space form:

$$\dot{\mathbf{z}}_s = \underbrace{\begin{bmatrix} \mathbf{0} & \mathbf{I} \\ -\mathbf{M}_s^{-1}\mathbf{K}_s & -\mathbf{M}_s^{-1}\mathbf{D}_s \end{bmatrix}}_{\mathbf{A}_s} \mathbf{z}_s + \underbrace{\begin{Bmatrix} \mathbf{0} \\ \mathbf{M}_s^{-1}\mathbf{F}_c \end{Bmatrix}}_{\mathbf{f}_s}, \quad (3.41)$$

where the subscript s denotes the stator system.

Having this, the full rotor stator system can now be described solving the following system of equations:

$$\begin{Bmatrix} \dot{\boldsymbol{\eta}} \\ \dot{\mathbf{z}}_s \end{Bmatrix} = \left[\begin{array}{cc|c} \ddots & \lambda & \mathbf{0} \\ & \ddots & \\ \hline \mathbf{0} & & \mathbf{A}_s \end{array} \right] \begin{Bmatrix} \boldsymbol{\eta} \\ \mathbf{z}_s \end{Bmatrix} + \begin{Bmatrix} \mathbf{L}^T \mathbf{f} \\ \mathbf{f}_s \end{Bmatrix}. \quad (3.42)$$

3.5 Simulation Codes

The two mathematical models presented in this chapter have been implemented numerically in MATLAB to be able to simulate the dynamic response of the rotor-stator system. This have resulted in two separate programs which implement the rigid- and the flexible model, respectively. The advantage of the rigid program is its efficiency in solving the analytical expressions for the rotor-stator system, however since it assumes rigidity of the rotor, it is potentially not adequate in describing the physical system when the effect of flexibility is pronounced. Conversely the flexible program was made for this very reason, however the finite element approach is taxing in terms of time, even when employing modal reduction. In the following section the details pertaining to the programming of these codes is presented.

Numerical Integration

The nature of the rotor-stator system is such that the two states, pertaining to whether contact is present or not, changes the problem of solving for the dynamic response in the numerical implementation. While no contact is present, the problem can be defined as being *structural*, that is loads vary relatively slow. Conversely, upon contact the employed penalty method causes a rapid change in the load on the rotor, which can

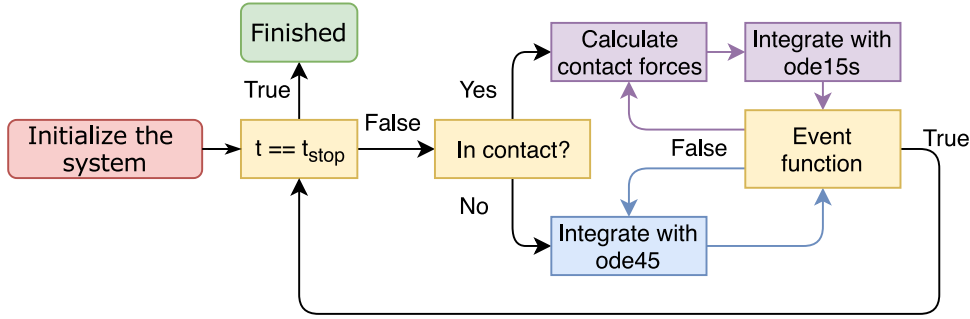


Figure 3.21: The overall scheme of the numerical integration procedure for simulating the dynamics of the rotor-stator system.

induce high-frequency responses. Furthermore, during contact the system become *stiff*, which is a subtle definition that generally depends on the eigenvalues of the system being spread apart, such that the ratio between largest and the smallest eigenvalue become large. This transition of the problem from a non-stiff to stiff one introduce some difficulties regarding the numerical integration.

MATLAB provides a plethora of solvers for solving ODEs [5]. The most commonly used solver is the `ode45` solver, which is an implementation of the classic 4th order explicit Runge-Kutta (RK4) method [2]. This particular solver is apt for the task of integrating the present equations of motion in the non-contact (non-stiff) state of the simulations. However, upon contact the solver becomes infeasible to use. Instead, the `ode15s` solver can be used. This solver is a variable-step, variable-order (VSVO) solver, which is able to handle stiff problems.

On the basis of these two solvers, and given the issue related to the stiffness of the problem, there are two possible solutions for integrating the system of equations. Either `ode15s` is used solely, or alternatively the solution space is partitioned into two parts according to the contact states, and then both solvers can be used separately in the two domains. In the two programs the latter solution has been implemented. The motivation for using both solvers is to try to improve the efficiency of the programs with respect to time as `ode45` may operate faster in the non-contact zone.

A great task of implementing the dual-solver solution is to detect exactly when the rotor transcends the clearance and vice versa. In MATLAB, *event functions* can be used together with the ODEs solvers to search for distinct locations in the solution space while the integration is in progress. In this case the solvers evaluate an event function at each time step, evaluating whether the clearance perimeter is traversed. Upon overstepping the clearance perimeter the currently active solver terminates, after which the other solver takes over from the last solution step. The flowchart shown in Figure 3.21 illustrates the conceptual scheme of this procedure. Both the rigid and the flexible implementation follows this concept.

In terms of speedup, the flexible program appears to benefit the most from this implementation. Since its execution is also much longer than that of the rigid program,

the effect is even more useful. Quantitative measures for the speedup in the particular rotational impact case, presented in the Results chapter, showed both programs to be faster with the dual-solver solution. Specifically a speedup of 17% and 21% was recorded for the rigid- and flexible program, respectively. For comparison the average execution times went down from 11.9 s to 9.78 s in the rigid program, while for the flexible program the numbers were 255 s and 210 s.

Chapter 4

Experimental Model Fitting

The models presented in the previous chapter employ a number of parameters to accurately describe any system belonging to the same type as the experimental setup that was presented in the introduction. However, for the mathematical models to describe the particular physical system that is the test-rig, its intrinsic properties, i.e. inertia, restoring- and dissipative forces, and unbalance, must be determined and implemented into the models.

This chapter thus describes the identification procedure of the various model parameters, which allows for comparisons to be made between the experimental results and simulations resulting from the mathematical models.

4.1 Experimental Modal Analysis of Rotor System

As the mathematical model of the flexible rotor accommodate the flexible dynamics, it is of special interest to acquire the actual modal properties of the rotor system through experiment, in order to obtain an accurate mathematical model.

4.1.1 Experimental Setup

An experimental modal analysis (EMA) has been carried out for the rotor system in a simulated free-free condition, by hanging it in flexible springs. The EMA serves to fit the natural frequencies and the damping ratio of the experimental test with the mathematical model, as well as obtaining knowledge of the dynamics up till 1000 Hz.

It was chosen to perform the EMA using a hammer with a force transducer attached at the hammer tip, always impacting the rotor at measurement point 2, while the accelerometer was relocated throughout each measurement point for each sample (rowing output), as illustrated in Figure 4.1. For each measurement position where the accelerometer was placed, the rotor was excited by the hammer in measurement point 2 a total of 60 times.

Parameter	Force transducer	Accelerometer
Manufacture	Brüel & Kjær	Brüel & Kjær
Model	8230-001	4344
Sensitivity	22 mV/(m · s ⁻²)	0.336 pC/(m · s ⁻²)
Sample frequency	20 kHz	20 kHz
Conditioner	M33 (MMF)	2635 (<i>B&K</i>)
Signal gain	× 1	× 3.16
Filter setting	0 Hz – 5 kHz	2 Hz – 10 kHz
Tip type	Plastic	N/A

Table 4.1: Testing parameters during EMA.

Before acquiring the final fitting data, some preliminary test were made. Different types of hammer tips, i.e. rubber, plastic, and steel, were compared to investigate their frequency characteristics when exciting the rotor. Among the three tip types, plastic showed the best results, considering the FFT of the input and the coherence quality of the FRF in the frequency band of interest, that is 0–1000 Hz.

Acquiring the FRFs of the laterally positioned accelerometers along the rotor, the data showed that the system was slightly asymmetric, yielding two slight distinct peaks around each natural frequency. This is suspected to be caused by the excitation target being rotational asymmetric. To accommodate this the accelerometer was consistently positioned along the rotor in a 45 degree angle between the two principal planes of the excitation target, both perpendicular to the cross section of the shaft. With this approach only a single peak was found to occur at each natural frequency.

Exciting and acquiring data only in the 45 degree angle shows that three natural frequencies are present in the interval 0–1000 Hz. Extracting the mode shapes of the EMA shows that the first natural frequency is related to the first bending mode, that is the two-node shape, of the flexible rotor, whereas the second and third natural frequency both yield two distinct mode shapes with three nodes. This was thought to be caused by the flexibility of the disc, due to the thin acting like a disc membrane. Hence, the accelerometer was positioned at four locations on the disc to reveal the disc behaviour at the natural frequencies.

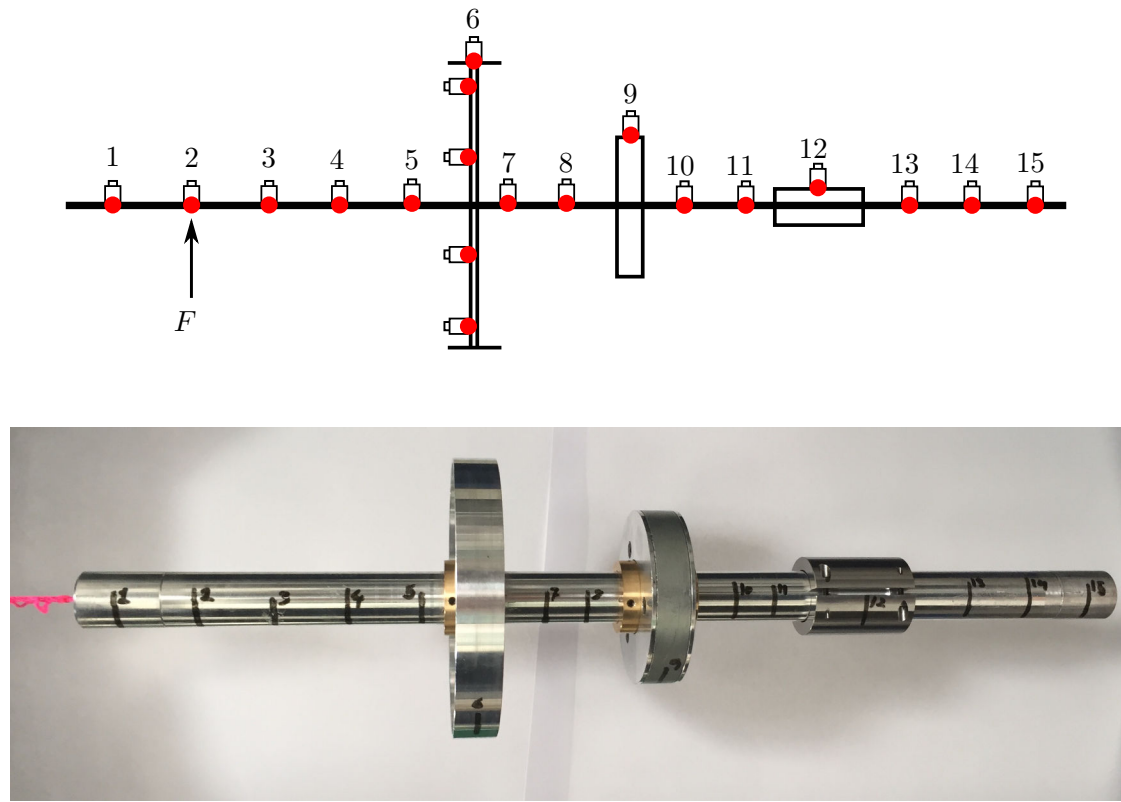


Figure 4.1: EMA rotor measurement points.

4.1.2 Experimental Results

The acceleration- and force data from the 19 sampling sessions were all processed in the following sequence: first the 60 segments were split up into uniform lengths, next an exponential window was applied to each segment, and lastly the segments were zero-padded in order to obtain a higher resolution in the resulting FRF [10], to be used for the subsequent fitting of the damping parameters. Lastly, the cross and power spectral density of the modified signals were obtained, from which the FRFs, i.e. the H1 and H2 estimators, were acquired as well as the coherence and phase shift [6].

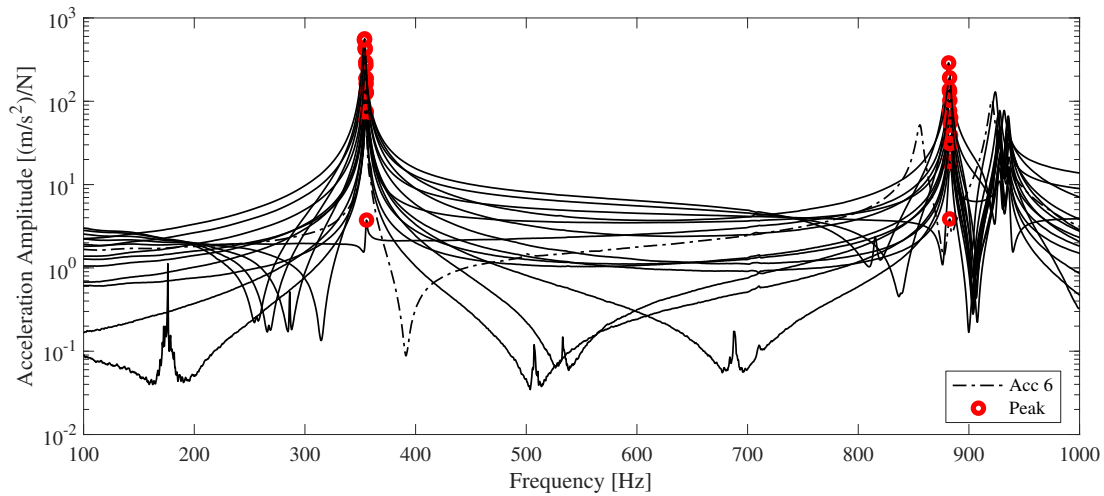


Figure 4.2: FRF H2 of lateral accelerations.

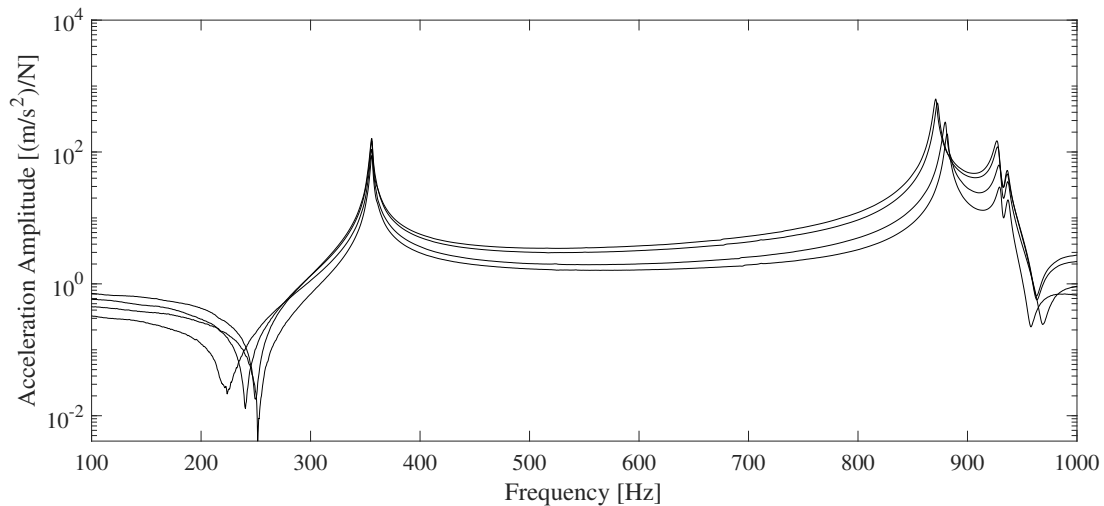


Figure 4.3: FRF H2 of axial disc accelerations.

Looking at the FRFs in Figure 4.2 the peaks for the first and second natural frequency, indicated with a red circle, are all seen to appear at approximately the same frequencies. This is also the case for the axial disc accelerations shown Figure 4.3. The overall coherence of all the FRFs used in this analysis is considered good (i.e. close to unity over the frequency range). Considering the response of the accelerometer in position 6, we see that an additional frequency appear just before the second natural frequency. Furthermore, the amplitude appearing at the second natural frequency is inconsistent with the rest of the amplitudes. The reason for this, is due to the accelerometer being mounted at the extremity of the disc, while the disc is in fact slightly flexible, rotating at

high frequencies. Thus, this FRF will be disregarded in the further analysis. In return, the flexibility of the disc is investigated obtaining the accelerations in the axial direction.

The mode shapes are now obtained using the FRFs and phase-diagrams, considering the amplitude at the resonance and the phase change.

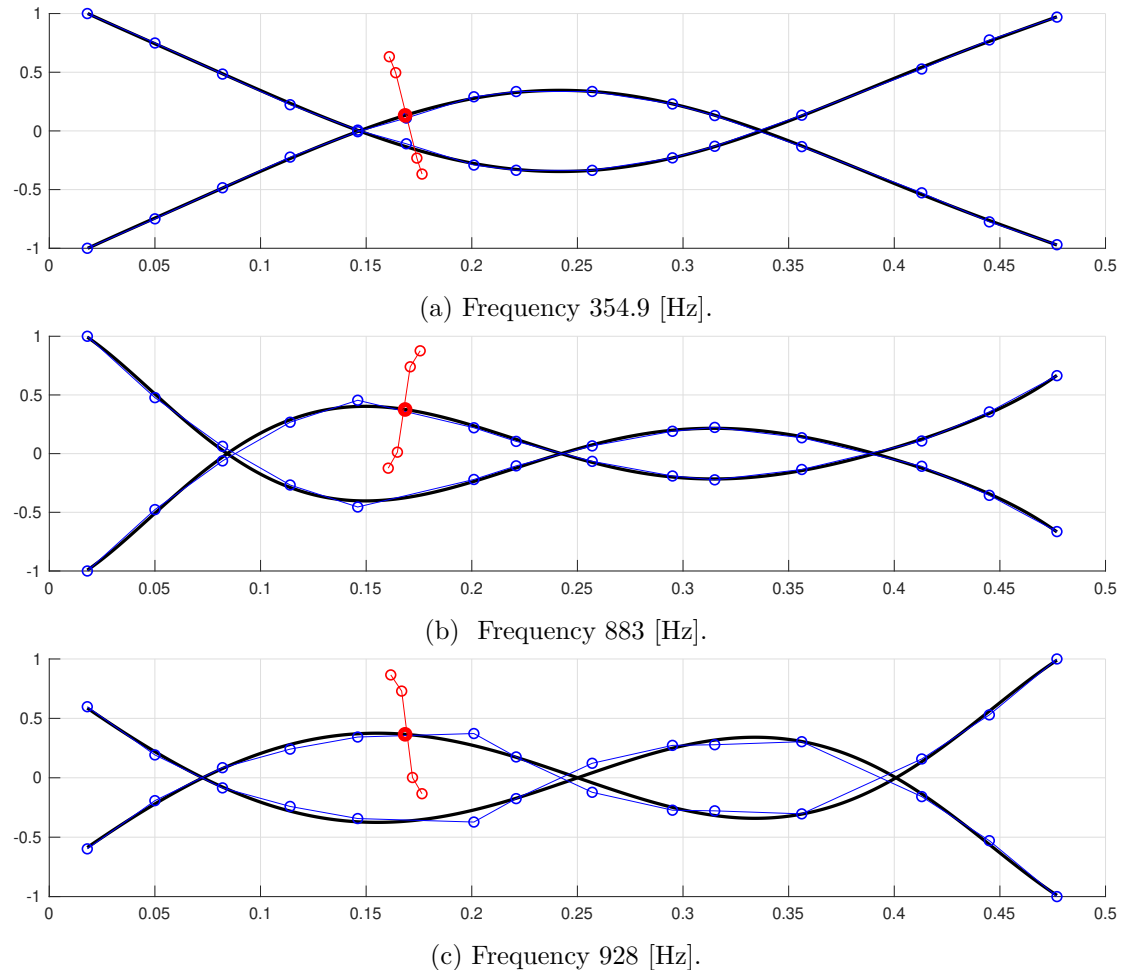


Figure 4.4: Modes shapes of the three first natural frequencies, fitted with splines.

Considering Figure 4.4, we see that the experimentally-obtained mode shapes are in accordance with what would be expected for the first- and second bending mode of a rotor system. Evaluating the disc mode shapes, we see that for the first natural frequency it acts approximately as a rigid body. Evaluating the disc mode shapes for the second and third natural frequency, we observe that the dynamics of the disc becomes more predominant, as the two disc mode shapes displays greater relative amplitudes while being in opposite phase, making the second and third mode shapes orthogonal.

4.1.3 Modal Damping Parameters

In order to acquire the proportional damping parameters, α and β , used in the mathematical model of the flexible rotor, the experimentally-obtained frequency response functions are utilized. An analytical expression of the FRF as a function of the modal mass, stiffness, and damping (m^* , k^* , d^*) is given by:

$$FRF(\omega) = \frac{-\omega^2}{(-m^*\omega^2 + id^*\omega + k^*)}, \quad (4.1)$$

from which the modal parameters can be estimated, inserting the experimentally found frequency response. The H2 is considered to be the best estimator around the resonances, thus this is used for the fitting [6].

The above equation (4.1) is split into K real and imaginary components, from which we can extract the parameters, where K is the number of fitting points chosen at each frequency response peak:

$$\begin{bmatrix} -\omega_1^2 & 1 \\ \vdots & \vdots \\ -\omega_K^2 & 1 \end{bmatrix} \begin{Bmatrix} m^* \\ k^* \end{Bmatrix} = \begin{Bmatrix} \text{Re} \left(\frac{-\omega_1^2}{FRF(\omega_1)} \right) \\ \vdots \\ \text{Re} \left(\frac{-\omega_N^2}{FRF(\omega_K)} \right) \end{Bmatrix} + \begin{Bmatrix} \varepsilon_1 \\ \vdots \\ \varepsilon_K \end{Bmatrix}, \quad (4.2)$$

$$\begin{Bmatrix} \omega_1 \\ \vdots \\ \omega_K \end{Bmatrix} \begin{Bmatrix} d^* \end{Bmatrix} = \begin{Bmatrix} \text{Im} \left(\frac{-\omega_1^2}{FRF(\omega_1)} \right) \\ \vdots \\ \text{Im} \left(\frac{-\omega_N^2}{FRF(\omega_K)} \right) \end{Bmatrix} + \begin{Bmatrix} \varepsilon_1 \\ \vdots \\ \varepsilon_K \end{Bmatrix}.$$

The parameters are estimated by the least squares method, as done in [20]. Having obtained the modal parameters, the following relations are used

$$\zeta_i = \frac{d^*}{2\sqrt{m^*k^*}}, \quad \omega_i = \sqrt{\frac{k^*}{m^*}}, \quad \zeta_i = \frac{\alpha}{2\omega_i} + \frac{\beta\omega_i}{2}. \quad (4.3)$$

Considering the mathematical model of the flexible rotor, we are only interested in being able to describe the two first mode shapes of the rotor, as all the machine elements mounted are assumed rigid. Hence, the mode shape of 355 Hz and 883 Hz are used to fit the mathematical model, while the mode at 928 Hz is neglected. Since we are only interested in fitting the two modes, we obtain two sets of damping ratios and natural frequencies, from which an exact set of α and β can be found.

For each FRF peak, three points ($K = 3$) in the vicinity of their respective peak are used to perform the fitting, from which a set of damping ratio and natural frequency are acquired. A box-plot of the parameters is shown in Figure 4.5.

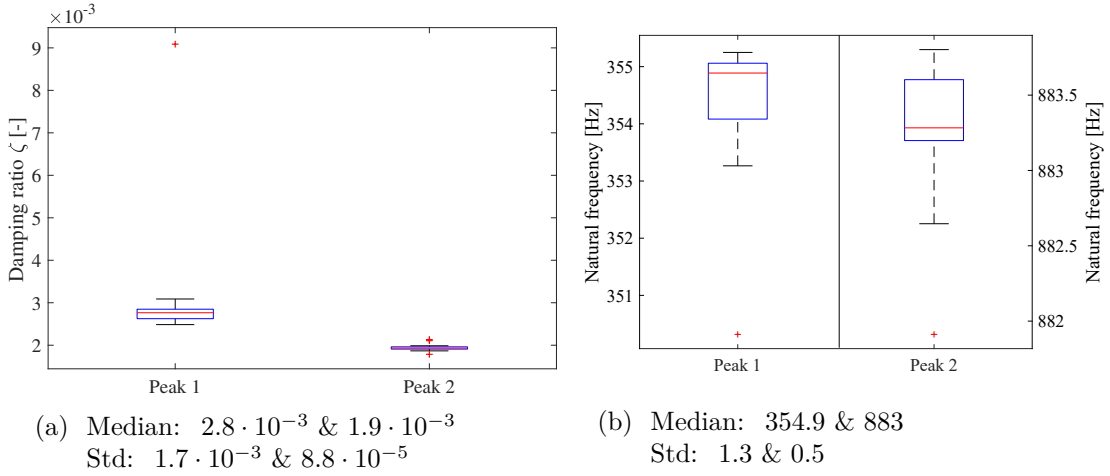


Figure 4.5: Box plot of the damping ratios and natural frequencies of FRFs, along with the median and standard deviation

Considering the box plots, only a few outliers are found. In order to represent the damping of the system most accurately, the median of the modal parameters is chosen for the model. Obtaining α and β , we equate to two equations with two unknowns, following equation (4.3). Using only α or β the first resonance peak is used for fitting. The obtained modal parameters are tabulated below:

ζ_1 [-]	ζ_2 [-]	ω_1 [Hz]	ω_2 [Hz]	α / β	α	β
$2.8 \cdot 10^{-3}$	$1.9 \cdot 10^{-3}$	354.9	883	$10.57 / 3.53 \cdot 10^{-7}$	12.32	$2.48 \cdot 10^{-6}$

Table 4.2: Modal parameters from EMA.

4.1.4 Comparison of Experimental Versus Theoretical Results

To compare the experimental and theoretical modal properties, the natural frequencies along with the percentage deviations are firstly juxtaposed in Table 4.3. From the deviations being less than one percent, we conclude that the frequencies obtained experimentally agree rather well with the theoretical frequencies generated from the model.

	Experimental	Theoretical	Deviation
ω_1	354.9 [Hz]	356.7 [Hz]	0.5 [%]
ω_2	883 [Hz]	886.8 [Hz]	0.4 [%]

Table 4.3: Experimental versus theoretical natural frequencies.

Considering the mode shapes in Figure 4.6, the theoretical mode shapes are depicted with the black vertical lines, whereas the ones found experimentally are shown by the

blue points with accompanying interpolation curves, as they were shown on their own in Figure 4.4. For the first mode shape the results are found to agree well. The only minor deviation is found in the vicinity of the unbalance disc, however this is likely to be a cause of the fact that the disc is modeled as being rigid in the mathematical model. Studying the second mode shape, the experimental data is found to be in general accordance with the prediction obtained from the mathematical model. However, upon further inspection the right half of the mode shape reveal a clear deviation in terms of the amplitude. Again the discrepancy is thought to be a consequence of the rigid disc assumption, since only one of the two *two-node* modes, i.e. the latter two mode shapes displayed in Figure 4.4, can be represented by the mathematical model.

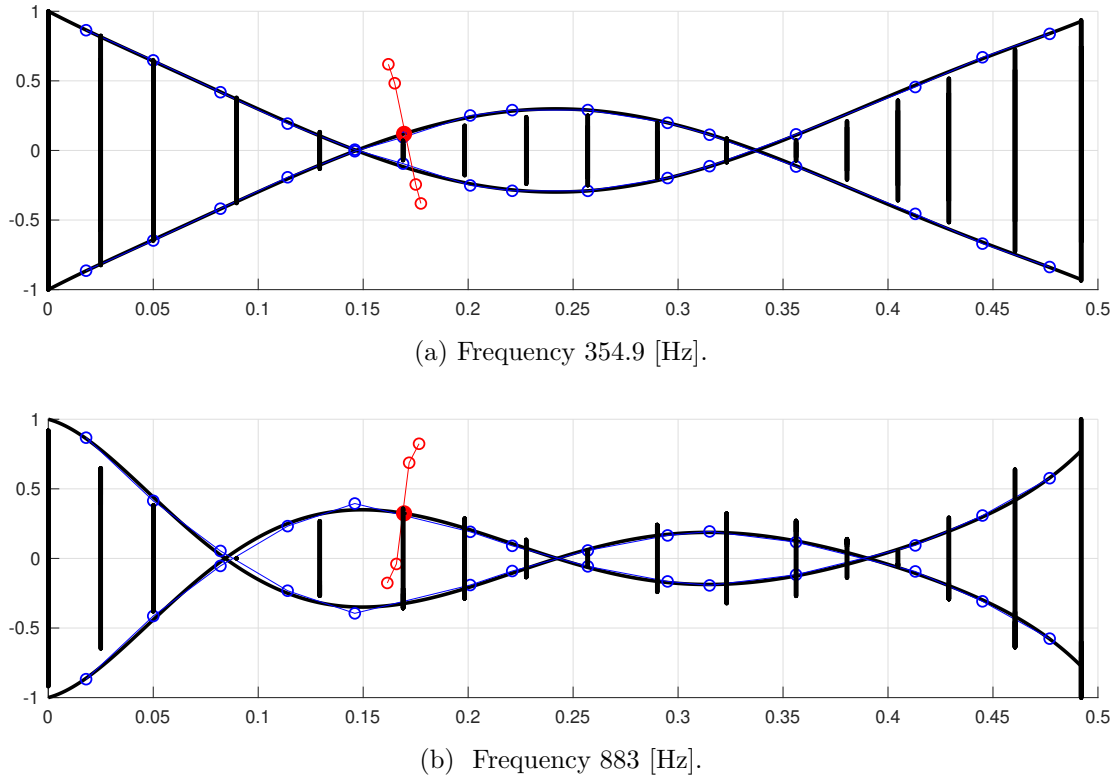


Figure 4.6: The experimental versus the theoretical mode shapes.

Having adjusted the mathematical model such that the natural frequencies and damping parameters fit, a theoretical FRF can be obtained and compared with the ones extracted from the experimental modal analysis. An example of such a comparison is illustrated in Figure 4.7, which shows the theoretical and experimental FRFs governing the location on the rotor corresponding to the aforementioned measurement-point 2, wherein both the excitation and response has been applied and recorded, respectively. With the FRFs plotted in a log-scaled y-axis, we observe from Figure 4.7 that the natural frequencies as well as amplitudes seem compatible. Even though amplitudes just around

the resonances are not an exact match, the discrepancies seem acceptable when taking into account that the mathematical model employs proportional damping, for which the damping coefficients are acquired such they match the fifteen experimentally obtained FRFs, overall. Furthermore, the theoretical FRF is plotted using both the α and β damping parameters, as well as individually. Here it must be noted that using both the damping parameters it is possible to fit both the resonance amplitudes, while using only one damping parameter just a single resonance amplitude can be fitted. Thus, using a single damping parameter (α or β) the first bending resonance is fitted.

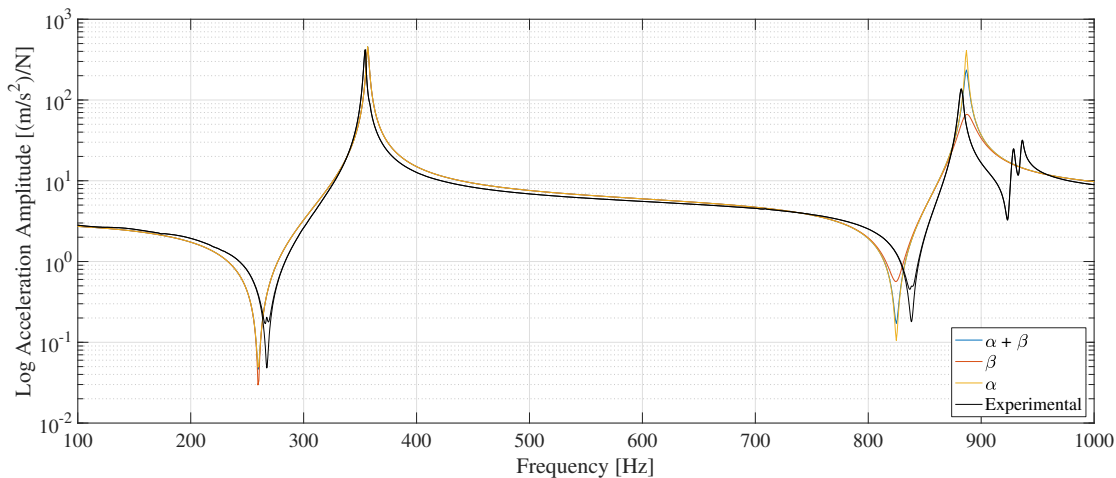


Figure 4.7: The experimental- and theoretical FRFs for measurement-point 2 superimposed.

4.2 Experimental Test of Coupling

The coupling, connecting the motor to the rotor system, is a crucial component to investigate, as the dynamic system is highly sensitive to a possible inertia, damping or stiffness of this. Thus, an experimental setup has been made, aiming to isolate the properties of the coupling.

4.2.1 Experimental Setup

As is shown in Figure 4.8 the PMB has been removed, leaving the rotor system in an overhung position around the spherical bearing and the coupling mounted at the end. The overhung end is additionally supported by a free hanging mass through a pulley system, at which a specified mass/force can be applied, yielding an angular displacement around the spherical bearing. A laser displacement sensor of type HSDR-CMOS ZX1-LD100A81 has been deployed near the overhung end, in order to track the lateral displacement of the rotor system.

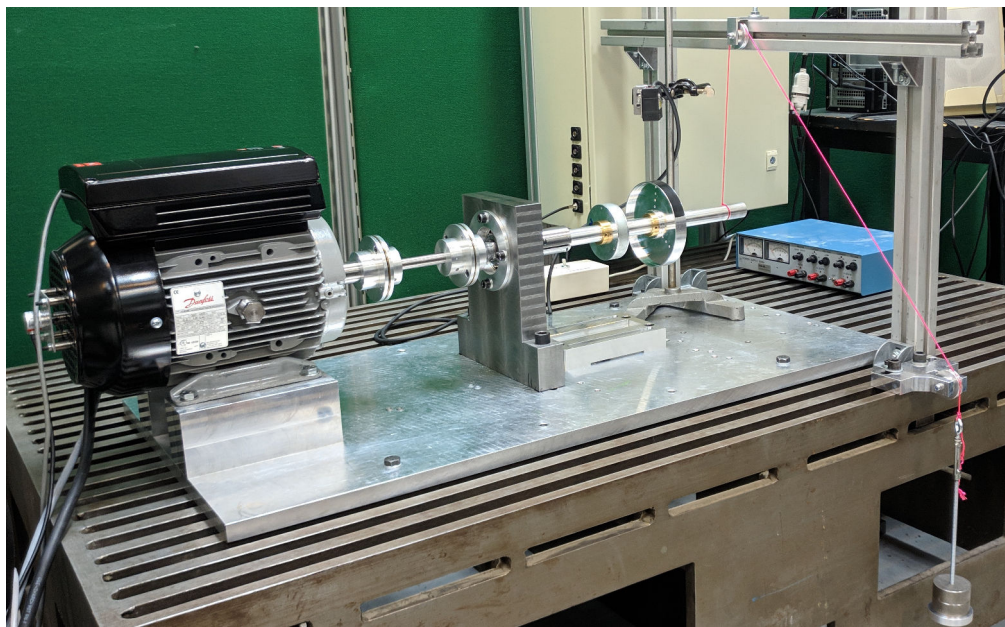
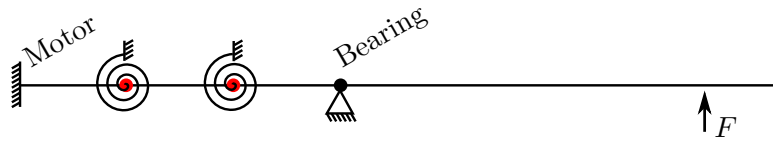


Figure 4.8: Experimental setup of coupling test.

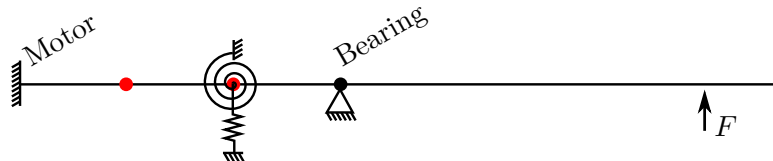
The following assumptions have been made doing the experiment:

- The rotor is rigid.
- The system can be reduced to a SDOF system in the vertical plane parallel to the rotor axis, due to rotational symmetric properties.
- The coupling, consisting of two sub coupling connections, acts as two torsional springs around the lateral axes normal to the vertical plane.
- Only small angular displacements of the rotor is applied.
- The stiffness force of the coupling varies linearly with the angular displacement of the rotor.
- The spherical bearing is frictionless.

Using this setup, a specific mass can initially be applied, using the pulley system, such that the rotor system is positioned in an approximately horizontal equilibrium position for which the stiffness of the coupling is considered linear around. Small increments of mass/force is subsequently added yielding a small angular displacement of the rotor, tracked by the laser displacement sensor. It is then possible to find the equivalent angle of rotation and moment force at the spherical bearing location. Using the known dimensions and some kinematics, it is possible to represent an equivalent system having only stiffnesses applied to one of the sub couplings, for which moment equilibrium can be used to determine the stiffness.



(a) Mechanical system of coupling test setup.



(b) Equivalent mechanical system of coupling test setup.

4.2.2 Experimental Results

Doing the experiment it was found that multiple, slightly distinct, horizontal equilibria existed for the rotor. The reason for this, is said to be caused by a small static friction in the spherical bearing. It was recognized that the system including the coupling and the bearing had a very small stiffness/restoring force. This unexpected small restoring force is thought to be caused by rebuilding the test-rig, using new coupling discs and a new unworn spherical bearing.

Hence, in doing the experiment, it is concluded that the stiffness of the coupling is of same insignificance as the spherical bearing.

4.3 Experimental Modal Analysis of the Impact House

In the previous studies conducted on the test-rig, e.g. [13], [16], [15], the dynamics of the impact house was found to have a significant influence on the contact forces. That is the duration of the contact state, relative to the natural frequencies of the inner houses, is so that the response of the inner houses appears in the time series obtained from the force transducers. Because of this, the dynamics of the impact house has been identified experimentally using EMA in the frequency range 50 – 1000 Hz.

4.3.1 Experimental Setup

The EMA for the impact house has been conducted in stages with the assembled impact house subjected to three different support conditions. All the support conditions are shown in Figure 4.10. For each of these experimental setups, the impact house has been excited in the vertical- and horizontal principal direction, respectively. In the support cases shown in Figure 4.10a and 4.10b, the EMA was performed using an electromagnetic shaker attached to the outer steel house of the assembly, while the setup shown in Figure 4.10c demanded a hammer to be used.

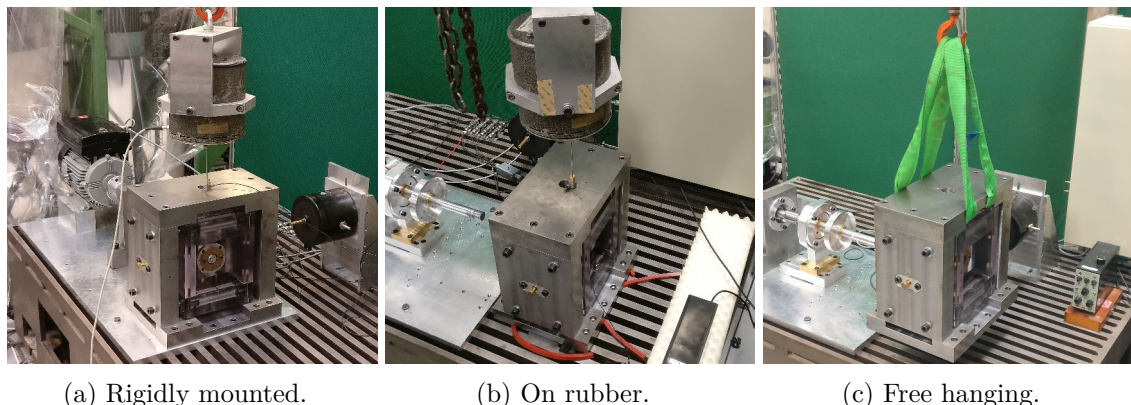


Figure 4.10: The investigated support conditions of the impact house.

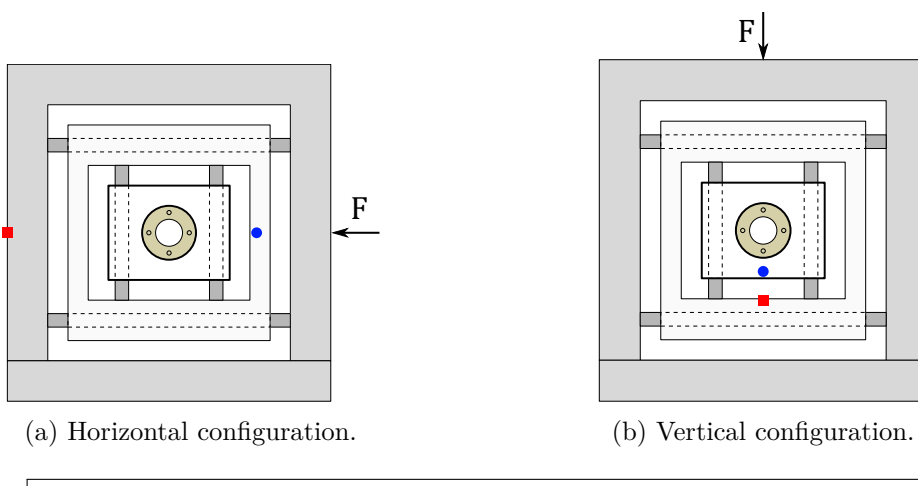


Figure 4.11: The two input-output configurations used in the EMA.

In all tests the permanently-mounted internal accelerometers, together with an external accelerometer, were used to record the response of the structure. The external accelerometer was installed consistently on the *nearest exterior component* with respect to the internal accelerometer active according to the excitation direction. As shown in Figure 4.11, the external accelerometer was mounted on the middle polycarbonate house when exciting the structure in the vertical direction, while, when exciting the structure horizontally, the accelerometer was installed on the exterior of the steel house. The purpose of obtaining the data from the external accelerometer is that it enables us to say whether the adjacent components are in phase, that is it provides a glimpse of the mode shape of the internal components in the impact house.

The tests that provided the best results were the ones using the shaker as the force input. An external hardware function generator was used to provide the input signal

to the shaker. For the results presented in the next section, an up-sweep, or up-chirp, with a sine signal was used. The function generator has a maximum ramp-up time of a 100 second, so to obtain a sufficient resolution of the steady-state response across the tested frequency range, it was necessary to split the sweeps, and hence data acquisition sessions, into two parts. Thus the EMAs were performed for the frequency range from 50 to 600 Hz and then subsequently from 500 to 1000 Hz. From the resulting data a complete representation is found from concatenating the frequency response, phase, and coherence results.

Parameter	Force transducer	Acc Int	Acc Ext
Manufacture	Brüel & Kjær	MMF	Brüel & Kjær
Model	8230-001	KS77C100	4338
Sample freq.	8 kHz	8 kHz	8 kHz
Conditioner	M33 (MMF)	M33 (MMF)	2635 (B & K)
Filter setting	0 Hz – 5 kHz	0 Hz – 5 kHz	2 Hz – 3 kHz
Sensitivity	22 mV/(m · s ⁻²)	10.081 mV/(m · s ⁻²)	10.08 pC/(m · s ⁻²)
Signal gain (low)	× 10	× 100	× 1000
Signal gain (high)	× 10	× 100	× 1000

Table 4.4: Parameters during horizontal up-sweep 50–600 Hz (low) / 500–1000 Hz (high).

Parameter	Force transducer	Acc Int	Acc Ext
Manufacture	Brüel & Kjær	MMF	Brüel & Kjær
Model	8230-001	KS77C10	4338
Sample freq.	8 kHz	8 kHz	8 kHz
Conditioner	M33 (MMF)	M33 (MMF)	2635 (B & K)
Filter setting	0 Hz – 5 kHz	0 Hz – 5 kHz	2 Hz – 3 kHz
Sensitivity	22 mV/(m · s ⁻²)	1.0390 mV/(m · s ⁻²)	10.08 pC/(m · s ⁻²)
Signal gain (low)	× 10	× 1000	× 1000
Signal gain (high)	× 1	× 1000	× 1000

Table 4.5: Parameters during vertical up-sweep 50–600 Hz (low) / 500–1000 Hz (high).

4.3.2 Results

The results obtained from the horizontal modal analysis are shown in Figure 4.12. The dotted vertical line depicts the concatenation of the two independent sweeps. For the horizontal tests the two data sets are found to be completely compatible, and thus a smooth transition is seen at the interface. The FRF part of the figure, shows that the first mode is found at 250 Hz. Comparing the amplitude of the internal- and external accelerometer, the FRF, which expresses displacements, shows that the middle house is vibrating with an order amplitude higher than the outer steel house, which would be expected at this frequency referring to the impact house model in Section 3.2. From

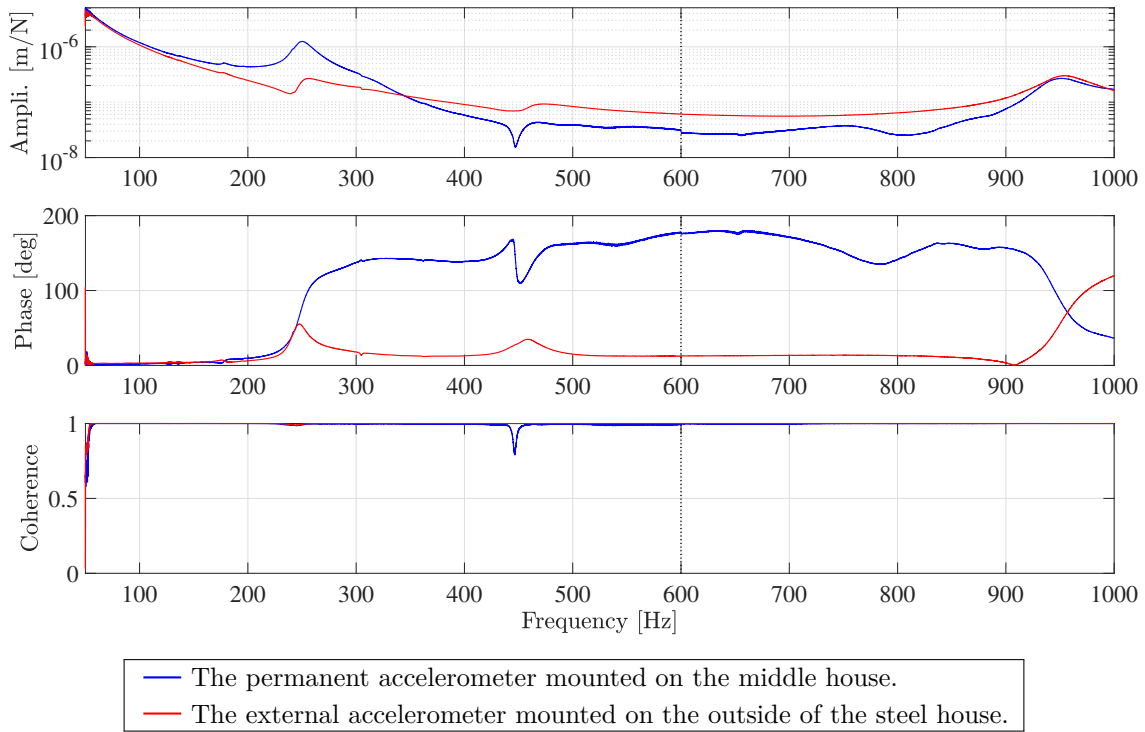


Figure 4.12: The FRF (peak at 250 Hz, 445 Hz and 945 Hz), phase, and coherence from the horizontal excitation.

the phase plot the data from both accelerometers indicates that the outer- and middle house are moving in phase before and at the resonance at 250 Hz, after which the two structures adopts opposite phases. This behavior is also in accordance with the analytical and numerical model of the houses obtained in Section 3.2, where the inner- and middle house are found to be in phase.

Another resonance is also found to appear at 445 Hz, at which a drop is found in the FRF amplitude for the accelerometer mounted on the middle house. This is in accordance with the behavior of the twisting mode shape of the middle house found in the flexible FE-model. As the accelerometer is mounted at the center of the "side plates" of the middle house, the FRF amplitude goes towards zero and a drop in coherence is found, since the mounting point is located at a node of this anti-resonance. Furthermore the quality of the data is validated by the coherence being close to unity over the whole frequency range, disregarding the anti-resonance.

Finally, a damped mode is found at 945 Hz showing a peak amplitude for both the middle- and outer house in the FRF. Considering the corresponding phase plot, a change in phase for both the middle- and outer house is found, implying that a mode for the impact house is present at this frequency. This mode could potentially be the middle- and inner house going from being in phase to being out of phase. However, considering the relatively small amplitude of the middle house mode, as well as the unknown dynamics

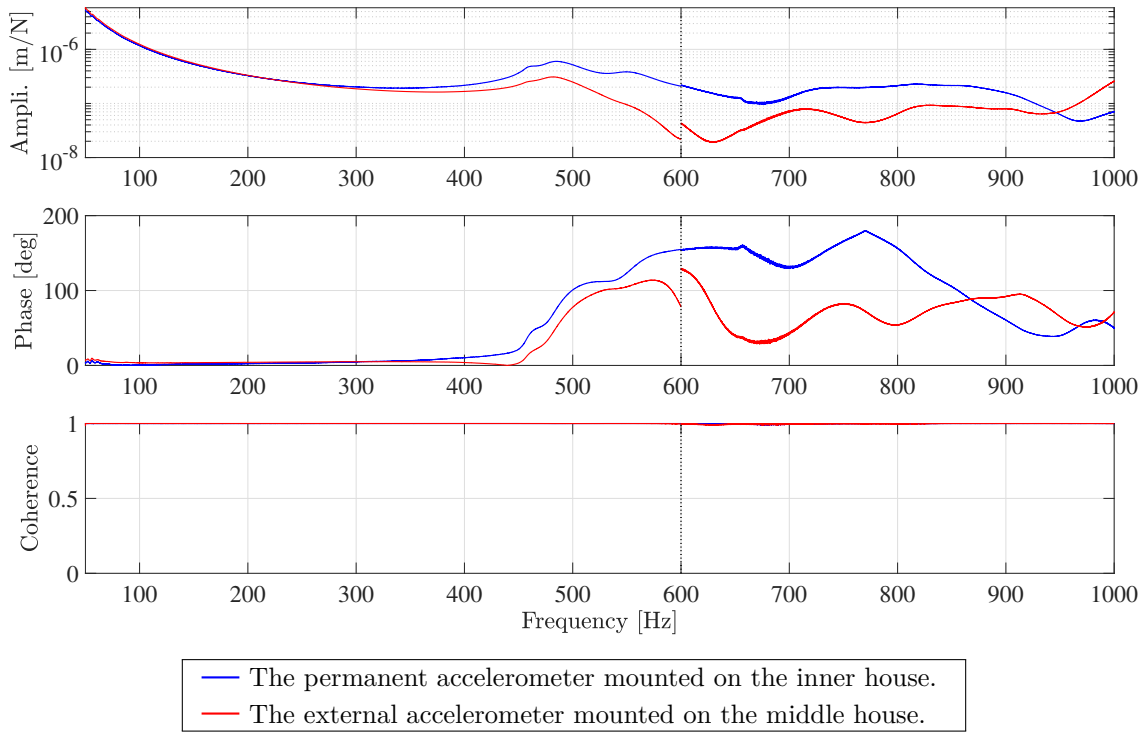


Figure 4.13: The FRF (peak at 485 Hz), phase, and coherence from the vertical excitation.

of the inner house, this mode is disregarded in the mathematical model.

Turning to the results obtained in the vertical direction, shown in Figure 4.13, the interface between the sweeps are only completely compatible for the internal accelerometer, while the external accelerometer displays a clear discontinuity in both the frequency response and the phase plot. During analysis it was found that in overlap between the sweep data set, i.e. from 500 – 600 Hz, it was possible to find a better matching interface between the graphs, so the discontinuity does not seem to be alarming even though a distinct jump is seen in the figure. Additionally, the FRF amplitudes are considered small at this frequency, for which the accelerometer accuracy can be distrustful.

Proceeding to the frequency response function, the first resonance appears to be attenuated compared with the resonance in Figure 4.13. However, a peak in amplitude is noted at approximately 485 Hz, at which a phase of 90° is also present in the phase plot. Considering the amplitudes and phases of the two accelerometers, it is seen that the inner and middle house are in phase, while the inner house amplitude is much greater than the middle house amplitude, as found in the impact house model in Section 3.2. Like in the previous case a consistently high coherence is found across the whole frequency band.

Finally, considering the FRFs obtained experimentally, it is shown that the impact

house is highly damped throughout the whole investigated frequency range, in comparison to the indicated static deflection. Thus, the presence of the impact house dynamics in the overall rotor-stator dynamic response can be considered questionable, especially at higher frequencies.

4.3.3 Comparison of Experimental versus Theoretical Results

Comparing the natural frequencies found by the analytical model and the two finite element models, found in Section 3.2, as well as the experimentally found, the natural frequencies and the percentage deviation are all tabulated in Table 4.6.

	Experimental	Analytical	FE-Rigid	FE-Flex
ω_1 / Error	250 [Hz] / (-)	249.7 [Hz] / 0.1%	248 [Hz] / 0.8%	254 [Hz] / 1.6%
ω_1 / Error	485 [Hz] / (-)	485.1 [Hz] / 0.02%	469 [Hz] / 3.3%	577 [Hz] / 19%

Table 4.6: Experimental versus theoretical natural frequencies of impact house.

Considering the natural frequencies an overall match is found between the experimental, analytical and FE-Rigid model. As discussed in Section 3.2, the flexible FE-model shows a disagreement, which is explained to be caused by the complexity of modeling the guiding bearings.

4.4 Transient response of rigid rotor

Having the rotor installed in the supportive system, being the spherical roller bearing and the PMB, it is possible to determine an equivalent stiffness of the PMB and the damping related to the first rigid mode shape, which is essential in modeling the dynamics of the system.

4.4.1 Experimental Setup

The rotor is supported by the spherical bearing and PMB, as well as having the coupling mounted at the end extremity. The rotor is given an initial displacement, from which the transient response is obtained. Having the transient response, it is possible to acquire the equivalent stiffness and damping of the PMB.

For this analysis it is assumed that, for a given initial displacement and zero velocity, only the rigid mode shape response is present, while the amplitudes of the bending modes are negligible.

It is assumed that the stiffness of the coupling and spherical bearing is negligible for small angular displacements, as found in Section 4.2. Thus the stiffness is assumed to stem from the PMB. It is also assumed that the PMB causes no significant damping, thus the damping is assumed to originate solely from the coupling and the spherical

bearing. Simplifying the system, an equivalent stiffness and damping located at the PMB is found.

Using this rigidity assumption, the system can be reduced to a decoupled 2 DOF system. Thus, for each SDOF system, the first natural frequency and the corresponding damping coefficient can be found using the following formulas:

$$\omega_d = \frac{N}{t_N - t_0} 2\pi, \quad \zeta = \frac{\frac{1}{2\pi N} \ln \left(\frac{x_0}{x_N} \right)}{\sqrt{1 + \left(\frac{1}{2\pi N} \ln \left(\frac{x_0}{x_N} \right) \right)^2}}, \quad (4.4)$$

where N is the number of periods, t is the time and x is the amplitude. The mechanical system is given as:

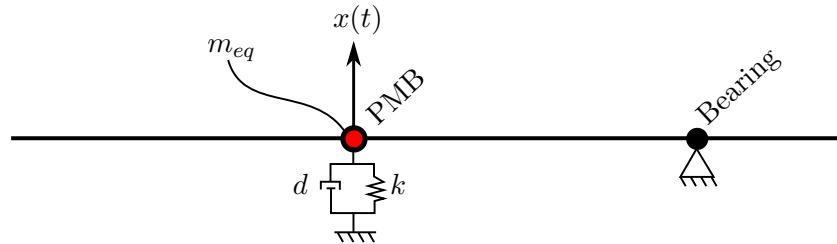


Figure 4.14: Mechanical system of simple rigid rotor.

In Figure 4.14 m_{eq} is an equivalent mass yielding an identical mass moment of inertia around the bearing, as found in Section 3.3, when positioned at the PMB. The equivalent mass m_{eq} is found by:

$$I = m_{eq} \cdot r^2, \quad \Rightarrow \quad m_{eq} = \frac{I}{r^2} = 2.403 \text{ [kg]}, \quad (4.5)$$

where r is the distance from the bearing to the PMB and I is the mass moment of inertia of the rotor around the bearing, both tabulated in Section 2.5. Having the mass, damping and stiffness all concentrated at the same position, and by the use of the small angle approximation, it is possible to obtain the standard equation of motion for the SDOF system:

$$m_{eq}\ddot{x} + d\dot{x} + kx = 0, \quad (4.6)$$

for which the following standard expressions can be used to obtain the equivalent stiffness and damping:

$$\omega_d = \omega_n \sqrt{1 - \zeta^2}, \quad \omega_n = \sqrt{\frac{k}{m_{eq}}}, \quad \zeta = \frac{d}{2\sqrt{km_{eq}}}. \quad (4.7)$$

4.4.2 Experimental Results

The transient decay response has been obtained both in the horizontal and vertical direction, given an initial deflection, as seen in Figure 4.15.

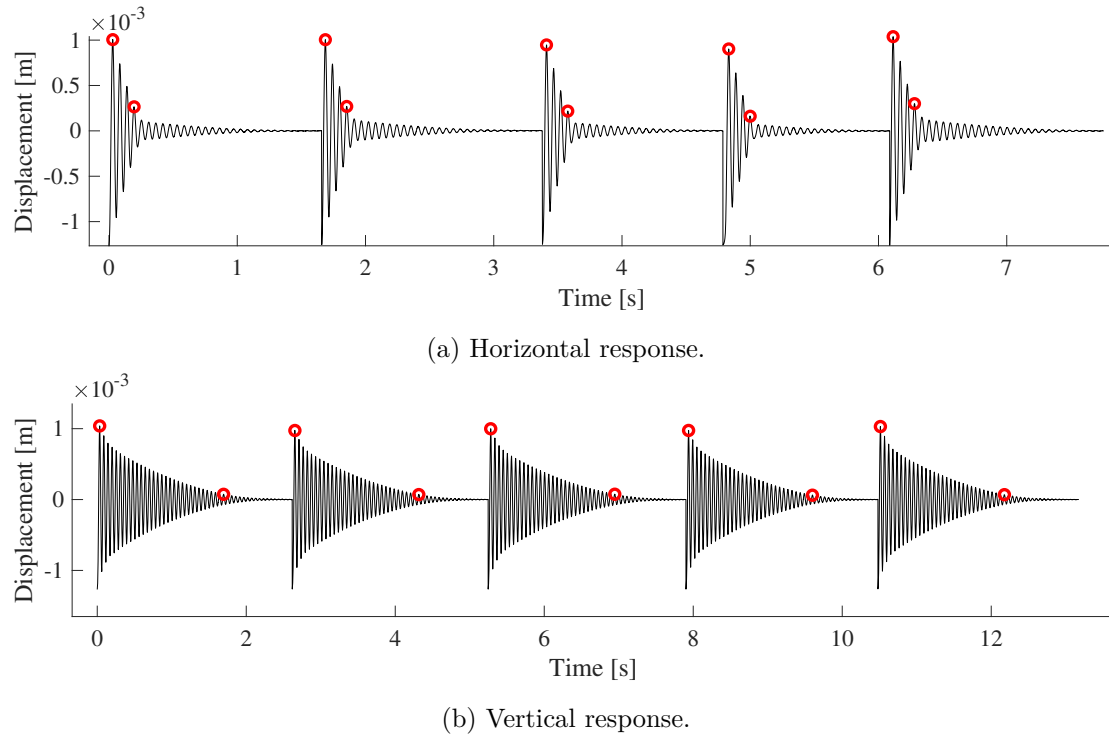


Figure 4.15: Decay response.

As can be seen in Figure 4.15, a different damping in the two directions is present. Since the damping in the horizontal direction is much greater than in the vertical direction, and it in practice is inevitable to deflect the rotor in an exact horizontal direction, a small vertical decay response component becomes present in the horizontal response as can be seen. Furthermore, a small cross coupled stiffness is found, however disregarded based on the apparent magnitude of this. Thus, only the first part of the response is considered. In the following table the modal parameters of the experimental tests are presented, as well as their corresponding mean and standard deviation:

	1	2	3	4	5	mean	std
Nat. Freq. Horizontal [Hz]	18.00	18.00	18.09	17.93	17.98	18.00	0.059
Nat. Freq. Vertical [Hz]	18.04	18.04	18.01	18.05	18.02	18.03	0.013
Damping Horizontal [-]	0.070	0.070	0.078	0.091	0.066	0.075	0.01
Damping Vertical [-]	0.014	0.014	0.014	0.015	0.014	0.014	0.004

Table 4.7: Experimental damped natural frequencies ω_d and damping ratios ζ .

Considering the found modal parameters in Table 4.7, we see that the natural frequencies in the two directions are found to be nearly identical. Hence, a damped natural frequency of 18 Hz is used and assumed valid for both directions.

Considering the damping ratios, a great difference in the two directions are seen. A possible explanation for this could be that the spherical bearing exhibits different damping characteristics in the two directions, as it is only laterally pre-loaded in the vertical direction by the weight of the rotor.

Using the experimentally found modal parameters, the stiffness k and damping coefficient d can be obtained using the expressions in Equation (4.7).

	k [N/m]	d [Ns/m]
Horizontal direction	$3.097 \cdot 10^4$	40.9
Vertical direction	$3.080 \cdot 10^4$	7.7

Table 4.8: Stiffness- and damping coefficient found experimentally.

As the damping ratios in the two directions are different, slightly different stiffness coefficients are found, as seen in Table 4.8. For simplicity the mean of the two stiffnesses are used as the discrepancy is considered negligible, hence equating to an isotropic stiffness of $k = 3.09 \cdot 10^4$ N/m.

4.4.3 Comparison of Experimental Versus Theoretical Results

The transient decay responses in the two directions are plotted in Figure 4.16 and 4.17 together with the response obtained by the rigid and flexible rotor mathematical model. The flexible model is plotted using 8 and 16 mode shapes, respectively, representing a rigid model, and a model containing the rigid mode shapes as well as the two first bending modes.

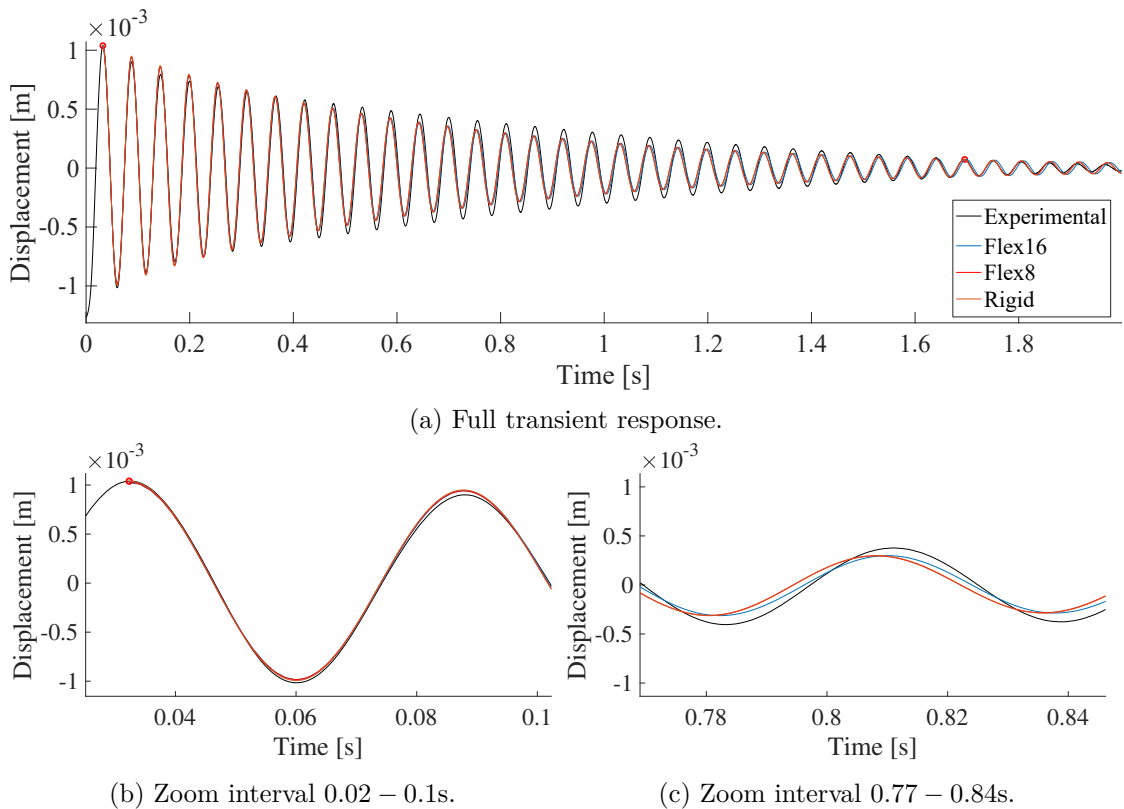


Figure 4.16: Vertical decay response.

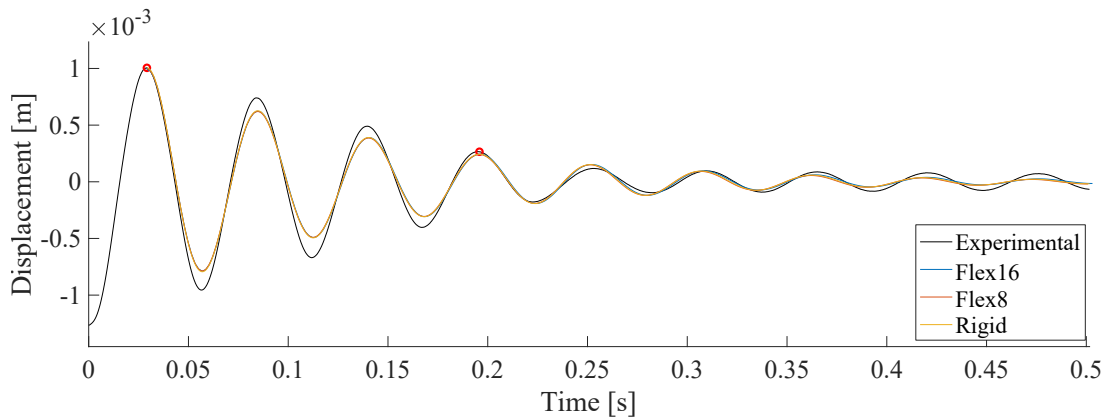


Figure 4.17: Horizontal decay response.

In Figure 4.16 we see that small discrepancies are found comparing the experimental and theoretical response. Considering the decay trend of the experimental response, it is evident that a sole exponential decay is not present, as opposed to what is assumed when fitting the mathematical model. The same is true for the horizontal response in

Figure 4.17. However, the response of the mathematical models are considered sufficient in describing the experimental response.

The discrepancy between the mathematical models are all found to be minimal, which verifies the implementation and simulation procedure. As would have been expected, the response of the rigid model and the flexible model using 8 mode shapes (rigid) is almost identical, and can not be distinguished in the above figures. Considering the natural frequency a good match between the mathematical and experimental model is found.

The natural frequencies of the experimental response and the two mathematical models are tabulated in Table 4.9:

	Experimental	Flexible	Rigid
Natural frequency	18.00 [Hz]	17.998 [Hz]	18.03 [Hz]
Error	-	0.01 [%]	0.16 [%]

Table 4.9: Experimental versus theoretical natural frequencies.

4.5 Experimental unbalance response

For the rotor system spinning at a rotational speed different from zero, precession of the rotor system appears, by which the precession trajectory shows an orbital response at steady state. This response is caused by an imbalance in the rotor, as it is impossible to craft a perfectly rotational symmetric rotor, causing an equivalent unbalance force.

The unbalance parameters, being the unbalance magnitude and phase, is in this project considered important to acquire, in order to accurately simulate the dynamics of the physical system, by the use of the mathematical model. Identifying the unbalance parameters makes it possible to determine the effect of the unbalance in the total system response, and gives the possibility of exciting the system at a specific unbalance position.

The unbalance response of the supported rotor system is obtained through experiments, varying the rotational speed. Using the acquired response data it is possible to extract the unbalance parameters by fitting a mathematical model containing the wanted parameters.

4.5.1 Experimental Setup

The mathematical model is obtained by the use of the rigid rotor equations of motion given in Equation (3.22), (3.23) and (3.24). These equations are linearized by the assumption of Γ and β being small angles and their products, as well as for their derivatives, being negligible. In doing so, the equations of motion can subsequently be put in

to a linear system of equations on matrix form:

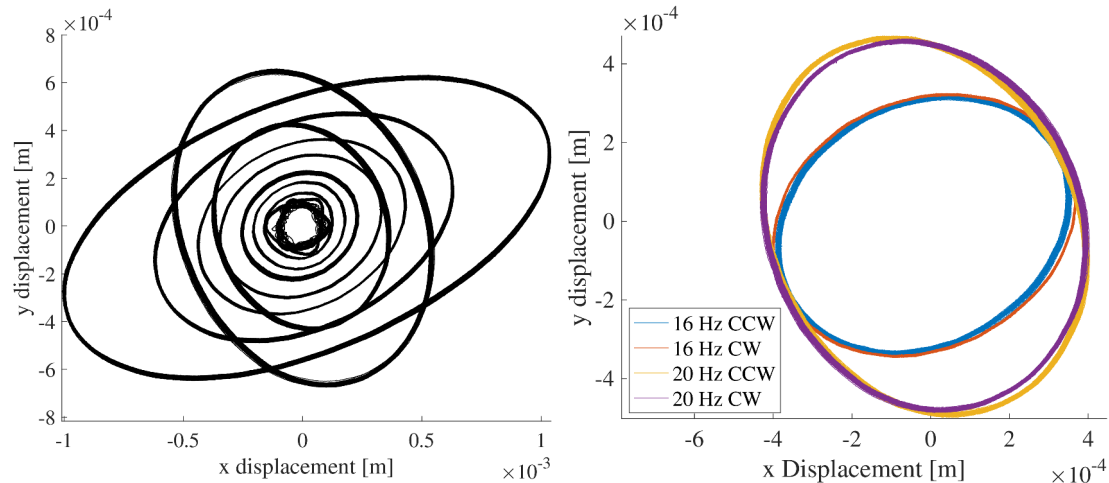
$$\begin{bmatrix} I_T & 0 \\ 0 & I_T \end{bmatrix} \begin{Bmatrix} \ddot{\Gamma}(t) \\ \ddot{\beta}(t) \end{Bmatrix} + \begin{bmatrix} l_{OM}^2 d_y & I_P \Omega \\ -I_P \Omega & l_{OM}^2 d_x \end{bmatrix} \begin{Bmatrix} \dot{\Gamma}(t) \\ \dot{\beta}(t) \end{Bmatrix} + \begin{bmatrix} l_{OM}^2 k & -l_{OM}^2 k_{yx} \\ -l_{OM}^2 k_{xy} & l_{OM}^2 k \end{bmatrix} \begin{Bmatrix} \Gamma(t) \\ \beta(t) \end{Bmatrix} \dots \\ \dots = \begin{bmatrix} -l_{ODM_0} \varepsilon \Omega^2 \sin(\Omega t + \varphi) \\ l_{ODM_0} \varepsilon \Omega^2 \cos(\Omega t + \varphi) \end{bmatrix} = \underbrace{\begin{bmatrix} -l_{ODM_0} \varepsilon_x \Omega^2 \\ -l_{ODM_0} \varepsilon_y \Omega^2 \end{bmatrix}}_{F_1} \sin(\Omega t) + \underbrace{\begin{bmatrix} -l_{ODM_0} \varepsilon_y \Omega^2 \\ l_{ODM_0} \varepsilon_x \Omega^2 \end{bmatrix}}_{F_2} \cos(\Omega t), \quad (4.8)$$

where $\varepsilon_x = \varepsilon \cos \varphi$, $\varepsilon_y = \varepsilon \sin \varphi$, Ω is the rotational speed, and I_T and I_P are the transverse- and polar mass moment of inertia, respectively. The introduction of the cross stiffnesses k_{xy} and k_{yx} is explained later in this section. Note that the reaction force in the axial direction (constituting one of the equations of motion) has been disregarded for this analysis. The steady state response is found by a superposition of the two particular solutions (\mathbf{p}_1 and \mathbf{p}_2) considering first the external unbalance force F_1 , and then F_2 . The solution form is given by:

$$\mathbf{p}_1 = \mathbf{A} \sin(\Omega t) + \mathbf{B} \cos(\Omega t) \quad \text{and} \quad \mathbf{p}_2 = \mathbf{C} \sin(\Omega t) + \mathbf{D} \cos(\Omega t). \quad (4.9)$$

The steady state solution $\mathbf{p} = \mathbf{p}_1 + \mathbf{p}_2$ is then evaluated using the up till now found system parameters, having only the desired fitting parameters as variables.

Preliminary unbalance response tests on the test-rig shows that the orbital trajectory is almost identical when changing the rotational speed direction, whereas the mathematical model response flips the orbit around the y-axis when no cross stiffness is used. The experimentally obtained response running at 16 Hz and 20 Hz, both in a clockwise and counterclockwise direction, is shown below in Figure 4.18b. It must be mentioned that the same coordinate system as used for the modeling of the rigid rotor in Section 3.3 is used, where x and y depicts the horizontal and vertical direction, respectively. The unbalance response of the CCW rotational speeds, driven in the range 2 – 20 Hz, is also presented below in Figure 4.18a, where a 90 degree angle shift is seen when crossing the first critical speed at around 18 Hz as was found in Section 3.4.



(a) Unbalance response for rotational speeds 2, 4, 6, 8, 10, 12, 15, 16, 16.5, 17, 17.4, 19.5, 20 Hz. CW and CCW.

Figure 4.18: Experimentally obtained unbalance response.

As already mentioned, the rotational direction in the mathematical model flips the orbital response around the y-axis, unless a cross stiffness is introduced. The effect of a cross stiffness is shown in Figure 4.19 for a system with symmetric stiffness $k = 3.09 \cdot 10^4$ N/m and asymmetrical damping $d_y = 7.7$ Ns/m, $d_x = 40.9$ Ns/m, being the system parameters found in Section 4.4. As can be seen, a cross stiffness of significant magnitude can ensure that the orbit stays more or less unaffected when changing the rotational direction. Hence, the cross stiffnesses are introduced and fitted, in order to replicate the experimentally obtained response.

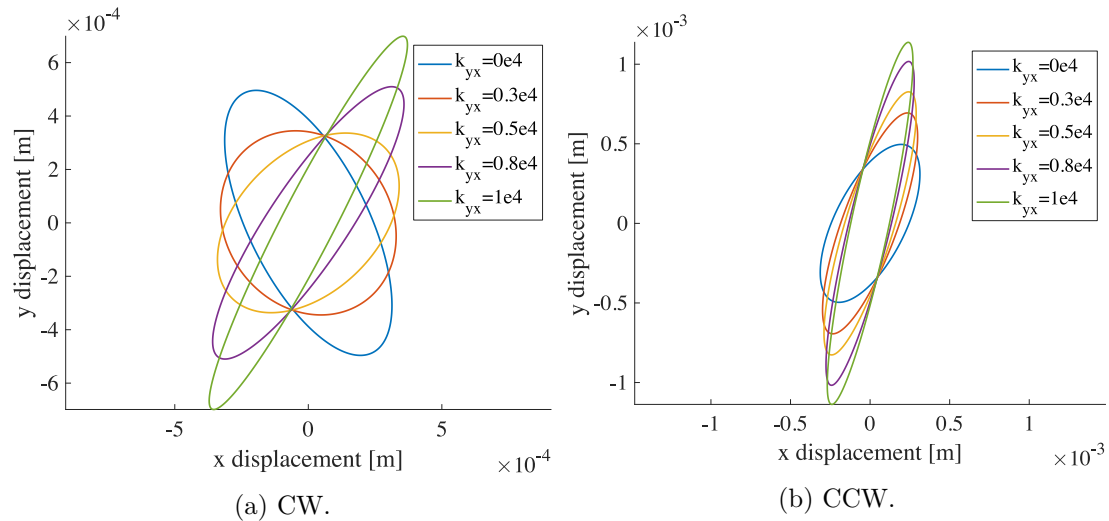


Figure 4.19: Theoretically obtained unbalance response.

4.5.2 Experimental Results

Fitting the mathematical model, the nonlinear least squares method is used. The mathematically obtained unbalance response is initially evaluated with the previously found system parameters, having only the desired fitting values as variables. This response function is put into MATLAB, where the algorithm `lsqnonlin` is utilized with the following objective function stated in Equation (4.12). Preliminary runs of the optimization problem reveals that including the damping coefficient d_x as a fitting variable significantly decreases the error. Thus, the optimization algorithm is run including this damping coefficient.

$$x_i = \{x_1 \ x_2 \ \dots \ x_N\}^T = \{\varepsilon_x \ \varepsilon_y \ k_{xy} \ k_{yx} \ d_x\}^T \quad \forall x_i \in \mathbb{R} \quad (4.10)$$

$$\theta_j = \{\theta_1 \ \theta_2 \ \dots \ \theta_n\}^T \quad \forall \theta_j \in [0, 2\pi[\quad (4.11)$$

$$Z = \min_x ||f(\theta_j, x_i)|| \quad (4.12)$$

s.t.

$$\mathbf{f}(\theta_j, x_i) = \left\{ \begin{array}{l} x_{exp}(\theta_1) \\ y_{exp}(\theta_1) \\ x_{exp}(\theta_2) \\ y_{exp}(\theta_2) \\ \vdots \\ x_{exp}(\theta_n) \\ y_{exp}(\theta_n) \end{array} \right\} - \left\{ \begin{array}{l} x_{theo}(\theta_1, x_i) \\ y_{theo}(\theta_1, x_i) \\ x_{theo}(\theta_2, x_i) \\ y_{theo}(\theta_2, x_i) \\ \vdots \\ x_{theo}(\theta_n, x_i) \\ y_{theo}(\theta_n, x_i) \end{array} \right\} \quad (4.13)$$

A range of different initial guesses have been tried, which showed that several local minima exists, at which the optimization algorithm converges at. Thus, the algorithm is considered sensitive to the initial guess. The optimization algorithm is run with the initial guess $x_j = \{0.1 \ 0.3 \ 1e4 \ 0 \ 40\}$, already mimicking the desired response trajectory as seen in Figure 4.20, which is found to generate the most optimal solution presented in Figure 4.21, fitting only the three rotational speeds 17 Hz, 17.4 Hz and 20 Hz.

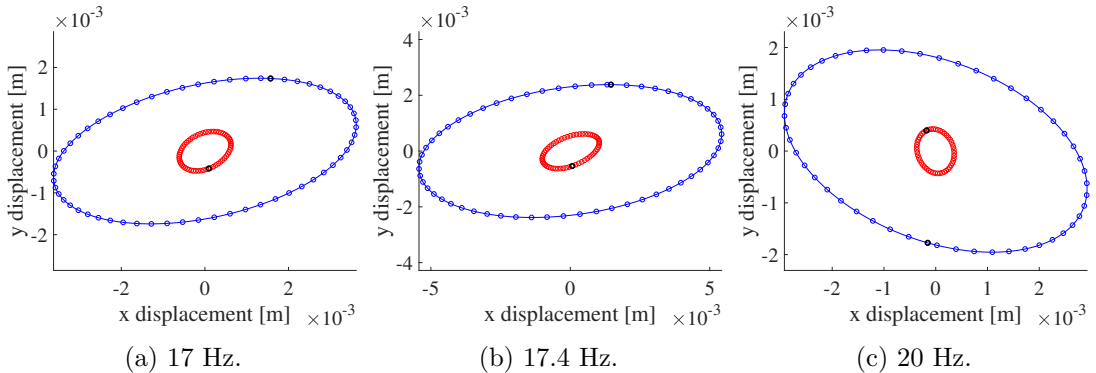


Figure 4.20: Unfitted unbalance responses: — Theoretical — Experimental

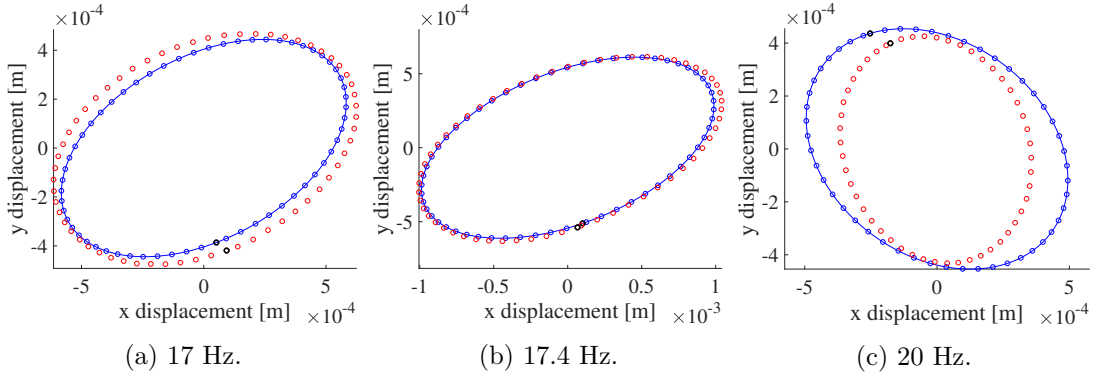


Figure 4.21: Fitted unbalance response: — Theoretical — Experimental

The fitted solution shown in Figure 4.21 generates the least squares of the objective function given in Equation (4.12), yielding the following set of variables, where the unbalance mass is set to $m_0 = 0.001$ kg:

$$\boldsymbol{x}_i = \begin{Bmatrix} \varepsilon_x \\ \varepsilon_y \\ k_{xy} \\ k_{yx} \\ d_x \end{Bmatrix} = \begin{Bmatrix} 0.027 \text{ [m]} \\ -0.072 \text{ [m]} \\ -2.456 \cdot 10^3 \text{ [N/m]} \\ 292 \text{ [N/m]} \\ 8.48 \text{ [Ns/m]} \end{Bmatrix}, \quad (4.14)$$

$$\varepsilon = \sqrt{\varepsilon_x^2 + \varepsilon_y^2} = 0.0767 \text{ [m]}, \quad \varphi = \tan \left(\frac{\varepsilon_y}{\varepsilon_x} \right)^{-1} = -1.209 \text{ [rad]}. \quad (4.15)$$

Considering the fitted variables we have that the unbalance mass m_0 is located at a radial distance ε away from the rotor center axis at an angle φ wrt. to the experimentally used angular zero-point. Cross coupled stiffnesses of significant magnitude are found, as would have been expected in order to mimic the experimentally found orbital trajectories. The cross coupled stiffnesses may physically be explained to stem from the imperfect setting of PMB. This imperfection is caused by not having the rotor equilibrium exactly located at the PMB center due to the gravitational force, as well as not having it perfectly aligned with the PMB in the axial direction due to the axial slip of the spherical roller bearing. It must be mentioned that the cross coupling stiffness is only well fitting the model when operating around the fitted value, i.e. the first critical speed. Thus, the cross coupling stiffness is only used when the rotational speed operates in the vicinity of the first critical speed, while it is disregarded when operated away from it, e.g. at zero rotational speed.

Considering the fitted damping coefficient d_x we see that it yields a similar magnitude to the vertical damping coefficient $d_y = 7.7$ Ns/m, which implies that the system is actually symmetrically damped when rotating at these rotational speeds, opposed to what was found for the non-rotating system in Section 4.4. The reason why an asymmetric damping of the non-rotating system was found in the transient decay response

test, was explained by the high friction in the spherical bearing when rotating around the vertical axis, as no pre-load was given in the horizontal direction opposed to the one of the vertical direction. However, when the rotor system operates over a certain rotational speed this pre-load imbalance in the spherical bearing reduces, hence smoothing out the potential friction. Having a rotor system supported by a symmetrical stiffness and damping produces a perfectly circular orbital trajectory, for which the cross stiffness generates the elliptical orbit with a major axis pointing in the same direction when changing the rotational direction.

A 3D plot of the experimentally-obtained unbalance trajectories at the different rotational speeds, along with 2D comparisons of the normalized theoretically- and experimentally-obtained trajectories near the first critical speed, is shown in Figure 4.22. The reason why no unbalance responses were obtained closer the the first critical speed, is that the rotor impacts the stator in the speed range 17.5–19.4 Hz.

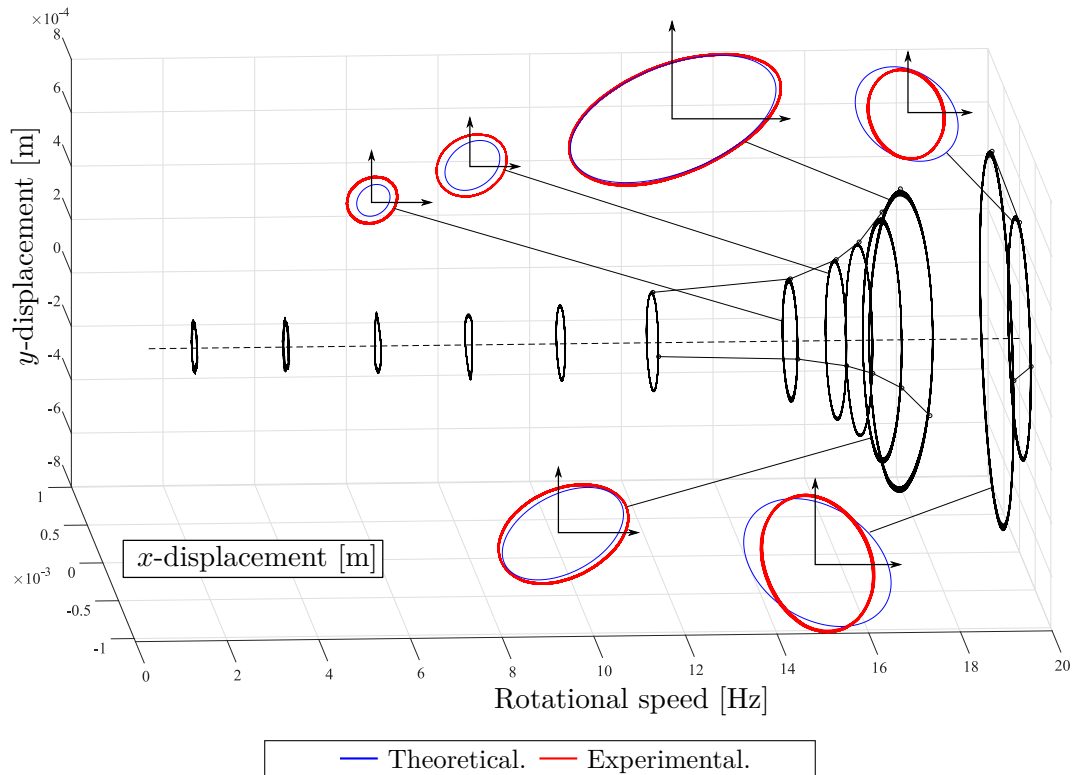


Figure 4.22: Unbalance response for rotational speeds 2–20 Hz.

Chapter 5

Results

In the following chapter the results of two impact cases are presented, for which the mathematical model established up till now has been employed.

5.1 Non-Rotating Impact Test Results

The first test is conducted having the rotor in a non-rotating condition, i.e. $\Omega = 0$, while the electromagnet applies a short-duration attraction magnetic force on the rotor steel target, causing the rotor to impact the stator. The scope of the experiment is to investigate the contact dynamics at rotor stator impact, by comparison of the full mathematical model. An advantage of keeping the rotor in a non-rotating condition is that it simplifies the dynamics while focusing on the impact dynamics related to the contact.

5.1.1 Experimental Setup

The rotor at rest is subjected to an electromagnetic force, in the horizontal direction, by the electromagnet supplied with at 48 voltage in a time-duration of 50 ms. A force transducer is mounted together with the electromagnet such that the equivalent reaction force is captured in order to recreate the test in a mathematical model simulation. The rotor displacement is captured by the proximity sensor at the unbalance disc, while the impact house dynamics are captured by the internal horizontal accelerometer mounted on the inside of the middle house, and the two force transducers (east and west) mounted on the outside of the middle house. Doing the experiment, it was found that the response of the rotor before and at impact was approximately confined to the horizontal plane, thus the vertical dynamics have been disregarded in this analysis. A total number of 6 impacts have been conducted, which showed a high repeatability. Hence, the data of only one impact is presented. In regards to the mathematical impact model, the model of Lankarani and Nikravesh is used with a coefficient of restitution $e = 0.5$.

The acceleration data have been filtered in MATLAB using a Butterworth low- and high-pass filter (`butter`) at 1200 Hz and 80 Hz, while the force data have been conditioned with the low-pass filter only. The obtained data is plotted in Figure 5.1.

5.1.2 Experimental Results

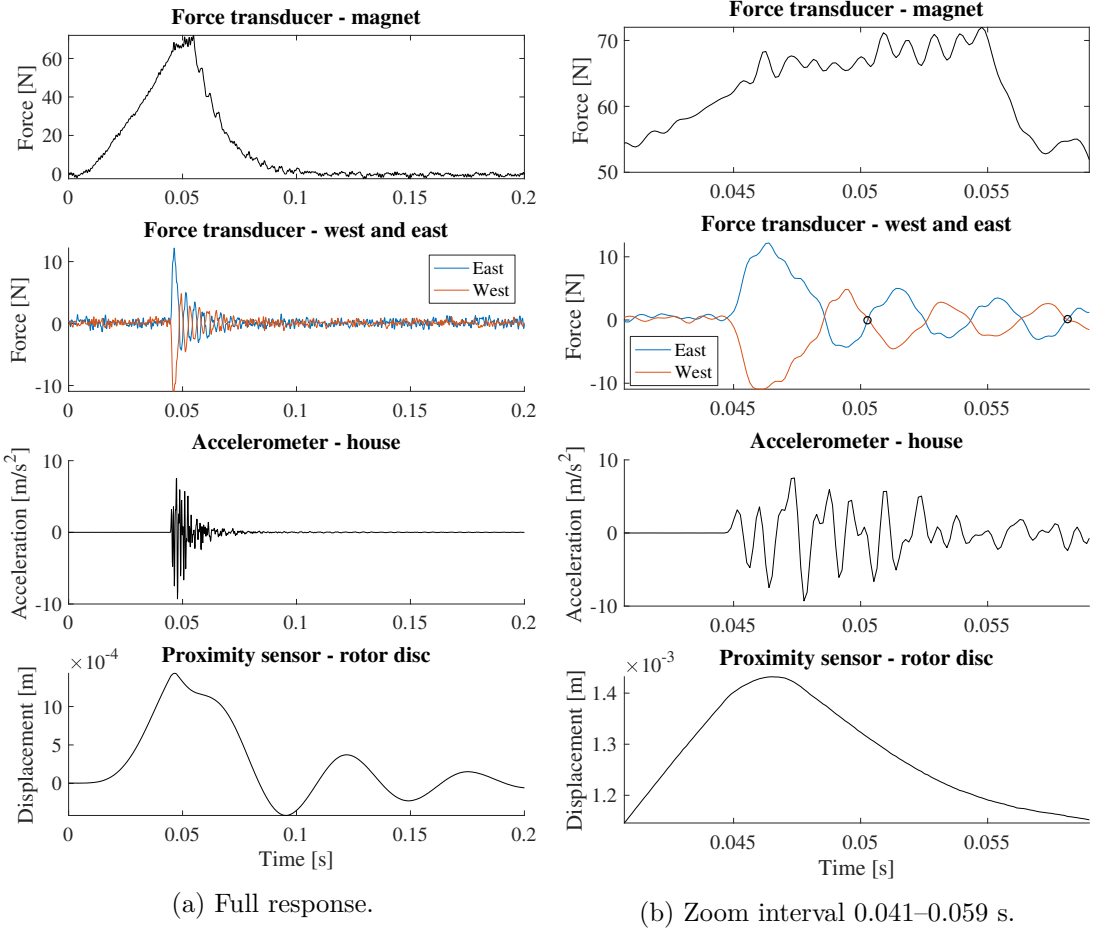


Figure 5.1: Time series of impact data.

Considering the data in Figure 5.1 we see that the east/west force transducer and the house accelerometer both reacts at a specific time when the rotor displacement gets sufficiently high. This instantaneous reaction is caused by the impact, from which the initial impact point is considered certain and defined.

The magnetic force is found to be present during the whole impact phase, as it gradually increases as the rotor approaches the stator, and the distance between the steel target and the electromagnet decreases. Even after the applied electromagnet time-duration, a magnetic force is still acting on the steel target due to the residual magnetization. Also, it must be mentioned that there is a certain latency time between the signal given to the electromagnet and the detectable magnetization, as discussed in Section 2.1.3.

As can be seen in the east/west force transducer zoom plot, a large amplitude force

of half a period is initially emerging caused by the impact, for which this time interval will be referred to as the impact phase. During this time interval, the corresponding accelerations of the impact house shows periodic responses within the frequency interval of 600 – 1000 Hz. A subsequent periodic oscillation is also found for the east/west force transducer, with a period frequency (found between the two black circular marks) of 254 Hz, matching the first natural frequency of the impact house found in Section 3.2.

Using the data, a series of equivalent derivations can be made, in order to obtain a better insight of the data. A sign dependent average of the east- and west force transducer F_{meas} can be derived by the following expression:

$$F_{meas} = \frac{1}{2}(F_{east} - F_{west}). \quad (5.1)$$

The inertia forces of the impact house can be derived by the use of the mass and accelerations of the middle house a_h , assuming that the relative displacements within this impact house is zero, from which the an estimate of the contact force F_c can be estimated by:

$$F_c = (m_{ih} + m_{mh}) a_h + F_{meas}. \quad (5.2)$$

Furthermore, the accelerations of the impact house can be integrated acquiring the velocity and the displacement. An estimate of the the impact indentation can be obtained by the difference of the house displacement and an extrapolation of the rotor displacement to the stator contact point. It must be mentioned that this is only valid under the assumption of the rotor being rigid.

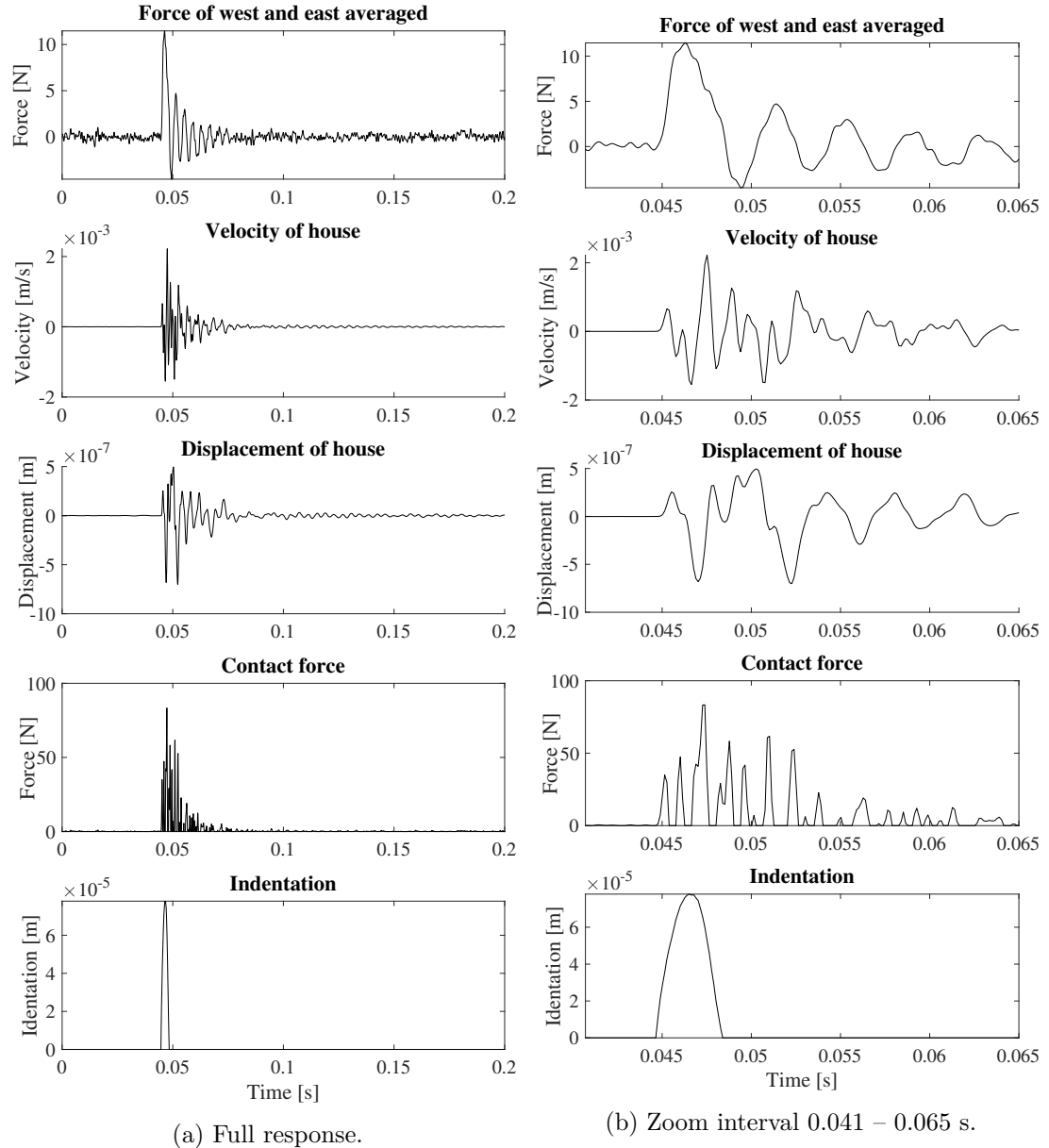


Figure 5.2: Time series of derived impact data.

Considering the derived data in Figure 5.2 we see that the displacements (derived by double integration of the acceleration) are inconsistent with the averaged force transducer data during the impact phase, and afterwards both in accordance with the transient oscillation of the impact house at around 250 Hz.

It is assumed that the force transducer data is defined as a restoring force proportional to the displacement of the house, thus comparable with the displacement of the house. The displacement of the house is obtained at the mounting location of the accelerometer,

which is not centered on the middle house. This means that the data contains certain discrepancies as the flexibility of the middle house plates is considered significant. Furthermore, by doing the double integration of the acceleration, the measurement errors will accumulate, thus not being very accurate for distance measurements. However, periodic dynamics are found in the acceleration, velocity and displacement data during the averaged force measurement impact phase.

As found in the acceleration data, frequencies around 600–1000 Hz are present during the impact phase, which potentially emerges from either the impact house dynamics or the flexibility of the rotor. The impact house horizontal dynamics were investigated in Section 3.2 showing that the first natural frequency is 250 Hz, while the higher natural frequencies are all above 1000 Hz. Considering the flexibility of the rotor, the natural frequencies of the rotor were investigated in Section 3.4, where the two first bending modes were found to be 518 Hz and 987 Hz. Hence, the flexibility of the rotor might introduce higher frequency dynamics to appear during contact in the time response, as well as potentially causing several impacts.

Considering the derived indentation estimate, we find that almost no dynamics are present. This is due to the measurement being captured at the unbalance disc from which the displacement at the stator is estimated by a linear extrapolation. Therefore, the flexibility of the rotor makes the indentation estimate invalid, as it is based on the assumption of the rotor being rigid.

The estimate of the contact force is based on the assumption of the impact house yielding no relative displacements between the inner house contact point and the middle house force transducer point, hence comprising the difference in the inertia force of the impact house and the force transducer reading. However, this assumption is violated for internal flexibility of the impact house, yielding a certain residual error related to the flexibility. This error diminishes as the displacement amplitudes decreases, as can be seen in the contact force estimate plot.

5.1.3 Comparison of Experimental Versus Theoretical Results

The experimental results are now compared with the theoretical results obtained by the mathematical model. The electromagnet force transducer time response is applied as an external force in the mathematical model, simulating the impact test-case. In doing so, the experimentally obtained horizontal displacement is compared with the response obtained by the mathematical model. The mathematical model consist of a rigid model, and the finite element model for a modal reduced rotor with only the rigid mode shapes (referred to as Flex8) and the two first mode shapes included (referred to as Flex16).

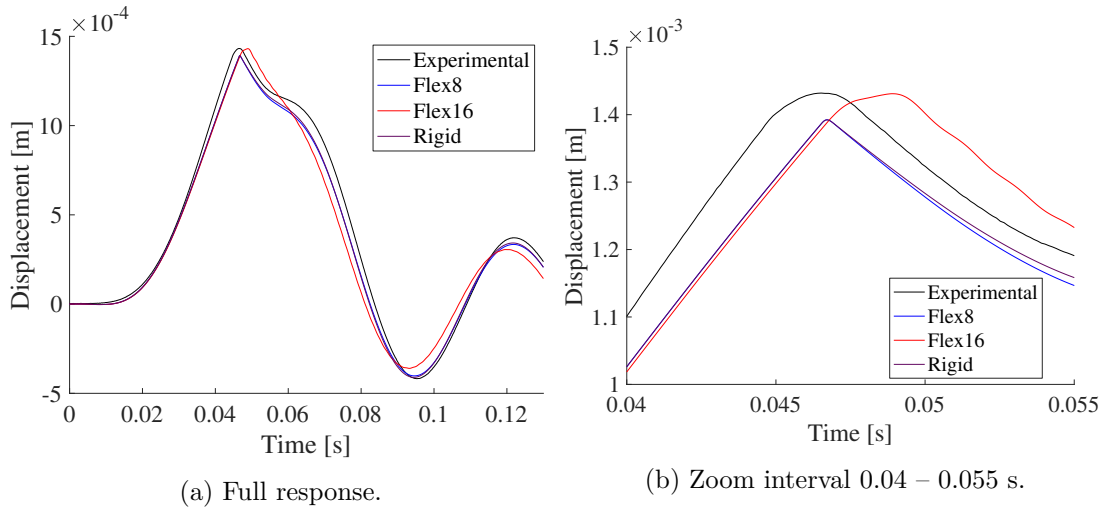


Figure 5.3: Horizontal displacement of rotor at unbalance disc.

In Figure 5.3 we see that the mathematical models are overall matching the experimental response. Considering the zoom plot, the discrepancies within the indentation phase becomes evident. A near-complete match between the rigid model and the FE-model Flex8 is found, as would be expected having the same electromagnetic force applied. Considering the top of the time response, a relatively quick deflection is found for the rigid models, compared to the FE-model Flex16 which is found to be in better agreement with the experimental response. Hence, Flex16 including the bending modes are considered to better represent the physical response of the experimental contact indentation, which further implies that the rotor is flexible.

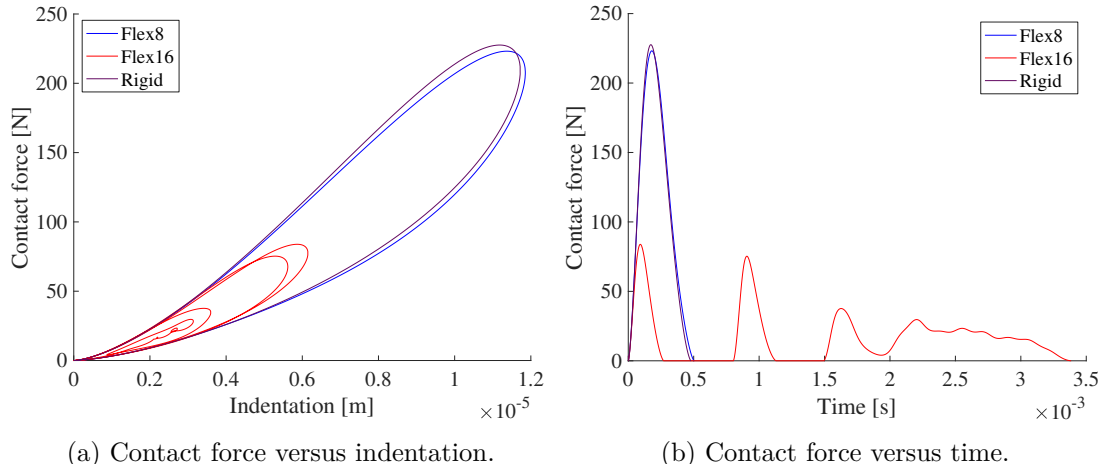


Figure 5.4: Contact force and indentation.

In Figure 5.4 we see that the indentation and the contact force for the rigid model

and the Flex8 are highly matching, both showing a great indentation and contact force, relative to the flexible model. This is expected as all the kinetic energy of the rigid rotor must be converted into potential energy of the stator, and elastic and dissipative energy of the indentation, within the single contact period. Considering the indentation and the contact force of the flexible rotor, the energy is allowed to be distributed over multiple impacts, as well as storing the potential energy in the rotor, yielding a lower indentation and contact force. As the indentation estimate of the experimental results are considered invalid, it is not possible to compare the the theoretically obtained indentation. However, considering the contact forces we see that the same order of magnitude is found numerically for the flexible beam and experimentally estimated in Figure 5.2, despite the reliability of the estimate.

5.1.4 Conclusion of Results

Concluding of the results of the non-rotating impact test, the numerical model and the experimental data suggests that higher frequency dynamics are present during the defined impact phase. Considering these higher frequency dynamics, the frequency interval was found to encompass the natural frequencies of the rotor bending modes. This implies that the rotors flexible dynamics are present during this impact phase and that several impacts might occur. The flexibility of the rotor was further shown experimentally by both considering the response of the proximity sensor at the unbalance disc showing no higher frequency dynamics during the impact phase in Figure 5.1, as well as better representing the experimental displacement response characteristics at the unbalance disc by the simulation shown in Figure 5.3.

Hence, it is concluded that the flexibility of the rotor is essential to include in the mathematical model in order to describe the rotor stator contact dynamics, as well as the dynamics related to the first horizontal mode of the impact house, based on the experiment conducted in the horizontal direction. Additionally, it is also found that the acquired data obtained from the impact experiment is not sufficient, in regards to the objective of a complete understanding and representation of the experimental rotor stator impact dynamics.

5.2 Rotating Impact Test Results

The second test is conducted having the rotor spinning at a constant rotational speed, i.e. $\Omega \neq 0$, starting from a steady state condition. Subsequently the electromagnet is applying a short-duration magnetic attraction force on the rotor steel target, causing the rotor to impact the stator. The scope of the experiment is to investigate the dynamics of the rotor and stator before, at and after impact has occurred, in order to validate the mathematical model established in this project. Furthermore, the impact dynamics are examined in regards to the response during contact.

5.2.1 Experimental Setup

The rotor is initially brought into steady state with the rotational speed $\Omega = 17$ Hz generating an elliptic orbital trajectory. Subsequently the rotor is subjected to an electromagnetic force, in the horizontal direction, by the electromagnet supplied with a 35 voltage in a time-duration of 50 ms. The electromagnet is activated at a specified angle of rotation by the use of the force transducer. It is important to mention that the activation of the electromagnet does not happen instantaneously, but with a small latency delay as discussed in Section 2.1.3, yielding an equivalent specific angular rotational delay.

In regards to the mathematical impact model, the model of Lankarani and Nikravesh is used for the indentation dynamics with a coefficient of restitution of $e = 0.5$, while the model of Ambrósio is used to model the friction with a friction coefficient of $c_f = 0.2$ and relative velocity tolerances of $v_0 = 1 \cdot 10^{-4}$ m/s and $v_1 = 2 \cdot 10^{-4}$ m/s.

5.2.2 Experimental Results

The rotor at steady state is subjected to the electromagnetic force under four different test-cases, being at 0, 90, 180 and 315 degree angle, each conducted three times in order to assess the repeatability. The displacement responses, obtained by the proximity sensor at the unbalance disc, are all presented in Figure 5.5.

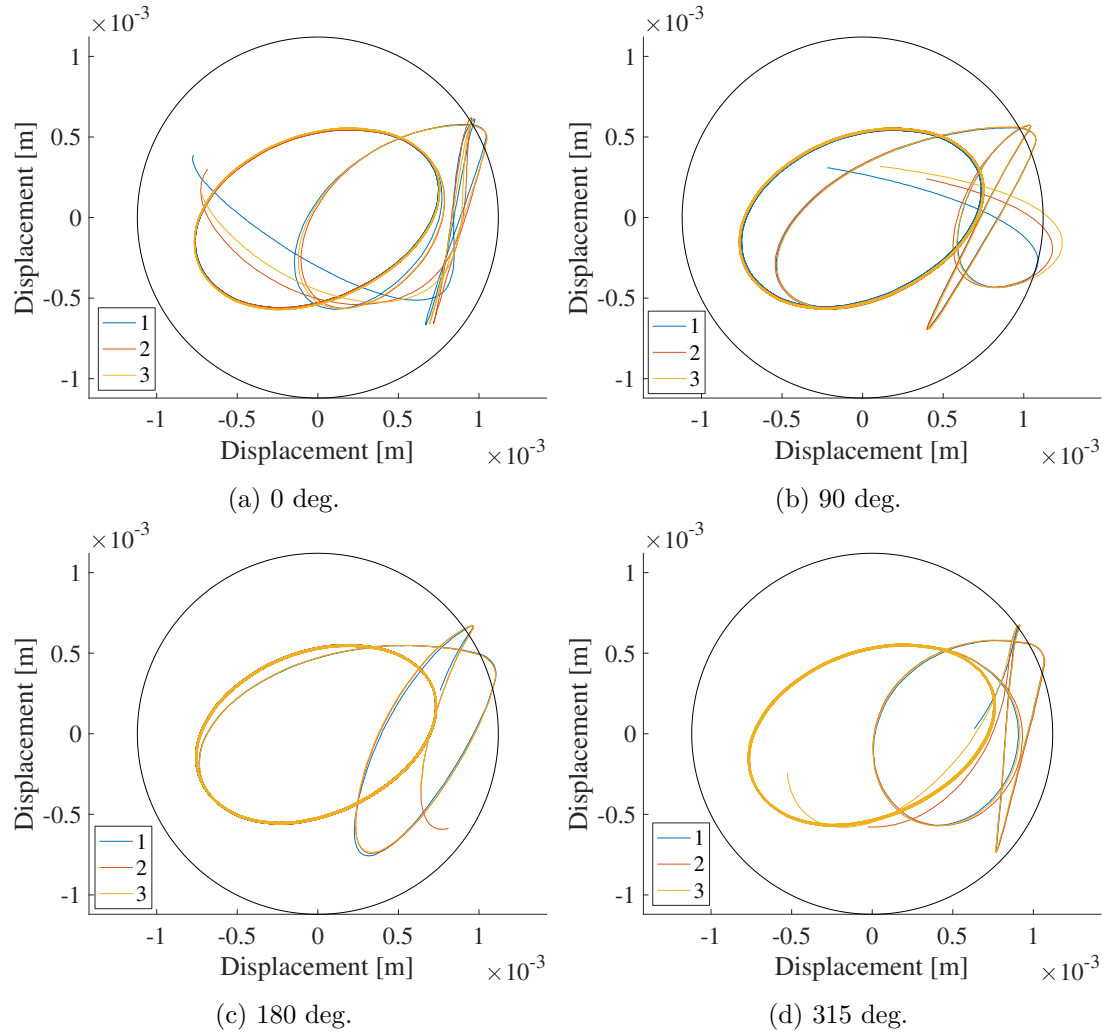


Figure 5.5: Experimental trajectories of the center of the unbalance disc within the bearing clearance.

Considering the experimental trajectories in Figure 5.5 it becomes evident that a high repeatability is present, as all the three trajectories are near-completely coinciding before, at and after impact, until a considerable time has passed and the three trajectories naturally diverge. Furthermore, it is noted that the rotor leaves the steady state orbit at exactly the same specified angle within each test-case, and that the specified angle of activation difference is in accordance with what would be expected considering the four different specified angles.

5.2.3 Comparison of Experimental Versus Theoretical Results

The test-case relating to the 0 and 315 degree angle excitation are now compared with the theoretical results obtained by the mathematical model. The electromagnet force transducer time response is applied as an external force in the mathematical model simulation, for which the displacement at the unbalance disc is compared. The mathematical model consists of a rigid model, and the finite element model of a modal reduced rotor with only the rigid mode shapes (referred to as Flex8) and the two first mode shapes included (referred to as Flex16).

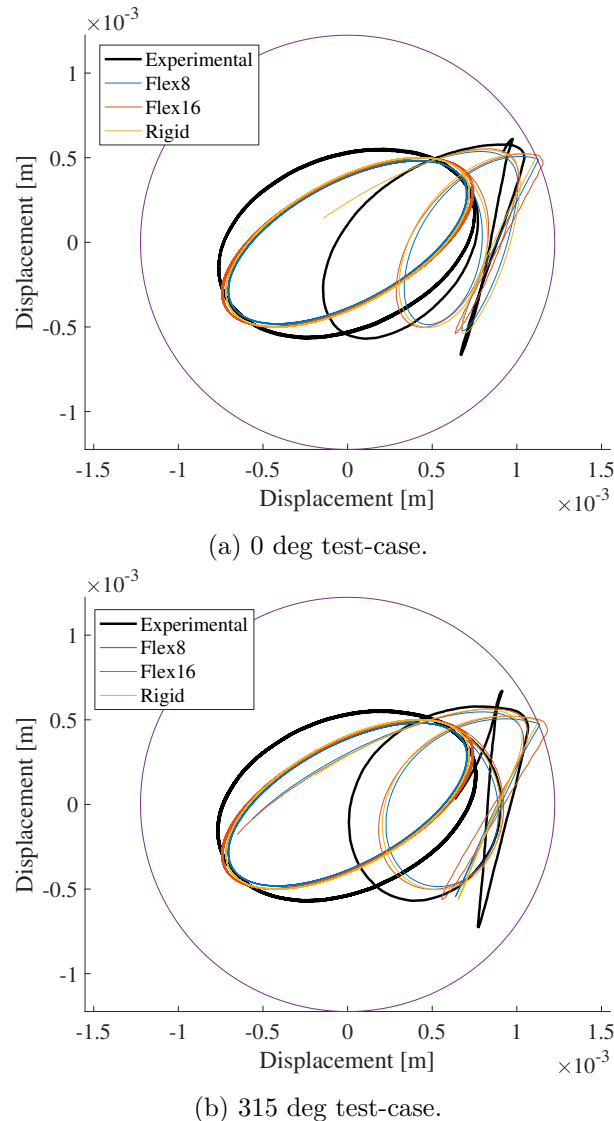


Figure 5.6: Experimental and theoretical trajectories of the center of the unbalance disc within the bearing clearance.

Considering the experimental and theoretical trajectories presented in Figure 5.6 we see that the angle where the trajectory leaves the steady state orbit are coinciding. The characteristics of the responses are showing the same trajectory trends up till impact, hitting the stator at approximately the same point. After impact, a closely related response curve is seen, for which the unavoidable divergence in trend first occurs after some time. It also seen that the two steady state elliptical orbits are not entirely coinciding, which is caused by the difficulty in matching the cross coupled stiffnesses of the system. However, considering the steady state response found in Section 4.5 a slightly better match between the experimental and mathematical model was found. Although the steady state response amplitudes are highly sensitive to a small change in rotational speed, which could cause some amplitude differences, the experimental steady state response amplitude obtained doing this experiment seems to be slightly larger than the one captured when conducting the fitting of the model in Section 4.5. An explanation for this could be that a slight change in the physical properties of the system has taken place, in between the time of conducting the fitting of the model and the experiment presented in this section. Lastly, the trajectory of the mathematical model including the flexibility of the rotor is found to represent the experimental response better during the impact, as was also found in the non-rotating experimental in Section 5.1, although the rigid model seems to represent the overall dynamics as well.

5.2.4 Conclusion of Results

Concluding on the results of the rotating impact test, it was first found that a high repeatability was obtained by the implementation of the angle triggered electromagnet, showing closely coinciding response trajectories for a given angle. Although the electromagnet seems to affect the dynamics during the investigated response trajectory, due to the phase-out of the demagnetization, the mathematical model was found to represent the experimental response well, for which the flexibility of the rotor again became prominent, as for the non-rotating experiment.

Chapter 6

Conclusion

In the present work, the dynamics concerning a rotor-stator system has been investigated, with the objective of applying and comparing different theoretical models with experimental results obtained from a test-rig made for the purpose of examining the contact forces originating during rotor to stator impacts.

The newly rebuilt test-rig showed various shortcomings, that needed to be rectified before a thorough analysis could be made. Additionally, a series of new components and features were implemented, aiming to obtain a better insight of the system dynamics. In regards to this, an electromagnet, together with an excitation steel target, was implemented such that all unwanted dynamics were minimized while exciting the rotor. This implementation also gave rise to the possibility of exciting the rotor at an exact specified angle of rotation, yielding highly repeatable experimental results.

A mathematical model was established with aim of describing the rotor-stator dynamics within the frequency range of 0–1000 Hz, constituting a mathematical representation of the rotor, impact house and the contact between these.

A special interest was put into describing the rotor both as a rigid- and flexible body, in order to examine the presence and influence of flexibility during contact. The flexibility of the rotor was fitted through an experimental modal analysis, showing good agreement between the experimental and mathematical model. The flexibility of the unbalance disc was found to cause two almost identical mode shapes of the shaft to appear, while the disc was found to be in opposite phase. As a simplification, the unbalance disc was modeled as being rigid in the mathematical model. This model was then fitted to the experimental data for the modes, which originally showed the disc to be flexible. Hence, this resulted in there being a total of two rotor modes in the model valid within the frequency band of interest.

An experimental transient decay response and unbalance response were conducted in order to obtain the external dissipative- and restoring forces, as well as the magnitude and phase of the unbalance mass, pertaining to the rotor system. The two tests were performed under a non-rotating and rotating condition, respectively, showing different characteristics in terms of the damping and cross-coupled stiffness. The damping at standstill was found to be highly anisotropic with a minimal appearance of cross stiffness, while in the rotating condition the system showed an almost isotropic damping with a

significant cross stiffness, on which the unbalance response is decidedly dependent. The difference in damping was said to stem from the spherical bearing, yielding a change in characteristics under a standstill and rotating condition. The prominent cross-coupled stiffness under the rotating condition is said to stem from the non-linearity of the PMB, which was modeled as linear in this project.

A thorough analysis of the impact house dynamics was conducted, modeled analytically as a fitted 4 DOF system. The 4 DOF system was fitted through an experimental modal analysis of the impact house, showing that three modes are present within the dynamic range of interest. These modes constituted one pure translatory mode shape in the horizontal direction and in the vertical direction, as well as a twisting mode shape appearing in the horizontal direction. However, this twisting mode was assumed not to be excitable by rotor impacting the stator, thus disregarded in the model. The finite element method was employed in order to assess the flexibility of the impact house, as well as verify the rigidity assumption. The FE-model showed that the flexibility of the impact house was significant, dominating the first natural frequency in the horizontal direction. In spite of this, it was possible to model this flexibility in the 4 DOF system using equivalent stiffnesses.

The contact models, composed of the friction model of Ambrósio and the contact force model of Lankarani and Nikravesh, were incorporated into the mathematical model. The complete rotor-stator model was found to be stable and physically adequate in terms of the dynamic behavior during simulations. A non-rotating and rotating experimental impact test was performed and compared with the mathematical model. In the non-rotating impact test, the experimental data and mathematical model responses showed the presence of higher frequency dynamics in the approximate frequency band of 600–1000 Hz. This frequency interval contains the two first flexible modes of the rotor, implying that the flexible dynamics of rotor were present during impact, and furthermore that several impacts might occur, as suggested by the mathematical model. Additionally, the flexibility of the rotor became prominent when comparing the experimental displacement time series with the flexible and rigid rotor response from the mathematical model, showing good agreement with the physical nature of the flexible response during impact.

Furthermore, the flexibility of the impact house was also found in the experimental response conducted in the horizontal direction. The estimation of the first mode of the impact house was found to be in complete agreement with the experimental results, and considered essential in the modeling of the impact dynamics.

Considering the rotating impact test, a high repeatability of the experiment was obtained by the use of the external electromagnet synchronized with the angular position of the shaft. The experimental test cases were simulated by the mathematical model, for which the mathematically obtained trajectories were in good agreement with the experimental responses, before, at, and after impact. This implies a well established mathematical model capable of representing the dynamics of the test-rig.

Future Works

Having concluded the present master's project, it appears that there remains a considerable amount of work to be done. With reference to the overall topic of rotor to stator contact dynamics, a variety of other contact models are at one's disposal for implementation using the groundwork laid with this project. However, to be able verify any findings obtained from these models, the experimental setup must be improved further. The main stop block for this work was indeed the remaining shortcoming in the test-rig. Thus as a final contribution, recommendations as to which challenges may be tackled first are hereby given.

New bearing

A number of problems related to the spherical bearing in use currently was found. Firstly, the bearing is not able to lock the axial DOF of the rotor, due to the default axial clearance in the bearing. Secondly, the friction in the bearing introduces anisotropic damping (at least at low, or zero, angular velocities). Therefore a new bearing is called for. A possibility could be to try another of the double-row ball bearing of the *1306 EKTN9/C3* from *SKF*. This could potentially reduce the level of friction. However, the axial play would still be an issue with this bearing. Instead one could implement a new design, where an ordinary ball bearing is mounted in a *membrane* made from sheet-metal. The membrane should in theory reduce the axial play drastically, while still allowing the rotor to pivot by its small angles. This design was originally proposed by Professor Peder Klit from the Department of Mechanical Engineering at DTU.

Mathematical Modeling of the PMB

The cross-stiffness effect, found in the current work, points towards the PMB as being the source. If this is the case, there is a possibility that the effect is frequency dependent and perhaps non-linear. Therefore this trail ought to be explored in order to extend the frequency range of the mathematical model. Here the authors suggest to make an electrodynamic model using the finite elements method. Specifically, a convenient solution could be to use the open source FEMM suite¹ for the task.

Timing of the Excitation Solenoid

The newly implemented solution for disturbing the rotor externally using the solenoid was found to yield promising results. However, electrodynamic effects were found to introduce some latency to the application and removal of the magnetic field, and in turn the attraction force on the rotor. While the ramp-up time of the field is probably tied to the physical properties of the current solenoid, the delay of the remaining magnetization may be removed by employing an H-bridge. Such a device could be easy to implemented by adding an additional MOSFET-relay. With the H-bridge the current through the

¹Read more at: www.femm.info.

solenoid can be flipped after the desired duration of the external excitation. Reversing the polarity would then serve to rapidly demagnetize the steel target on the rotor.

Impact House Improvements

The flexibility effect of the internal polycarbonate houses was determined to be rather pronounced in this work. Thus, to simplify the response of the impact house upon rotor to stator impacts, the already available aluminum middle- and inner houses could be tested. Note that this would potentially have an impact on the size of the inertia forces, so that these magnitudes could increase a lot relative to the magnitude of the actual contact forces. To mitigate the potential negative effect, however, more sensors could be added to the inner house.

In any case it could be worthwhile to install more sensors to the inner house in order to gain greater insights into the house dynamics. Installing, for instance, an accelerometer (or velocity sensor) in the horizontal direction on the inner-most house would reveal more detailed information regarding the displacement of the inner house. Furthermore, while it was relatively clear to determine the onset of the contact period, it proved much harder to determine the end of the contact period. Therefore a proposal is to implement a sensor device for determining contact between the rotor and the stator. A solution could perhaps rely on tracking the electrical capacity of the stator (in the case it remains conductive). In this way the capacity would change when the rotor was engaged with the stator. This solution, however, is merely an unstructured idea at this point.

Bibliography

- [1] K. H. Hunt and F. R. E. Crossley. "Coefficient of Restitution Interpreted as Damping in Vibroimpact". In: *Journal of Applied Mechanics* (1975).
- [2] J.R. Dormand and P.J. Prince. "A family of embedded Runge-Kutta formulae". In: *Journal of Computational and Applied Mathematics* 6.6 (1980), pp. 19–26. ISSN: 18791778, 03770427.
- [3] H. M. Lankarani and P. E. Nikravesh. "A Contact Force Model With Hysteresis Damping for Impact Analysis of Multibody Systems". In: *Journal of Mechanical Design* 112 (1990).
- [4] Michael Baatz and Maik Hyrenbach. "Method of Calculating the Magnetic Flux Density and Forces in Contact-Free Magnetic Bearings". In: *ETEP* 1.4 (July 1991), pp. 195–199.
- [5] Lawrence F. Shampine and Mark W. Reichelt. "The MATLAB ODE Suite". In: *SIAM Journal on Scientific Computing* 18 (1997), pp. 1–22.
- [6] D. J. Ewins. *Modal Testing. Theory, practice and application*. Second edition. Research Studies Press Ltd., 2000. ISBN: 0-86380-218-4.
- [7] Jorge Ambrósio. "Impact of Rigid and Flexible Multibody Systems: Deformation Description and Contact Models". In: vol. 2. Jan. 2003, pp. 57–81. ISBN: 978-1-4020-1339-3. DOI: [10.1007/978-94-010-0203-5](https://doi.org/10.1007/978-94-010-0203-5).
- [8] P Flores et al. "Influence of the contact - impact force model on the dynamic response of multi-body systems". In: *Journal of Mechanical Design* 220 (2006).
- [9] Anders F. Lund Madsen. "Design af passivt-magnetiske bølge-folielejer og deres forsøgsopstilling". Danish. Master Thesis. Technical University of Denmark, Department of Mechanical Engineering, 2008.
- [10] Richard G. Lyons. *Understanding Digital Signal Processing*. Third edition. Pearson Education, Inc., 2011. ISBN: 978-0-13-702741-5.
- [11] Stefano Morosi. "From Hybrid to Actively-Controlled Gas Lubricated Bearings – Theory and Experiment". PhD Thesis. Technical University of Denmark, Department of Mechanical Engineering, 2011.
- [12] Niels Peter Pauli Petersen. "Rotor Drop Rig - Design & Simulation". Master Thesis. Technical University of Denmark, Department of Mechanical Engineering, 2011.

- [13] Said Lahriri. "On the Rotor to Stator Contact Dynamics with Impacts and Friction. Theoretical and Experimental Study". PhD Thesis. Technical University of Denmark, Department of Mechanical Engineering, 2012.
- [14] Daniel J. Inman. *Engineering Vibration*. Fourth edition. Pearson Education Limited, 2013. ISBN: 978-0-273-76844-9.
- [15] Svend Erik Andersen. "Experimental Characterisation of Backup Bearings Considering Lateral Rotordynamics. Application to Flywheels and Energy Storage". BEng. Thesis. Technical University of Denmark, Department of Mechanical Engineering, 2017.
- [16] Cesar Augusto Lampe Linhares da Fonseca. "A Theoretical-Experimental Study of Backup Bearings. The Pinned versus Ball Bearing". PhD Thesis. Technical University of Denmark, Department of Mechanical Engineering, 2017.
- [17] Svend Erik Andersen. *Modification of a Rotor-Stator Impact Test-Rig*. Tech. rep. Technical University of Denmark, Department of Mechanical Engineering, 2018.
- [18] Paulo Flores and Hamid M. Lankarani. "Contact Force Models for Multibody Dynamics. Solid Mechanics and Its Applications". Volume 226. Springer.
- [19] Byron Knapp, Dave Arneson, and Don Martin. *Electrical Runout Using an Eddy-Current Sensor for Roundness Measurements*. Technical Note. Professional Instruments Company, Hopkins, Lion Precision.
- [20] Ilmar F. Santos. "Least Square method - An example". Internal material from the course 41614. unpublished.
- [21] Ilmar F. Santos. "Vibrations in Rotating Machinery. Modelling, analysis, experimental tests, vibration monitoring and diagnostics". Internal material from the course 41514. unpublished.

Appendix A

Miscellaneous

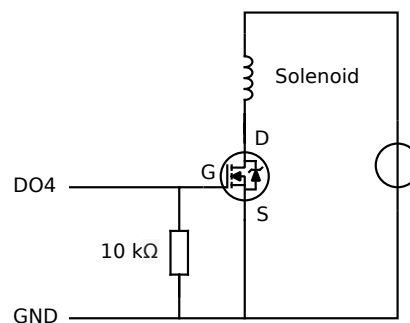
A.1 PMB Adjustment Tool



Figure A.1: Adjustment tool used for placing the PMB.

A.2 Excitation Circuit

	0	1	2	3	4	5	6	7
A								
B								
C								
D								
E								
F								
G								
H								
Author: Svend E. Andersen	External excitation circuit					File:		
Date: 30/08/2019						Folio: 1/1		



A.3 Rotor Properties from SolidWorks

Mass properties of mainshaft

Configuration: Default

Coordinate system: -- default --

Mass = 2.03708638 kilograms

Volume = 561592.69251902 cubic millimeters

Surface area = 0.19851250 square meters

Center of mass: (meters)

X = -0.00001040

Y = 0.13471074

Z = 0.00000321

Principal axes of inertia and principal moments of inertia: (kilograms * square meters)
Taken at the center of mass.

Ix = (0.00012136, 0.99999999, -0.00003391) Px = 0.00130053

Iy = (-0.70599726, 0.00010969, 0.70821456) Py = 0.03388615

Iz = (0.70821455, -0.00006201, 0.70599727) Pz = 0.03388732

Moments of inertia: (kilograms * square meters)

Taken at the center of mass and aligned with the output coordinate system.

Lxx = 0.03388674 Lxy = 0.00000395 Lxz = -0.00000059

Lyx = 0.00000395 Lyy = 0.00130053 Lyz = -0.00000110

Lzx = -0.00000059 Lzy = -0.00000110 Lzz = 0.03388673

Moments of inertia: (kilograms * square meters)

Taken at the output coordinate system.

Ixx = 0.07085371 Ixy = 0.00000110 Ixz = -0.00000059

Iyx = 0.00000110 Iyy = 0.00130053 Iyz = -0.00000022

Izx = -0.00000059 Izx = -0.00000022 Izz = 0.07085371

One or more components have overridden mass properties: inner_magnet

Appendix B

Datasheets

B.1 Damping Plates

www.iac-acoustics.com/dk

Anti-vibrationsplade

MF

Produktbeskrivelse

Pladen fremstilles i to versioner – begge med en gummihårdhed på 45° IRH.
Mafund-pladen med tværgående luftkanaler er 25 mm tyk og giver en relativ stor nedbøjning. Pladen kan optage et flade-tryk på op til 5 kg/cm² og er fremstillet i SBR-gummi. Den massive Mafund-plade er 15 mm tyk og anvendes til store fladetryk, idet den kan belastes op til 53 kg/cm² og er fremstillet i NR-gummi

Anvendelse

Mafund-pladen benyttes til vibrationsisolering af større, tunge maskinopstillinger, typisk under et betonfundament. Endvidere anvendes pladerne i byggerier til støj-/ vibrationsisolering mellem betonelementer.

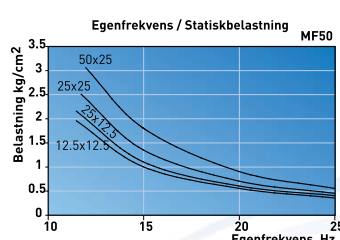
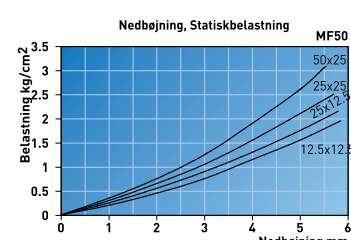
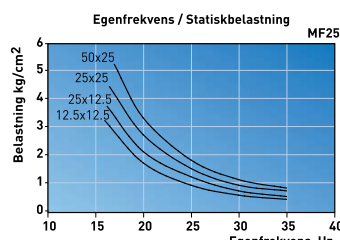
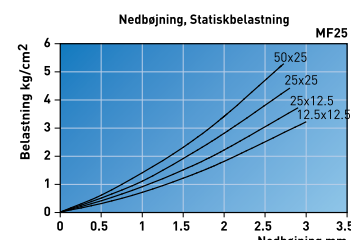
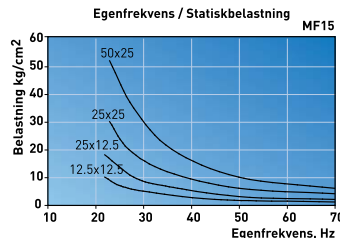
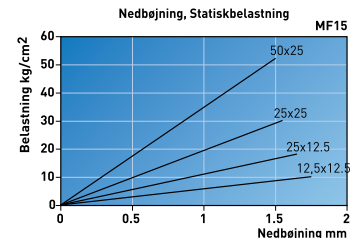
Dimensionering

Den normale statiske belastningsfordeling for Mafund hul er 5kg/cm², der giver en nedbøjning på 2,7mm.

For begge pladetyper gælder, at større nedbøjning kan opnås ved at lægge plader ovenpå hinanden.

Dimensioner

MF15: 50 x 25 x 1,5 cm (Mafund massiv)
MF25: 50 x 25 x 2,5 cm (Mafund hul)
MF50: 2 x MF25



B.2 Holding Magnet

www.nguyensexuong.com

Industrial Relays & Solenoids

ON-LINE



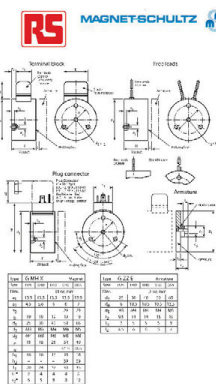
www.rssingapore.com

Actuators

Holding Magnets

Electro-magnets

- Energise to Hold/De-energise to release
- Ideal for use in machine mechanisms, door/guard locking and applications with remote hold/release requirement
- Optimum performance when used with RS armature plates (available separately) but suitable for holding any smooth ferrous surface of adequate thickness
- Use over size armature to ensure magnet face is fully covered
- Electrical connection by free leads (FL), terminal block (TB) or plug and connector (PC)
- Plug connector types include DIN 43650 male and female parts
- Coils are continuously rated at the specified supply voltages
- Remanence (approx. 5% of holding force) may be reduced by fitting a non-magnetic shim between magnet and armature



Dimensions

Magnet Diameter (mm)	Magnet Weight (g)	Stock no.
25	70	346-069
40	220	346-081
40	220	346-097
50	380	346-104
50	380	346-110
50	380	825-944
65	750	825-950
65	750	825-966
65	750	825-972

Operating Voltage	Power Consumption (W)	Holding Force (N)	Electrical Connection Type	Brand	Stock no.
12 Vdc	3.2	130	Free Leads	RS	346-069
12 Vdc	5.6	420	Terminal Block	RS	346-081
24 Vdc	5.6	420	Terminal Block	RS	346-097
12 Vdc	6.2	700	Terminal Block	RS	346-104
24 Vdc	6.2	700	Terminal Block	RS	346-110
240 V ac	6.2	700	Plug & Connector	Magnet-Schultz Ltd	825-944
12 Vdc	9.8	1200	Terminal Block	Magnet-Schultz Ltd	825-950
24 Vdc	9.8	1200	Terminal Block	Magnet-Schultz Ltd	825-966
240 V ac	9.8	1200	Plug	Magnet-Schultz Ltd	825-972

Manu. Part No.	Stock no.	Price per	OM	SS	SS	SS
GMHX 025 X00 A01	346-069	unit	1+	71.00		
GMHX 040 X20 A01 12V 100%	346-081	unit	1+	91.00		
GMHX 040 X20 A01 24V 100%	346-097	unit	1+	91.00		
GMHX 050 X20 A01 12V 100%	346-104	unit	1+	93.50		
GMHX 050 X20 A01 24V 100%	346-110	unit	1+	116.00		
GMHX 050 X20 D07	825-944	unit	1+	131.00		
GMHX 065 X20 A01 12V 100%	825-950	unit	1+	103.50		
GMHX 065 X20 A01 24V 100%	825-966	unit	1+	109.00		
GMHX 065 X20 D03	825-972	unit	1+	152.50		

Electro-Permanent Magnets

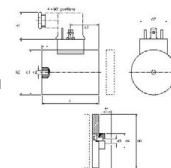
MAGNETSCHULTZ

ON-LINE



www.rssingapore.com

ON-LINE



- Holding function when de-energised and release when pulsed with the appropriate voltage

- Suitable for use in machine mechanisms, door/guard locking and remote hold/release requirements
- The hold without power design is ideal for fail-safe and heat sensitive applications
- Optimum performance when used with RS armature plates (available separately)
- Electrical connection by plug and connector (DIN 43650 male and female parts included)
- Coils are impulse rated at the specified supply voltages, ac or dc
- Remanence (nominally 10% of holding force) will vary with coil temperature

Caution: Avoid high temperatures and impact loads that may damage the permanent magnet

Magnet Diameter: 35 mm Operating Voltage: 240 V ac

Power Consumption: 6.6 W Magnet Weight: 280 g

Manu. Part No.	Stock no.	Price per	OM	SS	SS	SS
GMPX 035 X20 D01 214V Impulse	825-994	unit	1+	270.00		

Accessories

Description	Stock no.	Price per	OM	SS	SS	SS
25mm Ø 12g Armature Plates	346-126	unit	1+	20.50		
40mm Ø 50g Armature Plates	346-132	unit	1+	24.00		
50mm Ø 100g Armature Plates	346-148	unit	1+	22.50		
30mm Ø 28g Armature Plates	826-326	unit	1+	22.50		
65mm Ø 210g Armature Plates	826-032	unit	1+	25.00		

45

FIND IT.
DESIGN IT.
BUY IT.

www.rssingapore.com

RS Branded products.
Wide range, great value.

www.rssingapore.com

MAGNETSCHULTZ
SOLENOIDS AND SOLUTIONS



D.C. Holding Magnet Type GMH

Armature Type G ZZ
Rectifier for A.C. supply
Range up to 3630 N

9

Product group

Type **G MH G ZZ**

- According to VDE 0580 and ISO 9001 (conform with article 10 of direction 73/23/EEC – according to CENELEC memorandum no. 3 of march 1987).
- Robust cylindrical construction zinc plated and passivated with body mounting
- Seven sizes, 25 to 100 mm diameter
- Pole piece may be supplied with centre bore for push operation
- Armature, nickel plated, with self-aligning mounting, type G ZZ, provides optimum holding force and low remanence
- Increasing force characteristic (Fig. 2)
- Coil with insulation to class F for voltages up to 250 volts
- Protection classification – DIN VDE 0470 / EN 60529 – IP 20 (terminal block)
- Connections with free leads, terminal block or plug connector
- Plug connectors available with rectifier for A.C. supply (List Z KB G)
- Boxed, protective or weather-proof units
- Release Mechanisms for shutters and doors
- Strip magnets, 4 lengths type G HL
- Permanent magnets with electro-magnetic release (Range up to 500 N) – Product Group G MP
- General-purpose holding magnets for arduous service in the field of:
Machine tools
Lifting-locking-door holding
Feeder mechanisms
Short stroke/high force operations
Textile machinery



Fig. 1
Holding Magnet G MH X 065 X 20 A01
with armature G ZZ E 065 X 00 A01

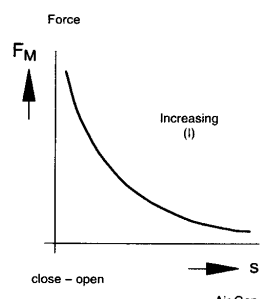


Fig. 2
Force characteristic



sales@magnetschultz.co.uk
Phone: ++44 (0) 1483 794700

Product group 9

Performance tables for type GMH magnet and armature GZZ

G MH X	025	030	040	050	065	080	100
Duty rating ED	S1	S1	S1	S1	S1	S1	S1
Power consumption P ₂₀ (W)	3,2	4	5,6	6,2	9,8	12,4	17
Magnet weight m _M (kg)	0,07	0,1	0,22	0,38	0,75	1,3	2,2
Armature weight m _A (kg)	0,012	0,029	0,05	0,1	0,21	0,4	0,74
Armature thickness (mm)	3	5	5	6	8	10	12
Armature diameter Ø (mm)	25	30	40	50	65	80	100
Air gap s (mm)	Holding force F _M (N)						
See note 1	0	150	280	520	800	1480	2280
	0,1	36,3	70	275	569	1128	1942
	0,16	18,2	38	157	373	883	1600
	0,25	9,8	20	80	216	618	1256
	0,4	3,5	10	30	93	294	657
	0,6	1,8	5	14	41	132	314
	1,0	0,9	2	6,2	18	61	128
	1,6	—	—	2,6	7	18	45
	2,5	—	—	1,3	2,2	10	18
	4	—	—	0,5	0,8	3,2	9,8
	6	—	—	—	0,4	2,6	4,9
Holding force F _M (N) with armature G ZZ (s = 0 mm) See note 2	130	230	420	700	1200	1850	3000

Note: - 0 mm is completion of energized stroke

NOTES

1. That force produced when using plain pole faces and plain steel armature of material ST 37 (9S Mn 28) with thickness as in tables and a surface finish of 15 µm.

The force will be altered if other material specifications, thicknesses and surfaces are used, or if the armature fails to make positive contact over the full diameter of the magnet face.

2. That force produced when using plain pole faces and plated (chemical nickel) armature

3. The pole faces of the magnet can be supplied electroplated for corrosion protection. This will marginally reduce holding force and remanence.

4. The magnetic remanence is approx. 5 % of the magnetic force F at 0 mm and can be reduced by increasing the air gap as in 2. and 3. above i. e. plating either or both surfaces or by machining away an area of pole piece or armature surface.

Conversion Factors

1 N = 0.102 kp ≈ 0.1 kg
1 kg = 2.2 lb.
1 mm = 0.039 in.
1 Ncm = 0.086 in. lb.

PERFORMANCE TABLE

Terms are explained in Technical Bulletin G XX & VDE 0580/35.

TABLE BASIS

24 V/100 % duty Ambient temperature 35° C

Heat insulated base Free air mounted

Lifting vertically Tolerance ± 10 % (inherent & manufacture).

MAGNETIC FORCE (F_M)

is listed in HOT condition at 90 % of rated voltage (increase approx. 20 % of rated voltage). Adjust for armature weight.

POWER CONSUMPTION (P₂₀)

is listed with a 20° C coil temperature (decrease/HOT). The temperature rise is limited to 60° K to provide a low surface contact temperature, the magnetic forces can therefore be increased with special coil winding for continuous or short duty.

DUTY RATING (ED %)

% of energized time per operation cycle: $\frac{t_{on}}{t_{on} + t_{off}}$ × 100.

Max. energized time/cycle:

100 % continuous: 40 % – 120 secs., 25 % – 75 secs., 15 % – 45 secs., 5 % – 15 secs.

Force figures available for respective duty ratings.)

SUPPLY VOLTAGES

The standard supply voltages are: 12 V, 24 V, 97 V, 205 V D.C. (for rectified 110 V, 230 V, 50/60 Hz A.C.).

DESIGN ARRANGEMENTS

Terminal block ...X 20 A 01 – 2 pole cable entry from magnet face.

Free leads ...X 00 A 01 – Side entry (rear entry on mounting pitch circle can be provided)

Plug connector ...X 20 A 02 – D.C. Z KB X 211 B 02 – A.C. Z KB G 211 A 02 (rectifier) – S 114 A 01 (overvoltage)

MOUNTING

3 tapped holes and centre thread for adjustable mounting in rear face. Any attitude may be used.

SPECIAL PROTECTION

The magnets may be provided with plated pole faces and protective or weatherproof boxed assemblies, with test switch and indicator light as required (page 4).

SPECIAL

Special magnets and armatures are available, including release and strip magnet assemblies to meet specific requirements. Please advise full application and operating details.

POLE DIAMETER

The centre pole piece may be bored for push operation or mounting, with a loss of magnetic force.

the pole diameters are:

G MH X	025	030	040	050	065	080	100
Ø mm	12	14	19	24	31	38	47

B.3 Magnet Force Transducer

14

U9B

7 Technical data

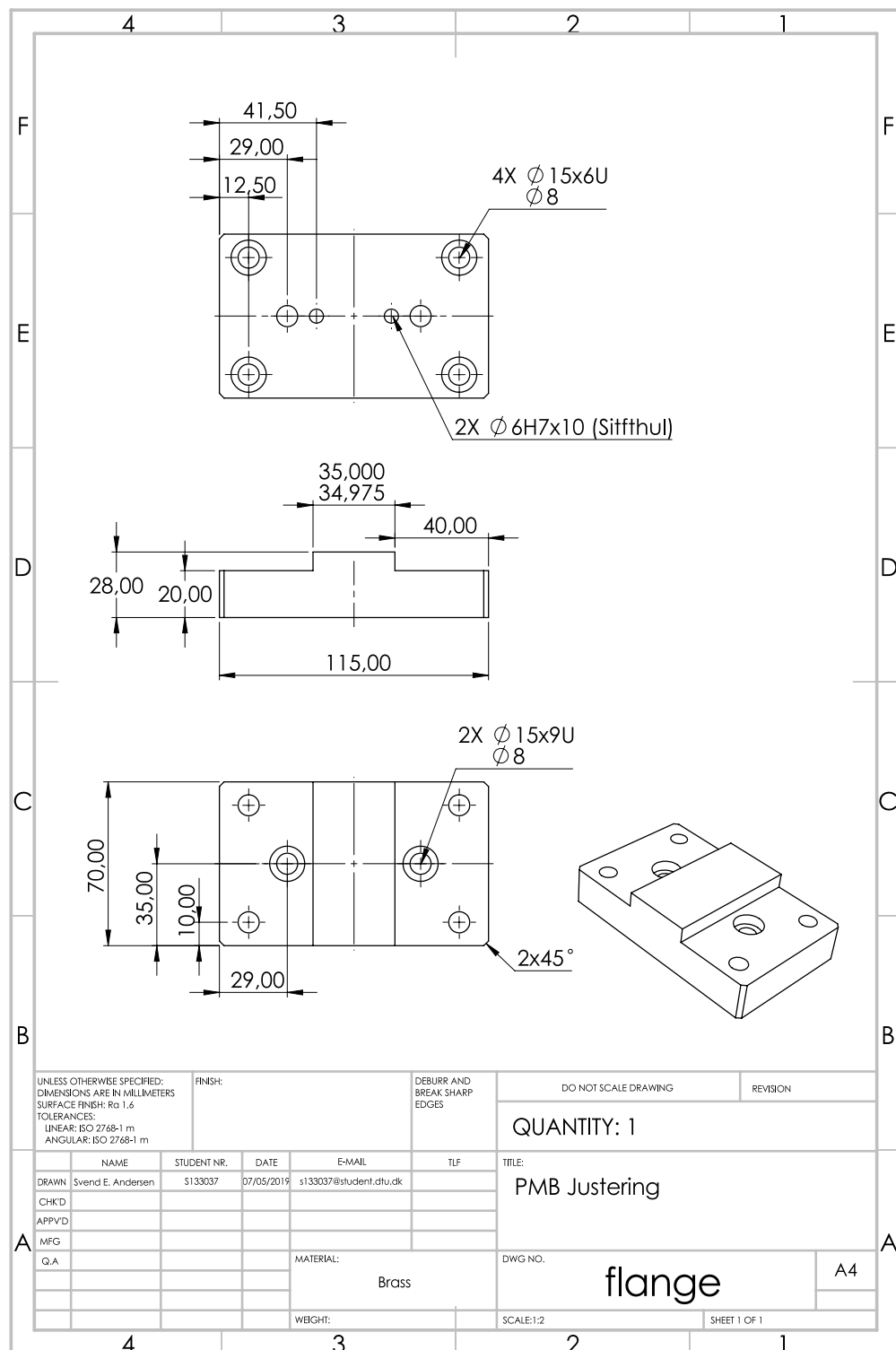
Type	U9B										
Nominal force	kN	0.5	1	2	5	10	20				
Accuracy class		0.5									
Nominal sensitivity	C _{nom}	mV/V	1								
Relative sensitivity deviation	d _c	%	$\leq \pm 1$ tens. / $\leq \pm 2$ compress.								
Effect of temperature per 10K on sensitivity	TK _C										
in the nominal temperature range		%	$\leq \pm 0.5$								
in the service temperature range		%	$\leq \pm 0.8$								
Effect of temperature per 10K on zero signal	TK ₀										
in the nominal temperature range		%	$\leq \pm 0.5$								
in the service temperature range		%	$\leq \pm 0.8$								
Linearity		%	$\leq \pm 0.5$								
Hysteresis related to measuring range limit	U	%	$\leq \pm 0.5$								
Span in fixed mounting orientation		%	$\leq \pm 0.5$								
Creep at nominal load and reference temperature over 30 min	d _{crF+E}	%	$\leq \pm 0.2$								
Input resistance (BK-BU) at reference temperature	R _e	Ω	> 345								
Output resistance (RD-WH) at reference temperature	R _a	Ω	300–400								
Insulation resistance	R _{Is}	GΩ	> 1								
Service range of supply voltage	B _{U,G}	V	0.5...12								
Reference supply voltage	U _{ref}	V	5								
Reference temperature	t _{ref}	°C [°F]	+23 [+73.4] -10..70 [+14...+158]								
Nominal temperature range	B _{t,nom}	°C [°F]	-30...+85 [-22...+185]								
Service temperature range	B _{t,G}	°C [°F]	-30...+85 [-22...+185]								
Storage temperature range	B _{t,S}	°C [°F]									
Protection class to EN 60 529			IP 67								
Nominal measurement displacement $\pm 15\%$	S _{nom}	mm	$< 0,1$								
Natural frequency $\pm 15\%$	kHz	15.5	23.7	18.7	20	23	27.8				
Service load	(F _G)	%	120								
Breaking load	(F _B)	%	>200								
Relative static side-load limit¹⁾	(F _O)	%	40	20							
Permissible vibration amplitude to DIN 50 100	F _{rb}	%	70								
Weight, approx.	g	65	100								
Cable length	m	1.5									

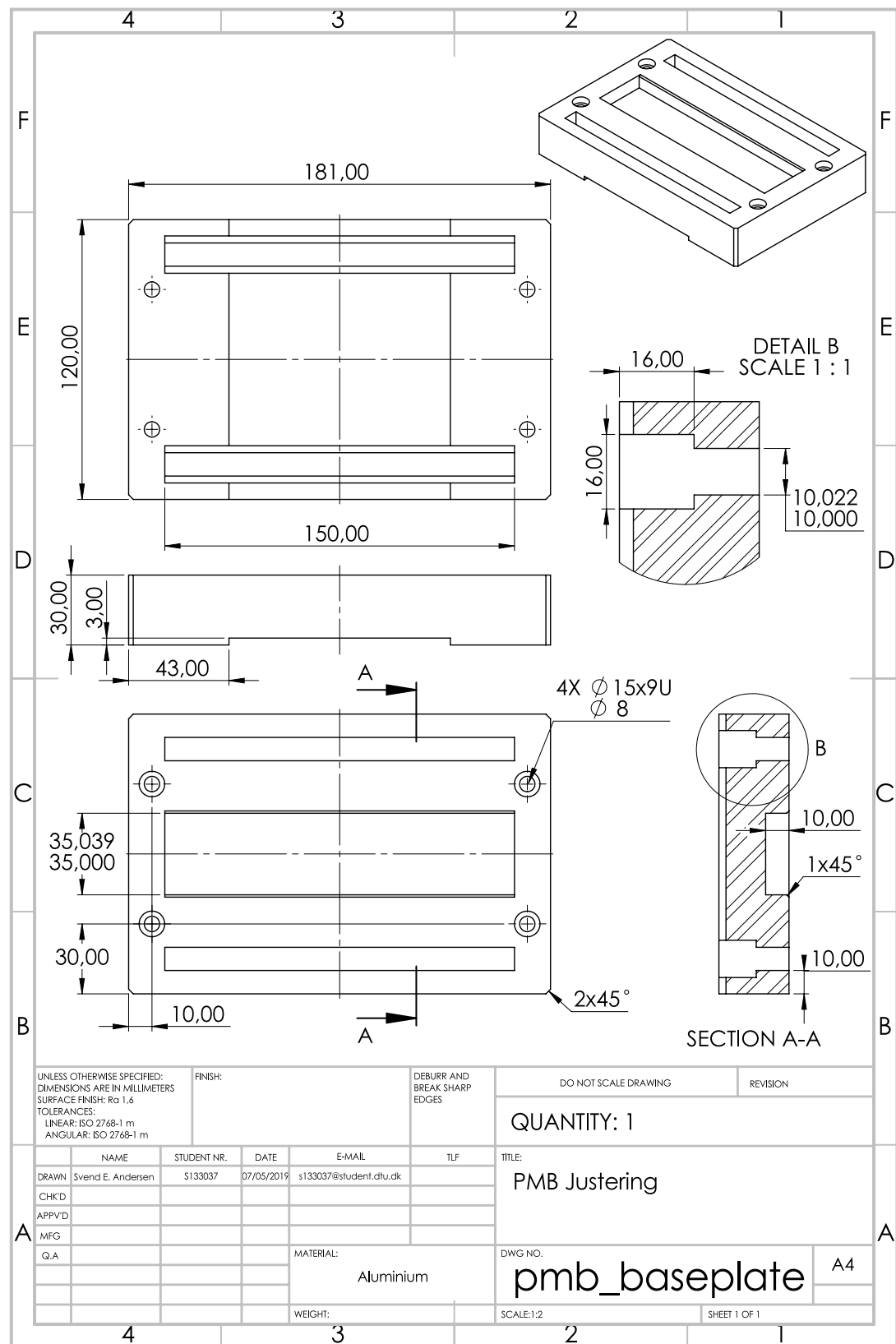
¹⁾ referred to the load transfer point 2mm above diaphragm

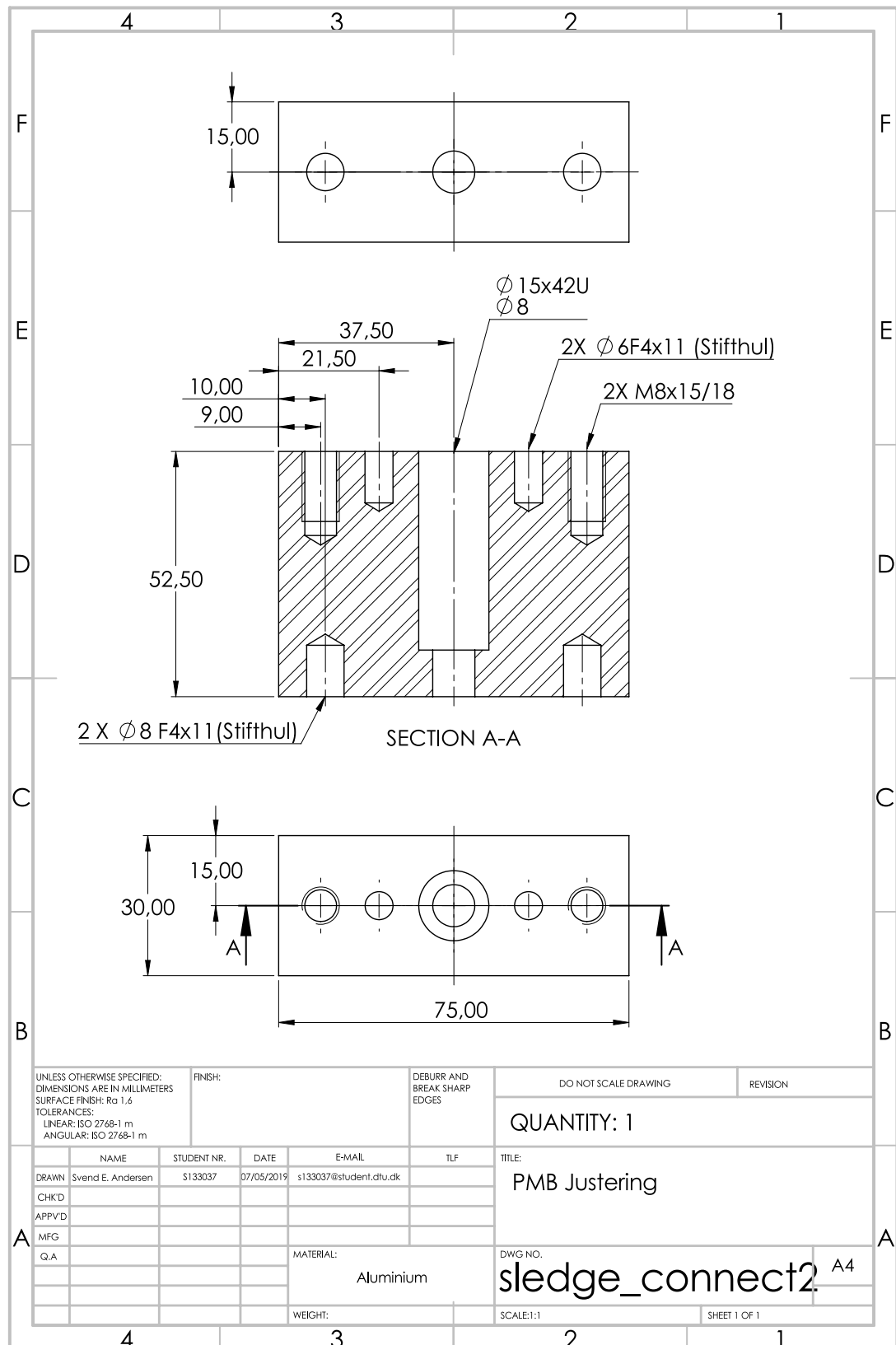
Appendix C

Machine Drawings

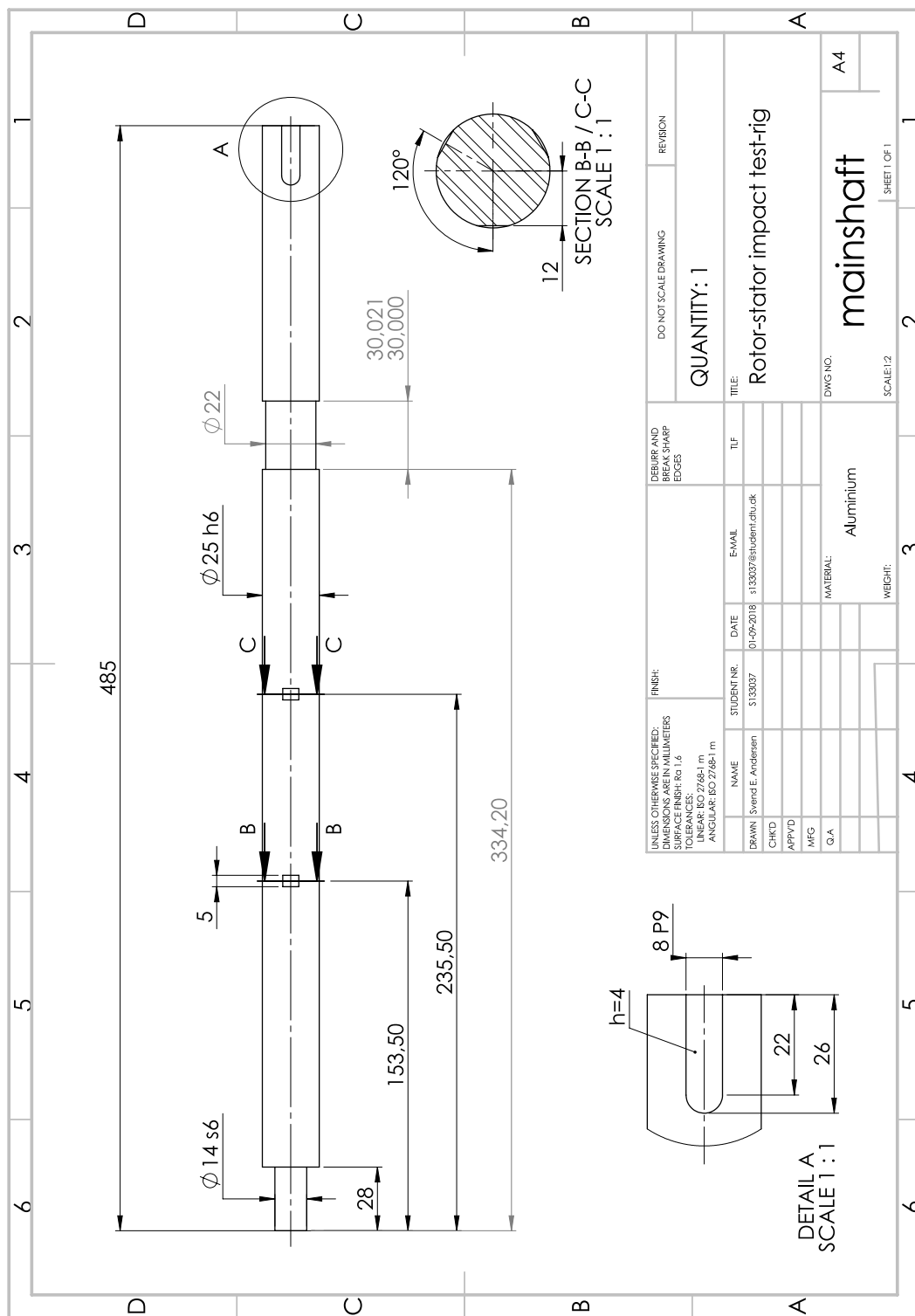
C.1 PMB Tower

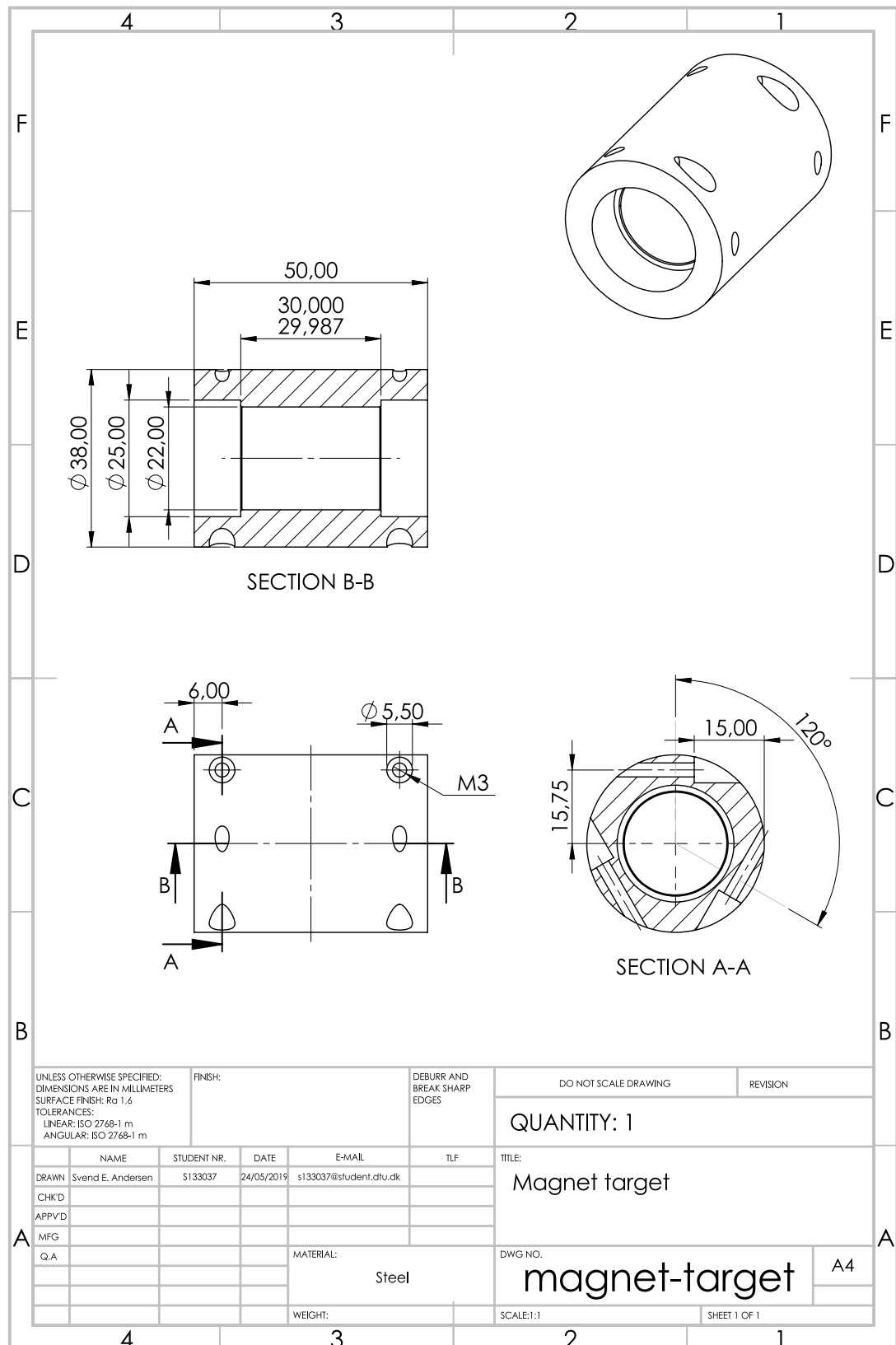


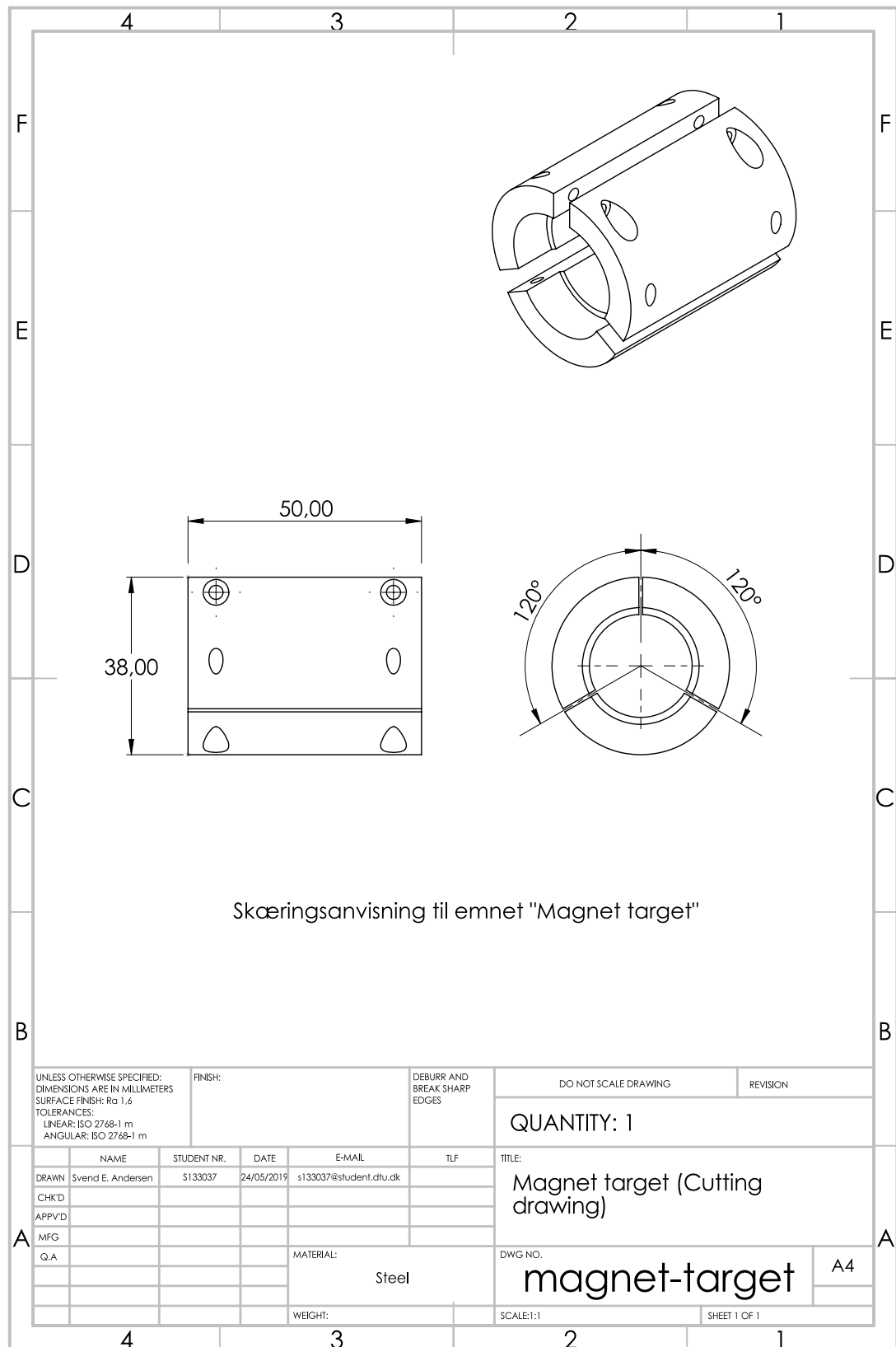




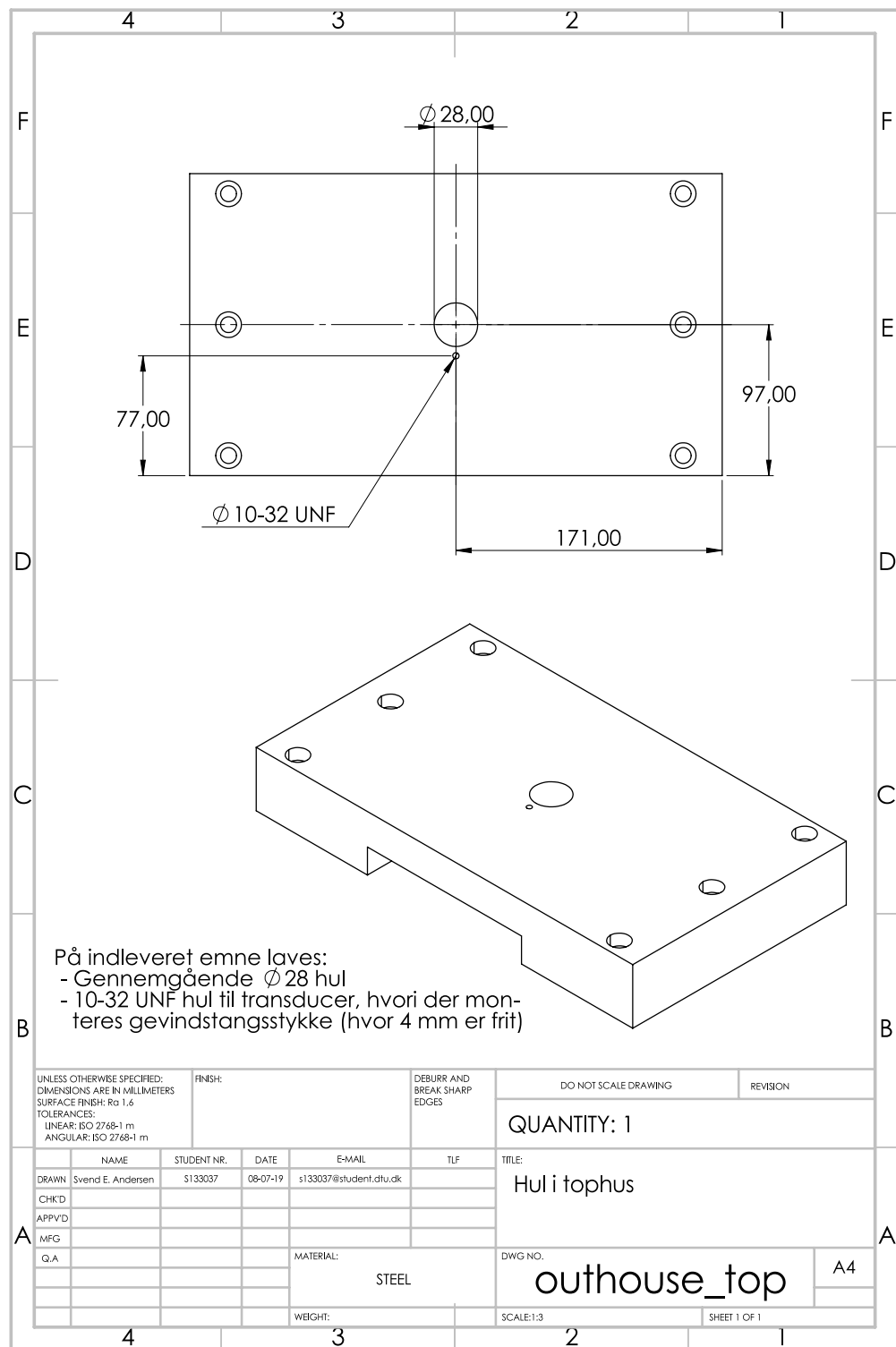
C.2 Steel Target

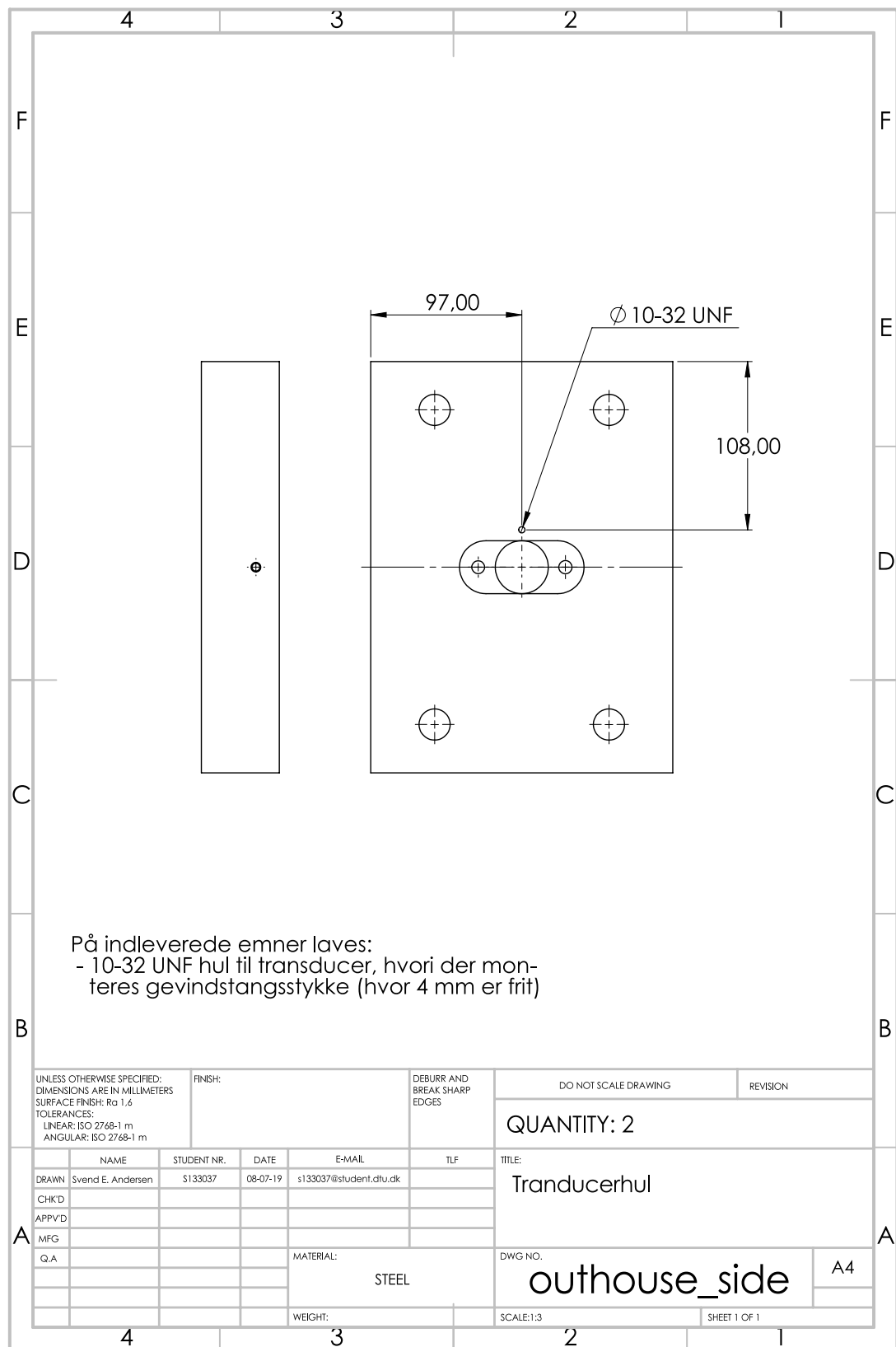




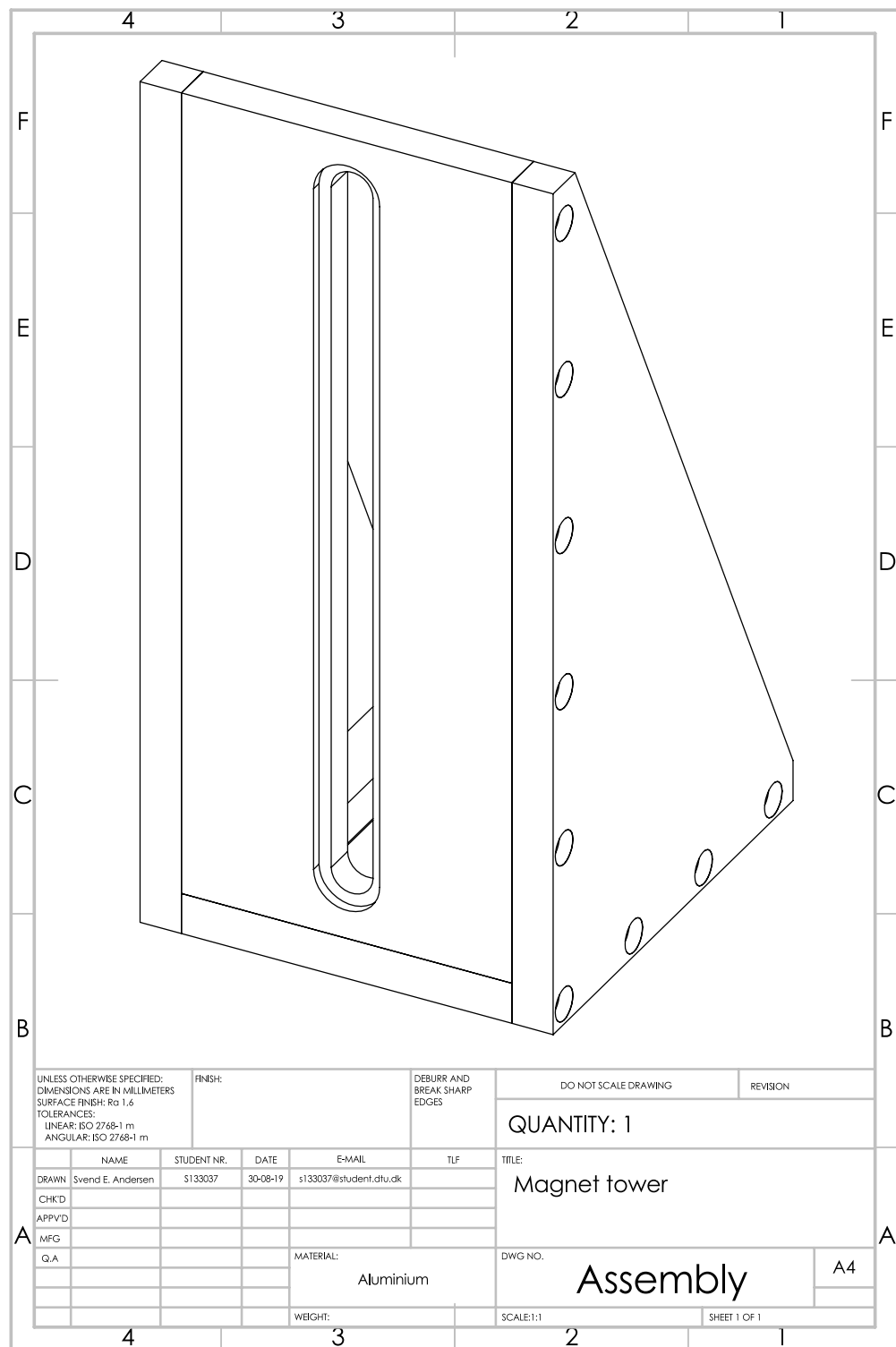


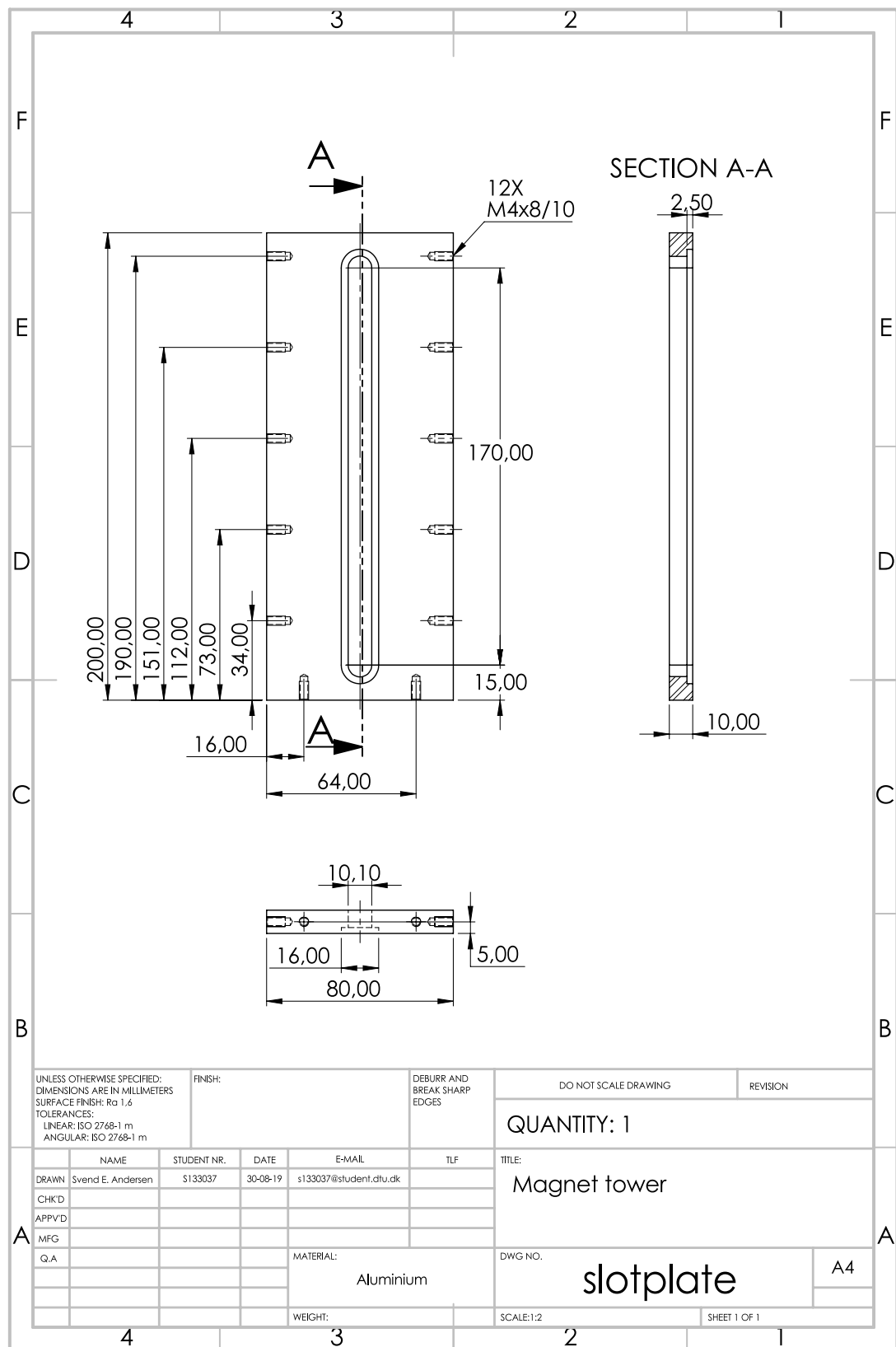
C.3 Steel House Modifications

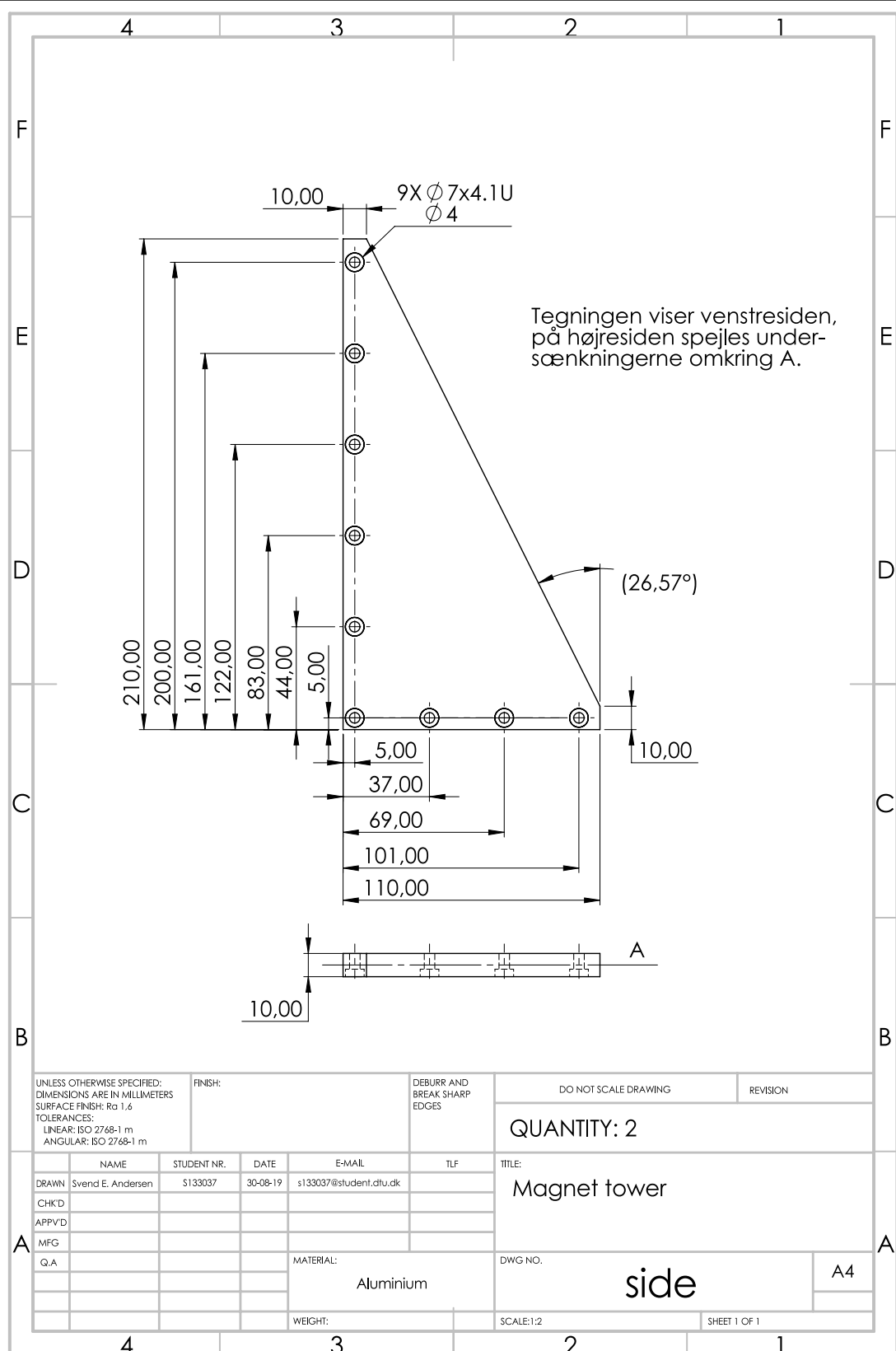


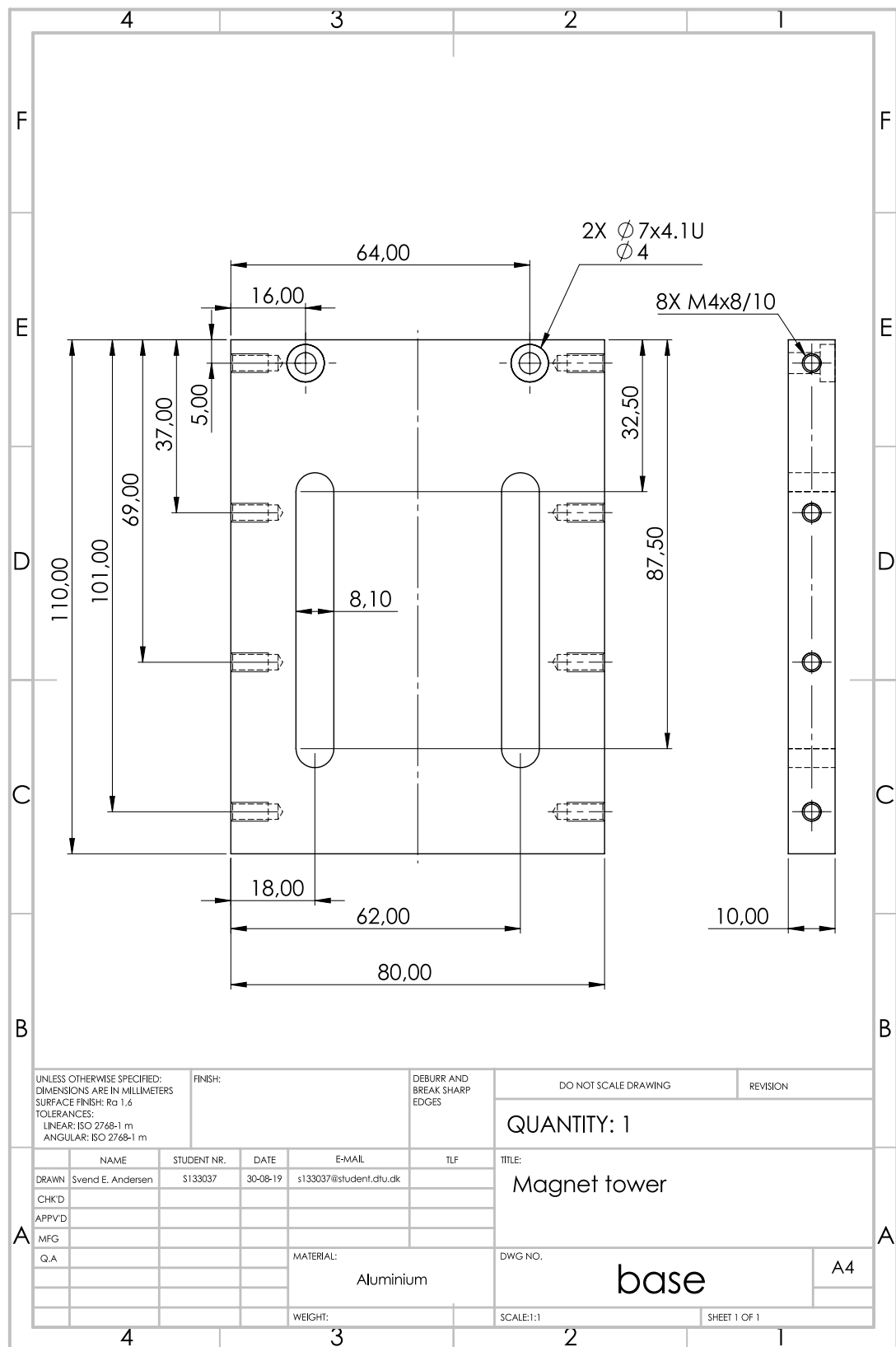


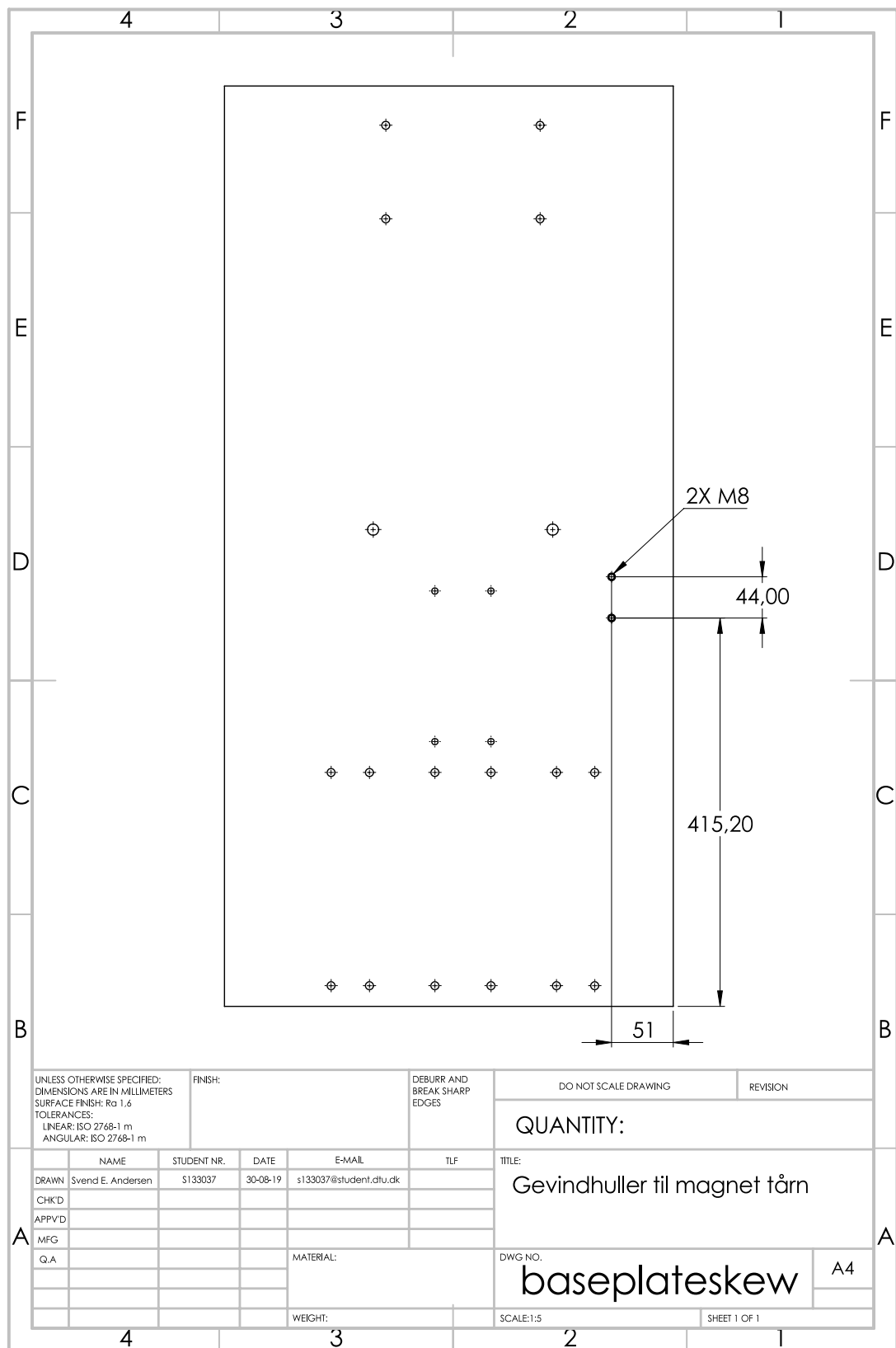
C.4 Excitation Magnet Tower







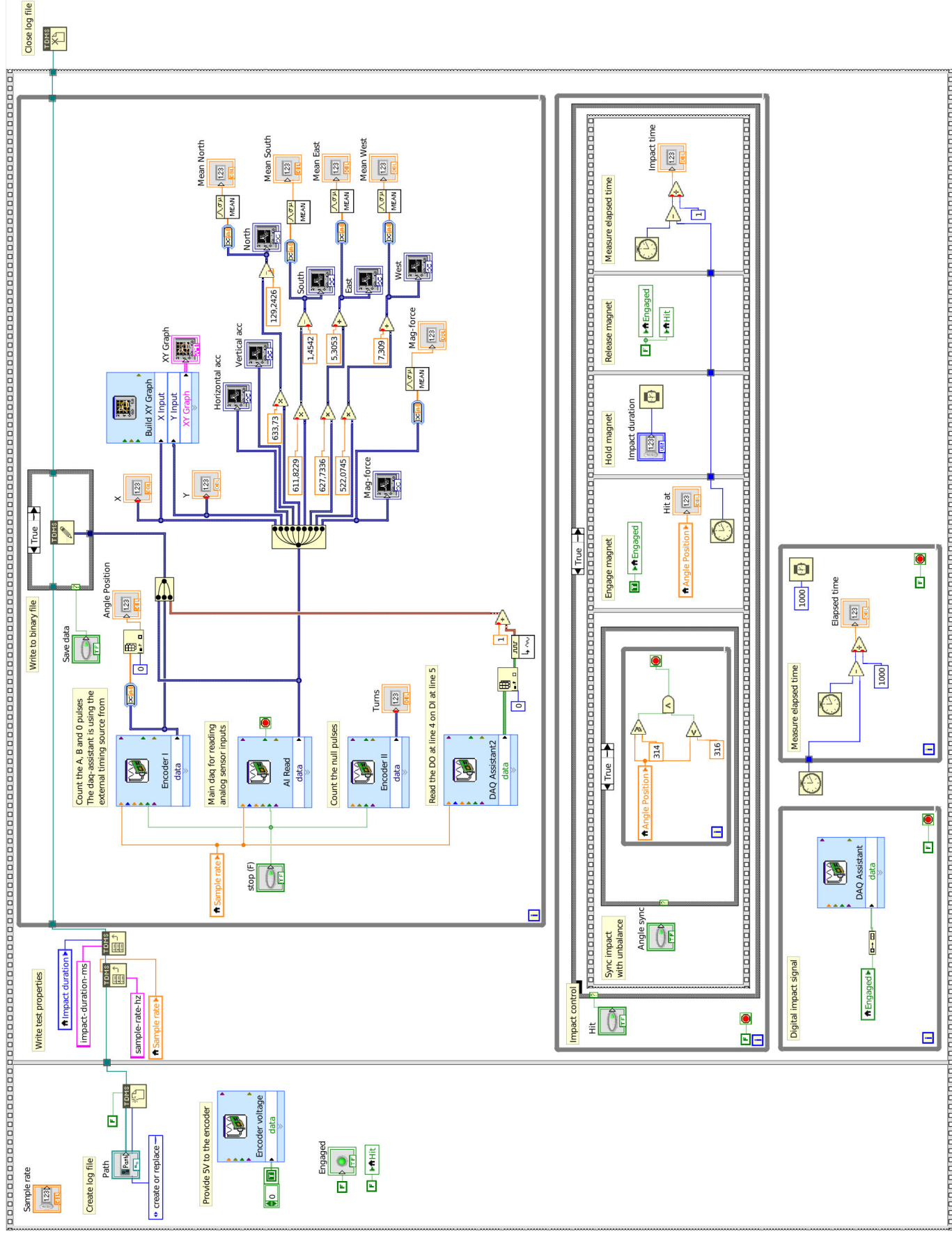




Appendix D

Code

D.1 G-code (LabVIEW)



D.2 Rigid Equations of Motion

```
> restart
> with(LinearAlgebra) : with(ArrayTools) : with(CodeGeneration) :
> interface(rttablesize = 25) :
```

Impact House Derivation

Newton's second law

```
> eq_sys := Matrix(7, 2) :
# Initiate matrix containing the lhs and rhs as 1. and 2. column, respectively.
> eq_sys(4, 1) := x_ih_dd : eq_sys(4, 2) :=  $\frac{1}{m_{ih}} \cdot (F_{cx} - k_{vg} \cdot (x_{ih} - x_{mh}) - d_{vg} \cdot (x_{ih\_d} - x_{mh\_d}))$  :
eq_sys(5, 1) := y_ih_dd : eq_sys(5, 2) :=  $\frac{1}{m_{ih}} \cdot (F_{cy} - 2 \cdot k_{ft1} \cdot (y_{ih} - y_{mh}))$  :
eq_sys(6, 1) := x_mh_dd : eq_sys(6, 2) :=  $\frac{1}{m_{mh}} \cdot (k_{vg} \cdot (x_{ih} - x_{mh}) + d_{vg} \cdot (x_{ih\_d} - x_{mh\_d}) - 2 \cdot k_{ft2} \cdot x_{mh})$  :
eq_sys(7, 1) := y_mh_dd : eq_sys(7, 2) :=  $\frac{1}{m_{mh}} \cdot (-k_{hg} \cdot y_{mh} - d_{hg} \cdot y_{mh\_d} + 2 \cdot k_{ft1} \cdot (y_{ih} - y_{mh}))$  :
```

Shaft Derivation

Transformation matrices

From inertial to B1:

$$\mathbf{T}_\Gamma := \Gamma \rightarrow \begin{bmatrix} 1 & 0 & 0 \\ 0 & \cos(\Gamma) & \sin(\Gamma) \\ 0 & -\sin(\Gamma) & \cos(\Gamma) \end{bmatrix} : \mathbf{T}_\beta := \beta \rightarrow \begin{bmatrix} \cos(\beta) & 0 & -\sin(\beta) \\ 0 & 1 & 0 \\ \sin(\beta) & 0 & \cos(\beta) \end{bmatrix} :$$

From B2 to B3:

$$\mathbf{T}_\theta := \theta \rightarrow \begin{bmatrix} \cos(\theta) & \sin(\theta) & 0 \\ -\sin(\theta) & \cos(\theta) & 0 \\ 0 & 0 & 1 \end{bmatrix} :$$

Angular velocities of reference frames

$$\mathbf{\Gamma}_{dot} := \begin{bmatrix} \Gamma_d \\ 0 \\ 0 \end{bmatrix} : \mathbf{\beta}_{dot} := \begin{bmatrix} 0 \\ \beta_d \\ 0 \end{bmatrix} : \mathbf{\theta}_{dot} := \begin{bmatrix} 0 \\ 0 \\ \theta_d \end{bmatrix} :$$

Position vectors defined in the B2 frame

$$> r_{OG} := \begin{bmatrix} 0 \\ 0 \\ l_{OG} \end{bmatrix}; r_{OM} := \begin{bmatrix} 0 \\ 0 \\ l_{OM} \end{bmatrix}; r_{OD} := \begin{bmatrix} 0 \\ 0 \\ l_{OD} \end{bmatrix}; r_{OC} := \begin{bmatrix} 0 \\ 0 \\ l_{OC} \end{bmatrix}; r_{OE} := \begin{bmatrix} 0 \\ 0 \\ l_{OE} \end{bmatrix};$$

Absolute angular velocity of reference frame B2

$$> \Omega_{B2} := T_\beta(\beta) \cdot T_\Gamma(\Gamma) \cdot \Gamma_{dot} + T_\beta(\beta) \cdot \beta_{dot}$$

$$\Omega_{B2} := \begin{bmatrix} \cos(\beta) \Gamma_d \\ \beta_d \\ \sin(\beta) \Gamma_d \end{bmatrix} \quad (1)$$

Absolute angular velocity of the rotor in reference frame B2

$$> \omega_{B2} := \Omega_{B2} + \theta_{dot}$$

$$\omega_{B2} := \begin{bmatrix} \cos(\beta) \Gamma_d \\ \beta_d \\ \sin(\beta) \Gamma_d + \theta_d \end{bmatrix} \quad (2)$$

Absolute angular acceleration of the rotor in reference frame B2

$$> \# \omega_{dot_B2} = \frac{d}{dt}(\omega_{B2}) + \Omega_{B2} \times \omega_{B2}$$

$$> \omega_{dot_B2} := \text{simplify} \left(\begin{bmatrix} \Gamma_{dd} \cdot \cos(\beta) - \sin(\beta) \cdot \Gamma_d \cdot \beta_d \\ \beta_{dd} \\ \Gamma_{dd} \cdot \sin(\beta) + \cos(\beta) \cdot \Gamma_d \cdot \beta_d + \theta_{dd} \end{bmatrix} + \Omega_{B2} \times \omega_{B2} \right)$$

$$\omega_{dot_B2} := \begin{bmatrix} \Gamma_{dd} \cos(\beta) - \beta_d (\sin(\beta) \Gamma_d - \theta_d) \\ -\cos(\beta) \Gamma_d \theta_d + \beta_{dd} \\ \Gamma_{dd} \sin(\beta) + \cos(\beta) \Gamma_d \beta_d + \theta_{dd} \end{bmatrix} \quad (3)$$

Forces and Euler's Equation

Unbalance force

Restoring- and damping force from PMB

$$> F_{unb} := \begin{bmatrix} m\theta \cdot e_x \cdot \theta_d^2 \\ m\theta \cdot e_y \cdot \theta_d^2 \\ 0 \end{bmatrix} : F_{pmb} := \begin{bmatrix} -k_{xx} \cdot l_{OM} \cdot \beta + k_{xy} \cdot l_{OM} \cdot \Gamma \\ k_{yy} \cdot l_{OM} \cdot \Gamma - k_{yx} \cdot l_{OM} \cdot \beta \\ 0 \end{bmatrix} + \begin{bmatrix} -d_{xx} \cdot l_{OM} \cdot \beta_d \\ d_{yy} \cdot l_{OM} \cdot \Gamma_d \\ 0 \end{bmatrix} :$$

Contact force

Excitation force

$$> F_c := \begin{bmatrix} -F_{cx} \\ -F_{cy} \\ 0 \end{bmatrix} : F_{exc} := \begin{bmatrix} F_{excx} \\ F_{excy} \\ 0 \end{bmatrix} :$$

Moment of inertia

$$> I_{0_B2} := \begin{bmatrix} I_{xx} & 0 & 0 \\ 0 & I_{yy} & 0 \\ 0 & 0 & I_{zz} \end{bmatrix} :$$

Perform the following summation of moments : $\sum M = I \cdot \frac{d}{dt}(\omega) + \Omega \times (I \cdot \omega) + r_{OG} \times (m_{tot} \cdot a)$

$$\begin{aligned} > rotor_eq := & r_{OC} \times (T_\beta(\beta) \cdot (T_\Gamma(\Gamma) \cdot F_c)) + r_{OM} \times (T_\beta(\beta) \cdot (T_\Gamma(\Gamma) \cdot F_{pmb})) + r_{OD} \\ & \times (Transpose(T_\theta(\theta)) \cdot F_{unb}) + r_{OE} \times (T_\beta(\beta) \cdot (T_\Gamma(\Gamma) \cdot F_{exc})) = I_{0_B2} \\ & \cdot \begin{bmatrix} \Gamma_{dd} \cdot \cos(\beta) - \sin(\beta) \cdot \Gamma_d \cdot \beta_d \\ \beta_{dd} \\ \Gamma_{dd} \cdot \sin(\beta) + \cos(\beta) \cdot \Gamma_d \cdot \beta_d + \theta_{dd} \end{bmatrix} + \Omega_{B2} \times (I_{0_B2} \cdot \omega_{B2}) + r_{OG} \times \left(m \cdot \begin{bmatrix} 0 \\ 0 \\ 0 \end{bmatrix} \right) : \end{aligned}$$

Add the rotor subsystem to the grand equation system

$$\begin{aligned} > eq_sys(1, 1) := & lhs(rotor_eq(1)) : eq_sys(1, 2) := rhs(rotor_eq(1)) : \\ eq_sys(2, 1) := & lhs(rotor_eq(2)) : eq_sys(2, 2) := rhs(rotor_eq(2)) : \\ eq_sys(3, 1) := & lhs(rotor_eq(3)) : eq_sys(3, 2) := rhs(rotor_eq(3)) : \end{aligned}$$

Solve the equation system

$$> solve(\{seq(eq_sys(i, 1) = eq_sys(i, 2), i = 1 .. 7)\}, \{\Gamma_{dd}, \beta_{dd}, \theta_{dd}, x_ih_dd, y_ih_dd, x_mh_dd, y_mh_dd\}) : assign(\%)$$

Print the equations of motion,

$$\begin{aligned}
 > \Gamma_{dd}' &= \Gamma_{dd}; \beta_{dd}' = \beta_{dd}; \theta_{dd}' = \theta_{dd}; x_{ih, dd}' = x_ih_dd; y_{ih, dd}' = y_ih_dd; x_{mh, dd}' = x_mh_dd; \\
 &y_{mh, dd}' = y_mh_dd; \\
 \Gamma_{dd} &= \frac{1}{I_{xx} \cos(\beta)} \left(-\cos(\theta) e_y l_{OD} m0 \theta_d^2 - \sin(\theta) e_x l_{OD} m0 \theta_d^2 - \Gamma \cos(\Gamma) k_{yy} l_{OM}^2 \right. \\
 &\quad + \cos(\Gamma) \beta k_{yx} l_{OM}^2 - \cos(\Gamma) d_{yy} l_{OM}^2 \Gamma_d + I_{xx} \sin(\beta) \beta_d \Gamma_d + \sin(\beta) \Gamma_d I_{yy} \beta_d \\
 &\quad \left. - I_{zz} \sin(\beta) \beta_d \Gamma_d + l_{OC} \cos(\Gamma) F_{cy} - l_{OE} \cos(\Gamma) F_{excy} - I_{zz} \beta_d \theta_d \right) \\
 \beta_{dd} &= -\frac{1}{I_{yy}} \left(-\Gamma \sin(\beta) \sin(\Gamma) k_{yy} l_{OM}^2 + \sin(\beta) \sin(\Gamma) \beta k_{yx} l_{OM}^2 \right. \\
 &\quad - \sin(\beta) \sin(\Gamma) d_{yy} l_{OM}^2 \Gamma_d - \cos(\theta) e_x l_{OD} m0 \theta_d^2 + \sin(\theta) e_y l_{OD} m0 \theta_d^2 \\
 &\quad - \Gamma \cos(\beta) k_{xy} l_{OM}^2 + \sin(\beta) \Gamma_d^2 I_{xx} \cos(\beta) - I_{zz} \cos(\beta) \sin(\beta) \Gamma_d^2 \\
 &\quad + \cos(\beta) \beta k_{xx} l_{OM}^2 + \cos(\beta) \beta_d d_{xx} l_{OM}^2 + F_{cy} \sin(\beta) \sin(\Gamma) l_{OC} \\
 &\quad \left. - F_{excy} \sin(\beta) \sin(\Gamma) l_{OE} - I_{zz} \cos(\beta) \Gamma_d \theta_d + F_{cx} \cos(\beta) l_{OC} - F_{excx} \cos(\beta) l_{OE} \right) \\
 \theta_{dd} &= -\frac{1}{I_{xx} \cos(\beta) I_{zz}} \left(-I_{zz} \sin(\beta) \cos(\theta) e_y l_{OD} m0 \theta_d^2 - I_{zz} \sin(\beta) \sin(\theta) e_x l_{OD} m0 \theta_d^2 \right. \\
 &\quad - \Gamma I_{zz} \sin(\beta) \cos(\Gamma) k_{yy} l_{OM}^2 + I_{zz} \sin(\beta) \cos(\Gamma) \beta k_{yx} l_{OM}^2 \\
 &\quad - I_{zz} \sin(\beta) \cos(\Gamma) d_{yy} l_{OM}^2 \Gamma_d - \cos(\beta)^2 \Gamma_d \beta_d I_{xx}^2 + \cos(\beta)^2 \Gamma_d \beta_d I_{xx} I_{yy} \\
 &\quad + \cos(\beta)^2 \Gamma_d \beta_d I_{xx} I_{zz} + I_{xx} I_{zz} \sin(\beta)^2 \beta_d \Gamma_d + I_{yy} I_{zz} \sin(\beta)^2 \beta_d \Gamma_d \\
 &\quad - I_{zz}^2 \sin(\beta)^2 \beta_d \Gamma_d + F_{cy} I_{zz} \sin(\beta) \cos(\Gamma) l_{OC} - F_{excy} I_{zz} \sin(\beta) \cos(\Gamma) l_{OE} \\
 &\quad \left. - I_{zz}^2 \sin(\beta) \beta_d \theta_d \right) \\
 x_{ih, dd} &= \frac{-d_vg x_ih_d + d_vg x_mh_d - k_vg x_ih + k_vg x_mh + F_cx}{m_ih} \\
 y_{ih, dd} &= \frac{-2 k_ft1 y_ih + 2 k_ft1 y_mh + F_cy}{m_ih} \\
 x_{mh, dd} &= \frac{d_vg x_ih_d - d_vg x_mh_d - 2 k_ft2 x_mh + k_vg x_ih - k_vg x_mh}{m_mh} \\
 y_{mh, dd} &= -\frac{d_hg y_mh_d - 2 k_ft1 y_ih + 2 k_ft1 y_mh + k_hg y_mh}{m_mh} \tag{4}
 \end{aligned}$$

Transform to system of first-order equations to be used in MATLAB

Define substitutions

```
> subvars :=  $\Gamma_d = \text{gamma\_d}, \theta_d = \text{theta\_d}, \beta_d = \text{beta\_d}, l_{OD} = l_{OD}, l_{OM} = l_{OM}, l_{OG} = l_{OG}, l_{OC}$   

 $= l_{OC}, l_{OE} = l_{OE}, F_{cy} = F_{cy}, F_{cx} = F_{cx}, I_{xx} = I_{xx}, I_{yy} = I_{yy}, I_{zz} = I_{zz}, k_{xx} = k_{xx}, k_{yy}$   

 $= k_{yy}, k_{xy} = k_{xy}, k_{yx} = k_{yx}, d_{xx} = d_{xx}, d_{yy} = d_{yy}, F_{excx} = F_{excx}, F_{excy} = F_{excy}, e_x = e_x,$   

 $e_y = e_y :$   

> subfirstorder :=  $\Gamma = y(1), \text{gamma\_d} = y(2), \beta = y(3), \text{beta\_d} = y(4), \theta = y(5), \text{theta\_d} = y(6),$   

 $x_{ih} = y(7), x_{ih\_d} = y(8), y_{ih} = y(9), y_{ih\_d} = y(10), x_{mh} = y(11), x_{mh\_d} = y(12),$   

 $y_{mh} = y(13), y_{mh\_d} = y(14) :$   

> subvars := subvars, subfirstorder :
```

Generate MATLAB code:

```
> y_dot2 := Matlab(subs(subvars,  $\Gamma_{dd}$ ), resultname = "cg", output = string) :  

y_dot4 := Matlab(subs(subvars,  $\beta_{dd}$ ), resultname = "cg", output = string) :  

y_dot6 := Matlab(subs(subvars,  $\theta_{dd}$ ), resultname = "cg", output = string) :  

y_dot8 := Matlab(subs(subvars,  $x_{ih\_dd}$ ), resultname = "cg", output = string) :  

y_dot10 := Matlab(subs(subvars,  $y_{ih\_dd}$ ), resultname = "cg", output = string) :  

y_dot12 := Matlab(subs(subvars,  $x_{mh\_dd}$ ), resultname = "cg", output = string) :  

y_dot14 := Matlab(subs(subvars,  $y_{mh\_dd}$ ), resultname = "cg", output = string) :
```

The following "code edit region" writes the eq. of motion to the MATLAB file "dydt.m"

```

1 with(StringTools):
2 fname := "dydt.m":
3 FileTools[Text][Open](fname):
4 fcontent := "":
5 # Get number of lines
6 line_num := FileTools[Text][CountLines](fname):
7 for i from 1 to line_num do
8   cur_line := FileTools[Text][ReadLine](fname):
9   fcontent := cat(fcontent,cur_line,"\\n"):
10  if cur_line[1..11] = "% * * * *" then
11    FileTools[Remove](fname):
12    FileTools[Text][WriteString](fname,fcontent);
13    FileTools[Text][WriteString](fname,cat(
14      " y_dot(1) = y(2);\\n", " y_dot(2) = ",y_dot2[6 .. length(y_dot2)],
15      " y_dot(3) = y(4);\\n", " y_dot(4) = ",y_dot4[6 .. length(y_dot4)],
16      " y_dot(5) = y(6);\\n", " y_dot(6) = ",y_dot6[6 .. length(y_dot6)],
17      " y_dot(7) = y(8);\\n", " y_dot(8) = ",y_dot8[6 .. length(y_dot8)],
18      " y_dot(9) = y(10);\\n", " y_dot(10) = ",y_dot10[6 .. length(y_dot10)],
19      " y_dot(11) = y(12);\\n", " y_dot(12) = ",y_dot12[6 .. length(y_dot12)],
20      " y_dot(13) = y(14);\\n", " y_dot(14) = ",y_dot14[6 .. length(y_dot14)], "\\n",
21      " y_dot = y_dot';\\n\\nend\\n"));
22    FileTools[Text][WriteString](fname,cat("% Maple part last updated: ",
23      FormatTime("%d-%m-%Y %H:%M")));
24    break;
25  end if:
26 end do:
27
28 FileTools[Text][Close](fname);

```

D.3 MATLAB Code

D.3.1 Rigid Program

Besides the following pages, the entire repository of the program is available online on GitHub and can be found at the repository: github.com/SV3A/masterproject-contact-code. The procedding code is from the `be0bb7e` commit.

main2.m

```

1 % Master thesis F2019
2 % Numerical integration of analytical solution
3 % Svend E. Andersen
4 clc; clearvars; %close all
5
6 % Initiate simulation
7 sim = Simulator;
8 sim.fric_mod = 'ambrosio';
9
10 % Enable magnet

```

```

11 load('magnet-force/rot_sim_exp315.mat', 'exp')
12 sim.set_magnet(11.9, 240, exp)
13
14 % Initial conditions
15 sim.y_0(6) = -17*2*pi;
16
17 % Solve
18 sim.solve([0 12.1])
19
20 % Calculate forces etc.
21 sim.postprocess();
22
23 %sim.export('mat')
24
25 % Plot stuff
26 pt = Plottools();
27
28 %pt.orbit(sim.r_OD(1, :), sim.r_OD(2, :), sim.clearance)
29 %pt.lateral(sim.time, sim.r_OD(1, :), sim.r_OD(2, :))
30 %pt.indent(sim.time, sim.d, sim.event_times)
31 %pt.indentf(sim.time, sim.d, sim.fn, sim.event_times)
32 %pt.states(sim.time, sim.solution(:, 1:2:end), {'\Gamma', '\beta', '\theta', ...
33 %'x_{ih}', 'y_{ih}', 'x_{oh}', 'y_{ih}'})

```

settings.toml (settings file)

```

1 [rotor]
2 radius = 12.5e-3    # Rotor radius [m]
3
4 I_xx = 7.085371e-2 # Mass moment of inertia component [kg*m^2]
5 I_yy = 7.085371e-2 # Mass moment of inertia component [kg*m^2]
6 I_zz = 0.106132e-2 # Mass moment of inertia component [kg*m^2]
7
8 k_xx = 3.09e4        # Stiffness of the magnetic bearing in x [N/m]
9 k_yy = 3.09e4        # Stiffness of the magnetic bearing in y [N/m]
10 k_xy = -2.456e3     # Cross stiffness term [N/m]
11 k_yx = -292          # Cross stiffness term [N/m]
12
13 d0_xx = 40.9        # Damping coefficient in x at theta = 0 [N*s/m]
14 d_xx   = 8.48         # Damping coefficient in x [N*s/m]
15 d_yy   = 7.7          # Damping coefficient in y [N*s/m]
16
17 l_OM = 171.7e-3      # Position vector, pivot point to the PMB [m]
18 l_OG = 195.9e-3      # Position vector, pivot point to centre of gravity [m]
19 l_OD = 259.7e-3      # Position vector, pivot point to the disc [m]
20 l_OC = 428.7e-3      # Position vector, pivot point to contact point [m]
21 l_OE = 72.5e-3       # Position vector, pivot point to excitation point [m]
22
23 [houses]
24 radius = 14.5e-3     # Stator radius [m]
25
26 m_ih = 1.79          # Inner house mass [kg]

```

```

27 m_mh = 8.44           # Middle house mass [kg]
28
29 k_ft1 = 8.42e6        # Stiffness of the force transducer [N/m]
30 k_ft2 = 1.26e7        # Stiffness of the force transducer [N/m]
31
32 k_vg = 9.709e8        # Stiffness of vertical beams [N/m]
33 k_hg = 1.41e9         # Stiffness of horizontal beams [N/m]
34
35 d_vg = 2168           # Damping coefficient of vertical beams [Ns/m]
36 d_hg = 12983          # Damping coefficient of horizontal beams [Ns/m]
37
38 l_OIH = 428.7e-3      # Position vector, pivot point to inner house [m]
39 l_OMH = 428.7e-3      # Position vector, pivot point to middle [m]
40
41 [unbalance]
42 e_x = 0.027           # Unbalance parameter [m]
43 e_y = -0.072          # Unbalance parameter [m]
44 m0 = 1e-3              # Unbalance mass [kg]

```

Simulator.m

```

1 classdef Simulator < handle
2 % 'Simulator' is a class defining a interface for simulating the rotor-stator
3 % system.
4
5 properties
6     % Solution properties
7
8     time           % Time
9     solution       % Solution
10    event_times    % Event times
11    contact_states % Contact state vector
12    y_0            % Initial condition vector
13
14    % Model objects
15
16    s               % Rotor-stator system
17    cmod           % Contact model
18
19    % Model properties
20
21    fric_mod       % Friction model
22    clearance       % Static clearance between the rotor and stator
23
24    % External excitation magnet
25
26    mag_enabled; % Boolean for knowing if the magnet has been enabled
27    mag_app_t; % Absolute time, rel. to sim. start, of when to apply the magnet
28    mag_app_angle; % Angle to sync the magnet application with
29    mag_forcedata; % Force data nx2 vector containing time [s] force [N]
30
31    % Derived parameters

```

```
32
33     r_OC      % Position vector of the rotor centre in the contact plane in I
34     r_OD      % Position vector of the rotor centre in the disc plane in I
35     s_OC      % Position vector of the stator centre in the contact plane in I
36     F_c       % Contact force vector
37     fn        % Magnitude of the normal force
38     d         % Radial indentation
39
40     % Solver tolerances
41
42     o45_reltol % Relative tolerance for the ode45 solver
43     o45_abstol % Absolute tolerance for the ode45 solver
44     o15_reltol % Relative tolerance for the ode15s solver
45     o15_abstol % Absolute tolerance for the ode15s solver
46 end
47
48
49 methods
50
51     function obj = Simulator()
52         % Constructor function.
53
54         % Set default solver tolerances
55         obj.o45_reltol = 1e-9;
56         obj.o45_abstol = 1e-9;
57         obj.o15_reltol = 1e-9;
58         obj.o15_abstol = 1e-9;
59
60         % Initial condition
61         obj.y_0 = zeros(14, 1);
62
63         obj.mag_enabled = false;
64 end
65
66
67 function set_magnet(obj, varargin)
68     % Enables the external excitation magnet and sets its properties.
69     %
70     % INPUT:
71     %   time : the rough point in time when to apply the magnet force
72     %   angle: (optional) the angle at which to apply the magnet
73     %   force: a nx2 vector containing the local time and force of the magnet
74
75     if ~obj.mag_enabled
76
77         % Handle optional arguments (note nargin is +1 due to object)
78         if nargin < 3
79             error('ERROR Not enough inputs supplied')
80         elseif nargin > 3
81             obj.mag_app_angle = varargin{2};
82             obj.mag_forcedata = varargin{3};
83         else
84             obj.mag_app_angle = 0;
```

```
85         obj.mag_forcedata = varargin{2};  
86     end  
87  
88     obj.mag_app_t = varargin{1};  
89  
90     if size(obj.mag_forcedata, 2) ~= 2  
91         error('ERROR Magnet force data not a vector of dimension nx2')  
92     end  
93  
94     obj.mag_enabled = true;  
95 else  
96     warning("Magnet already enabled, I'm ignoring this.")  
97 end  
98 end  
99  
100  
101 function ssolve(obj, tspan)  
102 % Performs the time integration using only the 15s solver.  
103  
104 % Init/clear  
105 obj.time          = 0;  
106 obj.solution      = [];  
107 obj.event_times   = [];  
108 obj.contact_states = 0;  
109  
110 % Initiate system object  
111 if obj.mag_enabled  
112     obj.s = Rotorsystem(obj.mag_app_t, obj.mag_app_angle, ...  
113                           obj.mag_forcedata);  
114 else  
115     obj.s = Rotorsystem();  
116 end  
117 obj.cmod = Nikravesh(obj.fric_mod, obj.s.r_s, obj.s.r_r);  
118  
119 % Solver options  
120 options_ode15 = odeset('RelTol', obj.o15_reltol, ...  
121                         'AbsTol', obj.o15_abstol, ...  
122                         'Events', @(t,y) impactDetect(t, y, obj.s, 0, 0));  
123  
124 tic  
125 [t, y, te] = ode15s(@(t,y) dydt(t, y, obj.s, obj.cmod, 0), tspan, ...  
126                         obj.y_0, options_ode15);  
127 toc  
128  
129 % Collect results  
130 obj.time      = [obj.time(1:end-1) ; t];  
131 obj.solution  = [obj.solution(1:end-1,:); y];  
132 obj.event_times = te;  
133  
134 % Find contact states  
135 for i = 1:size(y, 1)  
136     if obj.s.calc_indent(y(i,:)) <= 0  
         obj.contact_states(i) = 0;
```

```
138      else
139          obj.contact_states = 1;
140      end
141  end
142
143  fprintf('%i perimeter crossings detected\n', length(obj.event_times))
144 end
145
146 function solve(obj, tspan)
147 % Performs the time integration.
148
149 % Init/clear
150 obj.time = 0;
151 obj.solution = [];
152 obj.event_times = [];
153 obj.contact_states = 0;
154
155 % Initiate system objects
156 if obj.mag_enabled
157     obj.s = Rotorsystem(obj.mag_app_t, obj.mag_app_angle, ...
158                         obj.mag_forcedata);
159 else
160     obj.s = Rotorsystem();
161 end
162 obj.cmod = Nikravesh(obj.fric_mod, obj.s.r_s, obj.s.r_r);
163
164 % Solver options
165 options_ode45 = odeset('RelTol', obj.o45_reltol, ...
166                         'AbsTol', obj.o45_abstol, 'MaxStep', 1e-3, ...
167                         'Events', @(t,y) impactDetect(t, y, obj.s, 1, 1));
168
169 options_ode15 = odeset('RelTol', obj.o15_reltol, ...
170                         'AbsTol', obj.o15_abstol, ...
171                         'Events', @(t,y) impactDetect(t, y, obj.s, -1, 1));
172
173 loc_tst = tspan(1); % Integration time starting point
174 y0 = obj.y_0; % Initial condition
175
176 tic
177 while obj.time(end) ~= tspan(2)
178
179     indent = obj.s.calc_indent(y0);
180
181     if indent < 0 || (indent == 0 && obj.s.pen_rate(y0) < 0 )
182         contact_state = 0;
183         [t, y, te] = ode45(@(t,y) dydt(t, y, obj.s, obj.cmod, ...
184                             contact_state), [loc_tst, tspan(2)], y0, options_ode45);
185     else
186         contact_state = 1;
187         [t, y, te] = ode15s(@(t,y) dydt(t, y, obj.s, obj.cmod, ...
188                             contact_state), [loc_tst, tspan(2)], y0, options_ode15);
189     end
190
```

```

191      % Collect results
192      obj.time      = [obj.time(1:end-1)      ; t];
193      obj.solution = [obj.solution(1:end-1,:); y];
194      obj.contact_states = [obj.contact_states(1:end-1); ...
195                           contact_state*ones(length(t),1)];
196      obj.event_times = [obj.event_times; te];
197
198      % Assign new initial conditions
199      loc_tst = t(end);
200      y0      = y(end,:);
201
202      % Print feedback
203      fprintf('t_n = %f s\n', obj.time(end));
204  end
205  toc
206
207  fprintf('%i perimeter crossings detected\n', length(obj.event_times))
208 end
209
210
211 function postprocess(obj)
212 % Calculates the forces associated with a given solution.
213
214 % Check if solution is present
215 if isempty(obj.solution)
216     error('No solution present.')
217 end
218
219 % Init/clear
220 F_cxs    = zeros( length(obj.time), 1 );
221 F_cys    = zeros( length(obj.time), 1 );
222 obj.r_OC = zeros( 3, length(obj.time) );
223 obj.r_OD = zeros( 3, length(obj.time) );
224 obj.s_OC = zeros( 3, length(obj.time) );
225 obj.F_c  = zeros( 3, length(obj.time) );
226 obj.fn   = zeros( length(obj.time), 1 );
227 obj.d    = zeros( length(obj.time), 1 );
228
229 % Build orbit in I, get contact forces, retrieve the contact angle and get
230 % relative radial velocity
231 for i = 1:length(obj.time)
232     y_i = obj.solution(i,:);
233
234     T_gamma = obj.s.T_gam(obj.solution(i, 1));
235     T_beta  = obj.s.T_bet(obj.solution(i, 3));
236     obj.r_OC(:,i) = T_gamma' * (T_beta'*[0; 0; obj.s.l_OC]);
237     obj.r_OD(:,i) = T_gamma' * (T_beta'*[0; 0; obj.s.l_OD]);
238
239     if obj.contact_states(i) == 0, state = 0; else, state = 1; end
240
241     [F_cxs(i), F_cys(i)] = contactForce(y_i, obj.s, obj.cmod, state);
242
243     obj.d(i) = obj.s.calc_indent(y_i);

```

```
244     end
245
246     obj.F_c = [F_cxs'; F_cys'; zeros(1, size(obj.solution, 1))];
247
248     % Calculate resultant radial contact force
249     obj.fn = sqrt(F_cxs.^2 + F_cys.^2);
250
251     % Stator centre in the plane of contact
252     obj.s_OC = [obj.solution(:, 7)';
253                  obj.solution(:, 9)';
254                  zeros(1, size(obj.solution, 1))];
255
256     obj.clearance = obj.s.cl;
257 end
258
259
260 function export(obj, export_type)
261     % A handle for function to export the solution to a text file.
262
263     % Root of filename
264     fileroot = datestr(now, 'export-ddmm-HHMMss');
265
266     % Define parameter list
267     if strcmp(export_type, 'basic')
268         par_list = {'t', 'rotor_x', 'rotor_y', 'stator_x', 'stator_y', ...
269                     'theta', 'Fn', 'delta'};
270
271         value_vector = [obj.time'; obj.r_OD(1, :); obj.r_OD(2, :); ...
272                         obj.s_OC(1, :); obj.s_OC(2, :); obj.solution(:, 5)';
273                         obj.fn'; obj.d'];
274
275     elseif strcmp(export_type, 'all')
276         %par_list = {'t', 'rotor_x', 'rotor_y', 'stator_x', 'stator_y', ...
277                     '%theta', 'Fn', 'delta', 'x', 'y', 'z'};
278
279         %value_vector = [value_vector; x; y; z];
280     elseif strcmp(export_type, 'mat')
281         value_vector = [obj.time'; obj.r_OD(1, :); obj.r_OD(2, :); ...
282                         obj.s_OC(1, :); obj.s_OC(2, :); obj.solution(:, 5)';
283                         obj.fn'; obj.d'];
284
285         save([fileroot, '.mat'], 'value_vector')
286         return
287     else
288         error('ERROR Unknown export type.')
289     end
290
291     % Call external function
292     export_values(par_list, value_vector, [fileroot, '.txt'])
293 end
294
295 end % methods
296 end % class
```

Rotorsystem.m

```

1 classdef Rotorsystem < handle
2 % 'Rotorsystem' is a class containing all properties relevant to a particular
3 % rotor-dynamical system. The resulting object is pass-by-reference.
4 % The state vector substitution is given as:
5 %   y = [gamma, gamma_d, beta, beta_d, theta, theta_d,
6 %         x_ih, x_ih_d, y_ih, y_ih_d, x_mh, x_mh_d, y_mh, y_mh_d]^T
7
8 properties
9   r_r    % Rotor radius [m]
10  r_s    % Stator radius [m]
11
12  e_x    % Unbalance parameter [m]
13  e_y    % Unbalance parameter [m]
14  m0    % Unbalance mass [kg]
15
16  l_OM  % Position vector, pivot point to the PMB [m]
17  l_OG  % Position vector, pivot point to centre of gravity [m]
18  l_OD  % Position vector, pivot point to the disc [m]
19  l_OC  % Position vector, pivot point to contact point [m]
20  l_OE  % Position vector, pivot point to excitation point [m]
21
22  I_xx  % Mass moment of inertia component [kg*m^2]
23  I_yy  % Mass moment of inertia component [kg*m^2]
24  I_zz  % Mass moment of inertia component [kg*m^2]
25
26  k_xx  % Stiffness of the magnetic bearing in x [N/m]
27  k_yy  % Stiffness of the magnetic bearing in y [N/m]
28  k_xy  % Cross stiffness term [N/m]
29  k_yx  % Cross stiffness term [N/m]
30
31  d0_xx % Damping coefficient in x at theta = 0 [N*s/m]
32  d_xx  % Damping coefficient in x [N*s/m]
33  d_yy  % Damping coefficient in y [N*s/m]
34
35  l_OIH % Position vector, pivot point to inner house [m]
36  l_OMH % Position vector, pivot point to middle [m]
37
38  m_ih  % Inner house mass [kg]
39  m_mh  % Middle house mass [kg]
40
41  k_ft1 % Stiffness of the force transducer [N/m]
42  k_ft2 % Stiffness of the force transducer [N/m]
43
44  k_vg  % Stiffness of vertical beams [N/m]
45  k_hg  % Stiffness of horizontal beams [N/m]
46
47  d_vg  % Damping coefficient of vertical beams [Ns/m]
48  d_hg  % Damping coefficient of horizontal beams [Ns/m]
49
50  cl    % Clearance [m]
51
52  % External magnet

```

```
53
54     mag_enabled;    % Boolean for knowing if the magnet has been enabled
55     mag_app_t;      % Absolute time, rel. to sim. start, of when to apply the magnet
56     mag_app_angle;  % Angle to sync the magnet application with
57     mag_forcedata; % Force data nx2 vector containing time [s] force [N]
58     mag_flag;       % Boolean used to switch on the magnet wrt. angle
59 end
60
61
62 methods
63     function obj = Rotorsystem(mag_app_t, mag_app_angle, mag_forcedata)
64         % Constructor function.
65         % INPUT:
66
67         % Read the settings file
68         obj.read_settings('settings.toml');
69
70         % Calculate clearance
71         obj.cl = obj.r_s - obj.r_r;
72
73         % Handle external excitation
74         if nargin > 0
75
76             % Set trigger time and magnet flag
77             obj.mag_enabled = true;
78             obj.mag_flag = false;
79             obj.mag_app_t = mag_app_t;
80             obj.mag_app_angle = mag_app_angle;
81             obj.mag_forcedata = mag_forcedata;
82         else
83             obj.mag_enabled = false;
84         end
85     end
86
87
88     function T_gamma = T_gam(~, gamma)
89         % Transformation matrix from I to B1
90
91         T_gamma = [1          0          0
92                    0 cos(gamma) sin(gamma)
93                    0 -sin(gamma) cos(gamma)];
94     end
95
96
97     function T_beta = T_bet(~, beta)
98         % Transformation matrix from B1 to B2
99
100        T_beta = [cos(beta) 0 -sin(beta)
101                  0      1      0
102                  sin(beta) 0  cos(beta)];
103    end
104
105
```

```
106     function T_theta = T_the(~, theta)
107         % Transformation matrix from B2 to B3
108
109         T_theta = [ cos(theta) sin(theta) 0
110                     -sin(theta) cos(theta) 0
111                         0             0             1];
112     end
113
114
115     function r_OR = rot_centrepos(obj, y)
116         % Gets position of the rotor centre in the contact plane in the inertial
117         % coordinate system.
118         %
119         % INPUT:
120         %   y: State vector.
121
122         r_OR = obj.T_gam(y(1))' * (obj.T_bet(y(3))' * [0; 0; obj.l_OC]);
123     end
124
125
126     function indent = calc_indent(obj, y)
127         % Calculates the size of the indent between the rotor and stator.
128         %
129         % INPUT:
130         %   y: State vector.
131         %
132         % OUTPUT:
133         %   indent: The size of the 'indent', where the indent is represented as
134         %   the rotor centre position minus the clearance, thus the output is
135         %   negative when the rotor is not in contact with the stator, and
136         %   positive otherwise, during which the output signifies the penetration
137         %   of the rotor into the stator material.
138
139         % Get rotor centre position
140         r_OR = obj.rot_centrepos(y);
141
142         % Calculate the effective clearance (or penetration)
143         indent = sqrt( (r_OR(1)-y(7))^2 + (r_OR(2)-y(9))^2 ) - obj.cl;
144     end
145
146
147     function alpha = contact_ang(obj, y)
148         % Calculates the contact angle between houses and rotor.
149         %
150         % INPUT:
151         %   y: State vector.
152
153         % Get rotor centre position
154         r_OR = obj.rot_centrepos(y);
155
156         alpha = atan2(r_OR(2)-y(9), r_OR(1)-y(7));
157     end
158
```

```
159     function v_rc = rotor_linvel(obj, y)
160         % Calculates the linear velocity of the rotor centre in
161         % the inertial coordinate system.
162         % INPUT:
163         %   y: State vector.
164
165         % Absolute angular velocity of the reference frame B2
166         Omega_B2 = obj.T_bet(y(3)) * obj.T_gam(y(1)) * [y(2); 0; 0] + ...
167                         obj.T_bet(y(3)) * [0; y(4); 0];
168
169         % Absolute linear velocity of the rotor centre in the contact plane
170         v_rc = obj.T_gam(y(1))' * (obj.T_bet(y(3))' * ...
171                         cross( Omega_B2, [0; 0; obj.l_OC] ));
172     end
173
174
175     function v_rel = abs_rel_velocity(obj, y)
176         % Calculates the relative velocity between the rotor and
177         % the stator in the inertial coordinate system.
178         % INPUT:
179         %   y: State vector.
180
181         v_rel = obj.rotor_linvel(y) - [y(7); y(9); 0];
182     end
183
184
185     function vt_rel = tan_rel_velocity(obj, y)
186         % Calculates the tangential component of the relative
187         % velocity between the rotor and stator.
188         % INPUT:
189         %   y: State vector.
190
191         v_rel = obj.abs_rel_velocity(y);
192
193         % Get contact angle between rotor and inner house
194         alpha = obj.contact_ang(y);
195
196         vt_rel = obj.r_r*y(6) - v_rel(1)*sin(alpha) + v_rel(2)*cos(alpha);
197     end
198
199
200     function [delta_d, v_rel_r] = pen_rate(obj, y)
201         % Calculates the penetration rate.
202         % INPUT:
203         %   y: State vector.
204
205         % Get contact angle between rotor and inner house
206         alpha = obj.contact_ang(y);
207
208         % Unit vector in the radial direction
209         e_r = [cos(alpha); sin(alpha); 0];
210
211         % Relative velocity between the rotor and the inner house (stator)
```

```
212     v_rel = obj.abs_rel_velocity(y);
213
214     % Projection onto the radial direction
215     v_rel_r = dot(v_rel, e_r)*e_r;
216
217     % Determine direction of the indentation rate
218     if sign(v_rel_r(1)) == sign(e_r(1)) && sign(v_rel_r(2)) == sign(e_r(2))
219         dir = 1;
220     else
221         dir = -1;
222     end
223
224     % Penetration rate, i.e. the magnitude of the radial velocity
225     delta_d = norm(v_rel_r)*dir;
226 end
227
228
229 function [F_excx, F_excy] = magnetForce(obj, t, y)
230
231     % Delivers the force from the external electro magnet if the time 't' is
232     % between the application time and the current time + the length of the
233     % external magnet force data, apply the magnet (if theta = 0) else if
234     % rotating, then check the angle. When the angle crosses the threshold
235     % switch the magnet on and interpolate the force from the external data
236     % with respect to the 'local' time, i.e. 't - t_magapply'.
237
238     if t >= obj.mag_app_t && t < obj.mag_app_t + obj.mag_forcedata(end, 1)
239
240         if ~obj.mag_flag
241
242             % Are we rotating? Yes: sync with angle, no: just switch on the magnet
243             if abs(y(6)) > 0
244
245                 % Calculate the instantaneous angle
246                 angle = 360 * (abs(y(5))/(2*pi) - floor(abs(y(5))/(2*pi)));
247
248                 % Apply magnet when the current angle crosses the specified angle
249                 if angle > obj.mag_app_angle && angle < obj.mag_app_angle+2 && ...
250                     ~obj.mag_flag
251
252                     obj.mag_flag = true;
253                     fprintf('Applied the magnet at %.2f deg\n', angle)
254                 end
255             else
256                 obj.mag_flag = true;
257                 fprintf('Applied the magnet at t = %.2f\n', t)
258             end
259         end
260
261         % When magnet applied interpolate force
262         if obj.mag_flag
263             F_excx = interp1(obj.mag_forcedata(:, 1), obj.mag_forcedata(:, 2), ...
264                             t - obj.mag_app_t);
265             F_excy = 0;
```

```
265         return
266     end
267 end
268
269 F_excx = 0;
270 F_excy = 0;
271
272 end
273 % public methods
274
275
276 methods (Access = protected)
277     function read_settings(obj, filepath)
278         % Read the settings file and populate the properties of this class
279
280         d = toml.read(filepath);
281
282         obj.r_r    = d.rotor.radius;
283         obj.r_s    = d.houses.radius;
284         obj.e_x    = d.unbalance.e_x;
285         obj.e_y    = d.unbalance.e_y;
286         obj.m0     = d.unbalance.m0;
287         obj.l_OM   = d.rotor.l_OM;
288         obj.l_OG   = d.rotor.l_OG;
289         obj.l_OD   = d.rotor.l_OD;
290         obj.l_OC   = d.rotor.l_OC;
291         obj.l_OE   = d.rotor.l_OE;
292         obj.I_xx   = d.rotor.I_xx;
293         obj.I_yy   = d.rotor.I_yy;
294         obj.I_zz   = d.rotor.I_zz;
295         obj.k_xx   = d.rotor.k_xx;
296         obj.k_yy   = d.rotor.k_yy;
297         obj.k_xy   = d.rotor.k_xy;
298         obj.k_yx   = d.rotor.k_yx;
299         obj.d0_xx  = d.rotor.d0_xx;
300         obj.d_xx   = d.rotor.d_xx;
301         obj.d_yy   = d.rotor.d_yy;
302         obj.l_OIH  = d.houses.l_OIH;
303         obj.l_OMH  = d.houses.l_OMH;
304         obj.m_ih   = d.houses.m_ih;
305         obj.m_mh   = d.houses.m_mh;
306         obj.k_ft1  = d.houses.k_ft1;
307         obj.k_ft2  = d.houses.k_ft2;
308         obj.k_vg   = d.houses.k_vg;
309         obj.k_hg   = d.houses.k_hg;
310         obj.d_vg   = d.houses.d_vg;
311         obj.d_hg   = d.houses.d_hg;
312
313     end % private methods
314 end % class
```

Contactmodels.m

```
1 classdef Contactmodels < handle
2 % 'Contactmodel' is a class containing all properties relevant to contact
3 % models between a rotor and a stator.
4 % The resulting object is pass-by-reference.
5
6 properties (SetAccess = protected)
7     name % Name of the contact model
8 end
9
10
11 properties
12     mu_k          % Friction coefficient
13     v_0 = 1e-4;   % Lower velocity tolerance [m/s]
14     v_1 = 2e-4;   % Upper velocity tolerance [m/s]
15     calc_ff
16 end
17
18
19 methods
20
21     function obj = Contactmodels(friction_model)
22         % Constructor function.
23         % INPUT:
24         % friction_model: Parameter defining which friction model to use
25
26         obj.mu_k = 0.2;
27
28         % Assign function handle for the friction model
29         if strcmp(friction_model, 'ambrosio')
30             obj.calc_ff = @obj.calc_ff_ambrosio;
31         elseif strcmp(friction_model, 'none')
32             obj.calc_ff = @(~, ~) 0;
33         else
34             error('Invalid friction model')
35         end
36     end
37
38
39     function Ff = calc_ff_ambrosio(obj, Fn, vt_rel)
40         % Implements the friction model set forth in the article:
41         % "Influence of the contact-impact force model on the dynamic response
42         % of multi-body systems"
43         % In: Proc. IMechE, Year 2006, Volume 220.
44         % By: Flores, P. and Ambrosio, J. and Claro, J. C. P. and
45         % Lankarani, H. M.
46         %
47         % INPUT:
48         % Fn: Normal force (scalar)
49         % vt_rel: Relative tangential velocity
50
51         % Dynamical correction coefficient, this makes the friction force
52         % disappear close to 0 velocity, and introduces a linear increase from
```

```

53      % this 0 niveau to static values
54      if (obj.v_1 < norm(vt_rel))
55          n_d = 1;
56      elseif obj.v_0 < norm(vt_rel) & norm(vt_rel) <= obj.v_1
57          n_d = (norm(vt_rel) - obj.v_0)/(obj.v_1 - obj.v_0);
58      elseif norm(vt_rel) <= obj.v_0
59          n_d = 0;
60      end
61
62      % Magnitude of the friction force (notice the sign follows the velocity)
63      % | ____ + Ff
64      % _|_/
65      % - Ff ____/ |
66      % -----|----- v
67      % - 0 +
68      Ff = Fn * obj.mu_k * sign(vt_rel) * n_d;
69  end
70
71 end
72
73
74 methods (Access = protected)
75
76     function print_name(obj)
77         % Displays the current contact model in the console.
78         fprintf('Using the %s model.\n', obj.name)
79     end
80
81 end
82 end % class

```

Nikravesh.m

```

1 classdef Nikravesh < Contactmodels
2 % 'Nikravesh' is a subclass of 'Contactmodels' and defines the contact model set
3 % forth in the article:
4 % "A Contact Force Model With Hysteresis Damping for Impact Analysis of
5 % Multibody Systems"
6 % In: Journal of Mechanical Design, Year 1990, Volume 112, Issue 3, pp. 369.
7 % By: Lankarani, H. M. and Nikravesh, P. E.
8
9 properties (Constant)
10    E_r = 70e9; % Young's modulus sphere (rotor material part) [Pa]
11    E_s = 100e9; % Young's modulus sphere (stator material part) [Pa]
12    nu_r = 0.35; % Poisson's ratio for the rotor material [-]
13    nu_s = 0.35; % Poisson's ratio for the stator material [-]
14 end
15
16
17 properties
18    n % Penetration exponent
19    ce % Coefficient of restitution

```

```

20      K           % Generalized material parameter
21      delta_d_init % Relative velocity at impact instant
22  end
23
24
25  methods
26
27      function obj = Nikravesh(friction_model, r_s, r_r)
28          % Constructor function.
29          % INPUT:
30          %   r_s: stator inner radius
31          %   r_r: rotor radius
32
33          % Send friction model to super class constructor
34          obj = obj@Contactmodels(friction_model);
35
36          obj.name = "Nikravesh";
37          obj.print_name;
38
39          obj.n = 3/2;
40          obj.ce = 1/2;
41
42          % Material parameters
43          h_r = (1 - obj.nu_r^2)/(pi*obj.E_r);
44          h_s = (1 - obj.nu_s^2)/(pi*obj.E_s);
45
46          obj.K = (4/(3*pi*(h_r + h_s))) * ((r_r*r_s)/(r_r+r_s))^(0.5);
47          obj.delta_d_init = 0;
48  end
49
50
51  function Fn = calc_fn(obj, d, d_dot)
52      % Calculates the magnitude of the radial normal force
53      % INPUT:
54      %   d    : penetration
55      %   d_dot: relative velocity between rotor and stator
56
57      Fn = obj.K * d^obj.n * (1 + (3*(1-obj.ce^2)/4)*d_dot/obj.delta_d_init);
58
59  end
60
61  end
62 end % class

```

dydt.m

```

1  function y_dot = dydt(t, y, s, cmod, state)
2  % 'dydt' serves the equation of motion as a system of six first order equations.
3  %
4  % INPUT:
5  %   y      : State vector
6  %   s      : Rotor system object

```

```
7 %     cmod : The contact model object
8 %     state : Contact indicator (0|1)
9 % OUTPUT:
10 %     y_dot: Accelerations and velocities
11 %
12
13 l_OD    = s.l_OD;
14 l_OM    = s.l_OM;
15 l_OC    = s.l_OC;
16 l_OE    = s.l_OE;
17
18 I_xx    = s.I_xx;
19 I_yy    = s.I_yy;
20 I_zz    = s.I_zz;
21
22 k_xx    = s.k_xx;
23 k_yy    = s.k_yy;
24 k_xy    = s.k_xy;
25 k_yx    = s.k_yx;
26 k_ft1   = s.k_ft1;
27 k_ft2   = s.k_ft2;
28 k_vg    = s.k_vg;
29 k_hg    = s.k_hg;
30
31 m0      = s.m0;
32 e_x     = s.e_x;
33 e_y     = s.e_y;
34
35 m_ih    = s.m_ih;
36 m_mh    = s.m_mh;
37
38 d_vg    = s.d_vg;
39 d_hg    = s.d_hg;
40 d_yy    = s.d_yy;
41
42 % Damping switch to account for anisotropic damping at standstill
43 if abs(y(6)) > 5
44     d_xx  = s.d_xx;
45 else
46     d_xx  = s.d0_xx;
47 end
48
49 % Calculate contact forces
50 [F_cx, F_cy] = contactForce(y, s, cmod, state);
51
52 % Evaluate external magnet force if enabled
53 if s.mag_enabled
54     [F_excx, F_excy] = s.magnetForce(t, y);
55 else
56     F_excx = 0;
57     F_excy = 0;
58 end
59
```

```

60      % Initial damping to kill initial transients
61      %if t < 1
62          %d_xx = 50;
63          %d_yy = 50;
64      %elseif t >= 1 && t < 2
65          %d_xx = 40;
66          %d_yy = 40;
67      %elseif t >= 2 && t < 3
68          %d_xx = 30;
69          %d_yy = 30;
70      %elseif t >= 3 && t < 4
71          %d_xx = 20;
72          %d_yy = 20;
73  %end
74
75      % Remove cross stiffness
76      %k_xy = 0;
77      %k_yx = 0;
78
79  % Don't edit anything after this as it may be overwritten by Maple!
80  % * * * *
81  y_dot(1) = y(2);
82  y_dot(2) = 0.1e1 / I_xx / cos(y(3)) * (-cos(y(5)) * e_y * l_OD * m0 * y(6)^2 - sin(y(5)) * sin(y(3)) * sin(y(1)) * k_yy * l_OM^2 + sin(y(3)) * sin(y(1)) * y_dot(4));
83  y_dot(3) = y(4);
84  y_dot(4) = -(-y(1) * sin(y(3)) * sin(y(1)) * k_yy * l_OM^2 + sin(y(3)) * sin(y(1)) * y_dot(5));
85  y_dot(5) = y(6);
86  y_dot(6) = -(-I_zz * sin(y(3)) * cos(y(5)) * e_y * l_OD * m0 * y(6)^2 - I_zz * sin(y(5)) * sin(y(3)) * cos(y(5)) * e_y * l_OD * m0 * y(6)^2 + sin(y(3)) * cos(y(5)) * e_y * l_OD * m0 * y(6)^2 - I_zz * sin(y(5)) * sin(y(3)) * cos(y(5)) * e_y * l_OD * m0 * y(6)^2);
87  y_dot(7) = y(8);
88  y_dot(8) = (-d_vg * y(8) + d_vg * y(12) - k_vg * y(7) + k_vg * y(11) + F_cx) / m_ih;
89  y_dot(9) = y(10);
90  y_dot(10) = (-2 * k_ft1 * y(9) + 2 * k_ft1 * y(13) + F_cy) / m_ih;
91  y_dot(11) = y(12);
92  y_dot(12) = (d_vg * y(8) - d_vg * y(12) - 2 * k_ft2 * y(11) + k_vg * y(7) - k_vg * y(11));
93  y_dot(13) = y(14);
94  y_dot(14) = -1 / m_mh * (d_hg * y(14) - 2 * k_ft1 * y(9) + 2 * k_ft1 * y(13) + k_hg * y(13));
95
96  y_dot = y_dot';
97
98 end
99 % Maple part last updated: 22-09-2019 15:31

```

contactForce.m

```

1 function [F_cx, F_cy, delta, delta_d] = contactForce(y, s, cmod, state)
2 % 'contactForce' computes the contact force and related parameters.
3 %
4 % INPUT:
5 %   y      : State vector
6 %   s      : Rotor system object
7 %   cmod   : The contact model object
8 %   state  : Contact indicator (0|1)
9 % OUTPUT:

```

```
10 % F_c*      : Force components
11 % delta     : Indentation
12 % delta_d  : Indentation rate
13 %
14
15 if s.calc_indent(y) <= 0
16 % If the "indent" is negative the contact force and indentation is zero, while
17 % the initial relative impact velocity should be calculated
18
19 % Check which solver is calling the parent function, this is important since
20 % delta_d_init cannot change, when the event function is only "testing" the
21 % limit
22 if state == 0
23     cmod.delta_d_init = s.pen_rate(y);
24     delta_d = cmod.delta_d_init;
25 else
26     delta_d = 0;
27 end
28 F_cx = 0;
29 F_cy = 0;
30 delta = 0;
31
32 else
33     % Penetration
34     delta = s.calc_indent(y);
35
36     % Penetration rate
37     delta_d = s.pen_rate(y);
38
39     % Relative velocity between the rotor- and stator surface (that is the
40     % tangential component)
41     vt_rel = s.tan_rel_velocity(y);
42
43     % Normal- and friction force
44     Fn = cmod.calc_fn(delta, delta_d);
45     Ff = cmod.calc_ff(Fn, vt_rel);
46
47     % Contact angle
48     alpha = s.contact_ang(y);
49
50     % Contact forces in the inertial coordinate system
51     F = s.T_the(alpha)' * [Fn; Ff; 0];
52
53     F_cx = F(1);
54     F_cy = F(2);
55
56     % delta_d is overwritten here for debug purposes in 'debug1'
57     delta_d = cmod.delta_d_init;
58 end
59 end
```

impactDetect.m (event function)

```
1  function [value, isterminal, direction] = impactDetect(~, y, s, dir, term)
2  % 'impactDetect' used by the ode solvers to halt integration upon rotor-stator
3  % impact.
4  %
5  % INPUTS:
6  %   y   : State vector
7  %   s   : Rotor system object
8  %   dir : Direction of the rotor d = 1 if outgoing and d = -1 if ingoing
9  %   term: Terminate on trigger 0|1
10 %
11
12    value      = s.calc_indent(y);
13    isterminal = term;
14    direction  = dir;
15  end
```

D.3.2 Flexible Program

master_run.m

```

1  %%%%%%
2  %% Master Thesis - FEM model of rotor stator setup %%
3  %% Anders Markvorsen (s134130)                 %%
4  %% Svend Andersen (sXXXXXX)                      %%
5  %%%%%%
6  %%%%%%
7
8  clear all; clc; close all;
9
10 %%
11 %----- PRE PROCESSING -----
12 %%----- CONTROL PANEL -----
13 %%
14 %%
15 %% Control settings
16
17 par.Omegahz = 17; % 18.0      % Angular velocity [rounds/s] ([Hz])
18 par.free_springs = 1;        % (1/0) Inserting weak springs for stability
19 par.support = 0;             % (1/0) Inserting PMB and B stiffness
20 par.raydamp = 1;             % (1/0) Inserting rayleigh damping
21 %par.eig = 'stand';         % ('stand'/'general') Standard vs Generalized EVP
22 par.eig = 'general';        % ('stand'/'general') Standard vs Generalized EVP
23 par.evpcond = 0;            % (1/0) Plotting condition of EVP
24 par.analFRF = 0;             % (1/0) Calculating the FRF analytically
25 par.modeshapes = [];%[1 2 3 4 5 6 7 8 9 10]; % Enter what modes you want to see
26 par.campbell = 0;            % (1/0) Calculate and plot campbell diagram
27 par.stabilitymap = 0;        % (1/0) Calculate and plot stability map
28 par.unbalanceresp = 0;       % (1/0) Calculate and plot unbalance response (
29 par.time_int = 0;            % (1/0) Time integration without modal reduction
30 par.modal = 1;               % (1/0) Time integration with modal reduction
31 par.impact = 1;
32
33
34 % Rotational velocity
35 par.Omega = par.Omegahz *2*pi;      % Angular velocity [rad/s]
36 par.Omegarpm = par.Omega*60/2/pi;    % Angular velocity [rpm]
37
38 % Unbalance parameters
39 ME.D.e = 0.0767;                  % Unbalance eccentricity [m]
40 ME.D.m0 = 0.001;                  % Unbalance mass [kg]
41 ME.D.phi = pi+1.209;              % Unbalance phase angle [rad]
42
43 % System dofs
44 par.Ne = 16;                      % Number of elements 32 or 16
45 par.NEdof = 8;                    % Number of degree(s) of freedom for each element
46 par.Ndof = (par.Ne+1) * (par.NEdof/2); % Number of total degree(s) of freedom
47
48 % Machine element activation
49 ME.SLE.act = 1;                  % Stator sleeve activation (0/1)

```

```
50 ME.D.act = 1; % Unbalance disc activation (0/1)
51 ME.PMB.act = 1; % Permanent Magnetic Bearing activation (0/1)
52 ME.TAR.act = 1; % Excitation steel target activation (0/1)
53 ME.COUP.act = 1; % Coupling activation (0/1)
54
55 %% Excitation magnet data
56 % % Excitation magnet without rot
57 % force = load('./excdatal/exc_0hz_50ms-run2_v2.mat');
58 % par.exc_time = force.exc(:,1);
59 % par.exc_force = force.exc(:,2);
60
61
62 %Excitation magnet with rot
63 force = load('./excdatal/rot_sim_exp315');
64 keyboard
65 par.exc_time = force.exp(:,1);
66 par.exc_force = force.exp(:,2);
67 global mflag
68 mflag = 0;
69
70
71 %----- MACHINE ELEMENT LOCATION -----
72
73 [ME] = machineelement_location_fun(par,ME);
74
75 %----- GEOMETRY AND MATERIAL PROPERTIES-----
76
77 [MAT,mat,par,ME] = globmat(par,ME);
78
79 %----- IMPLEMENTING RAYLEIGH DAMPING -----
80 if par.raydamp==1
81 % Both parameters
82 %alpha = 10.571;
83 %beta = 3.533e-7;
84
85 % Only beta
86 alpha = 0;
87 beta = 2.4795e-6;
88
89 % Only alpha
90 %alpha = 12.3282;
91 %beta = 0;
92
93 MAT.D = MAT.D + alpha * MAT.M + beta * MAT.K;
94 end
95
96 %----- STATE SPACE -----
97
98 null = zeros(par.Ndof);
99 MAT.C = -par.Omega*MAT.G + MAT.D;
100
101 A = [null
102      -inv(MAT.M)*MAT.K
103                  eye(par.Ndof)
104                  -inv(MAT.M)*MAT.C];
```

```
103
104
105 Mglob= [null MAT.M
106         MAT.M
107         MAT.C];
108 Kglob = [-MAT.M
109         null
110         MAT.K];
111 %----- Solving EVP -----
112
113 % Static analysis (For debugging - set Omega to zero and compare)
114 [eigvec_s,eigval_s] = eig(MAT.K,MAT.M);
115 [eigval_s,p] = sort(diag(eigval_s));
116 eigvec_s = eigvec_s(:,p);
117 eigfreqhz_s = sqrt(eigval_s)/(2*pi);
118 for i=1:size(eigvec_s,2)
119     eigvec_s(:,i) = eigvec_s(:,i) ./ max(eigvec_s(:,i));
120 end
121
122 if strcmp(par.eig,'stand')==1
123     [eigval,eigvecL,eigvecR,eigfreqhz,eigfreqrad] = standevp_fun(A,par);
124 end
125
126 if strcmp(par.eig,'general')==1
127     [eigval,eigvecL,eigvecR,eigfreqhz,eigfreqrad] = ...
128     generalevp_fun(Kglob,Mglob,par);
129 end
130
131
132 %%
133
134 %----- Analytical FRF -----
135 if par.analFRF==1
136     analfrf_out = analfrf_fun(ME,par,MAT);
137 end
138
139 %----- MODE SHAPES -----
140
141 if length(par.modeshapes) ~= 0
142     modeshapes = modeshape_fun(eigvecR,eigfreqrad,eigfreqhz,par,ME)
143 end
144
145 %----- CAMPBELL DIAGRAM -----
146
147 if par.campbell==1
148     campbell_out = campbell_fun(par,MAT);
149 end
150
151 %----- STABILITY MAP -----
152
153 if par.stabilitymap==1
154     stabilitymap_out = stabilitymap_fun(par,MAT);
155 end
```

```

156
157
158 %----- UNBALANCE RESPONSE -----
159
160 if par.unbalanceresp==1
161     unbalanceresp_out = unbalanceresp_fun(par,MAT,ME);
162 end
163
164 %%
165 %%----- Time integrating -----
166 %%----- WITHOUT MODAL REDUCTION -----
167 %%----- WITH MODAL REDUCTION -----
168 %%----- WITH MODAL REDUCTION AND IMPACT -----
169
170 if par.time_int ==1
171     % Initial conditions
172     z0 = zeros(par.Ndof*2,1);
173     %Y-dir disp
174     z0(1:4:end/2) = z0(1:4:end/2) + 0.001;
175     %Z-dir disp
176     z0(2:4:end/2) = z0(2:4:end/2) + 0.000;
177     %Y-dir vel
178     z0((end/2)+1:4:end) = z0((end/2)+1:4:end) + 0.000;
179     %Z-dir vel
180     z0((end/2)+2:4:end) = z0((end/2)+2:4:end) + 0.2;
181     %Point disp
182     %z0(par.Ndof+1) = 0.01;
183     %Point vel
184     %z0(1) = z0(1) + 0.0000;
185     %z0(ME.D.dof) = z0(ME.D.dof) + 2;
186
187     tspan = [0 0.1];
188     tic
189     [t,z] = ode45(@(t,z) state_int(t,z,A,MAT.M,par,ME),tspan,z0);
190     toc
191
192     % Extracting data
193     q = z(:,1:end/2).';
194 end
195
196 %----- WITH MODAL REDUCTION -----
197
198 if par.modal==1 && par.impact ==0 && strcmp(par.eig,'general')==1
199     [q,t]=modalgeneral_fun(Kglob,Mglob,par,eigvecR,eigvecL,ME);
200 end
201
202 if par.modal==1 && par.impact ==0 && strcmp(par.eig,'stand')==1
203     [q,t]=modalstand_fun(A,par,MAT,eigvecR,eigvecL,ME);
204 end
205
206 %----- WITH MODAL REDUCTION AND IMPACT -----
207
208

```

```

209 if par.modal==1 && par.impact==1 && strcmp(par.eig,'general')==1
210     % q is the full disp. solution
211     % z is the full vel.+disp. solution
212     % t is the full time history
213     % te_total is the times at event
214     [q,t,te_total,z,R,par,ME]=rotorstator_fun(Kglob,Mglob,par,eigvecR,eigvecL,ME);
215 end
216 q = real(q); % Removing minor imaginary "noise"
217
218
219 %%
220 %----- POST-PROCESSING -----
221 %----- Exporting data -----
222 %% Recalculating data
223 contact = 0;
224 for i=1:length(z)
225     z0 = z(:,i);
226     z_r = R*z0(1:par.Nr);
227     z_s = z0(par.Nr+1:end);
228
229     impact_contact_prev = contact;
230     [contact,gap,alpha,delta,deltad] = contact_fun(z0,par,R,ME);
231     impact_contact_pos = contact;
232
233     if impact_contact_prev == 0 && impact_contact_pos ==1
234         imp.contact = contact;
235         imp.gap = gap;
236         imp.alpha = alpha;
237         imp.delta = delta;
238         imp.deltad = deltatad;
239     end
240
241     if contact ==1
242         % Calculating indentation normal contact forces
243         [Fn_y,Fn_z,Fn] = Nikravesh(imp,alpha,delta,deltad);
244
245         % Calculating indentation friction contact forces
246         [Fmu_y,Fmu_z] = Ambrosio(par,alpha,ME,z_r,z_s,Fn);
247
248         % Contact forces
249         F_cy = Fn_y + Fmu_y;
250         F_cz = Fn_z + Fmu_z;
251
252     else
253         F_cy = 0;
254
255
256
257
258
259
260
261

```

```

262     F_cz = 0;
263     Fn = 0;
264     delta = 0;
265 end
266
267 save_z_r_y(i,1) = z_r(par.Ndof+ME.STAT.dof);
268 save_z_r_z(i,1) = z_r(par.Ndof+ME.STAT.dof+1);
269 save_z_s_y(i,1) = z_s(1);
270 save_z_s_z(i,1) = z_s(2);
271 save_Fn(i,1) = Fn;
272 save_delta(i,1) = delta;
273 save_gap(i,1) = gap;
274 save_deltad(i,1) = deltatad;
275
276 end
277 save_t = t;
278 save_rot = t*par.Omega;
279
280
281 %% Export data
282 % File name and type
283 fileID = fopen('exp.txt','w');
284 % Print in header
285 fprintf(fileID,'%9s %9s %9s %9s %9s %5s %4s %9s \n','t',...
286 'r_y','r_z','s_y','s_z','theta','fn','delta');
287 % Print in data
288 for i=1:length(save_t)
289     fprintf(fileID,'%8.7f %9.8f %9.8f %9.8f %9.8f %5.4f %4.1f %9.8f \n',...
290     save_t(i), real(save_z_r_y(i)), real(save_z_r_z(i))...
291 ,real(save_z_s_y(i)), real(save_z_s_z(i)), save_rot(i), ...
292 save_Fn(i), save_delta(i));
293 end
294 fclose(fileID);

```

globmat.m

```

1 function [MAT,mat,par,ME] = globmat(par,ME)
2
3 ME.SLE.dof = (ME.SLE.loc - 1)*4+1; % First d.o.f. at sleeve node
4 ME.STAT.dof = ME.SLE.dof; % First d.o.f. at stator contact node
5 ME.D.dof = (ME.D.loc - 1)*4+1; % First d.o.f. at disc node
6 ME.PMB.dof = (ME.PMB.loc - 1)*4+1; % First d.o.f. at PMB node
7 ME.TAR.dof = (ME.TAR.loc - 1)*4+1; % First d.o.f. at target node
8 ME.B.dof = (ME.B.loc - 1)*4+1; % First d.o.f. at spherical bearing node
9 ME.COUP.dof = (ME.COUP.loc - 1)*4+1; % First d.o.f. at coupling
10
11 mat.E_alu = 71*10^9; % Young's Modulus of aluminium [Pa]
12 mat.R_alu = 2600; % Density of steel aluminium [kg/m^3]
13
14 % Shaft
15 ME.S.len = 0.492; % Length of shaft
16
17 ME.S.dia = 0.025; % Shaft diameter [m]

```

```

18 ME.S.rad = ME.S.dia/2; % Shaft radius [m]
19 ME.S.area = pi*ME.S.rad^2; % Shaft area [m^2]
20 ME.S.mass = 0.60+0.027; % Mass of shaft [kg] (foynd exp)
21
22 % Stator
23 ME.STAT.mi = 1.79; % Mass of inner house (found exp)
24 ME.STAT.mo = 8.44; % Mass of outer house (found exp)
25 ME.STAT.kVB = 9.709e8;
26 ME.STAT.kHB = 1.41e9;
27 ME.STAT.kFT1 = 8.42e6;
28 ME.STAT.kFT2 = 1.26e7;
29 ME.STAT.dVB = 2168;
30 ME.STAT.dHB = 12983;
31
32 % Stator sleeve
33 ME.SLE.mass = 0; % Equivalent mass of sleeve [kg] (found exp)
34 ME.SLE.It = 0; % Transverse mass moment of inertia [kg m^2] (found SW)
35 ME.SLE.Ip = 0; % Polar mass moment of inertia [kg m^2] (found SW)
36
37 % Disc
38 ME.D.mass = 0.250; % Mass of disc [kg] (found exp)
39 ME.D.It = 219584.55 / 10^9; % Transverse mass moment of inertia [kg m^2] (found SW)
40 ME.D.Ip = 426774.25 / 10^9; % Polar mass moment of inertia [kg m^2] (found SW)
41
42 % PMB
43 ME.PMB.mass = 0.560; % Mass of PMB [kg] (found exp)
44 ME.PMB.It = 287431.88 / 10^9; % Transverse mass moment of inertia [kg m^2] (found SW)
45 ME.PMB.Ip = 521378.74 / 10^9; % Polar mass moment of inertia [kg m^2] (found SW)
46 ME.PMB.Kty = 3.09*10^4; % Stiffness in Y-direction (translation) [N/m]
47 ME.PMB.Ktz = 3.09*10^4; % Stiffness in Z-direction (translation) [N/m]
48
49 ME.PMB.Ktzy = 2.456*10^3;
50 ME.PMB.Ktzy = 292;
51
52 ME.PMB.Kry = 0; % Stiffness around Y-direction (rotation) [Nm]
53 ME.PMB.Krz = 0; % Stiffness around Z-direction (rotation) [Nm]
54 if par.Omega~=0
55 ME.PMB.Dty = 8.48; % Damping in Y-direction (translation) [Ns/m]
56 else
57 ME.PMB.Dty = 40.9; % Damping in Y-direction (translation) [Ns/m]
58 end
59 ME.PMB.Dtz = 7.7; % Damping in Z-direction (translation) [Ns/m]
60 ME.PMB.Dry = 0; % Damping around Y-direction (rotation) [Nm s]
61 ME.PMB.Drz = 0; % Damping around Z-direction (rotation) [Nm s]
62
63 % Target
64 ME.TAR.mass = 0.2566; % Mass of target [kg] (found exp)
65 ME.TAR.It = 79854.29 / 10^9; % Transverse mass moment of inertia [kg m^2] (found SW)
66 ME.TAR.Ip = 63014.72 / 10^9; % Polar mass moment of inertia [kg m^2] (found SW)
67
68 % Spherical bearing
69 ME.B.mass = 0;
70 ME.B.Ip = 0;

```

```
71 ME.B.It = 0; % Stiffness in Y-direction (translation) [N/m]
72 ME.B.Kty = 1e9;
73 ME.B.Ktz = 1e9;
74 ME.B.Kry = 0;
75 ME.B.Krz = 0;
76 ME.B.Dty = 1e2;
77 ME.B.Dtz = 1e2;
78 ME.B.Dry = 0;
79 ME.B.Drz = 0; % Damping around Z-direction (rotation) [Nm s]
80
81 % Coupling
82 ME.COUP.mass = 0.429;
83 ME.COUP.Ip = 240578.44/ 10^9;
84 ME.COUP.It = 172380.0/ 10^9;
85 ME.COUP.Kty = 0;
86 ME.COUP.Ktz = 0;
87 ME.COUP.Kry = 0;
88 ME.COUP.Krz = 0;
89
90
91 %%%%%%%%%%%%%% % FEM shaft element definition %
92 %%%%%%%%%%%%%%
93 %%%%%%%%%%%%%%
94
95 % Length of shaft element [m]
96 %l(1:par.Ne,1) = (0.485+adj)/par.Ne;
97
98 if par.Ne==10
99     l(1:1,1) = (0.05)/1;
100    l(2:3,1) = (0.169-0.05)/2;
101    l(4:5,1) = (0.257-0.169)/2;
102    l(6:7,1) = (0.3562-0.257)/2;
103    l(8:9,1) = (0.4287-0.3562)/2;
104    l(10:10,1) = (0.492-0.4287)/1;
105 end
106
107 if par.Ne==16
108     l(1:2,1) = (0.05)/2;
109     l(3:5,1) = (0.169-0.05)/3;
110     l(6:8,1) = (0.257-0.169)/3;
111     l(9:11,1) = (0.3562-0.257)/3;
112     l(12:14,1) = (0.4287-0.3562)/3;
113     l(15:16,1) = (0.492-0.4287)/2;
114 end
115
116 if par.Ne==32
117     l(1:4,1) = (0.05)/4;
118     l(5:10,1) = (0.169-0.05)/6;
119     l(11:16,1) = (0.257-0.169)/6;
120     l(17:22,1) = (0.3562-0.257)/6;
121     l(23:28,1) = (0.4287-0.3562)/6;
122     l(29:32,1) = (0.492-0.4287)/4;
123 end
```

```

124
125 ME.S.l = 1;
126 ME.S.l2n = cumsum([0; ME.S.l]);
127
128 % Radius of shaft element [m]
129 for i=1:par.Ne
130     r(i,1) = ME.S.rad;
131 end
132
133 % Density of shaft element [kg/m^3]
134 for i=1:par.Ne
135     rho(i,1) = mat.R_alu;
136 end
137
138 % Cross sectional area of element [m^2]
139 for i=1:par.Ne
140     area(i,1) = pi * r(i,1)^2;
141 end
142
143 % Bending area moment of inertia of element [m^4]
144 for i=1:par.Ne
145     II(i,1) = pi * (r(i,1)^4) / 4;
146 end
147
148
149 %%%%%%
150 % Defining global matrices %
151 %%%%%%
152
153 M = zeros(par.Ndof,par.Ndof); % Mass matrix
154 G = zeros(par.Ndof,par.Ndof); % Gyroscopic matrix
155 D = zeros(par.Ndof,par.Ndof); % Damping matrix
156 K = zeros(par.Ndof,par.Ndof); % Stiffness matrix
157
158 %%%%%%
159 % Defining Mass, Gyro and Stiffness Matrix of Shaft %
160 %%%%%%
161 a=1; b=8;
162 for n=1:par.Ne; % Looping over each element
163
164 % Local mass matrix (considering linear/translational motion)
165 Mte = [156 0 0 22*l(n) 54 0 0
166 -13*l(n) 0 156 -22*l(n) 0 0 54 13*l(n)
167 0 0 -22*l(n) 4*l(n)^2 0 0 -13*l(n) -3*l(n)^2
168 22*l(n) 0 0 4*l(n)^2 13*l(n) 0 0
169 -3*l(n)^2 54 0 0 13*l(n) 156 0 0
170 -22*l(n) 0 54 -13*l(n) 0 0 156 22*l(n)
171 0 0 0 0 0 0 0 0

```

```

171      0           13*l(n)   -3*l(n)^2   0           0           22*l(n)   4*l(n)^2
172      0           -13*l(n)   0           0           -3*l(n)^2   -22*l(n)   0
173      4*l(n)^2];
174
175
176      % Local mass matrix (considering angular/rotational motion)
177 Mre = [36      0           0           3*l(n)   -36       0           0           3*l(n)
178      0           36        -3*l(n)   0           0           -36       -3*l(n)   0
179      0           -3*l(n)  4*l(n)^2   0           0           3*l(n)   -l(n)^2   0
180      3*l(n)   0           0           4*l(n)^2   -3*l(n)   0           0           -l(n)^2
181      -36      0           0           -3*l(n)   36        0           0           -3*l(n)
182      0           -36      3*l(n)   0           0           36        3*l(n)   0
183      0           -3*l(n) -l(n)^2   0           0           3*l(n)   4*l(n)^2   0
184      3*l(n)   0           0           -l(n)^2   -3*l(n)   0           0           4*l(n)^2];
185
186 Mre = Mre * ((rho(n) * area(n) * r(n)^2) / (120*l(n)));
187
188 Me = Mte + Mre; % Combined local element mass matrix
189
190 % Local gyroscopic matrix
191
192 Ge = [0      -36      3*l(n)   0           0           36       3*l(n)   0
193      36      0           0           3*l(n)   -36       0           0           3*l(n)
194      -3*l(n) 0           0           -4*l(n)^2  3*l(n)   0           0           l(n)^2
195      0           -3*l(n)  4*l(n)^2   0           0           3*l(n)   -l(n)^2   0
196      0           36      -3*l(n)   0           0           -36      -3*l(n)   0
197      -36      0           0           -3*l(n)   36        0           0           -3*l(n)
198      -3*l(n) 0           0           l(n)^2     3*l(n)   0           0           -4*l(n)^2
199      0           -3*l(n) -l(n)^2   0           0           3*l(n)   4*l(n)^2   0
];
200
201 Ge = Ge * ((2 * rho(n) * area(n) * r(n)^2) / (120 * l(n)));
202
203 % Local stiffness matrix (considering bending of the shaft)
204 Ke = [12      0           0           6*l(n)   -12       0           0           6*l(n)
205      0           12        -6*l(n)   0           0           -12      -6*l(n)   0
206      0           -6*l(n)  4*l(n)^2   0           0           6*l(n)   2*l(n)^2   0
207      6*l(n)   0           0           4*l(n)^2   -6*l(n)   0           0           2*l(n)^2
208      -12      0           0           -6*l(n)   12        0           0           -6*l(n)
209      0           -12      6*l(n)   0           0           12        6*l(n)   0
210      0           -6*l(n)  2*l(n)^2   0           0           6*l(n)   4*l(n)^2   0
211      6*l(n)   0           0           2*l(n)^2   -6*l(n)   0           0           4*l(n)^2];
212
213 Ke = Ke * (mat.E_alu*II(n)/(l(n)^3));
214
215
216 M(a:b,a:b) = M(a:b,a:b) + Me;
217 G(a:b,a:b) = G(a:b,a:b) + Ge;
218 K(a:b,a:b) = K(a:b,a:b) + Ke;
219
220 a = a + 4;

```

```

221      b = b + 4;
222  end
223
224 %----- Adding mass, gyro, stiffness and damping from Machine elements %
225 %----- Stator sleeve -----%
226
227 if ME.SLE.act==1
228     % Adding mass from the stator sleeve
229     M(ME.SLE.dof,ME.SLE.dof) = M(ME.SLE.dof,ME.SLE.dof) + ME.SLE.mass;
230     M(ME.SLE.dof+1,ME.SLE.dof+1) = M(ME.SLE.dof+1,ME.SLE.dof+1) + ME.SLE.mass;
231     M(ME.SLE.dof+2,ME.SLE.dof+2) = M(ME.SLE.dof+2,ME.SLE.dof+2) + ME.SLE.It;
232     M(ME.SLE.dof+3,ME.SLE.dof+3) = M(ME.SLE.dof+3,ME.SLE.dof+3) + ME.SLE.It;
233
234     % Adding the gyroscopic effect from the stator sleeve
235     G(ME.SLE.dof+2,ME.SLE.dof+3) = G(ME.SLE.dof+2,ME.SLE.dof+3) - ME.SLE.Ip;
236     G(ME.SLE.dof+3,ME.SLE.dof+2) = G(ME.SLE.dof+3,ME.SLE.dof+2) + ME.SLE.Ip;
237
238 end
239
240 %----- Unbalance disc -----%
241 if ME.D.act==1
242
243     % Adding mass from the unbalance disc
244     M(ME.D.dof,ME.D.dof) = M(ME.D.dof,ME.D.dof) + ME.D.mass;
245     M(ME.D.dof+1,ME.D.dof+1) = M(ME.D.dof+1,ME.D.dof+1) + ME.D.mass;
246     M(ME.D.dof+2,ME.D.dof+2) = M(ME.D.dof+2,ME.D.dof+2) + ME.D.It;
247     M(ME.D.dof+3,ME.D.dof+3) = M(ME.D.dof+3,ME.D.dof+3) + ME.D.It;
248
249     % Adding the gyroscopic effect from the unbalance disc
250     G(ME.D.dof+2,ME.D.dof+3) = G(ME.D.dof+2,ME.D.dof+3) - ME.D.Ip;
251     G(ME.D.dof+3,ME.D.dof+2) = G(ME.D.dof+3,ME.D.dof+2) + ME.D.Ip;
252
253 end
254
255 %----- PMB -----%
256 if ME.PMB.act==1
257
258     % Adding mass from the PMB
259     M(ME.PMB.dof,ME.PMB.dof) = M(ME.PMB.dof,ME.PMB.dof) + ME.PMB.mass;
260     M(ME.PMB.dof+1,ME.PMB.dof+1) = M(ME.PMB.dof+1,ME.PMB.dof+1) + ME.PMB.mass;
261     M(ME.PMB.dof+2,ME.PMB.dof+2) = M(ME.PMB.dof+2,ME.PMB.dof+2) + ME.PMB.It;
262     M(ME.PMB.dof+3,ME.PMB.dof+3) = M(ME.PMB.dof+3,ME.PMB.dof+3) + ME.PMB.It;
263
264     % Adding the gyroscopic effect from the PMB
265     G(ME.PMB.dof+2,ME.PMB.dof+3) = G(ME.PMB.dof+2,ME.PMB.dof+3) - ME.PMB.Ip;
266     G(ME.PMB.dof+3,ME.PMB.dof+2) = G(ME.PMB.dof+3,ME.PMB.dof+2) + ME.PMB.Ip;
267
268 end
269
270 %----- Target -----%
271 if ME.TAR.act==1
272
273     % Adding mass from the Target

```

```

274     M(ME.TAR.dof,ME.TAR.dof) = M(ME.TAR.dof,ME.TAR.dof) + ME.TAR.mass;
275     M(ME.TAR.dof+1,ME.TAR.dof+1) = M(ME.TAR.dof+1,ME.TAR.dof+1) + ME.TAR.mass;
276     M(ME.TAR.dof+2,ME.TAR.dof+2) = M(ME.TAR.dof+2,ME.TAR.dof+2) + ME.TAR.It;
277     M(ME.TAR.dof+3,ME.TAR.dof+3) = M(ME.TAR.dof+3,ME.TAR.dof+3) + ME.TAR.It;
278
279     % Adding the gyroscopic effect from the target
280     G(ME.TAR.dof+2,ME.TAR.dof+3) = G(ME.TAR.dof+2,ME.TAR.dof+3) - ME.TAR.Ip;
281     G(ME.TAR.dof+3,ME.TAR.dof+2) = G(ME.TAR.dof+3,ME.TAR.dof+2) + ME.TAR.Ip;
282
283 end
284
285 %----- Coupling -----%
286 if ME.COUP.act==1
287
288     % Adding mass from coupling
289     M(ME.COUP.dof,ME.COUP.dof) = M(ME.COUP.dof,ME.COUP.dof) + ME.COUP.mass;
290     M(ME.COUP.dof+1,ME.COUP.dof+1) = M(ME.COUP.dof+1,ME.COUP.dof+1) + ME.COUP.mass;
291     M(ME.COUP.dof+2,ME.COUP.dof+2) = M(ME.COUP.dof+2,ME.COUP.dof+2) + ME.COUP.It;
292     M(ME.COUP.dof+3,ME.COUP.dof+3) = M(ME.COUP.dof+3,ME.COUP.dof+3) + ME.COUP.It;
293
294     % Adding the gyroscopic effect from coupling
295     G(ME.COUP.dof+2,ME.COUP.dof+3) = G(ME.COUP.dof+2,ME.COUP.dof+3) - ME.COUP.Ip;
296     G(ME.COUP.dof+3,ME.COUP.dof+2) = G(ME.COUP.dof+3,ME.COUP.dof+2) + ME.COUP.Ip;
297
298 end
299
300
301 if par.free_springs==1
302     k_free1 = 3.468;
303     k_free2 = 10;
304     K(ME.PMB.dof,ME.PMB.dof) = K(ME.PMB.dof,ME.PMB.dof) + k_free1;
305     K(ME.PMB.dof+1,ME.PMB.dof+1) = K(ME.PMB.dof+1,ME.PMB.dof+1) + k_free1;
306     K(ME.B.dof,ME.B.dof) = K(ME.B.dof,ME.B.dof) + k_free2;
307     K(ME.B.dof+1,ME.B.dof+1) = K(ME.B.dof+1,ME.B.dof+1) + k_free2;
308 end
309
310
311 if par.support==1
312     K(ME.PMB.dof,ME.PMB.dof) = K(ME.PMB.dof,ME.PMB.dof) + ME.PMB.Kty;
313     K(ME.PMB.dof+1,ME.PMB.dof+1) = K(ME.PMB.dof+1,ME.PMB.dof+1) + ME.PMB.Ktz;
314
315     K(ME.PMB.dof,ME.PMB.dof+1) = K(ME.PMB.dof,ME.PMB.dof+1) + ME.PMB.Ktzy;
316     K(ME.PMB.dof+1,ME.PMB.dof) = K(ME.PMB.dof+1,ME.PMB.dof) + ME.PMB.Ktzy;
317
318     K(ME.B.dof,ME.B.dof) = K(ME.B.dof,ME.B.dof) + ME.B.Kty;
319     K(ME.B.dof+1,ME.B.dof+1) = K(ME.B.dof+1,ME.B.dof+1) + ME.B.Ktz;
320
321     D(ME.PMB.dof,ME.PMB.dof) = D(ME.PMB.dof,ME.PMB.dof) + ME.PMB.Dty;
322     D(ME.PMB.dof+1,ME.PMB.dof+1) = D(ME.PMB.dof+1,ME.PMB.dof+1) + ME.PMB.Dtz;
323     D(ME.B.dof,ME.B.dof) = D(ME.B.dof,ME.B.dof) + ME.B.Dty;
324     D(ME.B.dof+1,ME.B.dof+1) = D(ME.B.dof+1,ME.B.dof+1) + ME.B.Dtz;
325 end
326

```

```
327
328
329 %%%%%%%%%%%%%%%%
330 % Plotting shaft discretization with elements %
331 %%%%%%%%%%%%%%%%
332 figure();
333 %---- Shaft ----%
334 % Upper line
335 plot(ME.S.12n , ME.S.rad*ones(size(ME.S.12n)) , '-k')
336 hold on
337 % Under line
338 plot(ME.S.12n , -ME.S.rad*ones(size(ME.S.12n)) , '-k')
339 % Lateral lines
340 for i=1:length(ME.S.12n)
341 plot([ME.S.12n(i) ME.S.12n(i)] , [-ME.S.rad ME.S.rad] , 'k')
342 end
343 %---- Elements ----%
344 scatter(ME.S.12n(ME.SLE.loc) , 0 , 100 , 'or','filled')
345 text(ME.S.12n(ME.SLE.loc)-ME.S.rad , 2*ME.S.rad , 'Sleeve','FontSize',14)
346
347 scatter(ME.S.12n(ME.D.loc) , 0 , 100 , 'or','filled')
348 text(ME.S.12n(ME.D.loc)-ME.S.rad , 2*ME.S.rad , 'Disc','FontSize',14)
349
350 scatter(ME.S.12n(ME.PMB.loc) , 0 , 100 , 'or','filled')
351 text(ME.S.12n(ME.PMB.loc)-ME.S.rad , 2*ME.S.rad , 'PMB','FontSize',14)
352
353 scatter(ME.S.12n(ME.TAR.loc) , 0 , 100 , 'or','filled')
354 text(ME.S.12n(ME.TAR.loc)-ME.S.rad , 2*ME.S.rad , 'Target','FontSize',14)
355
356 scatter(ME.S.12n(ME.B.loc) , 0 , 100 , 'or','filled')
357 text(ME.S.12n(ME.B.loc)-ME.S.rad , 2*ME.S.rad , 'Bearing','FontSize',14)
358
359 scatter(ME.S.12n(ME.COUP.loc) , 0 , 100 , 'or','filled')
360 text(ME.S.12n(ME.COUP.loc)-ME.S.rad , 2*ME.S.rad , 'Coupling' , 'FontSize' , 14)
361
362 %---- Element numbers ----%
363 for i=2:length(ME.S.12n)
364 text(ME.S.12n(i)-ME.S.1(i-1)/2-0.001 , 0 , num2str(i-1))
365 end
366
367
368
369
370 hold off
371 %axis equal
372 %xlim([-0.05 0.6])
373 axis([-0.05 0.55 -0.03 0.05])
374 xlabel('Axial distance [m]')
375 ylabel('Radial distance [m]')
376 grid on
377 set(gca, 'FontSize', 18,'Fontname','Times')
378
379
```

```

380
381 %%%%%% Analytical nat. freq. of free free beam %%%%%%
382 %
383 %%%%%%
384 root = [4.73004074; 7.85320462; 10.9956078; 14.1371655; 17.2787597];
385 for i=1:length(root)
386     eigfreqhz_anal(i) = root(i)^2 * sqrt(mat.E_alu*II(1) / mat.R_alu / ...
387                                     ME.S.area / ME.S.len^4) / (2*pi);
388 end
389
390 MAT.M = M;
391 MAT.K = K;
392 MAT.D = D;
393 MAT.G = G;
394
395
396 end

```

standevp_fun.m

```

1 function [eigval,eigvecL,eigvecR,eigfreqhz,eigfreqrad]=standevp_fun(A,par)
2 % Checking
3 checksymA= norm(A-A.');
4
5 [eigvecR,eigvalR,eigvecL] = eig(A);
6 eigvalL = eigvalR;
7 eigvecL = conj(eigvecL);
8
9 % Checking
10 checkEIGR = norm(A*eigvecR - eigvecR * eigvalR);
11 checkEIGL = norm(eigvecL.*A - eigvalL*eigvecL.');
12
13 % Eigenvalues extracted
14 eigvalR = diag(eigvalR);
15 eigvalL = diag(eigvalL);
16
17 % Sorting left
18 [~,sortL] = sort(abs(imag(eigvalL)));
19 eigvalL = eigvalL(sortL);
20 eigvecL = eigvecL(:,sortL);
21
22 % Sorting right
23 [~,sortR] = sort(abs(imag(eigvalR)));
24 eigvalR = eigvalR(sortR);
25 eigvecR = eigvecR(:,sortR);
26
27 eigval = eigvalR;
28 eigfreqrad = abs(imag(eigval));
29 eigfreqhz = abs(imag(eigval)/(2*pi));
30 damp_ratio = -real(eigval) ./ abs(eigval);
31
32 % Normalizing eigenvalues
33 for i=1:2*par.Ndof

```

```

34     if eigvecL(:,i).' * eigvecR(:,i) == 0
35         keyboard
36     elseif eigvecL(:,i).' * eigvecR(:,i) < 0
37         eigvecL(:,i) = (-1) * eigvecL(:,i);
38     end
39     scalevec = sqrt(eigvecL(:,i).' * eigvecR(:,i));
40     eigvecL(:,i) = eigvecL(:,i) ./ scalevec;
41     eigvecR(:,i) = eigvecR(:,i) ./ scalevec;
42 end
43
44 % Checking orthogonality principles
45 % LMR
46 checkLR = eigvecL.' * eigvecR;
47 checkLRmax = max(max(checkLR - eye(size(checkLR,1)))); 
48 % LKR
49 checkLAR = eigvecL.' * A * eigvecR;
50 checkLARdiag = diag(checkLAR) + eigval;
51 checkLARmax = max(max(checkLAR - eye(size(checkLAR,1)) .* diag(checkLAR)));
52
53 if par.evpcond==1
54     test1 = abs(checkLR);
55     for i=1:length(checkLR)
56         for j=1:length(checkLR)
57             if test1(i,j) < 1e-3
58                 test1(i,j)=0;
59             end
60         end
61     end
62     figure();
63     spy(test1)
64     title('LR check above 1e-3')
65
66     test2 = abs(checkLAR);
67     for i=1:length(checkLAR)
68         for j=1:length(checkLAR)
69             if test2(i,j) < 100
70                 test2(i,j)=0;
71             end
72         end
73     end
74     figure();
75     spy(test2)
76     title('LAR check above 100')
77 end
78
79 eigval = eigvalR;
80 end

```

generalevp_fun.m

```

1 function [eigval,eigvecL,eigvecR,eigfreqhz,eigfreqrad]= ...
2 generalevp_fun(Kglob,Mglob,par)
3

```

```
4 % Checking
5 checksymMglob = norm(Mglob-Mglob.');
6 checksymKglob = norm(Kglob-Kglob.');
7
8 [eigvecR,eigvalR,eigvecL] = eig(Kglob,-Mglob);
9 eigvalL = eigvalR;
10 eigvecL = conj(eigvecL);
11
12 % Mglobt = Mglob.';
13 % Kglobt = Kglob.';
14 % [eigvecR,eigvalR] = eigs(Kglob,-Mglob,2*par.Ndof,'sm');
15 % [eigvecL,eigvalL] = eigs(Kglobt,-Mglobt,2*par.Ndof,'sm');
16
17 % Checking
18 checkEIGR = norm(Kglob*eigvecR + Mglob*eigvecR*eigvalR);
19 checkEIGL = norm(eigvecL.' * Kglob + eigvalL * eigvecL.' * Mglob);
20
21 sum1 = 0;
22 for i=1:2*par.Ndof
23     sum1 = sum1 + sum((eigvalR(i,i)*Mglob+Kglob)*eigvecR(:,i));
24
25 end
26 sum2 = 0;
27 for i=1:2*par.Ndof
28     sum2 = sum2 + sum(eigvecL(:,i).' * (eigvalL(i,i)*Mglob+Kglob));
29
30 end
31
32 % Eigenvalues extracted
33 eigvalR = diag(eigvalR);
34 eigvalL = diag(eigvalL);
35
36 % Sorting left
37 [~,sortL] = sort(abs(eigvalL));
38 %[~,sortL] = sort(abs(imag(eigvalL)));
39 eigvalL = eigvalL(sortL);
40 eigvecL = eigvecL(:,sortL);
41
42 % Sorting right
43 [~,sortR] = sort(abs(eigvalR));
44 %[~,sortR] = sort(abs(imag(eigvalR)));
45 eigvalR = eigvalR(sortR);
46 eigvecR = eigvecR(:,sortR);
47
48 eigval = eigvalR;
49 eigfreqrad = abs(imag(eigval));
50 eigfreqhz = abs(imag(eigval)/(2*pi));
51 damp_ratio = -real(eigval) ./ abs(eigval);
52
53 % Normalizing eigenvalues
54 for i=1:2*par.Ndof
55     if eigvecL(:,i).' * Mglob * eigvecR(:,i) < 0
56         eigvecL(:,i) = (-1) * eigvecL(:,i);
```

```

57     end
58     scalevec = sqrt(eigvecL(:,i) .* Mglob * eigvecR(:,i));
59     eigvecL(:,i) = eigvecL(:,i) ./ scalevec;
60     eigvecR(:,i) = eigvecR(:,i) ./ scalevec;
61 end
62
63 % Checking orthogonality principles
64 % LMR
65 checkLMR = eigvecL.' * Mglob * eigvecR;
66 checkLMRmax = max(max(checkLMR - eye(size(checkLMR,1)))); 
67 % LKR
68 checkLKR = eigvecL.' * Kglob * eigvecR;
69 checkLKRdiag = diag(checkLKR) + eigval;
70 checkLKRmax = max(max(checkLKR - eye(size(checkLKR,1)) .* diag(checkLKR))); 
71
72
73
74 if par.evpcond==1
75     test1 = abs(checkLMR);
76     for i=1:length(checkLMR)
77         for j=1:length(checkLMR)
78             if test1(i,j) < 0.1
79                 test1(i,j)=0;
80             end
81         end
82     end
83     figure();
84     spy(test1)
85     title('abs(L^TM_{glob}R)')
86     set(gca, 'FontSize', 16, 'Fontname', 'Times')
87
88     test2 = abs(checkLKR);
89     for i=1:length(checkLKR)
90         for j=1:length(checkLKR)
91             if test2(i,j) < abs(eigval(i))*0.1
92                 test2(i,j)=0;
93             end
94         end
95     end
96     figure();
97     spy(test2)
98     title('abs(L^TK_{glob}R)')
99     set(gca, 'FontSize', 16, 'Fontname', 'Times')
100 end
101
102 end

```

rotorstator_fun.m

```

1 function [q,t_total,te_total,z_total,R,par,ME]= ...
2     rotorstator_fun(Kglob,Mglob,par,eigvecR,eigvecL,ME)
3
4 %% Rotor system - Truncating mode shapes and def. LKR

```

```
5 % Number of modes included
6 % 8 modes = rigid body
7 % 12 modes = rigid body + 1st bending in each plane
8 % 16 modes = rigid body + 1st and 2nd bending in each plane
9 par.Nr = 16;
10
11 % Finding left and right eigenvector
12 R = eigvecR;
13 L = eigvecL;
14
15 % Reducing the the nr of mode shapes used
16 R = R(:,1:par.Nr);
17 L = L(:,1:par.Nr);
18 LKR = L.*Kglob*R;
19 LKR = eye(length(LKR)) .* diag(LKR);
20
21
22 %% Stator system
23 mi = ME.STAT.mi; mo = ME.STAT.mo;
24 dVB = ME.STAT.dVB; dHB = ME.STAT.dHB;
25 kVB = ME.STAT.kVB; kHB = ME.STAT.kHB;
26 kFT1 = ME.STAT.kFT1; kFT2 = ME.STAT.kFT2;
27
28 M = [mi 0 0 0;
29        0 mi 0 0;
30        0 0 mo 0;
31        0 0 0 mo];
32
33 invM = inv(M);
34
35 D = [dVB 0 -dVB 0;
36        0 0 0 0;
37        -dVB 0 dVB 0;
38        0 0 0 dHB];
39
40 K = [kVB 0 -kVB 0;
41        0 2*kFT1 0 -2*kFT1;
42        -kVB 0 2*kFT2+2*kVB 0;
43        0 -2*kFT1 0 2*kFT1+2*kHB];
44
45
46 A_STAT = [zeros(4) eye(4);
47            -invM*K -invM*D];
48
49
50 %% Full system
51 A = [-LKR zeros(par.Nr,8)
52       zeros(8,par.Nr) A_STAT];
53
54
55 %% Initial conditions
56 z0 = zeros(par.Ndof*2+8,1);
57
```

```
58 %----- Rotor ----- %
59 % Displacements
60 %Y-dir
61 z0(par.Ndof+1:4:2*par.Ndof) = z0(par.Ndof+1:4:2*par.Ndof) + 0.000;
62 %Z-dir
63 z0(par.Ndof+2:4:2*par.Ndof) = z0(par.Ndof+2:4:2*par.Ndof) + 0.000;
64 %Point
65 z0(par.Ndof+1) = z0(par.Ndof+1) + 0.00;
66 % Velocities
67 %Y-dir
68 z0(1:4:par.Ndof) = z0(1:4:par.Ndof) + 0.0;
69 %Z-dir
70 z0(2:4:par.Ndof) = z0(2:4:par.Ndof) + 0.0;
71 %Point
72 z0(ME.TAR.dof) = z0(ME.TAR.dof) + 0.0;
73 z0(ME.TAR.dof+1) = z0(ME.TAR.dof+1) + 0.0;
74
75 % Initial rotation of rotor at bearing position
76 gamma = 0.0;
77 gammad = 0.0;
78 % vel at bearing rel to shaft end
79 pin_point_disp = gamma * ME.S.12n(ME.B.loc);
80 pin_point_vel = gammad * ME.S.12n(ME.B.loc);
81 % Assigning disp & velocities in initial vector (z0)
82 z0(par.Ndof+2:4:2*par.Ndof) = z0(par.Ndof+2:4:2*par.Ndof) + ...
83     gamma * ME.S.12n(:)-pin_point_disp;
84 z0(1:4:par.Ndof,1) = z0(1:4:par.Ndof,1) + gammad * ME.S.12n(:) - pin_point_vel;
85 z0(2:4:par.Ndof,1) = z0(2:4:par.Ndof,1) + gammad * ME.S.12n(:) - pin_point_vel;
86
87 figure();
88 plot(ME.S.12n,z0(1:4:par.Ndof))
89 hold on
90 plot(ME.S.12n,z0(2:4:par.Ndof))
91 legend('Y','Z')
92 title('Before - velocity')
93 figure();
94 plot(ME.S.12n,z0(par.Ndof+1:4:2*par.Ndof))
95 hold on
96 plot(ME.S.12n,z0(par.Ndof+2:4:2*par.Ndof))
97 legend('Y','Z')
98 title('Before - displacement')
99
100 % Initial condition modal coordinate for rotor
101 eta0 = L.' * Mglob * z0(1:par.Ndof*2);
102
103
104 %----- Stator ----- %
105 % Displacement
106 %Y-dir
107 z0(2*par.Ndof+1) = z0(2*par.Ndof+1) + 0.000;
108 %Z-dir
109 z0(2*par.Ndof+2) = z0(2*par.Ndof+2) + 0.000;
110
```

```
111
112 %----- Check initial condition -----%
113 % Initial condition real coordinate for rotor
114 z0check = R*eta0;
115
116 figure();
117 plot(ME.S.l2n,z0check(1:4:par.Ndof) )
118 hold on
119 plot(ME.S.l2n,z0check(2:4:par.Ndof) )
120 legend('Y','Z')
121 title('After - velocity')
122 figure();
123 plot(ME.S.l2n,z0check(par.Ndof+1:4:end) )
124 hold on
125 plot(ME.S.l2n,z0check(par.Ndof+2:4:end) )
126 legend('Y','Z')
127 title('After - displacement')
128
129
130
131 keyboard
132
133
134
135 %----- Full system ----- %
136 z0 = [eta0; z0(2*par.Ndof+1:end) ];
137
138
139 %% Simulation options
140
141 % Solver options
142 %'MaxStep', 1e-3
143 options_ode45 = odeset('RelTol', 1e-9, 'AbsTol', 1e-9, ...
144                         'Events', @(t,z) impactDetect(t, z, -1,par,R,ME));
145 options_ode15s = odeset('RelTol', 1e-9, 'AbsTol', 1e-9, ...
146                         'Events', @(t,z) impactDetect(t, z, 1,par,R,ME));
147
148 t_total = 0;      % time hist for whole sim
149 z_total = [];    % var hist for whole sim
150
151 ze_total = [];   % var at event
152 te_total = [];   % time at event
153 ie_total = 1;    %
154
155 contact_index = [];
156
157 imp.contact = 0;
158 %% Simulation loop
159
160 % Integration methods
161 tspan = [0 9.2]; % For rot simulation
162 %tspan = [0 0.5];
163 tic
```

```
164 while t_total(end) < tspan(2)
165     % Checking for contact
166     [contact,gap,~,~,deltad_dir] = contact_fun(z0,par,R,ME);
167
168     if gap > 0 || gap==0 && deltad_dir <0 % In air
169         [t,z,te,ze,ie] = ode45(@(t,z) fullode_int_fun(t,z,A,L,R,invM,par,ME,imp) ...
170                             ,tspan,z0,options_ode45);
171
172     z0 = z(end,:).';
173     [contact,gap,alpha,delta,deltad] = contact_fun(z0,par,R,ME);
174     imp.contact = contact;
175     imp.gap = gap;
176     imp.alpha = alpha;
177     imp.delta = delta;
178     imp.deltad = deltatad;
179
180
181     fprintf('Event nr.: %d Contact at time: %.5f \n',ie_total,t(end))
182
183 else % In contact
184     [t,z,te,ze,ie] = ode15s(@(t,z) fullode_int_fun(t,z,A,L,R,invM,par,ME,imp) ...
185                             ,tspan,z0,options_ode15s);
186
187     imp.contact = 0;
188
189     fprintf('Event nr.: %d Separation at time %.5f \n',ie_total,t(end))
190 end
191
192
193 % Collect results
194 t_total = [ t_total(1:end-1) ; t ]; % Prev. times + just run times
195 z_total = [ z_total(1:end-1,:) ; z ]; % Prev. resp. + just run resp.
196 te_total = [te_total; te]; % Prev. times at event + just run ...
197 ie_total = ie_total + 1; % Specifies what event occurred
198 %The event times in te correspond to the solutions returned in ye,
199 % and ie specifies which event occurred.
200
201 % Assign new initial condition
202 z0 = z(end,:).';
203 tspan(1) = t(end);
204
205 end
206 toc
207
208 %% Post processing
209 %
210 t = t_total;
211 z_total = z_total.';
212
213 % Physical coordinates of rotor (transforming from modal)
214 z_r = R * z_total(1:par.Nr,:);
215
216 % Physical coordinates of stator
```

```
217 z_s = z_total(par.Nr+1:end,:);
218 % Physical coordinates of full system
219 z = [z_r;
220     z_s];
222
223 % Extracting displacement data from rotor and stator
224 q = [z(par.Ndof+1:2*par.Ndof,:);
225     z(2*par.Ndof+1:2*par.Ndof+4,:)];
226
227 keyboard
228
229
230 end
```

contact_fun.m

```
1 function [contact,gap,alpha,delta,deltad] = contact_fun(z,par,R,ME)
2 z_r = R*z(1:par.Nr);
3 z_s = z(par.Nr+1:end);
4
5 %% Positions/coordinates (p)
6 % Getting two lateral positions of rotor
7 p_r = [real(z_r(par.Ndof+ME.STAT.dof,1)); real(z_r(par.Ndof+ME.STAT.dof+1,1))];
8 % Getting two lateral positions of stator
9 p_s = [real(z_s(1,1)); real(z_s(2,1))];
10
11 %% Velocities (v)
12 % Getting two lateral velocities of rotor
13 v_r = [real(z_r(ME.STAT.dof,1)); real(z_r(ME.STAT.dof+1,1))];
14 % Getting two lateral velocities of stator
15 v_s = [real(z_s(5,1)); real(z_s(6,1))];
16
17
18 %% Difference position (d)
19 % Position vector
20 p_d = p_r - p_s;
21
22 % Position vector length
23 p_d_len = sqrt(p_d(1)^2 + p_d(2)^2);
24
25 % Angle of position vecotor
26 alpha = atan2(p_d(2),p_d(1));
27
28 % Stator geometry
29 [stat_r] = stator_geo_fun(alpha);
30
31 %% Clearance and contact
32 % Clearance
33 gap = stat_r - (p_d_len + ME.S.rad);
34
35 % if gap<0
36 %   keyboard
```

```

37 % end
38
39 %% Difference velocity
40 % Velocity vector
41 v_d = v_r - v_s;
42
43 % Transformation matrix cartesian into cylindrical
44 transM = [cos(alpha) sin(alpha);
45           -sin(alpha) cos(alpha)];
46
47 % Rotating coordinate system into tangential and radial direction
48 v_d_rn = transM * v_d;
49
50 % Extracting components
51 v_d_n = v_d_rn(1);
52 v_d_r = v_d_rn(2);
53
54 %% Contact properties
55 % Contact 0/1
56 if gap <= 0
57     contact = 1;
58 else
59     contact = 0;
60 end
61
62 % delta and deltad
63 if contact==1
64     delta = -gap;
65     deltad = v_d_n;
66 else
67     delta = 0;
68     deltad = 0;
69 end
70
71
72 end

```

stator_geo_fun.m

```

1 function [stat_r] = stator_geo_fun(alpha)
2
3 %stat_r = 29.5722e-3/2;
4 %stat_r = (0.029 - 0.0003486)/2;
5 stat_r = 14.52e-3;
6 %stat_r = 100;
7 end

```

fullode_int_fun.m

```

1 function [zd] = fullode_int_fun(t,z,A,L,R,invM,par,ME,imp)
2 % Physical coordinates (not modal coordinates)
3 z_r = R*z(1:par.Nr);

```

```
4 z_s = z(par.Nr+1:end);
5
6 % Magnet excitation force
7 angle = ((t*par.Omegahz) - floor(t*par.Omegahz))*2*pi;
8 [magexc] = mag_exc_fun(t,angle,par,z_r(par.Ndof+ME.D.dof,1), ...
9 z_r(par.Ndof+ME.D.dof+1,1));
10
11
12 %%
13 if t<1
14 ME.PMB.Dty = 50;
15 ME.PMB.Dtz = 50;
16 elseif t>= 1 && t<=2
17 ME.PMB.Dty = 40;
18 ME.PMB.Dtz = 40;
19 elseif t>2 && t<=3
20 ME.PMB.Dty = 30;
21 ME.PMB.Dtz = 30;
22 elseif t>3 && t<=4
23 ME.PMB.Dty = 20;
24 ME.PMB.Dtz = 20;
25 else
26 ME.PMB.Dty = 8.48;
27 ME.PMB.Dtz = 7.7;
28 end
29
30 %% Contact force evaluation
31 if imp.contact==1
32 %keyboard
33 % Getting the current indentation properties
34 [contact,gap,alpha,delta,deltad] = contact_fun(z,par,R,ME);
35
36 % Calculating indentation normal contact forces
37 [Fn_y,Fn_z,Fn] = Nikravesh(imp,alpha,delta,deltad);
38
39 % Calculating indentation friction contact forces
40 [Fmu_y,Fmu_z] = Ambrosio(par,alpha,ME,z_r,z_s,Fn);
41
42 % Contact forces
43 F_cy = Fn_y + Fmu_y;
44 F_cz = Fn_z + Fmu_z;
45
46 else
47 F_cy = 0;
48 F_cz = 0;
49 end
50
51
52 %% Forces acting on rotor
53 Q_r = zeros(par.Ndof,1); % Physical forces
54
55 % External force - Unbalance
56 Q_r(ME.D.dof,1) = ME.D.m0 * ME.D.e * par.Omega^2 * ...
```

```

57             cos(par.Omega * t + ME.D.phi);
58 Q_r(ME.D.dof+1,1) = ME.D.m0 * ME.D.e * par.Omega^2 * ...
59             sin(par.Omega * t + ME.D.phi);
60
61 % External force - Bearing stiffness
62 Q_r(ME.PMB.dof,1) = Q_r(ME.PMB.dof,1) - z_r(par.Ndof+ME.PMB.dof,1) ...
63             * ME.PMB.Kty;
64 Q_r(ME.PMB.dof+1,1) = Q_r(ME.PMB.dof+1,1) - z_r(par.Ndof+ME.PMB.dof+1,1) ...
65             * ME.PMB.Ktz;
66
67 Q_r(ME.PMB.dof,1) = Q_r(ME.PMB.dof,1) - z_r(par.Ndof+ME.PMB.dof+1,1) ...
68             * ME.PMB.Ktyz;
69 Q_r(ME.PMB.dof+1,1) = Q_r(ME.PMB.dof+1,1) - z_r(par.Ndof+ME.PMB.dof,1) ...
70             * ME.PMB.Ktzy;
71
72 Q_r(ME.B.dof,1) = Q_r(ME.B.dof,1) - z_r(par.Ndof+ME.B.dof,1) * ME.B.Kty;
73 Q_r(ME.B.dof+1,1) = Q_r(ME.B.dof+1,1) - z_r(par.Ndof+ME.B.dof+1,1) * ME.B.Ktz;
74
75
76 % External force - Bearing damping
77 Q_r(ME.PMB.dof,1) = Q_r(ME.PMB.dof,1) - z_r(ME.PMB.dof,1) * ME.PMB.Dty;
78 Q_r(ME.PMB.dof+1,1) = Q_r(ME.PMB.dof+1,1) - z_r(ME.PMB.dof+1,1) * ME.PMB.Dtz;
79 Q_r(ME.B.dof,1) = Q_r(ME.B.dof,1) - z_r(ME.B.dof,1) * ME.B.Dty;
80 Q_r(ME.B.dof+1,1) = Q_r(ME.B.dof+1,1) - z_r(ME.B.dof+1,1) * ME.B.Dtz;
81
82 % External force - Impact force
83 Q_r(ME.STAT.dof,1) = Q_r(ME.STAT.dof,1) + F_cy;
84 Q_r(ME.STAT.dof+1,1) = Q_r(ME.STAT.dof+1,1) + F_cz;
85
86 % Magnetic force excitation
87 Q_r(ME.TAR.dof,1) = Q_r(ME.TAR.dof,1) - magexc;
88
89 f_r = [zeros(par.Ndof,1);
90         Q_r];
91
92 g = L.'*f_r; % Modal forces
93
94 %% Forces acting on stator
95
96 Q_s = zeros(4,1);
97
98 Q_s(ME.STAT.dof,1) = Q_s(ME.STAT.dof,1) - F_cy;
99 Q_s(ME.STAT.dof+1,1) = Q_s(ME.STAT.dof+1,1) - F_cz;
100
101 f_s = [zeros(4,1);
102         invM*Q_s];
103
104 %% Force state-vector
105 f = [g;
106         f_s];
107
108 %% Equating
109 zd = A * z + f;

```

```
110
111 end
```

Ambrosio.m

```
1 function [Fmu_y,Fmu_z] = Ambrosio(par,alpha,ME,z_r,z_s,Fn)
2 %% Ambrosio friction constants and dynamic friction coefficient
3 v_0 = 1e-4;
4 v_1 = 2e-4;
5 mu = 0.2;
6
7 % Transformation matrix cartesian into cylindrical
8 transM1 = [cos(alpha) sin(alpha);
9             -sin(alpha) cos(alpha)];
10
11 % Transformation matrix cylindrical into cartesian
12 transM2 = [cos(-alpha) sin(-alpha);
13             -sin(-alpha) cos(-alpha)];
14
15 %% Velocity of rotor center
16 v_r = [real(z_r(ME.SLE.dof,1)); real(z_r(ME.SLE.dof+1,1))];
17
18 % Rotating coordinate system into tangential and radial direction
19 v_r_nt = transM1 * v_r;
20
21 % Splitting velocity vector into radial and tangential component
22 v_r_n = v_r_nt(1);
23 v_r_t = v_r_nt(2) + par.Omega * ME.S.rad;
24
25
26 %% Velocity of stator center
27 v_s = [real(z_s(5,1)); real(z_s(6,1))];
28
29 % Rotating coordinate system into tangential and radial direction
30 v_s_nt = transM1 * v_s;
31
32 v_s_n = v_s_nt(1);
33 v_s_t = v_s_nt(2);
34
35 %% Finding relative tangential velocity
36 v_rel = v_r_t - v_s_t;
37
38 %% Calculating c_d
39 if abs(v_rel) < v_0
40     c_d = 0;
41 elseif v_0 <= abs(v_rel) && abs(v_rel) <= v_1
42     c_d = (abs(v_rel)-v_0)/(v_1-v_0);
43 elseif abs(v_rel) < -v_1 || v_1 < abs(v_rel)
44     c_d = 1;
45 end
46
47 %% Calculating friction force
48 Ft = -sign(v_rel) * mu * c_d * Fn;
```

```

49 %% Calculating friction force components
50 % Rotating coordinate system into cartesian
51 Ft_yz = transM2 * [0 Ft].';
52
53 Fmu_y = Ft_yz(1);
54 Fmu_z = Ft_yz(2);
55
56 % if Ft>0 || Ft<0
57 % keyboard
58 % end
59
60 end

```

Nikravesh.m

```

1 function [Fn_y,Fn_z,Fn] = Nikravesh(imp,alpha,delta,deltad)
2
3 E_r = 70e9; % Young's modulus sphere (rotor material part) [Pa]
4 E_s = 100e9; % Young's modulus sphere (stator material part) [Pa]
5 nu_r = 0.35; % Poisson's ratio for the rotor material [-]
6 nu_s = 0.35; % Poisson's ratio for the stator material [-]
7
8 n = 3/2; % Penetration exponent
9 ce = 0.5; % Coefficient of restitution
10
11 r_r = 0.025/2; % Radius of rotor
12 r_s = 0.029/2; % Radius of stator
13
14 % Material properties
15 h_r = (1 - nu_r^2)/(pi*E_r);
16 h_s = (1 - nu_s^2)/(pi*E_s);
17 K = ( 4/(3*pi*(h_r + h_s)) ) * ((r_r*r_s)/(r_r+r_s))^(0.5);
18
19 % Contact forces
20 Fn = K * delta^n * (1 + (3*(1-ce^2)/4) * deltad/imp.deltad );
21
22 % Transformation matrix cylindrical to cartesian
23 transM = [cos(-alpha) sin(-alpha);
24 -sin(-alpha) cos(-alpha)];
25
26 % Rotating coordinate system into inertial coordinatesystem
27 Fn_yz = transM * [-Fn 0].';
28
29 % Contact forces in inertial coordinates
30 Fn_y = Fn_yz(1);
31 Fn_z = Fn_yz(2);
32
33 end

```

DTU Mechanical Engineering
Section of Solid Mechanics
Technical University of Denmark

Nils Koppels Allé, Bld. 404
DK-2800 Kgs. Lyngby
Denmark
Phone (+45) 4525 4250
Fax (+45) 4593 1475
www.mek.dtu.dk